



HAL
open science

Ge/SiGe quantum well devices for light modulation, detection, and emission

Papichaya Chaisakul

► **To cite this version:**

Papichaya Chaisakul. Ge/SiGe quantum well devices for light modulation, detection, and emission. Other [cond-mat.other]. Université Paris Sud - Paris XI, 2012. English. NNT : 2012PA112241 . tel-00764154

HAL Id: tel-00764154

<https://theses.hal.science/tel-00764154>

Submitted on 26 Nov 2014

HAL is a multi-disciplinary open access archive for the deposit and dissemination of scientific research documents, whether they are published or not. The documents may come from teaching and research institutions in France or abroad, or from public or private research centers.

L'archive ouverte pluridisciplinaire **HAL**, est destinée au dépôt et à la diffusion de documents scientifiques de niveau recherche, publiés ou non, émanant des établissements d'enseignement et de recherche français ou étrangers, des laboratoires publics ou privés.

UNIVERSITE PARIS-SUD

ÉCOLE DOCTORALE : STITS
Institut d'électronique fondamentale

DISCIPLINE PHYSIQUE

THÈSE DE DOCTORAT

soutenue le 23/10/2012

par

Papichaya CHAISAKUL

Ge/SiGe quantum well devices for light
modulation, detection, and emission

Composition du jury :

Isabelle SAGNES
Dries VAN THOURHOUT
Jean-Jacques GREFFET
Bert Jan OFFREIN
Alain CHANTRE
Delphine MARRIS-MORINI
Laurent VIVIEN

CNRS/LPN
Ghent University-IMEC
Institut d'Optique
IBM Research - Zurich
STMicroelectronics
Université Paris-Sud, IEF
Université Paris-Sud, IEF

Rapporteur
Rapporteur
Président du jury
Examineur
Examineur (invité)
Co-directrice de thèse
Directeur de thèse

Acknowledgements

This PhD thesis is a truly memorable experience for me and clearly it will not be feasible without supports from various people.

Throughout three years, I feel fortunate and grateful to work on a daily basis with Dr. Delphine Marris-Morini, my PhD thesis co-director. From GDS designs to publications, Delphine's guidances and recommendations are included in every step of the development. Experimentally, we managed to conceive and realize several new exciting measurements. I never forget our winning moments like (finally) getting a clean QCSE, seeing the first electroluminescence, and managing several successful high speed measurements without an optical amplifier! I also like to acknowledge Delphine's attentions beyond scientific world; I feel that I can speak with Delphine on any issue and it contributes significantly to the progress of my works and life.

Dr. Laurent Vivien is my PhD thesis director and he is instrumental in the direction of my investigation. My motivation to investigate Ge/SiGe MQWs for different photonic functionalities largely stems from Laurent's comments on the possibilities during my internship at IEF. Laurent is one of the first persons showing me how to use optical characterization test bench. Thanks to his extensive experiences with Ge photodetector, Laurent also gave me several useful advices in device's design, fabrication, and characterizations of Ge/SiGe MQW devices. I also would like to acknowledge Laurent's effort in Silicon Photonics team management and ensure the necessities for the on-going research.

Dr. Giovanni Isella and Dr. Daniel Chrastina from L-NESS, Politecnico di Milano are clearly the fundamental persons of Ge quantum wells activity since the beginning. All of the Ge/SiGe MQW epitaxies leading to the results in this PhD thesis were grown by Giovanni and Danny, and I really want to make our collaboration fruitful since our first meeting in October 2009. Significantly, I would like to acknowledge Giovanni and Danny's contributions regarding several physical comments for experimentally-observed phenomena. I also like to acknowledge XRD measurement data which are necessary in device development.

I would like to express my sincere thanks to Dr. Dries Van Thourhout and Dr. Isabelle Sagnes who accept to be the reviewers of my PhD thesis. During my PhD studies, I have been following several published works from the Ghent-IMEC and LPN teams. It is my great pleasure to have my thesis reviewed by the researchers whose works I feel enthusiastic on. It is also my honour that Dr. Jean-Jacques Greffet, Dr. Bert Jan Offrein, and Dr. Alain Chantre accept to become the president and jury members of my PhD thesis. Laboratoire Charles Fabry is famous for its fundamental and technological research; the research progress from IBM Photonics team always draws significant attention from Silicon Photonics community all over the world, while STMicroelectronics is one of the world leaders in Ge-on-Si research.

I cannot say enough how much I appreciate and value Dr. Jean-René Coudeville's consultations during my device fabrication at the University of Paris-Sud cleanroom. Jean-René always provides me with a lot of useful and pinpointed suggestions. His expertise in cleanroom technology and willingness to share them with PhD students and other researchers were crucial to the achievement of every photonic device I developed and fabricated.

I would like to thank Dr. Eric Cassan and Dr. Nicolas Izard for every scientific and non-scientific conversation we have had during the past three years. Eric is an active professor in our team and Eric has been an example for me on dealing with different responsibilities. I also like to express my appreciation to Nicolas who always explains me enthusiastically and detailedly each technical question I have during electroluminescence and other measurements.

I acknowledge the guidance from our cleanroom engineers during my fabrication. Xavier Le Roux has given me several useful tips during the process development. In many aspects, I have learnt to handle and manage the whole fabrication process from Xavier. Xavier's suggestion on H₂O₂ usage is one of the most important tricks used in my fabrication. Samson Edmond gave me his parameters for very deep etching process, which is useful for device characterization. Moreover, Samson always tells me several important practices in order to be better protected during working in the cleanroom. I also like to acknowledge Samson's kindness in teaching PhD students.

I would like to acknowledge every PhD student and Postdoctoral researcher at our Silicon Photonic team (MINAPHOT). Firstly, I am glad to share the office with Gilles Rasigade (with Delphine and Eric). Gilles work ethic is admirable to me, and that motivates me to keep doing my jobs well. Etienne Gaufrès is a very nice person to talk with; personally, I feel an additional positive energy after speaking to him. I feel fortunate to have Gilles and Etienne as seniors during the early years. It is my pleasure to be friend with every current PhD student at Silicon Photonics team: Van Do Khanh, Melissa Ziebell, Charles Caër, Mohamed-said Rouifed, Andrien Noury, Nicolás Abadiá. Van and I began the PhD at the same time; so, we normally went through each stage of a PhD work at the same moment. Melissa and I always have professional and personal discussions with each other. Her experience is fascinating and I learnt a lot from her regarding several aspects of professional life. I enjoy talking to Charles and listening to his opinion on the recent interesting publications and scientific issues. Charles is an active PhD student who has a concrete idea on his research career. Talking to him gave me courage to realize my research, as he gave me an impression that there was a person with a more challenging research plan! Mohamed is a PhD student in Ge/SiGe MQWs since 2011; so, we have been working directly with each other. I have a pleasure to teach and show him several fabrication and characterization techniques. Mohamed always aim to do his work efficiently, and I hope that he will succeed in fulfilling his research objectives. Working with a new PhD student is a very instructive experience for me. Andrein is another person whom everyone, including me, enjoy having conversation with. I always hope to see him getting the results, which he is aiming for, during his PhD works. Nicolás is working enthusiastically since Nov 2011; he always wants to solve the problems effectively. I am truly appreciated to be part of the same project as him since then; it has been a real valuable experience professionally and personally.

I also like to acknowledge Eleonora Gatti from Univ. Milano-Bicocca and Jacopo Frigerio from Politecnico di Milano, who are playing significant role in our collaboration with L-NESS. Eleonora is a very organized person who is willing to share her expertise and experience in optical characterization and material properties with us. Jacopo is an expert in Epitaxy using LEPECVD and knows very well cleanroom fabrication. Jacopo is the grower of all the Ge/SiGe MQW samples we received recently; he usually comes up with a new idea or explanation to further improve or diversify our works.

I would like to thank Dr. Johann Osmond, with whom I was working during my internship at IEF in 2009. Johann was teaching me on how to handle optical and electrical connections. He also showed me how to handle the RF probe and high speed photodetector characterizations.

I am truly grateful to everyone working at the University of Paris-Sud cleanroom who is always willing to give me various advices. PhD students from the Photis team like Salam Sakr, Andres De Luna Bugallo, and Daniele Costantini and from the Minasys team like Guillaume Schelcher and Mériam Azzouz are always helpful. Salam is an enthusiastic researcher who I enjoy having conversation with him professionally and personally. Andres is an E-beam lithography expertise, and the only one in IEF with whom I can talk about NFL. Several University of Paris cleanroom engineers including Nathalie Isac, François Maillard, Jean-Luc Perrossier, David Bouville, Benoît Belier, Cédric Villebasse, and Fabien Bayle are helpful and supportive to me in several moments. I sincerely acknowledge Dr. Anatole Lupu, who always allows us to use his equipment. All of the results during the first half of my PhD thesis will be difficult to obtain without the tunable laser from Anatole. Moreover, Dr. Paul Crozat, Dr. Nicolas Zerounian, Dr. Lorenzo Rigutti, Dr. Adel Bousseksou, Dr. Maria Tchernycheva, Dr. Raffaele Colombelli, Dr. François Julien, Dr. Marion Woytasik, Dr. Arnaud Bournel, Dr. Juliette Mangeney, Dr. Jérôme Saint-Martin, Dr. Philippe Dollfus are acknowledged for their various practical helps during my PhD thesis.

I express my sincere gratitude toward the French Ministry of Research for the 3 year PhD fellowships, and the French ANR GOSPEL project for research funding, which make possible the works on Ge/SiGe MQWs at our team in the long run.

I deeply appreciate the constant helps and thoughtfulness from my parents, Surin and Panthong Chaisakul, as well as those from my sister, Sakulrat Chaisakul. They constantly support me throughout my life. I hope that I will be able to look after you properly in the near future.

I am truly grateful for the supports and patience of Pornuma Thongsawai, my girlfriend, and her mother. My girlfriend always tries to understand me and she is the one who always listen and endure with me during my past five year in Europe despite the long distance between us for the past three years. There is no way to translate into words my appreciation and thankfulness. Her mother always looks after me as her son, and takes care of me very well. I will try to look after her daughter as well as she has done to me.

Table of contents

Acknowledgements	iii
Table of contents	vii
Résumé en français :	x
Chapter 1. Introduction	1
1.1 Optics for interconnect	2
1.2 Silicon-based photonics	5
1.3 Ge/SiGe multiple quantum well structures for optoelectronics.....	13
1.4 Ge/SiGe multiple quantum wells: state of the art.....	18
Chapter 2. Ge/SiGe quantum well epitaxial growth and optoelectronic device fabrication	23
2.1 Ge multiple quantum wells grown by LEPECVD.....	23
2.2 Fabrication of Ge quantum well optoelectronic devices	27
2.2.1 DC surface illuminated p-i-n diode fabrication	28
2.2.2 High speed surface-illuminated and waveguide optoelectronic device fabrication.	30
2.3 Conclusion	42
Chapter 3. Light modulation by QCSE from Ge/SiGe MQWs.....	44
3.1 QCSE measurements from surface illuminated Ge/SiGe MQWs p-i-n diode	46
3.1.1 Optical transmission measurements.....	46
3.1.2 Photocurrent measurements	52
3.1.3 Differential transmission measurements	56
3.2 QCSE measurements from Ge/SiGe MQWs planar waveguides for TE and TM polarization light.....	58
3.2.1 Polarization dependence of quantum-confined Stark effect in Ge/SiGe quantum well planar waveguides.....	62
3.2.2 QCSE for optical modulation in planar waveguides.....	69
3.3 High speed performance of Ge/SiGe MQW electro-absorption modulator	71
Chapter 4. Light detection and emission characteristics of Ge/SiGe MQWs	80

4.1 High speed light detection from Ge/SiGe MQWs.....	81
4.1.1 Surface-illuminated Ge/SiGe MQW photodiodes	81
4.1.2 Ge/SiGe MQW waveguide photodetector	90
4.2 Room temperature direct-gap electroluminescence from Ge/SiGe MQWs	100
4.3 Conclusion	108
Chapter 5. Conclusions and perspectives	110
5.1 General conclusions.....	110
5.2 Perspectives and future works	112
5.2.1 Optimized Ge/SiGe MQW waveguide for high performances electro-absorption modulator and photodetector	112
5.2.2 Operating wavelength	113
5.2.3 Light emission efficiency.....	114
5.2.4 Direct growth of Ge/SiGe MQWs on Si and waveguide integration with SOI platform.....	115
5.2.5 Ge/SiGe MQWs on SiGe waveguide.....	115
Publications	120
Bibliography.....	126

Résumé en français :

Composants à puits quantiques Ge/SiGe pour la modulation, la détection et l'émission de lumière

La photonique silicium est un domaine en pleine expansion depuis quelques années. A terme, l'intégration de l'optique et de l'électronique sur les mêmes circuits doit permettre une augmentation des performances des circuits intégrés. Les télécommunications optiques également bénéficieront du développement de solution bas coût et haute performance pour les liens optiques rapides. Les composants optoélectroniques à base de silicium sont les points clefs pour le développement de ces circuits intégrés photoniques. Malgré les démonstrations récentes de modulateur silicium, photodétecteur germanium, et la réalisation de sources optiques utilisant des matériaux III-V reportés sur silicium, l'intégration de ces différents éléments sur un même circuit électronique est difficile, à cause des différents matériaux et technologies utilisés pour chaque bloc de base. De plus les modulateurs optiques silicium à large bande passante optique nécessitent des régions actives de plus de un millimètre de long, présentant une consommation électrique importante. Finalement, une source optique efficace en silicium est toujours le Saint Graal des chercheurs du domaine.

Dans ce contexte, cette thèse est consacrée à l'étude des propriétés optiques et optoélectroniques autour de la bande interdite directe et à température ambiante des structures à puits quantiques Ge/SiGe. Dans un premier temps, les propriétés de modulation optique sont étudiées, permettant ensuite le développement d'un modulateur optique rapide et à faible puissance électrique, basé sur l'Effet Stark Confiné Quantiquement (ESCQ) dans les puits quantiques Ge/SiGe. Puis les propriétés de photodétection et d'émission de lumière à température ambiante sont étudiées, dans le but d'utiliser ces structures comme brique de base pour l'ensemble des composants optoélectroniques formant un lien optique.

La croissance des structures Ge/SiGe a été réalisée par G. Isella et D. Chrastina du laboratoire Laboratory for Epitaxial Nanostructures on Silicon and Spintronics (L-NESS), Politecnico di Milano, en Italie. En raison du désaccord de maille entre le silicium et le

germanium, la croissance directe de germanium sur silicium crée des dislocations. Un moyen de les éviter consiste à utiliser une couche tampon graduelle en SiGe permettant de passer très progressivement du silicium à un alliage à forte concentration en germanium (typiquement 90 %) tout en restant relaxé (sans contraintes). La structure à puits quantiques germanium peut ensuite être réalisée sur cette couche supérieure, avec une concentration de dislocations minimales. Dans cette thèse, les structures sont réalisées par une épitaxie originale de type « Low Energy Plasma Enhanced Chemical Vapour Deposition » (LEPECVD).

Les échantillons réalisés sont constitués de la manière suivante : sur un substrat de silicium, une couche tampon graduelle de 13 μm d'épaisseur est épitaxiée, avec une concentration de germanium augmentant linéairement avec un gradient de 7%/ μm , allant du Si au $\text{Si}_{0.1}\text{Ge}_{0.9}$. Ensuite une couche de 2 μm d'épaisseur est déposée sur la couche graduelle, formant un substrat virtuel relaxé, sur lequel il est possible de faire croître des hétérostructures à forte concentration en germanium et de très bonne qualité cristalline. Pour intégrer les multipuits dans une diode pin, une couche $\text{Si}_{0.1}\text{Ge}_{0.9}$ de 500 nm dopé au bore est utilisée pour obtenir un contact p, suivi d'une couche intrinsèque de 50 nm et de l'empilement des multipuits. Finalement une couche de 50 nm de $\text{Si}_{0.1}\text{Ge}_{0.9}$ non dopé suivi d'une couche de 100 nm de $\text{Si}_{0.1}\text{Ge}_{0.9}$ dopé au phosphore sont ajoutées pour le contact n.

Après réception des structures épitaxiées, j'ai fabriqué l'ensemble des dispositifs de tests en salle blanche (CTU/IEF Minerve). L'ensemble des techniques de fabrication ne sont pas reportées dans ce résumé mais figurent dans le manuscrit complet. Puis j'ai caractérisé les échantillons et les principaux résultats expérimentaux obtenus concernant la modulation, la photodétection et l'émission de lumière dans les structures à puits quantiques Ge/SiGe sont résumés ci-dessous.

1. Modulateur optique par Effet Stark Confinement Quantiquement dans les structures à puits quantiques Ge/SiGe

Dans cette thèse, les caractéristiques de modulation optique des structures à puits quantiques Ge/SiGe sont étudiées dans trois configurations différentes : des diodes à illumination par la surface, des guides d'onde planaire de 100 μm de large, et des diodes en guide d'onde de largeur 3 μm fonctionnant à haute fréquence. Les diodes à illumination par la surface sont les premières structures que nous avons utilisées pour vérifier la présence et

étudier l'ESCQ dans nos structures. Ensuite l'ESCQ a été étudié dans le cas où la lumière se propage parallèlement aux plans des puits quantiques, grâce aux structures à guides d'onde planaires. Enfin un guide d'onde de 3 μm de large et de 90 μm de long comportant des électrodes coplanaires hyperfréquences a été fabriqué et caractérisé pour démontrer un modulateur optique compact et rapide.

1.1 Mesures de l'ESCQ dans des diodes pin à puits quantiques Ge/SiGe à illumination par la surface

Pour ces premières démonstrations nous avons utilisé une diode pin à illumination par la surface (figure 1a), de grande surface ($1 \times 1 \text{ mm}^2$) afin de pouvoir directement comparer les résultats obtenus avec la référence 1. La région à multipuits à proprement parler est formée de 50 périodes comprenant chacune un puits de germanium de 10 nm et une barrière de 15 nm de $\text{Si}_{0.15}\text{Ge}_{0.85}$. La concentration moyenne de germanium dans les multipuits est ainsi égale à celle du substrat virtuel (90 %), permettant ainsi d'obtenir une compensation des contraintes dans la structure.

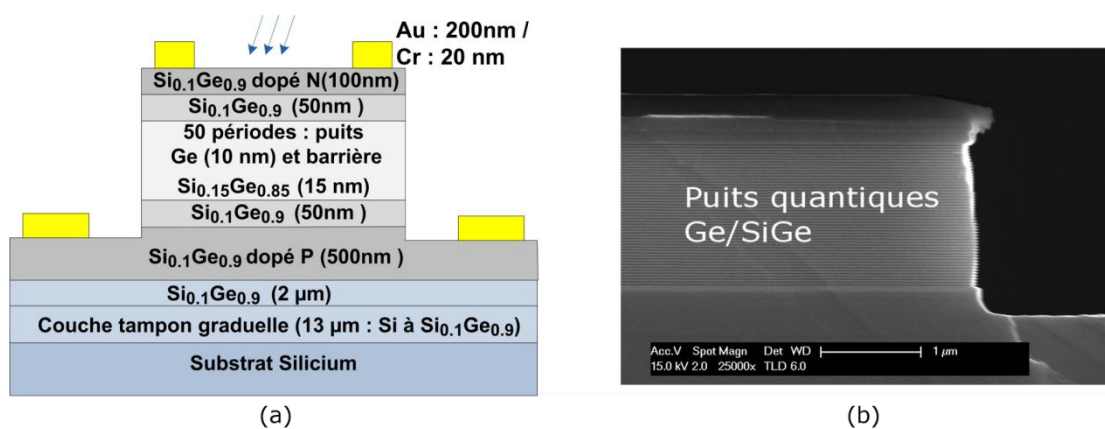


Figure 1 : Diode pin à puits quantiques Ge/SiGe à illumination par la surface pour la démonstration de l'Effet Stark Confiné Quantiquement (a) : schéma en coupe (b) : photographie en coupe prise par un microscope électronique à balayage

Nous avons caractérisé ces structures en comparant les spectres de photocourant et de transmission optique. La fraction de lumière absorbée par les puits quantiques en fonction de la longueur d'onde et du champ électrique appliqué est reportée sur la figure 2a. A 0 V un pic d'absorption est clairement visible à 1410 nm, lié à la transition excitonique entre le premier

niveau électronique de la bande de conduction et le premier niveau de trous lourds de la bande de valence au point Γ (centre de la zone de Brillouin), suivi d'une brusque diminution du coefficient d'absorption lié à la bande interdite directe de la structure à multipuits. La demi-largeur à mi-hauteur du pic d'absorption excitonique a été mesurée à 6 meV, ce qui est significativement plus faible que les 8 meV reportés dans une précédente étude [1] alors que le nombre total de puits quantiques est supérieur (50 dans notre cas contre 10 dans la référence 1). Cette mesure indique la très bonne qualité et l'uniformité des multipuits.

Lorsqu'une tension inverse est appliquée aux bornes de la diode, un champ électrique apparaît dans la région intrinsèque donc au niveau des multipuits quantiques, et les deux caractéristiques de l'ESCQ sont visibles : décalage vers les hautes longueurs d'onde du bord de bande d'absorption, et diminution du pic d'absorption excitonique (figure 2a). Pour nous assurer que les mesures n'étaient pas perturbées par d'éventuels effets thermiques nous avons effectué des mesures différentielles de transmission en appliquant sur la diode une tension sinusoïdale à 1 kHz et en envoyant le signal optique modulé en sortie de la structure à puits Ge/SiGe sur une détection synchrone. Les résultats sont présentés sur la figure 2b. Pour chaque amplitude de la tension sinusoïdale appliquée, l'amplitude de la transmission optique à 1 kHz présente deux maxima en longueur d'onde, dont les positions coïncident avec les longueurs d'onde pour lesquelles la variation de la transmission est la plus grande d'après les mesures statiques de la figure 2a. Ce résultat indique donc qu'il n'y a pas de contribution thermique aux mesures statiques.

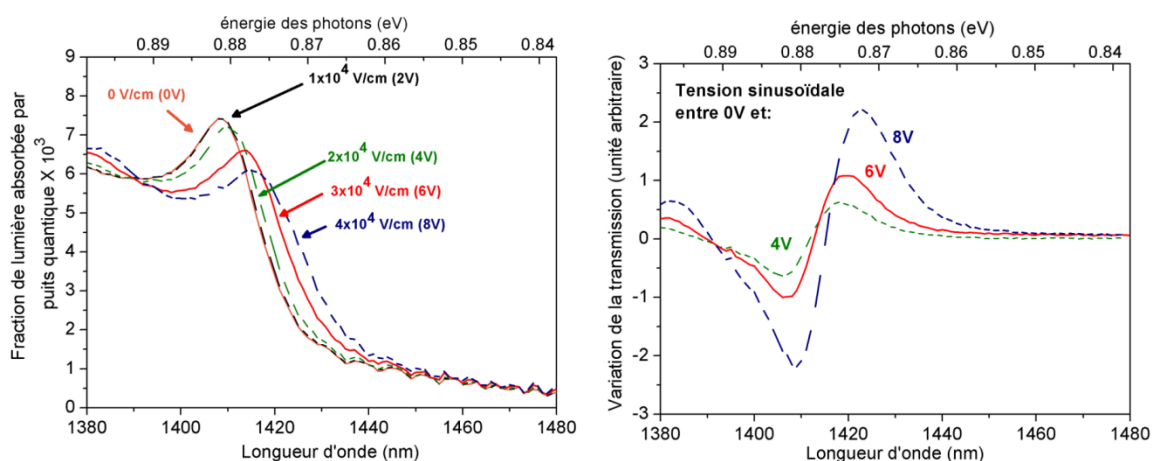


Figure 2 : Spectres d'absorption en fonction de la tension appliquée (a) mesure statique ;
(b) amplitude de la transmission à 1kHz mesurée par détection synchrone

Les mesures des figures 2 illustrent la possibilité de réaliser un modulateur optique à électro-absorption avec cette structure. En effet à une longueur d'onde fixée (à 1425 nm par exemple) une variation de tension appliquée sur la diode crée une variation de l'absorption dans les puits quantiques et donc de la transmission optique.

1.2 ESCQ dans des guides d'onde planaires Ge/SiGe

Dans les applications que nous considérons le modulateur optique doit être intégré dans un guide d'onde, la lumière se propageant parallèlement au plan des couches. Nous avons donc fabriqué des dispositifs de tests pour étudier l'ESCQ pour cette configuration et sa dépendance à la polarisation de la lumière incidente. Les dispositifs fabriqués sont représentés schématiquement sur la figure 3a. Il s'agit de guides d'onde plans, de largeur 100 μm et de différentes longueurs (34 et 64 μm). Le confinement vertical est assuré par la couche tampon graduelle de 13 μm entre le silicium (d'indice 3.5) et le $\text{Si}_{0.1}\text{Ge}_{0.9}$ (d'indice 4.2). La région active est formée de 20 périodes comprenant un puits de germanium de 10 nm et une barrière de 15 nm de $\text{Si}_{0.15}\text{Ge}_{0.85}$ (figure 3b).

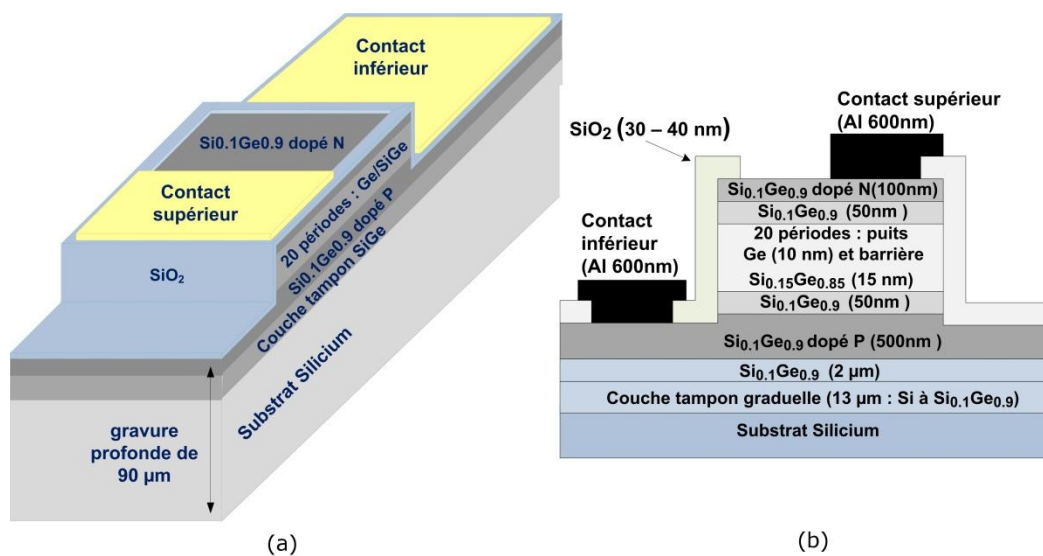


Figure 3 : Diode pin à puits quantiques Ge/SiGe à éclairage latéral

(a) : schéma de principe du composant (b) : schéma en coupe de la structure

Les spectres de transmission ont été mesurés pour les polarisations incidentes de la lumière TE et TM et pour différentes tensions appliquées sur la diode. Pour en déduire

l'absorption due à la région active à multipuits Ge/SiGe, il est important de dissocier la contribution due aux pertes de couplage. Pour cela nous avons considéré que les pertes de couplages sont constantes en fonction de la longueur d'onde alors que l'absorption dans la région active dépend de la longueur d'onde. Les spectres de transmission mesurés ont alors été normalisés à 0 à la longueur d'onde de 1540 nm (longueur d'onde la plus élevée de la mesure). En effet des mesures distinctes de photocourant nous ont permis d'évaluer que l'absorption dans ces guides planaires est inférieure à 1 dB à cette longueur d'onde. Ainsi bien que cette méthode soit approchée, nous obtenons une précision sur les niveaux d'absorption dans la région active meilleure que 1 dB.

En polarisation TE (figure 4a) les résultats sont similaires à ceux obtenus pour une illumination verticale : un pic d'absorption excitonique est clairement visible à 0 V. Lorsque la tension inverse augmente, on observe à la fois le décalage vers les plus hautes longueurs d'onde du bord de bande, ainsi que la diminution du pic d'absorption excitonique. Ce résultat est conforme aux études théoriques, prévoyant une transition entre le premier niveau électronique de la bande de conduction et le premier niveau de trous lourds dans la bande de valence au point Γ pour une lumière incidente TE [2]. En polarisation TM par contre cette transition est théoriquement impossible [2]. Les résultats expérimentaux sont reportés sur la figure 4b. Le pic d'absorption à 1405 nm disparaît clairement pour cette polarisation. Les variations de l'absorption avec la tension appliquée s'expliquent par l'absorption due au pic excitonique entre le premier niveau électronique de la bande de conduction et le premier niveau de trous légers dans la bande de valence. A 0 V le pic excitonique correspondant se situe à plus basse longueur d'onde, malheureusement inaccessible avec la source laser utilisée lors de la mesure. Ce résultat forme néanmoins la 1ère démonstration expérimentale de la dépendance à la polarisation de l'Effet Stark Confiné Quantiquement dans des guides d'onde à multipuits quantiques Ge /SiGe.

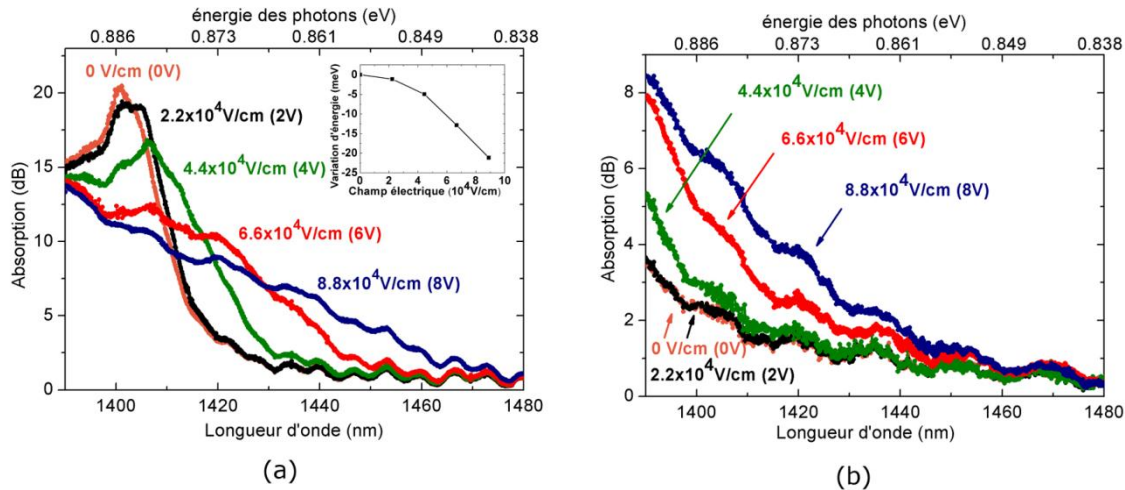


Figure 4 : Spectres d'absorption de la structure du guide plan à puits quantiques Ge/SiGe de longueur 34 μm (a) en polarisation TE ; (b) en polarisation TM. Dans l'encadré : décalage du bord de bande d'absorption en fonction du champ électrique.

Un modulateur optique intégré en guide d'onde doit présenter simultanément un fort taux d'extinction (variation de l'absorption en fonction de la tension appliquée dans le cas d'un modulateur à électro-absorption) mais aussi des pertes d'insertion faibles dans l'état passant. Pour évaluer les performances de modulation des structures à puits quantiques Ge/SiGe le taux d'extinction en fonction de la longueur d'onde pour différentes tensions appliquées a été déduit des mesures précédentes en polarisation TE (figure 5a). L'absorption à 0 V est également reportée.

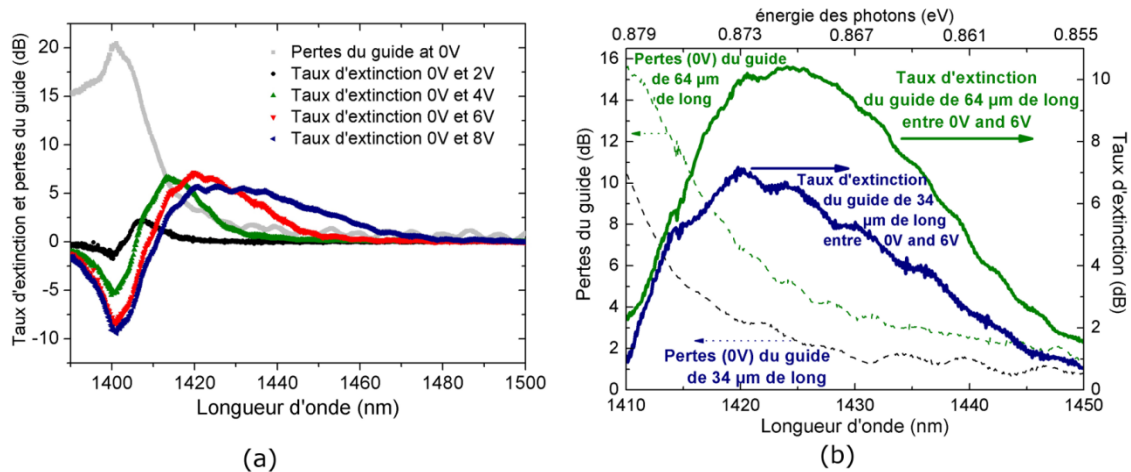


Figure 5 : - Taux d'extinction et pertes du guide plan à puits Ge/SiGe en polarisation TE (a) : guide de 34 µm, en fonction de la tension appliquée (b) comparaison des guides de 34 et 64 µm de long.

Les taux d'extinction entre 0 et 6 V ainsi que les pertes d'insertions à 0 V sont reportés sur la figure 5b pour les deux longueurs de région active : 34 et 64 µm, en polarisation TE. Pour une longueur de 34 µm, le taux d'extinction atteint 7 dB avec simultanément un niveau de pertes de l'ordre de 3 dB vers 1420 nm. Comme attendu le taux d'extinction et les pertes d'insertion augmentent quand la longueur augmente. Le guide de 64 µm de long présente un taux d'extinction supérieur à 5 dB dans une gamme spectrale comprise entre 1413 and 1439 nm, et une valeur de 10 dB est même atteinte entre 1420 et 1427 nm. De plus un taux d'extinction supérieur à 5 dB est obtenu simultanément avec des pertes d'insertion inférieures à 4 dB dans une gamme spectrale de 11 nm entre 1428 et 1439 nm. Ces premiers résultats sont donc extrêmement prometteurs pour la réalisation de modulateurs optiques compacts et performants.

1.3 Modulateur optique haute fréquence à électroabsorption à base de puits quantiques Ge/SiGe

Dans cette partie, les performances en rapidité des structures à puits quantiques Ge/SiGe sont étudiées, pour évaluer leur potentiel dans les futurs circuits intégrés. Pour réaliser des composants haute fréquence, la capacité équivalente à la diode pin polarisée en inverse doit être réduite, ce qui peut être obtenu principalement par une réduction de sa

surface. Pour cela nous avons fabriqué des diodes en guide d'onde de $3\mu\text{m}$ de large, $90\mu\text{m}$ de long pour obtenir un modulateur optique à puits quantiques. Le dispositif fabriqué est représenté schématiquement sur la figure 6.

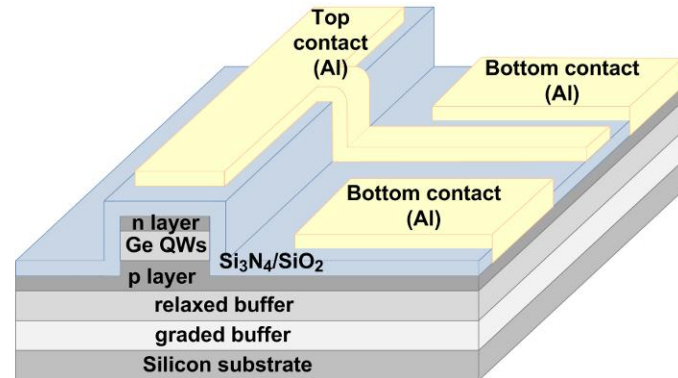


Figure 6 : Vue schématique du modulateur à puits quantiques Ge/SiGe de largeur $3\mu\text{m}$ et de longueur $90\mu\text{m}$.

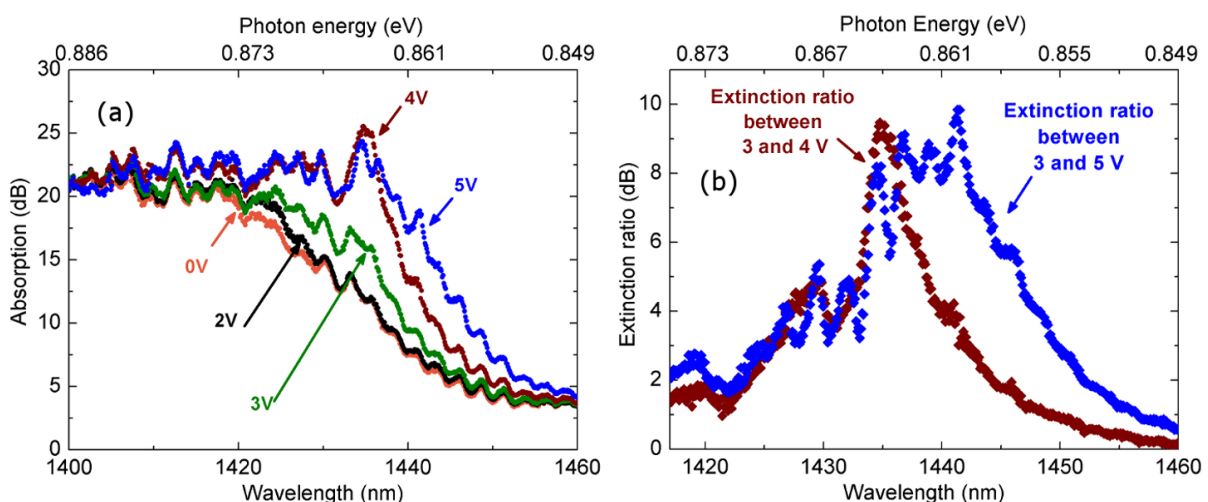


Figure 7 : (a) Spectre d'absorption du modulateur de largeur $3\mu\text{m}$ et de longueur $90\mu\text{m}$, en fonction de la longueur d'onde et de l'énergie des photons, pour des tensions inverses de 0, 2, 3, 4 et 5V. (b) Taux d'extinction pour une variation de tension de 1 V (entre 3 et 4 V) et de 2 V (entre 3 et 5 V).

Les mesures de transmission des guides d'onde pour différentes tensions inverses appliquées sur la diode, pour les longueurs d'onde de 1400 à 1460nm présentent un décalage vers les hautes longueurs d'onde du spectre d'absorption (figure 7(a)), dû à l'ESCQ. Un taux d'extinction supérieur à 6 dB pour une large bande spectrale entre 1425 et 1446 nm a été

obtenu, avec une valeur maximale d'environ 10dB entre 1433 et 1442 nm pour une tension inverse de 5 V et entre 1433 and 1437 nm pour une tension inverse de 4 V. Sur la figure 7(b) on peut voir qu'un taux d'extinction supérieur à 6 dB peut être obtenu avec une variation de tension de 1 V entre 3 et 4 V ou de 2 V entre 3 et 5 V, pour les longueurs d'onde respectivement comprises entre 1433 et 1437 nm et entre 1433 et 1444 nm.

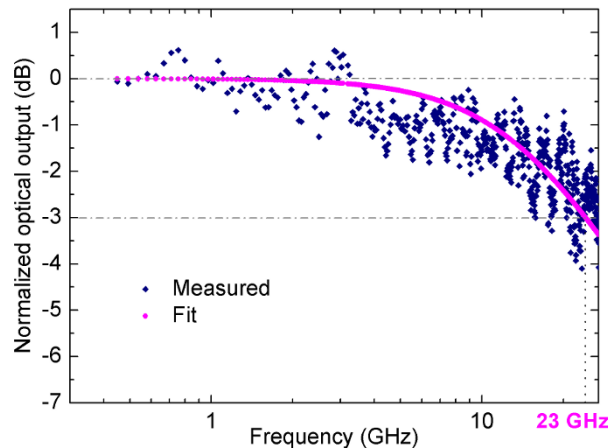


Figure 8 : Réponse optique normalisée en fonction de la fréquence, pour une tension statique inverse de 4.5 V.

La réponse en fréquence du modulateur a été évaluée grâce à un analyseur de réseau vectoriel optique/électrique (Agilent 86030A) à la longueur d'onde de 1448 nm. La réponse obtenue est reportée sur la figure 8. La fréquence de coupure à -3dB est de 23 GHz, pour une tension inverse statique de - 4.5 V. En utilisant la relation énergie/bit = $1/4 (CV_{\text{off}}^2 - CV_{\text{on}}^2)$, la consommation énergétique de ce modulateur à électroabsorption peut être estimée à 108 fJ/bit pour une variation de tension de 1 V (entre 3 et 4 V). Ainsi, le modulateur à puits quantiques Ge/SiGe présente une réduction d'environ un facteur 20 sur la taille et 50 sur la consommation en comparaison avec les modulateurs en silicium à large bande passante optique en silicium (c'est-à-dire en excluant les structures résonantes) [3]. Les performances du modulateur à puits quantiques Ge/SiGe pourront encore être améliorées, par une optimisation du nombre de puits quantiques et du facteur de recouvrement entre le mode optique et la région des puits. Ces résultats consistent la première démonstration de modulateur optique performant, compact et à faible puissance consommée, à base de puits quantiques Ge/SiGe pour la photonique silicium.

2. Photodétecteurs à base de puits quantiques Ge/SiGe

La possibilité d'utiliser le même matériau à la fois pour la modulation optique et pour la photodétection présente un grand intérêt pour la simplification des procédés de fabrication des circuits intégrant des liens optiques complets. C'est pourquoi nous avons étudié et caractérisé les propriétés de photodétection en configuration statique puis haute fréquence des structures à puits quantiques Ge/SiGe, dans des structures à illumination par la surface et dans des guides d'onde, le tout à température ambiante.

2.1 Photodiodes à puits quantiques Ge/SiGe à illumination par la surface

Les photodiodes à illumination par la surface présentent un intérêt pour des applications où la lumière se propage en espace libre. De plus, grâce à un couplage simple avec une fibre optique, elles sont largement utilisées pour étudier les propriétés physiques de nouveaux matériaux optoélectroniques[4-6]. Nous avons donc caractérisé ces photodiodes en terme de courant d'obscurité, de sensibilité et de bande passante optique. Une vue schématique en coupe et au microscope électronique à balayage des photodiodes réalisées sont reportées sur la figure 9. La lumière incidente est couplée par la surface de la photodiode. Celle-ci intègre une électrode coplanaire pour la caractérisation à haute fréquence.

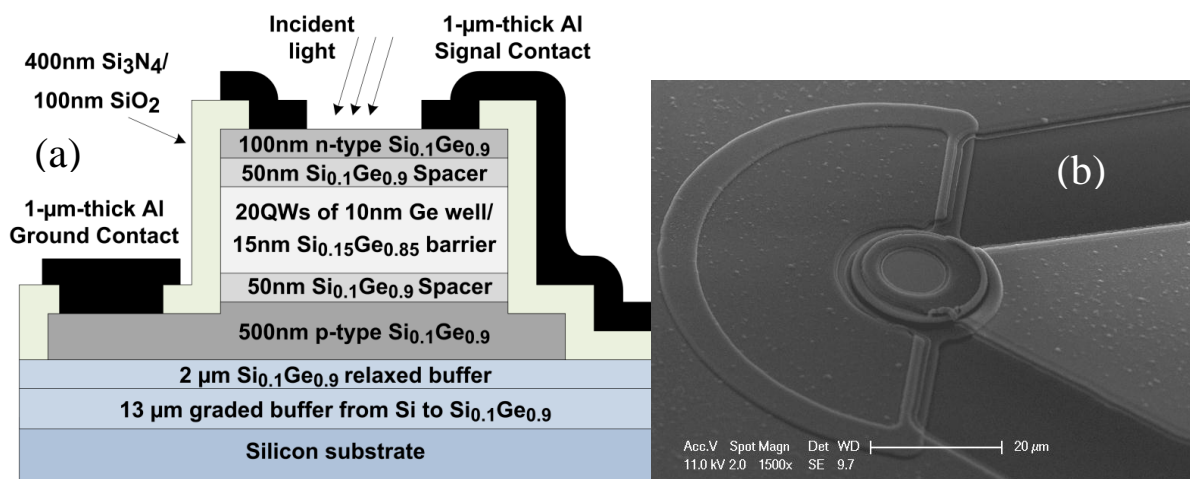


Figure 9 : (a) Vue schématique en coupe de la diode pin à puits quantiques Ge/SiGe à illumination par la surface. Des diodes de diamètres 12, 16, 20, 30, et 50 μm ont été fabriquées (b) Vue au microscope électronique à balayage d'une photodiode à éclairage par la surface.

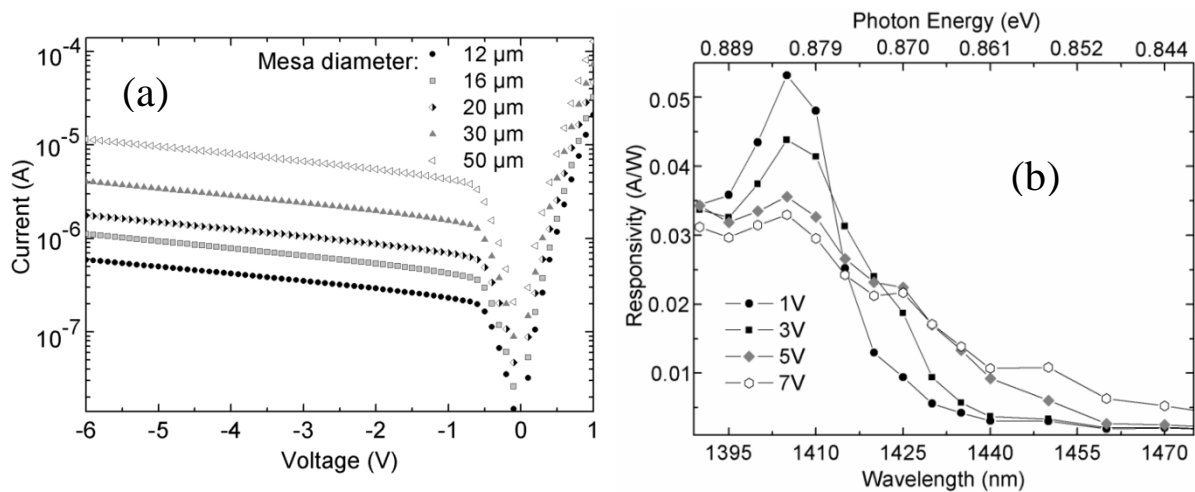


Figure 10 : (a) Courants d'obscurité en fonction de la tension inverse pour des photodiodes à puits quantiques Ge/SiGe de différents diamètres. (b) Sensibilité optique en fonction de la tension inverse et de la longueur d'onde.

Les courants d'obscurité mesurés sur les différentes photodiodes pour différentes tensions inverses sont reportés figure 10 (a). Sous -1V, des courants de 231, 231, 423, 696, 1500, et 4200 nA sont obtenus respectivement pour les diodes de diamètre 12, 16, 20, 30, et 50 μm , ce qui correspond à un courant d'obscurité d'environ 200 mA/cm^2 . Ces valeurs sont comparables aux valeurs obtenues pour des diodes germanium sur silicium à illumination par la surface de tailles équivalentes [7], ce qui prouve la bonne qualité des structures à puits quantiques Ge/SiGe et du potentiel de ces structures pour la détection de lumière. La sensibilité optique mesurée pour la diode de 50 μm de diamètre est reportée sur la figure 10(b) en fonction de la tension inverse et de la longueur d'onde. La valeur maximale a été obtenue autour de la longueur d'onde 1405 nm (0.88 eV) à -1V. Ces conditions correspondent à l'absorption par la transition excitonique entre les niveaux HH1 et c Γ 1 dans les structures à puits quantiques Ge/Si_{0.15}Ge_{0.85} à température ambiante, comme illustré dans le paragraphe 1.1. De plus, lorsque la tension inverse augmente, la sensibilité optique présente les deux caractéristiques de l'ESCQ : le décalage vers le rouge du spectre d'absorption, et la réduction du pic lié à l'absorption excitonique. Grâce à la figure 10 (b) on peut constater que la modulation de lumière et la photodétection peuvent être obtenues dans la même région de longueur d'onde entre 1395 et 1440 nm. De plus, il peut être mentionné à titre de comparaison

que la sensibilité obtenue est comparable à celle des photodiodes en germanium massif à illumination par la surface présentant une épaisseur de germanium similaire [4, 8].

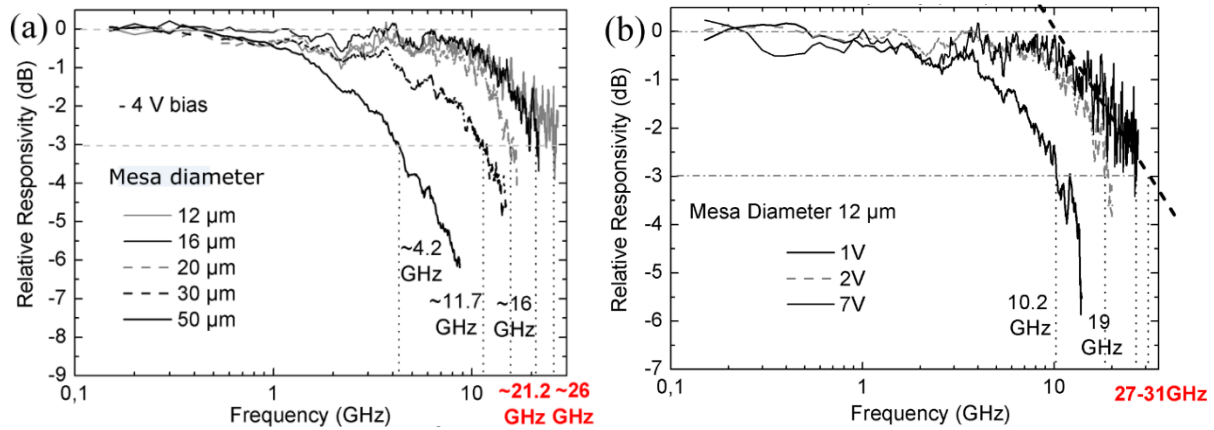


Figure 11 : (a) Réponse optique normalisée des photodiodes de différents diamètre pour une tension de -4V. (b) Réponse optique normalisée de la photodiode de diamètre 12 μm pour différentes tensions inverses.

Les réponses en fréquence des photodiodes à puits quantiques Ge/SiGe ont été mesurées à la longueur d'onde de 1405 nm, avec un analyseur de réseau vectoriel optique/électrique (Agilent 86030A). Les réponses des différentes photodiodes pour une tension de polarisation de -4 V sont reportées sur la figure 11(a). Les bandes passantes optiques sont de 4, 12, 16, 21, et 26 GHz respectivement pour les photodiodes de diamètre 50, 30, 20, 16, and 12 μm. Sur la figure 11(b) est tracée la réponse optique normalisée de la photodiode de 12 μm à différentes tensions de fonctionnement. Une bande passante optique supérieure à 30 GHz est obtenue pour une tension inverse de -7 V. De plus une bande passante de 10 GHz peut être obtenue avec une tension de polarisation de seulement 1V. La mesure et l'analyse de la réflexion électrique des photodiodes (paramètres S_{11}) ont permis de conclure que la bande passante des composants est limitée à la fois par le produit RC (résistance-capacitance), et par le temps de transit des porteurs dans la région active. Les capacités théoriques varient entre 0.36 pF pour la diode la plus grande et 0.02 pF pour la plus petite. La limitation par le produit RC est dominante pour les diodes les plus grandes, alors que pour les plus petites la limitation de la bande passante vient de mécanismes intrinsèques liés à la dynamique des porteurs dans les puits Ge/SiGe [11].

En résumé, les photodiodes pin à puits quantiques Ge/SiGe à illumination par la surface ont démontré un courant d'obscurité faible de 200 mA/cm^2 et une grande bande passante, compatible avec des transmissions de données à 40 Gbit/s . Une augmentation de la sensibilité autour de la transition excitonique $\text{HH1-c}\Gamma_1$ due au confinement quantique dans les puits a été clairement observée. Enfin, le compromis sensibilité / bande passante pourra être amélioré par l'utilisation d'une configuration guide d'onde [9, 10], qui fait l'objet du chapitre suivant.

2.2 Photodétecteur à puits quantiques Ge/SiGe en guide d'onde

Les photodétecteurs en guide d'onde présentent de nombreux intérêts, parmi lesquels la différenciation de la longueur d'absorption et du chemin de collection des porteurs, ce qui permet l'obtention de photodétecteurs avec une plus grande sensibilité que les photodiodes à éclairage par la surface, tout en maintenant de bonnes performances fréquentielles [12]. Le composant fabriqué utilise la même configuration que le modulateur à électroabsorption décrit dans le chapitre 1.3. Une vue schématique en coupe du composant est présentée sur la figure 12. Les guides fabriqués sont de largeur $3 \mu\text{m}$ et de longueurs 20 ou $80 \mu\text{m}$.

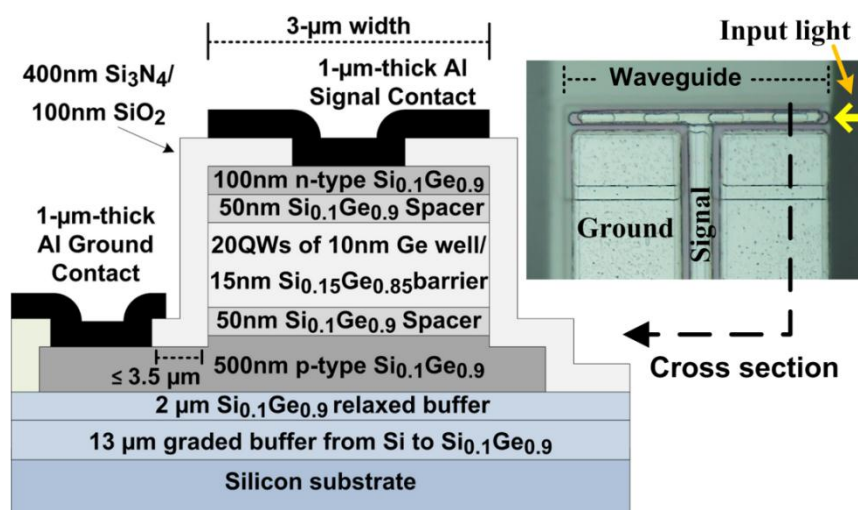


Figure 12 : Vue schématique en coupe et photographie au microscope optique d'un photodétecteur à puits quantiques Ge/SiGe.

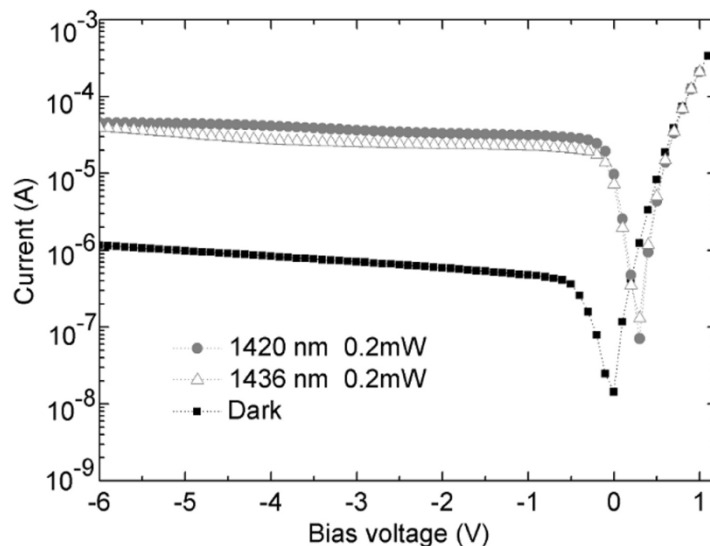


Figure 13 : Caractéristiques courant/tension des photodétecteurs à puits quantiques Ge/SiGe en guide d'onde, avec et sans illumination, aux longueurs d'onde de 1420 et 1436 nm.

Sur la figure 13 sont reportées les caractéristiques courant/tension (I-V) sans illumination (Dark) et avec illumination, pour une puissance incidente de 0.22 mW, aux longueurs d'onde de 1420 et 1436 nm.

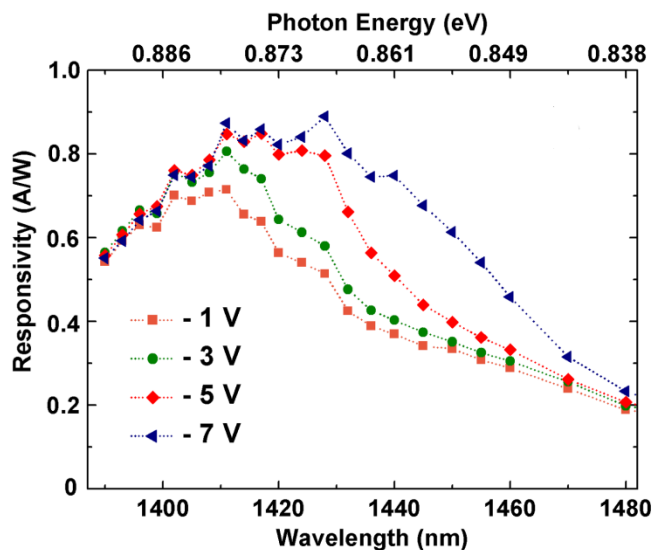


Figure 14 : Spectre de sensibilité optique du photodétecteur Ge/SiGe en guide d'onde, à différentes tension de polarisation.

La sensibilité optique a été mesurée en fonction de la tension inverse appliquée et de la longueur d'onde (figure 14). La sensibilité a été obtenue en divisant le photocourant par la

puissance optique incidente, en prenant en compte les corrections dues aux pertes de couplage entre la fibre incidente et le guide d'onde Ge/SiGe [13]. Une valeur maximale de 0.8 A/W est obtenue sous -3 V à la longueur d'onde de 1411 nm, correspondant à la transition excitonique HH1-c Γ 1 de cette structure. Le spectre de sensibilité présente une bonne correspondance avec les mesures de transmission de la figure 7(a): le décalage vers le rouge du spectre de sensibilité est accompagné d'une augmentation de la sensibilité aux plus hautes longueurs d'onde lorsque la tension inverse augmente, en raison de la grande longueur d'absorption dans cette configuration guide d'onde [14].

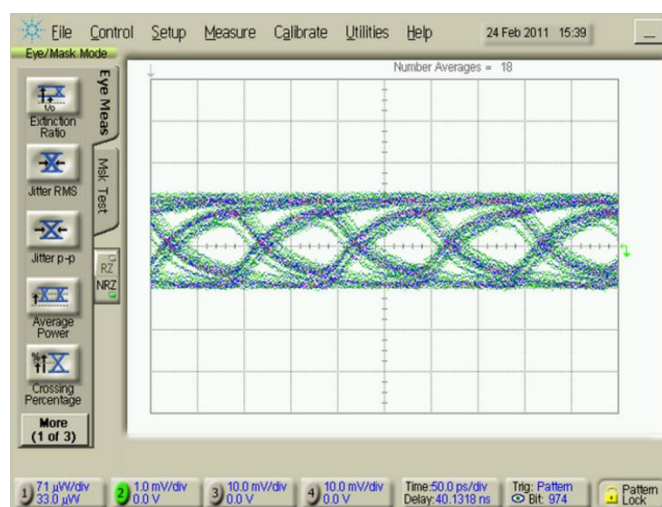


Figure 15 : Diagramme de l'œil électrique à 10 Gbit/s en sortie du photodétecteur à puits quantiques Ge/SiGe à la longueur d'onde de 1420 nm.

La rapidité de fonctionnement des photodétecteurs a été évaluée par la mesure du diagramme de l'œil électrique à 10 G/s en sortie du photodétecteur, à la longueur d'onde de 1420 nm. Un pattern de longueur $2^{10}-1$ provenant d'un générateur PRBS (Pseudo-Random Bit Sequence) est utilisé pour alimenter électriquement un modulateur optique commercial au niobate de lithium. Le signal optique à 10 Gbit/s issu du modulateur est ensuite couplé dans le photodétecteur. Une tension électrique constante est appliquée sur le photodétecteur, de manière à collecter efficacement les porteurs photo-générés. Le photocourant est ensuite collecté par une sonde RF fonctionnant jusque 40 GHz, et enregistré sur l'entrée électrique d'un oscilloscope présentant une impédance d'entrée de 50 Ω . Un diagramme de l'œil ouvert est obtenu à 10 Gbit/s sous une tension inverse de -3 V et à la longueur d'onde de 1420 nm (figure 15).

En conclusion, le photodétecteur en configuration guide d'onde présente un faible courant d'obscurité, de même densité que les photodiodes à illumination par la surface. Contrairement aux structures à illumination par la surface, l'utilisation d'une structure guide d'onde nous a permis d'obtenir un photodétecteur présentant simultanément une grande sensibilité optique et de bonnes performances fréquentielles. Une sensibilité optique de 0.8 A/W a été obtenue simultanément à un taux de transmission de 10 Gb/s.

3. Electroluminescence à température ambiante des structures à puits quantiques Ge/SiGe

Les propriétés d'émission de lumière dans les structures à puits quantiques Ge/SiGe ont été étudiées dans des diodes pin à illumination par la tranche. Pour la première fois l'électroluminescence (EL) autour de la bande interdite directe de ces structures a été démontrée et étudiée. Les mesures ont été faites dans la même gamme spectrale que celle utilisée pour le modulateur et le photodétecteur, et l'émission de lumière autour de la transition excitonique HH1-c Γ 1 a été étudiée pour différents courants électriques injectés dans la diode, et différentes températures, dans le but de comprendre les phénomènes physiques mis en œuvre. La polarisation de la lumière émise a également été étudiée, pour confirmer l'origine de l'EL

Le spectre d'EL est enregistré avec un spectromètre (Jobin Yvoni HR320) couplé à un détecteur InGaAs refroidit à l'azote. La lumière émise par des guides d'onde est collectée par la tranche du guide grâce à un objectif. L'injection électrique est réalisée par un pulse de tension, à 1kHz et 30% de « duty cycle ».

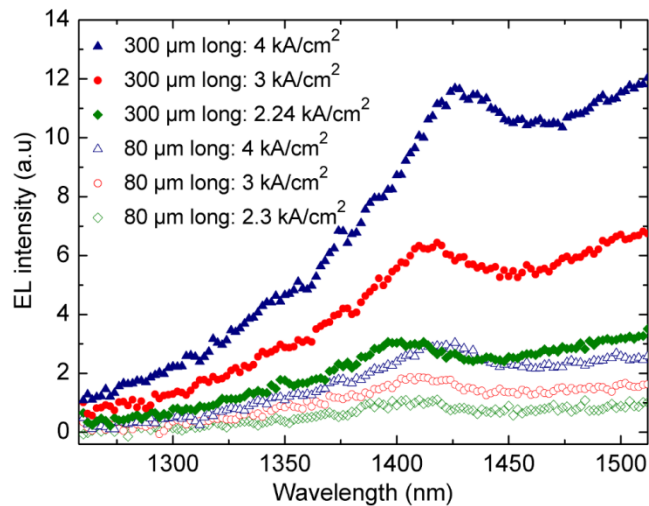


Figure 16 : Spectres d'électroluminescence à température ambiante des diodes de 80 et 300 μm de long en fonction du courant injecté. Le pic visible dans les spectres autour de 1420 nm correspond à la transition excitonique $\text{HH1-c}\Gamma_1$.

Sur la figure 16 sont reportés les spectres d'EL des diodes à puits quantiques Ge/SiGe, mesurés à température ambiante et sans stabilisation de température. Le pic visible dans les spectres autour de 1420 nm coïncide avec les pics d'absorption et de photoluminescence observés dans des structures identiques [15, 16]. L'intensité d'EL augmente avec le courant électrique injecté, indiquant que le signal optique mesuré provient bien des électrons injectés. De plus sur la figure 16 les spectres d'EL des diodes de longueurs 80 et 300 μm sont comparés. L'augmentation de l'intensité d'EL d'un facteur 3.5 est cohérente avec la différence de longueur des 2 diodes, confirmant l'origine de la lumière détectée.

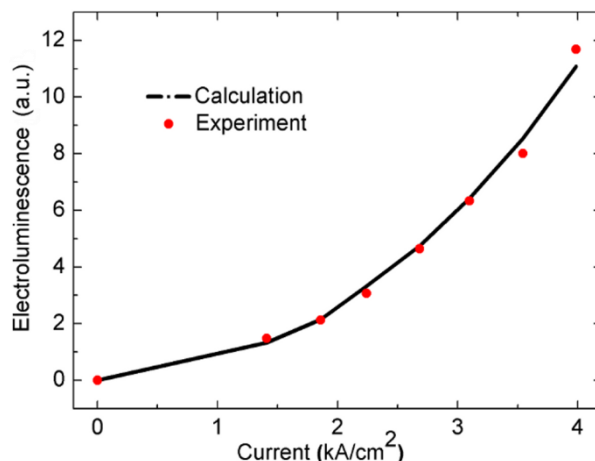


Figure 17: Intensité du pic d'EL (transition HH1-c Γ 1) en fonction de la densité de courant, pour la diode de longueur 300 μm

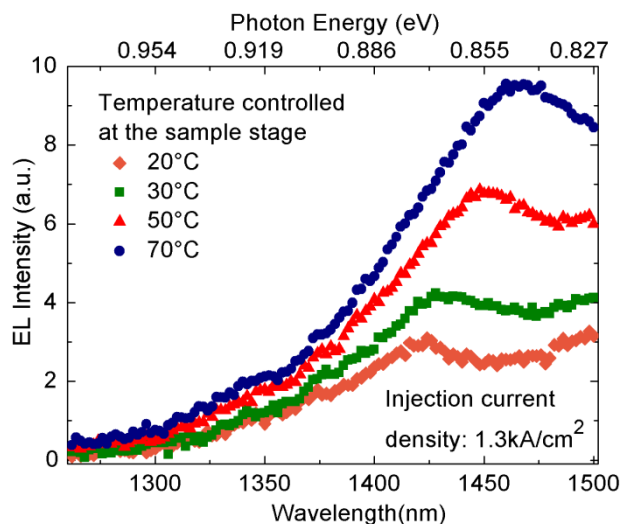


Figure 18 : Spectre d'EL à différentes températures, pour une densité de courant de 1.3 kA/cm², pour la diode de 300 μm de long

Sur la figure 16 on peut constater un décalage vers les hautes longueurs d'onde du spectre d'EL, lors de l'augmentation du courant électrique, dû à l'échauffement de l'échantillon, créant une réduction de la bande interdite. L'intensité du pic d'EL (transition HH1-c Γ 1) en fonction du courant injecté pour le guide de 300 μm de long est reportée sur la figure 17. Les valeurs mesurées suivent la loi $A \times J \times \exp(-\Delta E_{\Gamma L} / kT)$, où J est la densité de courant, T la température pour chaque valeur de densité de courant, estimée par la méthode des coefficients de Varshni, $\Delta E_{\Gamma L}$ est la différence d'énergie entre les états Γ et L , k est la

constante de Boltzmann et A un coefficient de proportionnalité. En prenant en compte les effets liés à la contrainte et au confinement quantique, la différence d'énergie entre les états Γ et L , $\Delta E_{\Gamma L}$, est estimée à 180 meV dans notre échantillon [17]. Le comportement superlinéaire de l'intensité d'électroluminescence en fonction du courant injecté a pu ainsi être attribué à l'excitation thermique des électrons leur permettant de passer du minimum de la bande de conduction (L) au minimum local correspondant à la bande interdite directe (Γ). Cette augmentation de l'intensité d'électroluminescence de la transition $HH1-c\Gamma1$ en fonction de la température a été confirmée par une mesure des spectres d'électroluminescence à densité de courant constante, et à différentes températures imposées extérieurement à l'aide d'un peltier. (figure 18). Entre 20 et 50°C l'intensité d'électroluminescence est doublée, ce qui correspond avec l'équation ci-dessus. Ces résultats sont également cohérents avec les mesures de photoluminescence dans une structure similaire (référence 16), dans lesquelles l'excitation thermique des porteurs de L vers Γ a été également observée.

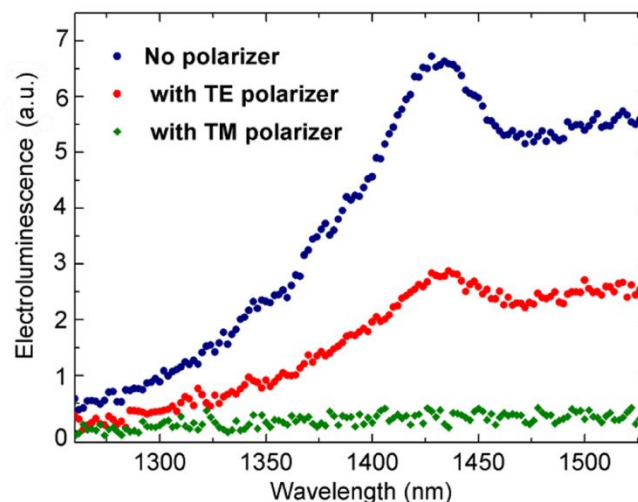


Figure 19 : Spectre d'EL obtenu avec et sans polariseur optique entre la facette de sortie du guide et le détecteur. En polarisation TM, il n'y a pas d'EL.

Finalement les mesures d'absorption dans les structures à multi-puits quantiques Ge/SiGe en configuration guidée nous ayant montré que seule la lumière polarisée TE (champ électrique parallèle au plan des puits quantiques) est absorbé par la transition $HH1-c\Gamma1$ [18], nous avons étudié la polarisation de l'électroluminescence mesurée. Pour cela nous avons utilisé un polariseur en espace libre entre la sortie de l'échantillon et l'entrée du détecteur. En ajustant le polariseur sur les polarisations TE ou TM nous avons pu constater que la lumière émise est effectivement polarisée TE (figure 19), confirmant que l'EL provient de la

recombinaison de porteurs mettant en jeu un état de trous lourds (HH). La différence de niveau entre les mesures sans polariseur et avec le polariseur en position TE sont dues aux pertes optiques du polariseur.

4. Conclusion

Le but de cette thèse a été d'étudier en détail les propriétés optiques et optoélectroniques des structures à puits quantiques Germanium/Silicon-Germanium (Ge/SiGe) pour la modulation, la photodétection et l'émission de lumière. J'ai ainsi réalisé le premier modulateur optique à électroabsorption à puits quantiques Ge/SiGe, en configuration guide d'onde, et présentant simultanément une grande rapidité et une faible puissance consommée. Concernant la photodétection, j'ai montré que des photodiodes rapides pouvaient être obtenues à la fois pour des structures à illumination par la surface et en configuration guide d'onde. Une bande passante compatible avec des transmissions de données à 40 Gbit/s a ainsi pu être démontrée pour la première fois. Enfin pour l'émission de lumière, j'ai réalisé les premières caractérisations d'électroluminescence (EL° à température ambiante, autour de la bande interdite directe (transition excitonique HH1-c Γ 1). Une augmentation de l'efficacité d'EL à plus grande température a pu être expliquée par l'excitation thermique des porteurs des vallées L vers Γ . En raison des règles de sélection dans les structures à puits quantiques Ge/SiGe, une polarisation TE de la lumière émise a été constatée. Finalement l'ensemble des résultats obtenus durant cette thèse montrent que les structures à puits quantiques Ge/SiGe sont un candidat de choix pour l'intégration monolithique de l'ensemble des composants optoélectroniques sur la plateforme silicium.

Références :

1. Y.-H. Kuo, Y. K. Lee, Y. Ge, S. Ren, J. E. Roth, T. I. Kamins, D. A.B. Miller, and J. S. Harris, "Strong quantum-confined Stark effect in a germanium quantum-well structures on silicon," *Nature* 437, 1334–1336 (2005).
2. M. Virgilio and G. Grosso, "Quantum-confined Stark effect in Ge/SiGe quantum wells: A tight-binding description," *Phys. Rev. B* 77, 165315 (2008).
3. D. Marris-Morini, L. Vivien, G. Rasigade, E. Cassan, J. M. Fédéli, X. Le Roux, P. Crozat, Recent progress in high speed silicon-based optical modulators, *Proc. IEEE* 97 7, p. 1199-1215 (2009).
4. M. Jutzi, M. Berroth, G. Wöhl, M. Oehme, and E. Kasper, "Ge-on-Si Vertical Incidence Photodiodes with 39-GHz Bandwidth," *IEEE Photonics Technology Letters* 17, 1510-1512 (2005).
5. S. Jongthammanurak, J. F. Liu, K. Wada, D. D. Cannon, D. T. Danielson, D. Pan, L. C. Kimerling and J. Michel, "Large electro-optic effect in tensile strained Ge-on-Si films," *Applied Physics Letters* 89, 161115 (2006).
6. Y. Luo, J. Simons, J. Costa, I. Shubin, W. Chen, B. Frans, M. Robinson, R. Shafiiha, S. Liao, N.-N. Feng, X. Zheng, G. Li, J. Yao, H. Thacker, M. Asghari, K. Goossen, K. Raj, A. V. Krishnamoorthy and J. E. Cunningham, "Experimental studies of the Franz-Keldysh effect in CVD grown GeSi_{epi} on SOI," *Proc. SPIE* 7944, 79440P (2011).
7. J. Osmond, L. Vivien, J.M. Fédéli, D. Marris-Morini, P. Crozat, J. F. Damlencourt, E. Cassan, and Y. Lecunff, "40 Gb/s surface-illuminated Ge-on-Si photodetectors," *Appl. Phys. Lett.* 95, 151116 (2009).
8. T. H. Loh, H. S. Nguyen, R. Murthy, M. B. Yu, W. Y. Loh, G. Q. Lo, N. Balasubramanian, D. L. Kwong, J. Wang, and S. J. Lee, "Selective epitaxial germanium on silicon-on-insulator high speed photodetectors using low-temperature ultrathin Si_{0.8}Ge_{0.2} buffer," *Appl. Phys. Lett.* 91, 073503 (2007).
9. L. Vivien, D. Marris-Morini, J. M. Fédéli, M. Rouvière, J. F. Damlencourt, L. E. Melhaoui, X. L. Roux, P. Crozat, J. Mangeney, E. Cassan, and S. Laval, "Metal-semiconductor-metal Ge photodetectors integrated in silicon waveguides," *Appl. Phys. Lett.* 92, 151114 (2008).
10. L. Vivien, M. Rouvière, J. M. Fédéli, D. Marris-Morini, J. F. Damlencourt, J. Mangeney, P. Crozat, L. E. Melhaoui, E. Cassan, X. L. Roux, D. Pascal, and S. Laval,

- "High speed and high responsivity germanium photodetector integrated in a Silicon-On-Insulator microwaveguide", *Opt. Express* 15, 9843-9848 (2007).
11. S. A. Claussen, E. Tasyurek, J. E. Roth, and D. A. B. Miller, "Measurement and modeling of ultrafast carrier dynamics and transport in germanium/silicon-germanium quantum wells," *Opt. Express* 18, 25596-25607 (2010).
 12. J. Michel, J. F. Liu, and L. C. Kimerling, "High-Performance Ge-on-Si Photodetectors," *Nature Photonics* 4, 527-534 (2010).
 13. O. Fidaner, A. K. Okyay, J. E. Roth, R. K. Schaevitz, Y.-H. Kuo, K. C. Saraswat, J. S. Harris, and D. A. B. Miller, *IEEE Photon. Tech. Lett.*, vol. 19, 1631-1633 (2007).
 14. P. Chaisakul, D. Marris-Morini, G. Isella, D. Chrastina, M.-S. Rouifed, X. Le Roux, S. Edmond, E. Cassan, J.-R. Coudevylle, and L. Vivien, *IEEE Photon. Tech. Lett.* 23, 1430-1432 (2011).
 15. P. Chaisakul, D. Marris-Morini, G. Isella, D. Chrastina, X. Le Roux, E. Gatti, S. Edmond, J. Osmond, E. Cassan, and L. Vivien, "Quantum-confined Stark effect measurements in Ge/SiGe quantum-well structures," *Opt. Lett.* 35, 2913-2915 (2010).
 16. E. Gatti, E. Grilli, M. Guzzi, D. Chrastina, G. Isella, and H. von Känel, *Appl. Phys. Lett.* 98, 031106 (2011).
 17. P. Chaisakul, D. Marris-Morini, G. Isella, D. Chrastina, N. Iazard, X. Le Roux, S. Edmond, J.-R. Coudevylle, and L. Vivien, *Appl. Phys. Lett.* 99, 141106 (2011).
 18. P. Chaisakul, D. Marris-Morini, G. Isella, D. Chrastina, X. Le Roux, S. Edmond, J.-R. Coudevylle, E. Cassan, and L. Vivien, *Opt. Lett.* 36, 1794-1796 (2011).

Chapter 1. Introduction

Silicon-based photonic components have exhibited a truly remarkable development for the past ten years. Passive control of light using compact Silicon (Si) waveguides has been impressively developed since early 2000s [1-3]. For active control of light, the announcement of the first gigahertz (GHz) silicon modulator by Intel in 2004 [4] can be regarded as the milestone toward the development of active building blocks used in nowadays Si-based optoelectronic integrated circuits (IC) including silicon modulators, germanium photodetectors, and III-V lasers on silicon [5-7]. These developments are now resulting in commercially-available Si-based 100 Gigabit (Gb) optical transceiver chip, which already become one of the premier options for data communication in server clusters or data storage centers, considered high-volume markets [8, 9].

On the other hand, the silicon photonic promises [10] of chip scale electronic-photonic integration based on complementary metal oxide semiconductor (CMOS) fabrication process are hardly fulfilled [11]. It is challenging to efficiently employ the present Si Photonic technology at the chip scale. For light modulation technology, wideband Si modulators typically consume high energy due to the large size of Mach-Zehnder interferometer (MZI) [12]; while, Si modulator based on resonator structures generally have a narrow working wavelength and require considerable additional energy for precise tuning. Other innovative low energy and compact Si modulators based on photonic crystal and electro-optics polymer still show a rather high insertion loss, high temperature sensitivity, and/or limited operation bandwidth. For laser technology, the III-V on Si heterogeneous/hybrid integration approaches employed for present Si-based lasers are expected to entail costly implementation at the chip scale. In fact, at the moment, an efficient and reliable electrically-pumped laser monolithically integrated on Si still remains the most challenging component [5, 13]. Regarding integration issues, the use of three different materials in a photonic link (III-V material grown or bonded on silicon for optical sources, silicon for carrier depletion-based modulators, and germanium (Ge) for photodetectors) also complicates the technology and makes the cost-effective promise of silicon photonics rather challenging [11]. Therefore, silicon photonics need a new breaking concept in order to meet the promised and required performances [14] especially for the chip scale optical interconnect applications.

The first aim of this thesis is to develop a high performance and low energy silicon-compatible electro-absorption modulator based on quantum-confined Stark effect from Ge/SiGe multiple quantum wells (MQWs). The second aim is to investigate the use of the same Ge/SiGe MQW devices (i.e. the same epitaxial growth and fabrication process) for light detection and emission functionalities with a view to developing all main active photonic devices from Ge/SiGe MQWs. Potentially, it could pave the way for a new photonic platform based on Ge/SiGe MQWs that could be fabricated within Si-CMOS technology in a cost effective manner, allowing the realization of the photonic-electronic integration vision [15].

1.1 Optics for interconnect

For more than fifty years, electronic IC based on Si has met with a great success. Today, electronic IC has been employed in almost every electronic device including the computer. This development has been enabled mainly by the continuous shrinkage of devices' size, leading to progressively improved computation speeds, higher integration capability, and drastically lowering cost [16]. To illustrate, Fig. 1.1 shows a typical schematic cross section of electronic IC in which billions of CMOS transistors are employed for data computing along with passive metal interconnects for data transmission, signaling, and clocking [17]. With this configuration, it can be seen that when more and more transistors are shrunk and integrated within the same surface area, higher speed and functionality can be obtained from the CMOS chip.

As the transistor's size continues to be smaller, the aforementioned benefits of device shrinkage and higher integration become much less evident especially at the global interconnect level. At smaller device's size, the global interconnects cannot retain the down-scaling benefit, because while its cross section needs to be reduced according to denser devices per unit area, its total length is almost the same according to the chip size itself. This leads to an exponential growth in resistance-capacitance (RC) delay due to an unavoidable increased resistance and capacitance from the metal wires. In other words, the increasing bandwidth of reducing transistor's size and denser integration will be beneficial only as long as the required bandwidth does not exceed that of metal interconnects, in which its data carrying capacity does not increase with reduced size [18]. Additionally, the skin-depth effect

further worsens wire resistance at higher frequency [14, 19]. Fig. 1.2 shows report from International Technology Roadmap for Semiconductors (ITRS) [17] predicting gate and interconnect delays versus technology node. While gate delay and local interconnect (Metal 1) delay tend to decrease in proportion to the feature size, the global interconnect exhibits drastically higher delay. Although repeaters can be employed to mitigate the delay, they consume significant power and chip area.

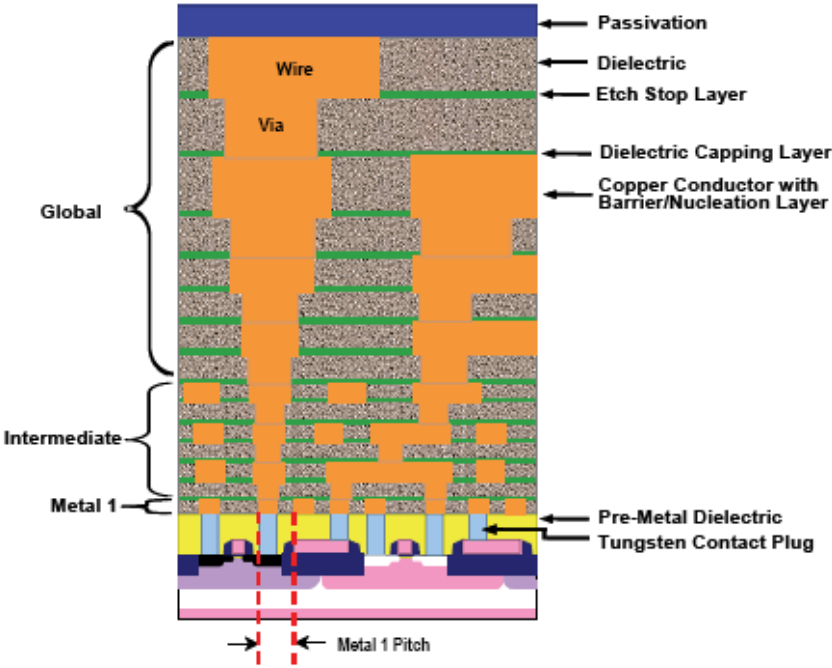


Figure 1.1: Schematic view of a typical cross section of a CMOS chip [17]

It is also worth mentioning that thanks to the latest development of Intel 22nm 3-D Tri-Gate Transistor Technology [20], the half-a-century trend that number of transistors on an IC doubles approximately every eighteen months [16] will probably continue for many years to come. Each transistor will continue to get smaller, faster, cheaper, and less energy consuming. However, the interconnect bottleneck of metal is seriously predicted to become a performance wall of the IC within five to ten years, and make the Moore’s law irrelevant [21]. It won’t matter how fast transistors are if the data flow between them is restricted. Silicon photonic links are regarded as a prime candidate to solve the interconnect bottleneck problems [21-23].

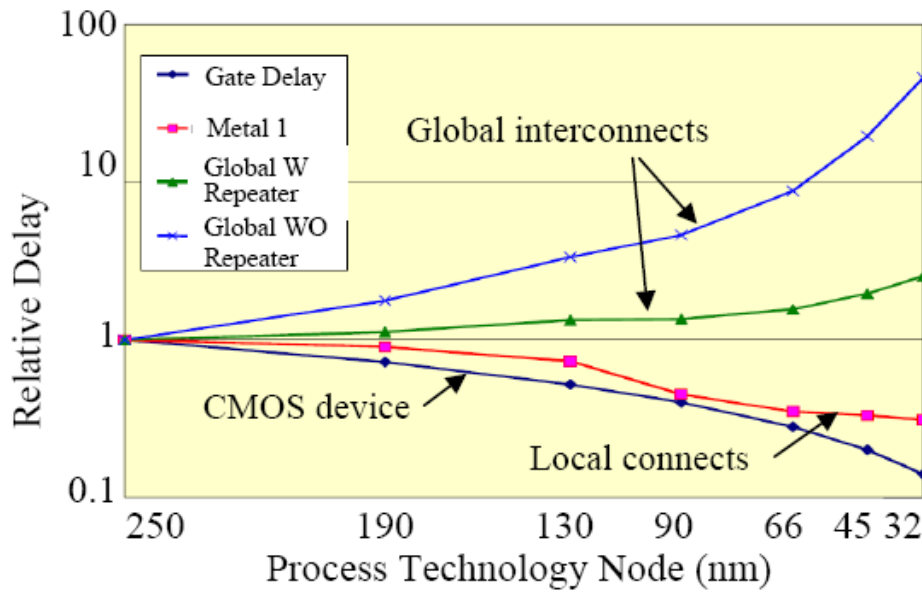


Figure 1.2: Gate, metal 1, and global interconnect delays versus feature size from 2007 ITRS [17]

Moreover, power dissipation from dense network of metal interconnects also leads to considerable heating problem in metal interconnect systems. Total length of metal interconnect within today Si microprocessor of 1 square inch has already reached 20 kilometers [17]. Obviously, such a highly dense metal wire has created a lot of heating due to the current flows. In fact, in 2005, it was the first time in thirty five year history of computer electronic IC that its clock speed cannot be increased mainly because of the enormous power dissipation created by the passive metal interconnects [24]. Due to scaling and heating problems, on-chip metal interconnect will become a bottleneck limiting the performance of CMOS chip, called “interconnect bottleneck”, and it has been firmly predicted by ITRS that in the long term new design or solutions such as 3D IC or optical interconnects are needed to overcome the delay, power, and also bandwidth limitations of metal interconnects [17].

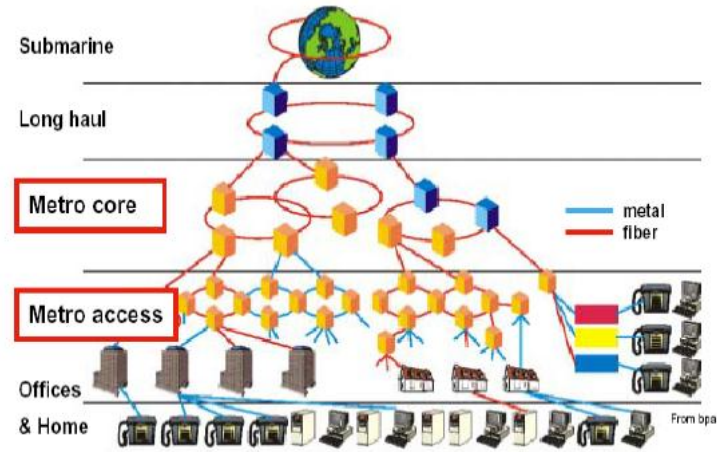
At the moment, manufacturers are utilizing multiple processor cores on a single chip to enhance the processor performance instead of increasing the clock frequency [25]. Since its commercial adaptation in 2006, numbers of cores in multicore processors have now been continuously increasing up to several 10 cores with an expectation to even reach 1000 cores or more in the future. Nevertheless, the increased performance at increased number of cores would be reached only if the inherent scaling problems and exponentially increasing

programming complexity at higher numbers of cores are tackled. Thanks to much higher bandwidth and a potential to have an inexpensive broadcast mechanism, optical interconnect is also considered as a viable option to overcome these problems of electrical interconnects currently employed for the communication among different cores [26].

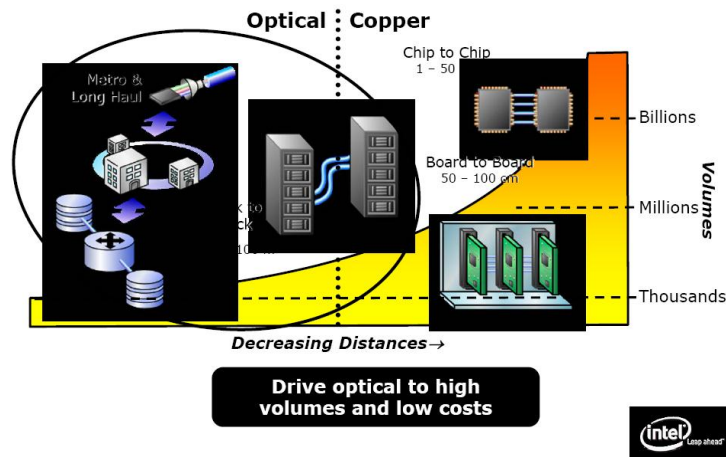
1.2 Silicon-based photonics

Since its inception in the transatlantic telecommunications between USA, UK, and France in 1988, optical fiber has nowadays replaced all of the electronic wires for long-haul telecommunication systems [15]. Regarding information transmission, optics offer several advantages over electronics including mainly: [27, 28] (1) Optics provides much higher bandwidth than electronics due to the lack of resistance-capacitance (RC) delay and the ability to simultaneously transmit multiple wavelengths within the same optical fiber, called the wavelength-division multiplexing (WDM) technique, and (2) Optical fibers have a very low loss, leading to much less power dissipation due to heating effect than the electronic wires, which are lossy and need a considerable level of currents to be guided within the wires. Obviously, the superior characteristics of optical data transmission have contributed critically to the worldwide rapid growth of the internet through submarine optical communication systems [29].

Besides long-haul trans-ocean telecommunications, at present optics has been increasingly deployed in intermediate distance telecommunication networks like metropolitan area networks (up to 50 km), campus networks (~1 km), local-area networks (~100 m), and fiber-to-the-home (FTTH) applications as shown in Fig. 1.3(a) [30, 31]. One of the main hurdles preventing the use of optics at shorter distance scales is the cost of optical components which are significantly higher than the electronic devices [10, 32]. Nevertheless, the comprehensive adaptation of optics has been expected due to the aggressive growth of data traffic resulting from the widespread and increasingly heavy use of the internet [33].



(a)



(b)

Figure 1.3: (a) The use of optics and electronics in today telecommunication networks [30]

(b) Distance and interconnect types in today telecommunication networks [31]

As a result, the integration of silicon photonics components into an integrated chip using CMOS platform has been pursued by several companies with a view to obtaining the performances of optics at the price of electronics. For server clusters and data storage center applications, Luxtera and Kotura have already made commercially available silicon photonics-based 100 Gigabit (Gb) optical transceivers [8, 9]. Intel has demonstrated end-to-end silicon photonics integrated link at 50 Gb/s using a single optical fiber [34, 35]. IBM has included VCSEL-based optical interconnects in its 10 PetaFlop supercomputer: Blue Waters [36, 37]. Generally, these photonic integrated chips consist mainly of III-V lasers integrated

on silicon [38-43], silicon optical modulator [44-56], and fully integrated Ge detector [57-65]. These provide the necessary active building blocks typically required in an optical interconnect system as shown in Fig.1.4 [66]. An optical interconnect system for waveguide approach normally consists of a laser to provide optical signal, a modulator to transfer information from the electrical signal into an optical signal, a waveguide to direct the optical signal, and a detector to convert the optical signal back to an electrical signal. Moreover, it should be noted that a directly modulated laser can also be used to convert electrical information into optical one without using an optical modulator.

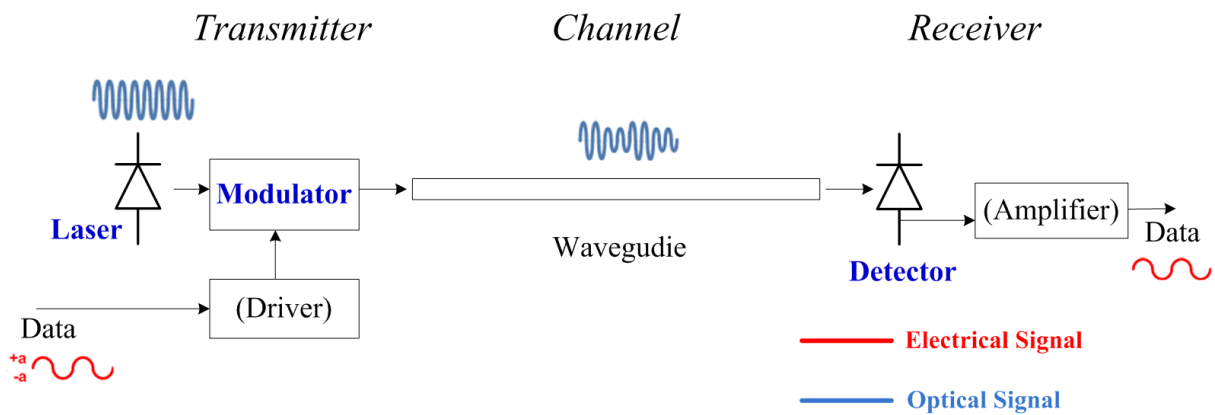


Figure 1.4: An optical interconnect system [66]

On the other hand, the use of optical interconnects at the chip-scale data transmission are also being actively investigated. The projected applications are chip-to-chip (interchip) and on-chip (intrachip) interconnects [14, 31, 67] as shown in Fig. 1.3(b) [31]. However, to be competitive with the electrical interconnects at the chip scale, optical interconnects have to meet several aggressive requirements in terms of power consumption, data density, and preferably monolithic integration of optical components in silicon [14, 67, 68].

In term of power consumption, to be a viable solution at the chip scale, it has been predicted that a total energy consumption of an inter chip optical interconnect system should be as less as 100 fJ/bit [14]. Therefore, the energy consumption of optical output devices such as modulator and laser should be as less as 10 fJ/bit so that there is enough energy for every function like driver, receiver, and possibly timing circuits. Obviously, this is unobtainable with the present technology of silicon-photonic based optoelectronic devices. To illustrate,

typical energy consumption of a wideband silicon optical modulator is 5,000 fJ/bit [50, 51] due to the large size and high driving voltages of the device. Although silicon modulator's footprint can be drastically decreased by the use of a resonant structure [44, 49], the device has a limited operation wavelength, and a high sensitivity to temperature change, making its operation more difficult.

In term of monolithic integration, efficient monolithic light source on Si remains the most challenging component in silicon photonic community. Lasers based on heterogeneous or hybrid integration by die or wafer bonding of III-V material on Si [38-43], and the direct growth of III-V material quantum well or quantum dot on Si using SiGe or Ge buffer [69, 70] have been impressively demonstrated. Nevertheless, using III-V compounds in CMOS process provide a particular challenge as they also act as dopants in Si. Moreover, previous complete lifetime trials of continuous wave (CW) operation from the GaAs/AlGaAs quantum well lasers growth on SiGe buffer on Si was shown severely degraded device lifetime of as low as 4 hours due to unavoidable defects in the materials [13]. InGaAs QW nanopillar optically-pump laser directly grown on Si has also recently shown [71]; however, it is still challenging to obtain an efficient electrically pump laser due to the employed pillar configuration. As a result, a reliable monolithic laser on Si appears to be the ultimate goal to be fulfilled, and up to now hybrid integration of III-V material on Si is the most advanced option. In fact, it is worth noting that an off-chip light source could possibly be more preferable over an integrated one in certain applications due to on-chip heat dissipation issues.

Interestingly, recent development based on tensile strained Ge grown on Si from MIT and the University of Tokyo [72] has shown to be a promising option to realize a complete chip scale optical interconnects on Si. This leads to recent demonstrations of various innovative Ge-on-Si photonic devices working around C and L band telecommunication wavelength including GeSi electro-absorption (EA) modulator [73] based on Franz-Keldysh effect (FKE) [74], wideband Ge photodetector [59], and optically and electrically pumped Ge laser on Si [75-77]. Some of these devices have potential to meet performance, power consumption, and monolithic integration requirements of chip scale optical interconnect in the future. Additionally, the works on light emission from tensile strained bulk Ge have spurred various teams to expand the investigations and favorable characteristics of Ge as light emitting diodes have been reported [78-81]. However, the recent impressive demonstration of

the first electrically-pumped Ge laser has indicated that the device tended to require fairly high levels of injection currents to obtain a lasing effect. This poses a challenge to practically employ such device for low-energy consumption application.

For light modulation, a typical EA modulator based on FKE from bulk Ge on Si has been reported to have around 8-10 dB extinction ratio at 1600 nm using a reverse bias voltage between 0 and 4 V for a device with an active area of less than $45 \mu\text{m}^2$, with a corresponding insertion loss of 5-10 dB and ~ 100 fJ/bit dynamic energy consumption [82, 83]. Typical absorption characteristics from bulk Ge on Si at different bias voltages due to Franz-Keldysh effect are shown in Fig. 1.5. Moreover, using $\text{Ge}_{0.9925}\text{Si}_{0.0075}$ on Si, GeSi modulator demonstrates 8 dB extinction ratio between a reverse bias voltage of 4 and 7 V at 1550 nm for a device with $30 \mu\text{m}^2$ active area and 50 fJ/bit energy consumption [73]. In 2011, Oracle, Lawrence Semiconductor Research Lab, and Kotura [84] studied FKE spectra from $3 \mu\text{m}$ thick $\text{Si}_{0.006}\text{Ge}_{0.994}$ grown on Si(100) wafers. The FKE spectra of $\text{Si}_{0.006}\text{Ge}_{0.994}$ are given in Fig. 1.6. The sharp raise of direct gap absorption band edge is degraded as expected when integrated onto Silicon, or when alloyed with dilute Si for blue shifting to the C-band operation.

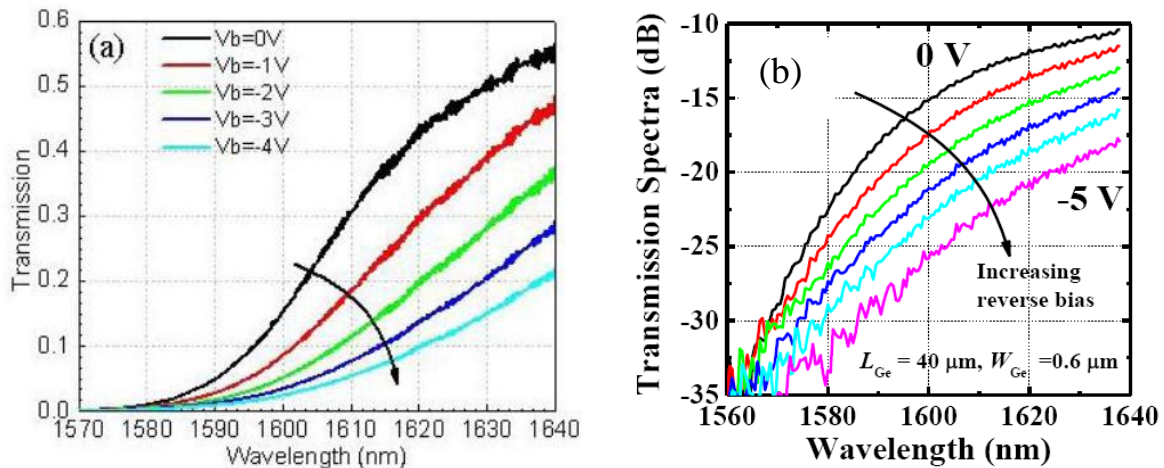


Figure 1.5: Typical transmission characteristics from bulk Ge on Si at different bias voltages due to Franz-Keldysh effect from Ref. (a) 82 and (b) 83.

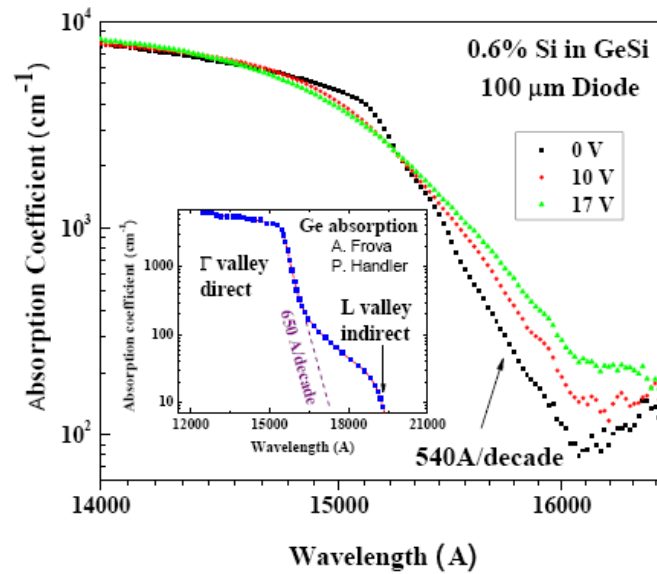


Figure 1.6: Franz-Keldysh effect spectra from $3\mu\text{m}$ thick $\text{Si}_{0.006}\text{Ge}_{0.994}$ grown on Si(100) wafers [84].

The use of bulk Ge for light modulation based on FKE has shown two main limitations. Firstly, the operating wavelength will be limited to material band gap energy. Although small amount of Si in Ge was used to tune the operating wavelength of Ge, the modulation efficiency was proven to be degraded. Moreover, it is unlikely that bulk Ge can be used as an efficient optical modulator at a shorter telecommunication wavelength of $1.3\mu\text{m}$ as exceedingly high absorption loss could be expected. Secondly, swing bias voltages of considerably higher than 1V are required in order to obtain a sufficiently high modulation depth from bulk Ge modulator based on FKE. Devices with required swing bias voltage of higher than 1V will be complicated to be integrated with a Si electronic chip. Both of these limitations could potentially be overcome by using an optical modulator based on quantum-confined Stark effect (QCSE) of Ge MQWs [85]. Essentially, the benefits of quantum well structures result from its discrete energy levels and thanks to the quantum confinement effect [86]. For optical modulator applications, this leads to a sharp rise of this absorption edge; hence, a large variation of absorption coefficients with a relatively small amount of applied electric fields is possible. Additionally for light emission, quantum well structures give a more favorable density of states in the active layers, allowing population inversion to be achieved with a lower electron-hole density.

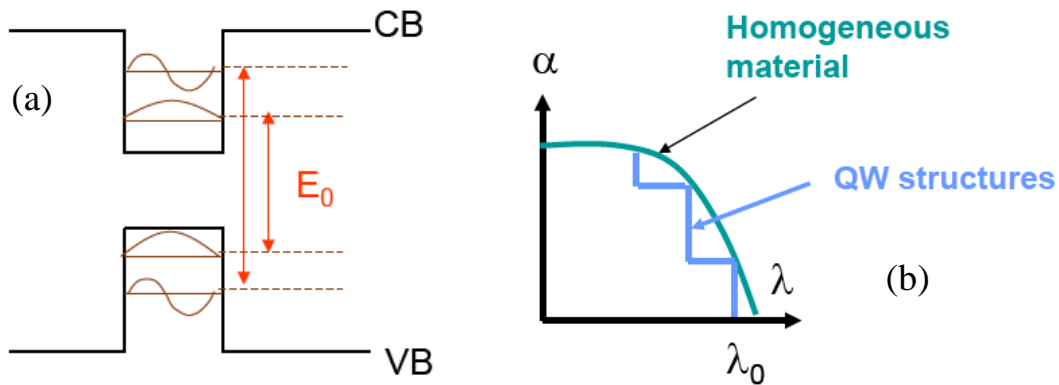


Figure 1.7: (a) Electron and hole energy levels and wavefunctions in a quantum well system (b) Comparison of typical absorption spectra obtained from a material in quantum well structure and in bulk (homogeneous) forms [87].

A quantum well system typically consists of a thin layer (typically less than 25 nm [85]) of a narrower-gap semiconductor (i.e. well) sandwiched by wider-gap ones (i.e. barriers). When the barrier is chosen to have higher conduction and lower valence band edges than those of the well, the electrons and holes are both confined in the well layer with discretized energy levels due to the quantum confinement effect as shown in Fig 1.7(a). These discrete energy levels in the quantum wells (QWs) lead to step-like absorption spectra, which results in a sharper rise in absorption coefficient than bulk material as in Fig 1.7(b).

As shown in Fig. 1.8(a), when electric field is applied perpendicularly to the quantum well plane, the potential profile is tilted and the separation energy between the conduction and valence allowed energy level is decreased. This leads to a red shift of the absorption spectra as shown in Fig 1.8(b). The reduction of the absorption peak due to the Coulomb attraction between electron-hole pairs (i.e. the exciton) with applied electric field is due to the fact that electric field pulls electron and hole wavefunctions to the opposite site of the quantum well system; hence, its overlap integral is reduced. This phenomenon is called QCSE which is one of the strongest physical mechanisms to obtain optical absorption modulation.

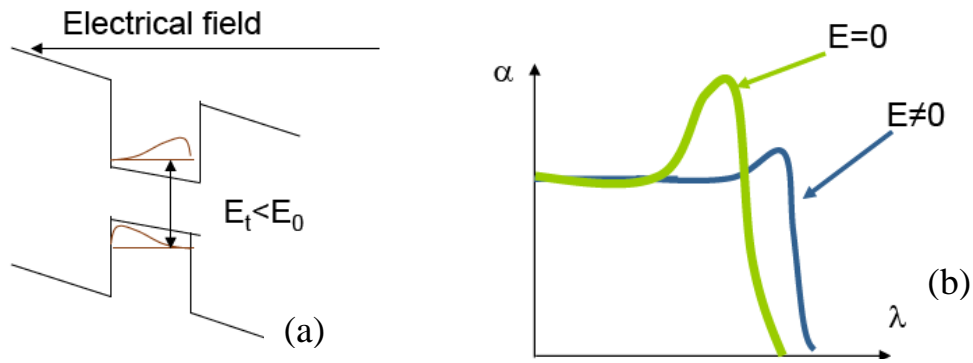


Figure 1.8: (a) Electron and hole energy levels and wavefunctions in a quantum well system when electric field, E_0 , is applied; the typical electric field, E_t , required to observe the QCSE is 10^4 - 10^5 V/cm. (b) Red shift of the absorption spectra with applied electric field. [87].

Fig. 1.9 shows typical experimental absorption spectra of III-V based quantum well system at different electrical fields [88]. Two characteristics of QCSE, i.e. red shift of the absorption spectra and reduction of the excitonic absorption peaks were obtained. It is also worth mentioning that III-V semiconductors in quantum well structures are conventionally the materials of choice to realize high performance photonic devices including vertical cavity surface emitting laser (VCSEL) [89, 90], quantum well modulators integrated with quantum well lasers [91, 92], and high performance EA modulator [93]. Furthermore, as the quantum well materials are used in the laser and modulator parts, quantum well detectors are becoming increasingly important in photonic integrated circuits (PICs) in order to have the same material for all optoelectronic devices [94, 95].

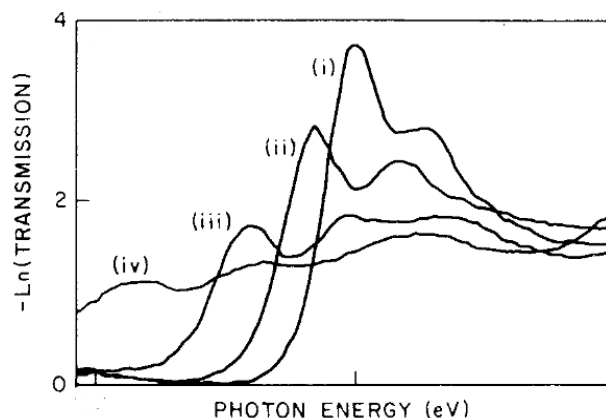


Figure 1.9: Absorption spectra of GaAs/AlGaAs quantum well system at electrical field of 1.6×10^4 V/cm, 10^5 V/cm, 1.3×10^5 V/cm, and 1.8×10^5 V/cm [88].

1.3 Ge/SiGe multiple quantum well structures for optoelectronics

As a breakthrough, in 2005 Kuo et al. from Stanford University reported the discovery of strong QCSE at room temperature from 10 periods of 10 nm thick Ge well sandwiched by 16 nm thick $\text{Si}_{0.15}\text{Ge}_{0.85}$ barriers (Ge/ $\text{Si}_{0.15}\text{Ge}_{0.85}$ MQWs) directly grown on $\text{Si}_{0.1}\text{Ge}_{0.9}$ buffer on Si substrate [96, 97]. The schematic view and the QCSE spectra deduced from photocurrent measurements are shown in Fig 1.10 (a) and (b). The mechanism is based on the direct-gap transition of Ge, which is actually an indirect-gap semiconductor, and yet the QCSE from Ge quantum wells (QWs) is as strong as or even stronger than that from the direct-gap III-V semiconductors due to a strong absorption coefficient of Ge [98]. This discovery could potentially open the way for a reliable monolithic integration of high performance photonic devices with silicon CMOS chip, as Ge has already been included into today's CMOS chip in order to improve Si electrical properties [99-101].

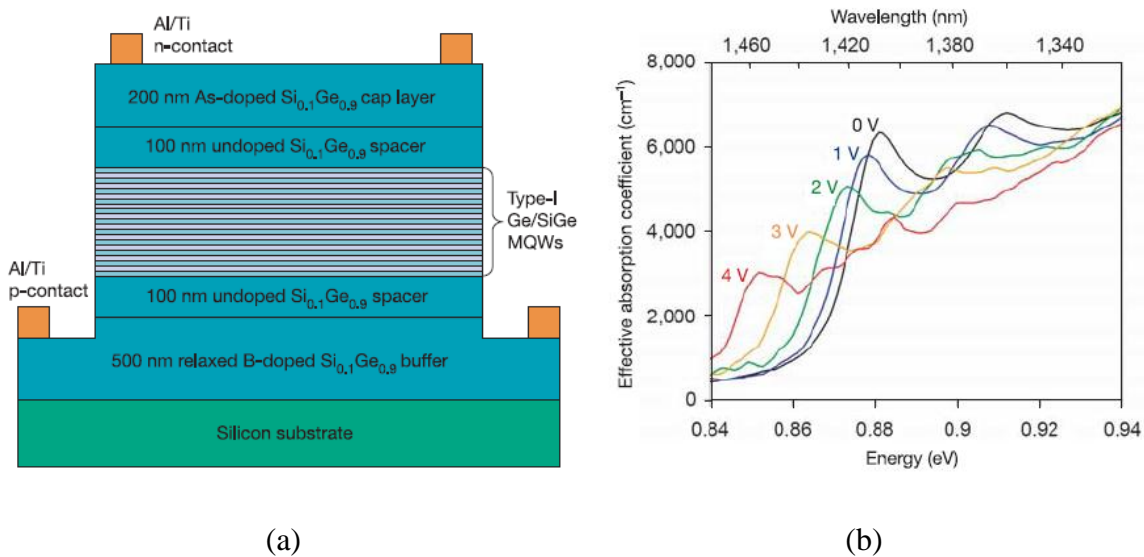


Figure 1.10: (a) The Ge/SiGe multiple quantum wells p-i-n diode structure. (b) Effective absorption coefficient at different reverse bias voltages [96].

The main underlying reason for the observation of the QCSE in Ge quantum wells is the similarity between the band diagram of Ge at the zone center (Γ point) and that of direct gap III-V semiconductor such as GaAs, as shown in Fig 1.11. Indeed, Ge has the global maximum of the valence band at the zone center, the global minima of the conduction band at

the L valley, but interestingly, there is a local minimum at the zone center (forming a Kane-shaped structure as in direct-gap semiconductors [102]) with the energy level very close to the global minima [103]. At room temperature the direct and indirect transitions of Ge are ~ 0.8 eV [104] and ~ 0.64 eV respectively [105]. Importantly, Ge direct gap energy of 0.8 eV corresponds well to the C band telecommunication wavelength regions, making Ge a possible candidate to be engineered for active photonic devices. On the contrary in Si, the global minimum of the conduction band is at the Δ valley and very far from the zone center [103, 106] as in Fig 1.11 (b). Therefore, the indirect absorption dominates all of the optical processes, leading to a poor efficiency of optical devices made of Si. Although Si also has a local minima of conduction band and the global maxima of the valence band at the zone center with the Kane-shape structure like in III-V semiconductor, it corresponds to a very high energy of ~ 4 eV in the ultraviolet range; therefore, it is not applicable for the considered applications of optical interconnects.

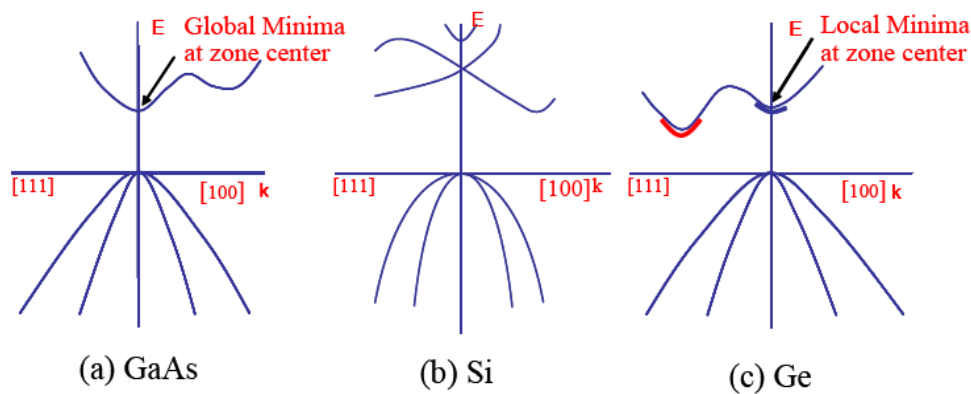


Figure 1.11: Simplified Energy band diagrams for (a) GaAs (b) Si (c) Ge [66].

This behavior can be seen in Fig 1.12 from Ref. 107 which summarizes absorption coefficient of widely-used semiconductors. It can be seen that bulk Ge has a sharp rise of absorption coefficient, similarly to that of typical direct-gap III-V materials like GaAs or InP, at its direct-gap energy of around 0.8 eV. Ge also has an absorption tail extending to 0.65 eV due to its indirect-gap transition, of which the absorption coefficient is considerably weaker than that of the direct-gap transition and has a linear dependence on the square root of the energy as also observed in Si.

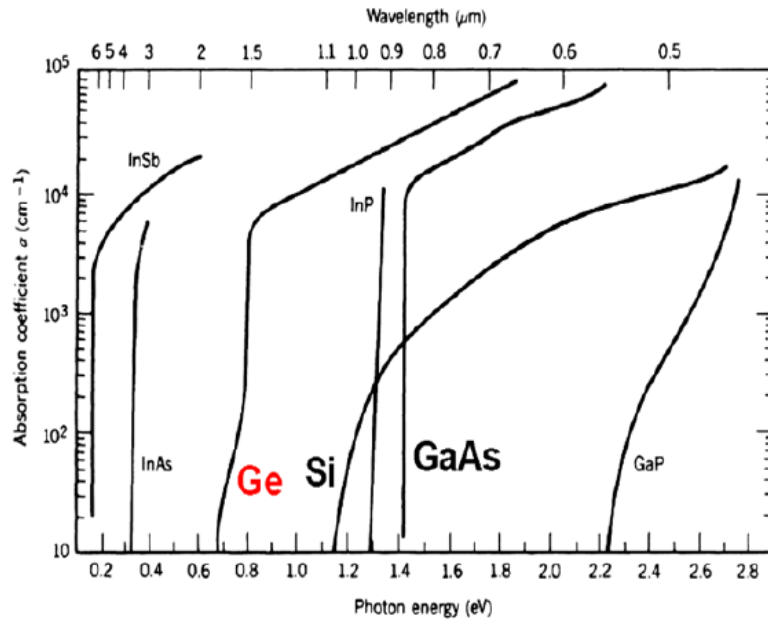


Figure 1.12: Bulk absorption coefficient as a function of the photon energy and wavelength for widely-used semiconductors at room temperature [107].

$\text{Si}_{1-x}\text{Ge}_x$ compound also plays a vital role in the demonstration of QCSE based on the direct-gap transition of Ge by Kuo et al. [96]. Si and Ge are completely miscible; in other word, the $\text{Si}_{1-x}\text{Ge}_x$ compound will always have the cubic diamond lattice with an almost linearly-increasing lattice parameter over the x range from 0 to 100%. J. Weber et al. [108] studied the variation of direct- and indirect-gap band energies of $\text{Si}_{1-x}\text{Ge}_x$ at low temperature as in Fig. 1.13. We can see that the value of $\text{Si}_{1-x}\text{Ge}_x$ direct-gap energy linearly varies with the Ge x composition. The variation of $\text{Si}_{1-x}\text{Ge}_x$ direct-gap energy with Ge x fraction is very fast (~ 33 meV per percentage point) because of the large difference between Si and Ge direct-gap energy. The direct-gap energy of $\text{Si}_{1-x}\text{Ge}_x$ compound at low temperature can be expressed by the following equation from Ref. 107:

$$E_{\text{direct-gap}}(\text{eV}) = 4.185 - 3.296x \quad (1.1)$$

For the indirect-gap transition, $\text{Si}_{1-x}\text{Ge}_x$ alloy has the global minima of the conduction band at the Δ valley (Si-like) if x is less than 0.85, and at the L valley (Ge-like) if x is more than 0.85. The indirect-gap energy of $\text{Si}_{1-x}\text{Ge}_x$ compound at low temperature can be expressed by the equation [108]:

$$E_{\text{indirect-gap}}(eV) = \begin{cases} 1.155 - 0.43x + 0.206x^2 & E_g^{\Delta}(x) \text{ for } x < 0.85 \\ 2.010 - 1.27x & E_g^L(x) \text{ for } x > 0.85 \end{cases} \quad (1.2)$$

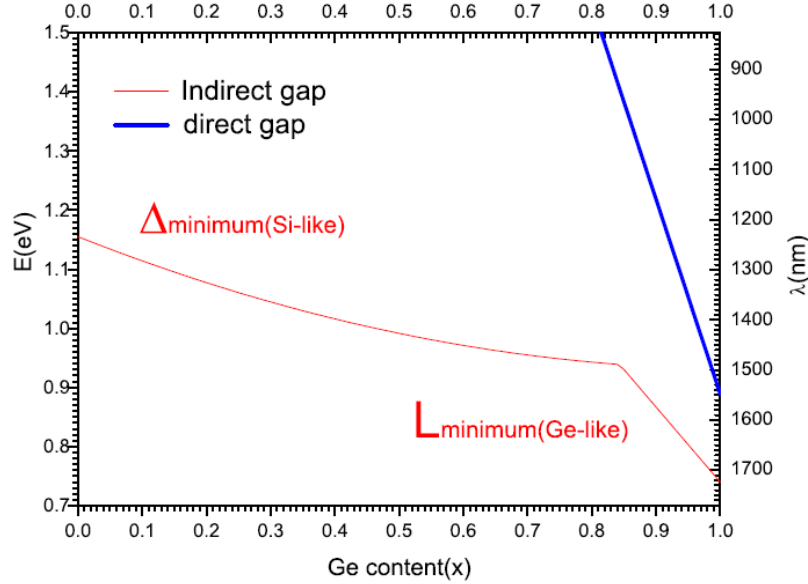


Figure 1.13: Band gap of bulk $\text{Si}_{1-x}\text{Ge}_x$ compound with varied Ge content x . [108, 109]

From equation 1.1, using higher Si concentration in the barriers results in the barrier with higher direct-band gap energy than that of Ge QWs; hence, a potential well at Ge direct-gap transition can be formed. The thickness of Ge well should be thin enough (< 25 nm) to preserve the quantum confinement effect, and the barrier thickness and Si composition should be large enough to prevent tunneling of carrier wavefunction between the two adjacent QWs. Furthermore, in order to grow Ge/SiGe MQWs on Si, Ge-rich SiGe relaxed buffer with the same Ge concentration as that in Ge MQWs, was employed. As a result, the MQW structure is strain balanced, preventing the strain to be accumulated and allows the growth of MQW structures with a high number of Ge quantum well period on Si. To explain, as shown in Fig. 1.14, on Ge-rich SiGe relaxed buffer, Ge well is under compressive strain relative to the relaxed buffer. To compensate, Ge-rich SiGe barrier (with lower Ge concentration than that of relaxed buffer) is chosen so that the barrier will be under tensile strain relative to the relaxed buffer. Additionally, the thickness ratio between Ge well and SiGe barrier is needed to be selected to achieve the aimed weighted average of Ge concentration in the MQWs region. With this configuration, QWs with type I alignment (the bottom of the conduction band and

the top of the valence band is in the same material) can be expected at the direct-gap transition as in Fig. 1.15 [66] which is the origin of strong QCSE from the Ge QWs sandwiched by Ge-rich SiGe barriers.

Significantly, due to the compressive strain in the well, the heavy hole becomes the top most valence band for the Ge wells (Fig. 1.15) which allows stronger Stark shift of direct-gap transition from Ge wells thanks to the heavier effective mass. Furthermore, SiGe barrier with Ge concentration not less than 0.85 still has the global minima of the conduction band at the L valley like Ge; therefore, Type I alignment is also obtained at the L valleys with a weak confinement as shown in Fig. 1.15. This enable an easy sweeping out of photo-generated carriers after scattering from Γ to L valleys [66, 110], and helps prevent carrier saturation effect which is a performance-limiting factor in III-V QWs [111].

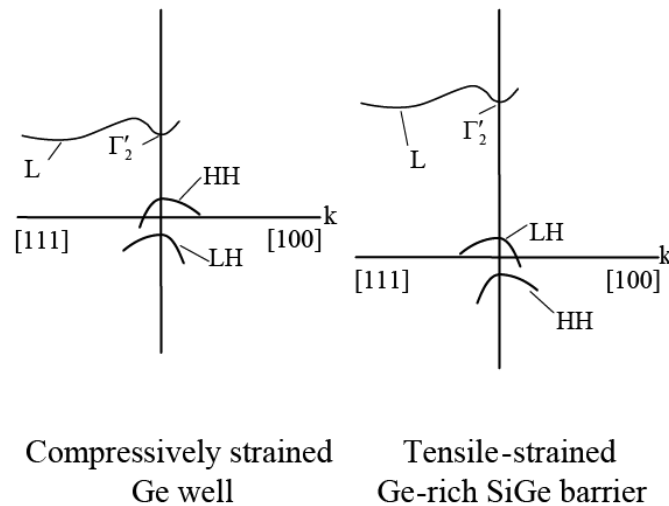


Figure 1.14: Schematic band diagrams of compressively strained Ge well and tensile strained Ge-rich SiGe barrier [66]. The valence band has a heavy-hole (HH) character for compressive strain, and a light-hole (LH) character for tensile strain.

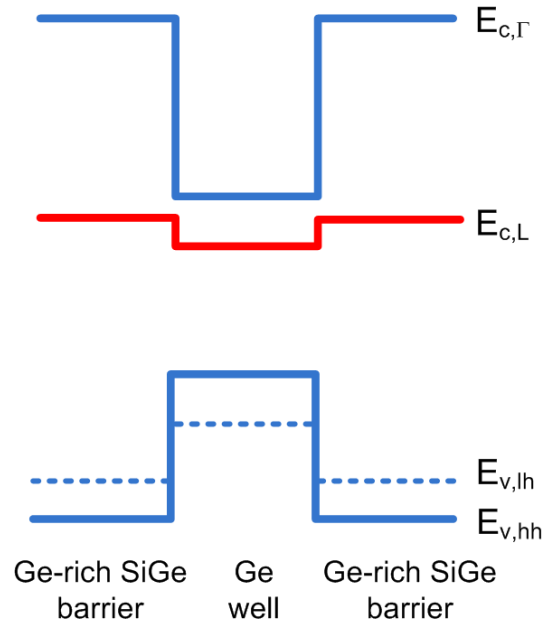


Figure 1.15: Schematic view of the band alignment (not to scale) of the Ge/SiGe quantum well structure, with compressive strain Ge well and tensile strain Ge-rich SiGe barriers on a relaxed SiGe buffer [66].

1.4 Ge/SiGe multiple quantum wells: state of the art

After the discovery of strong QCSE at room temperature from Ge/Si_{0.15}Ge_{0.85} MQWs grown on a silicon substrate by reduced pressure chemical vapor deposition (RPCVD) in 2005 [96], several experimental works regarding its modulation and detection properties were reported using the same growth technique. In 2006, Kuo et al. [97] presented the possibility of applying the Ge/Si_{0.15}Ge_{0.85} MQWs at the telecommunications wavelength of 1.55 μm . The quantum confinement and the compressive strain in Ge wells shift the direct-gap absorption edge of Ge from 0.8 eV (1.55 μm) to 0.88 eV (1.4 μm). The authors demonstrate that the absorption edge can be shifted back to the C-band range by heating the quantum well structures to 90°C comparable to the working temperature of silicon chips. 12.5 nm thick Ge wells and 5 nm thick Si_{0.175}Ge_{0.825} barriers are employed in order to decrease the effect of quantum confinement and the compressive strain in the Ge well. In Fig 1.16(a), at the reverse bias voltage of 0.5 V, it is obvious that operating at higher temperature shifts the absorption edge toward longer wavelength. In Fig 1.16(b), at 90°C the absorption edge is shifted from approximately 1,500 nm to 1,560 nm by applying reverse bias voltage from 0 to 2 V. The

maximum effective absorption coefficient change is $2,703 \text{ cm}^{-1}$ at $1,538 \text{ nm}$ with bias voltage of 1.5 V .

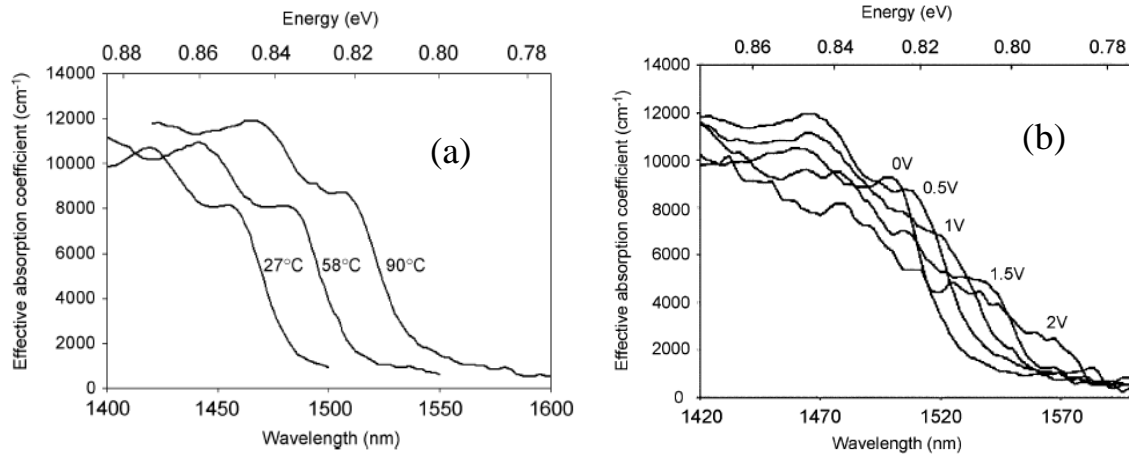


Figure 1.16: (a) Effective absorption coefficient of Ge/SiGe quantum wells at three temperatures with the use of 0.5 V reverse bias voltage [97].

(b) Effective absorption coefficient of Ge/SiGe under each reverse bias voltage at 90°C [97].

In 2008, J. E. Roth et al. [112, 113] demonstrated side-entry Ge quantum-well electro-absorption modulator on SOI substrate in C-band wavelength with a swing voltage of 1 V by using a frustrated total internal reflection structure (Fig. 1.17). By adding a thin layer of 50 nm SiO_2 , oblique incidence on the buried oxide layer results in frustrated total internal reflection between two high-index layers of $\text{Si}_{0.1}\text{Ge}_{0.9}$; hence, allowing control of the reflectivity. 70% reflectivity is obtained which increases the quality factor of the resonator. The operating wavelength of the electroabsorption modulator also extends to the telecommunication wavelength of around $1.55 \mu\text{m}$ as shown in Fig 1.18 (a) by working at 100°C which is similar to operating temperatures of CMOS chips. In Fig 1.18 (b), J. E. Roth et al. shown that with the use of 1 V swing (from 3.625 to 4.625 V), a contrast ratio of more than 3 dB can be obtained from 1539 to 1542.5 nm . Besides, for 4 V swing (from 0.875 to 4.875 V) the contrast ratio of more than 3 dB can be obtained from 1536 to 1545 nm with a peak of 6 dB at 1541 nm . Additionally in 2006, the QCSE has been demonstrated at low temperature (17 K) in a Schottky diode configuration with reverse bias voltages lower than 1 V from Ge/SiGe MQWs grown by low energy plasma enhance chemical vapor deposition (LEPECVD) technique [114]. For light detection, in 2007 Ge/SiGe MQW waveguide

detectors were reported with a data transmission rate of 2.5 Gb/s at - 8 V reverse bias with a responsivity of 0.3 A/W [115].

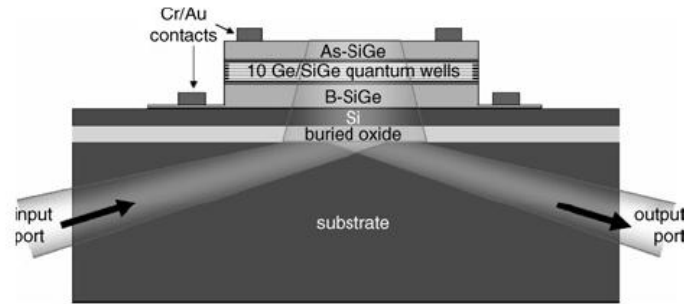


Figure 1.17: side-entry Ge quantum-well electroabsorption modulator on SOI substrate [112]

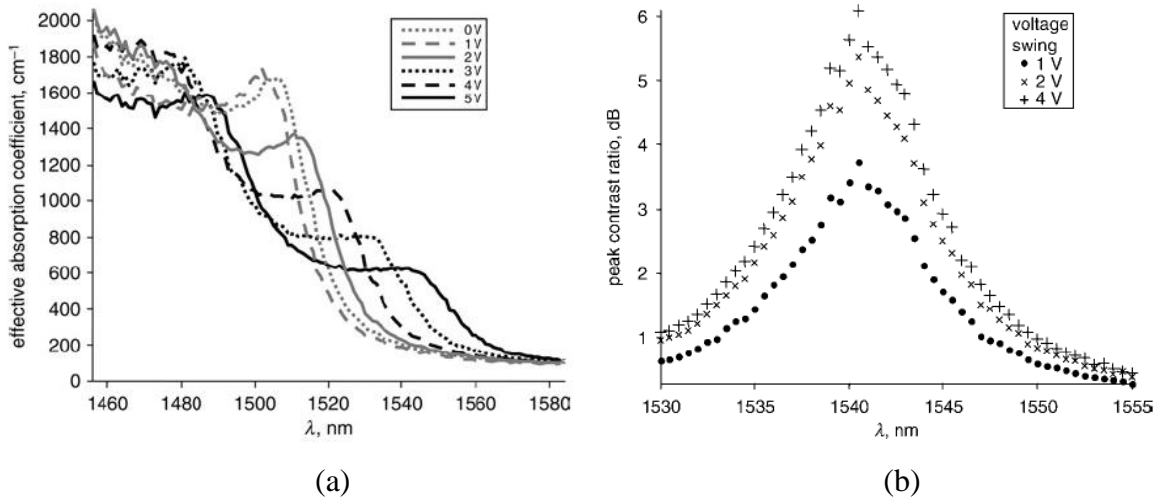


Figure 1.18: (a) Absorption coefficient at 100°C with different bias voltage
(b) Peak contrast of the proposed modulator at different wavelengths [113].

Moreover, there are several significant works on the Ge/SiGe MQWs recently reported during the time frame of my PhD thesis. In 2010, S. A. Claussen et al. used a pump-probe measurement to prove an ultrafast carrier dynamics and transport properties in Ge/SiGe MQWs [110]. In 2011, L. Lever et al. experimentally demonstrated the QCSE at the wavelength of 1.3 μm from Ge/SiGe MQWs [116]. R. K. Schaevitz et al. theoretically and experimentally studied the contributions of the indirect gap absorption in Ge/SiGe MQWs which is the main contribution to the insertion loss (IL) of the device based on the material systems [117]. In 2012, S. Ren et al. reported a Ge/SiGe MQW waveguide modulator

integrated with silicon-on-insulator waveguides with a 3.5 GHz bandwidth and a photocurrent contrast ratio of 3.2 dB was obtained with 1 V swing [118]. Significantly in 2011, E. Gatti et al. reported the observation of room temperature photoluminescence based on the excitonic direct gap transition of Ge/SiGe MQWs [119]. Also in 2011, E. Gatti et al. used photoluminescence study at 10 K to understand the scattering, thermalization, and recombination processes occurring in Ge/SiGe MQWs [120].

In summary, Ge/SiGe MQWs have opened the way to efficiently harness the direct-gap properties of Ge, which is a silicon compatible semiconductor. The first aim of the thesis is to investigate the light modulation performance at room temperature of Ge/SiGe MQWs based on QCSE with an emphasis on a waveguide configuration for photonic IC application. Moreover, light detection and emission properties at room temperature of the Ge/SiGe MQWs will be also investigated with a view to employing the same structure as a ubiquitous photonic building block towards electronic-photonic integration, revolutionizing the chip scale photonic integrated circuits. Ge/SiGe multiple quantum well structures were grown by low energy plasma enhanced chemical vapour deposition (LEPECVD) at L-NESS laboratory, (Como - Politecnico di Milano, Italy). The use of LEPECVD ensures the deposition of ultra-high quality Ge/SiGe MQWs using a SiGe graded buffer with Ge concentration continuously increasing from zero to the final concentration to obtain a high quality relaxed Ge-rich SiGe buffer, on which high quality Ge/SiGe quantum wells can be grown and investigated.

The remainder of this thesis is organized as follows. Chapter 2 summarizes the epitaxial growth and fabrication techniques used to fabricate the optoelectronic devices in this thesis. Chapter 3 includes the characterization setup and experimental results on the Ge/SiGe MQWs modulation characteristics. DC modulation properties are reported for both surface illumination and waveguide configurations; high speed modulation characteristics are reported from an electro-absorption waveguide modulator based on Ge/SiGe MQWs. Chapter 4 includes detection and emission properties of the Ge/SiGe MQWs. The DC and high speed detection capabilities are experimentally reported from devices with surface illumination and waveguide configurations. Moreover, electroluminescence measurements of the Ge/SiGe MQWs are reported at room temperature. Emission characteristics of the MQWs will be discussed at different current injections and temperatures. Finally, chapter 5 summarizes the results obtained during this PhD thesis and discusses possible future research route.

Chapter 2. Ge/SiGe quantum well epitaxial growth and optoelectronic device fabrication

This chapter summarizes the epitaxial growth and fabrication techniques used to fabricate optoelectronic devices for my PhD thesis. Active photonic devices with different configurations were fabricated to investigate modulation, detection, and emission properties of the Ge/SiGe multiple quantum wells (MQWs). Through collaboration, the Ge/SiGe MQW structures were obtained from G. Isella and D. Christina at the Laboratory for Epitaxial Nanostructures on Silicon and Spintronics (L-NESS), Politecnico di Milano, Italy using a Low-Energy Plasma-Enhanced Chemical Vapour Deposition (LEPECVD) technique. Then, I fully developed the technology process flows and fabricated the devices at the nanocenter Centrale de Technologie Universitaire (CTU) - IEF/MINERVE, which is an in-house 1000 m² cleanroom dedicated mainly to group IV materials at Université Paris-Sud XI.

2.1 Ge multiple quantum wells grown by LEPECVD

LEPECVD aims to tackle the need of Ge rich Si_xGe_{1-x} buffer for the epitaxial growth of Si_xGe_{1-x} electronic or photonic devices on Si as the lattice parameter of Ge is 4.2% larger than the one of Si. Buffer layer should have low surface roughness and dislocation density, and can be deposited with a fast rate at low substrate temperatures [121]. These are difficult through standard methods. Molecular Beam Epitaxy (MBE) usually has a very low deposition rate and reduced wafer size [122]. Ultrahigh Vacuum (UHV) or Reduced-Pressure (RP) Chemical Vapour Deposition (CVD) necessitate the use of high growth temperature (~900°C) to realize such buffer resulting in significant surface roughness [123]. For LEPECVD, with the use of a low energy plasma to enhance and control the deposition [124], the system gives deposition rate as high as 10 nm s⁻¹ on 4-inch silicon wafer at substrate temperatures down to 400°C with crystalline quality as good as (or even better than) the quality of standard CVD [125, 126]; the use of plasma with low ion energies (~10 eV) helps to avoid damage in the crystal structure. Moreover, the growth rate can be controlled by the plasma density, enabling a fast growth of Si_xGe_{1-x} graded buffer on which a high quality Ge/SiGe MQW structures can be deposited with lower deposition rate. This allows us to investigate the properties of the MQW structures with very good material quality.

Fig. 2.1 shows a schematic view of the LEPECVD system [109, 127]. A tantalum filament, which acts as the plasma source, is heated by a high current so that electrons are emitted through thermoionic process. Argon gas is passed from the plasma source into the growth chamber. As a negative voltage (20–30 V) is applied to the filament while the chamber wall and anode ring are kept grounded, a direct current arc discharge (30–50 A) is then sustained between the tantalum filament and the growth chamber. The anode ring is employed with a view to stabilizing the discharge. Magnetic fields, created by coils placed outside the growth chamber, are used to focus, defocus, and deviate the plasma onto the substrate. Precursor gases are introduced via the gas inlet below the substrate. The process gases of SiH_4 and GeH_4 are used for the growth of SiGe. PH_3 and B_2H_6 diluted in Ar are used for n and p doping respectively. A carrier gas, H_2 , is employed to dilute the precursor gases and/or to tune the surface mobility of absorbed atoms. Thanks to the highly-reactive environment at the surface of substrate surrounded by the plasma, the material can be deposited quickly onto the substrate. These characteristics give LEPECVD system the ability to control the growth rate by varying the plasma intensity and the amount of the precursor gases. Moreover, the growth rate was found to be independent of the substrate temperature in a wide range, and almost linearly dependent on plasma intensity, confirming that the deposition is plasma driven.

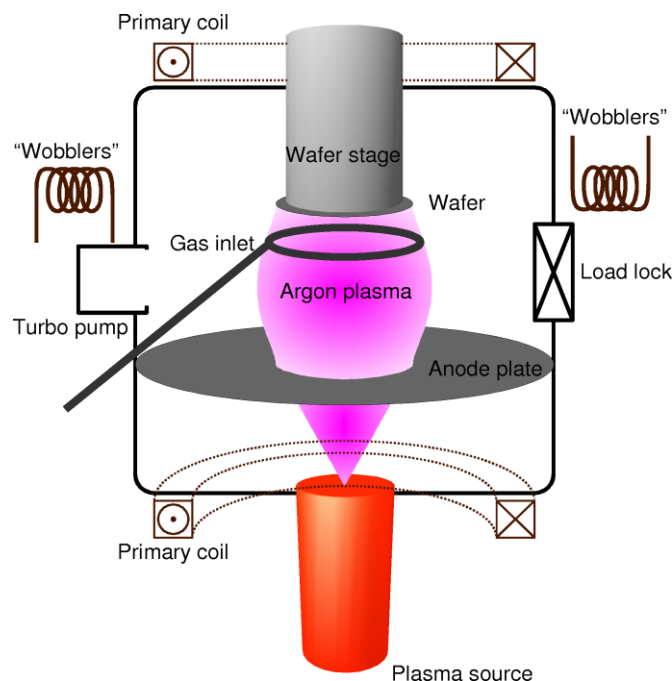


Figure 2.1: Schematic view of the LEPECVD system [figure taken from 109]

Ge/SiGe MQWs with 10 nm thick Ge well and 15 nm thick $\text{Si}_{0.15}\text{Ge}_{0.85}$ barriers with different number of periods (10, 20, and 50) grown on 4 inch Si wafers by LEPECVD system were obtained from L-NESS. As the lattice parameter of Ge is 4.2% larger than that of Si, $\text{Si}_{1-x}\text{Ge}_x$ relaxed buffer is required to grow Ge/SiGe MQWs on Si. The 10 nm well and 15 nm barrier thickness are used so as to have the weighted average of Ge concentration within the MQWs equal to that of $\text{Si}_{0.1}\text{Ge}_{0.9}$ buffer. As a result, the MQW structure is strain balanced, preventing the strain to be accumulated and allows the growth of MQW structures with high number of Ge QWs. Benefits of Ge/ $\text{Si}_{0.15}\text{Ge}_{0.85}$ MQWs used for the first investigation are also discussed in chapter 1.

The epitaxial steps are as follows: On a 100 mm Si(001) substrate, a 13 μm thick $\text{Si}_{1-x}\text{Ge}_x$ graded buffer was deposited with linearly increasing Ge concentration y at a rate of $7\%/ \mu\text{m}$ from Si to $\text{Si}_{0.1}\text{Ge}_{0.9}$. Then, 2 μm of $\text{Si}_{0.1}\text{Ge}_{0.9}$ was grown on the top of the graded layer, forming a fully relaxed virtual substrate (VS) on which high quality Ge rich heterostructures could be grown. Subsequently, a 500 nm boron-doped $\text{Si}_{0.1}\text{Ge}_{0.9}$ layer was grown to serve as a p-type contact. The epitaxial steps from the graded buffer to the p-type layer were conducted with a high growth rate of $5-10 \text{ nms}^{-1}$ for maximum efficiency. Next for optimum layer and interface control, a low rate growth of $\sim 0.3 \text{ nms}^{-1}$ was used to deposit a 50 nm $\text{Si}_{0.1}\text{Ge}_{0.9}$ spacer, the MQWs, and a 50 nm $\text{Si}_{0.1}\text{Ge}_{0.9}$ cap layer. The MQWs itself consisted of ten, twenty, or fifty 10 nm Ge quantum wells (QWs) sandwiched between 15 nm $\text{Si}_{0.15}\text{Ge}_{0.85}$ barriers. Finally, a 100 nm phosphorus-doped $\text{Si}_{0.1}\text{Ge}_{0.9}$ n-type contact was grown in an alternative reactor to avoid cross-contamination. Cross section of epitaxy steps and a typical x-ray diffraction $\omega - 2\theta$ scan are shown in Fig. 2.2 and 2.3 respectively.

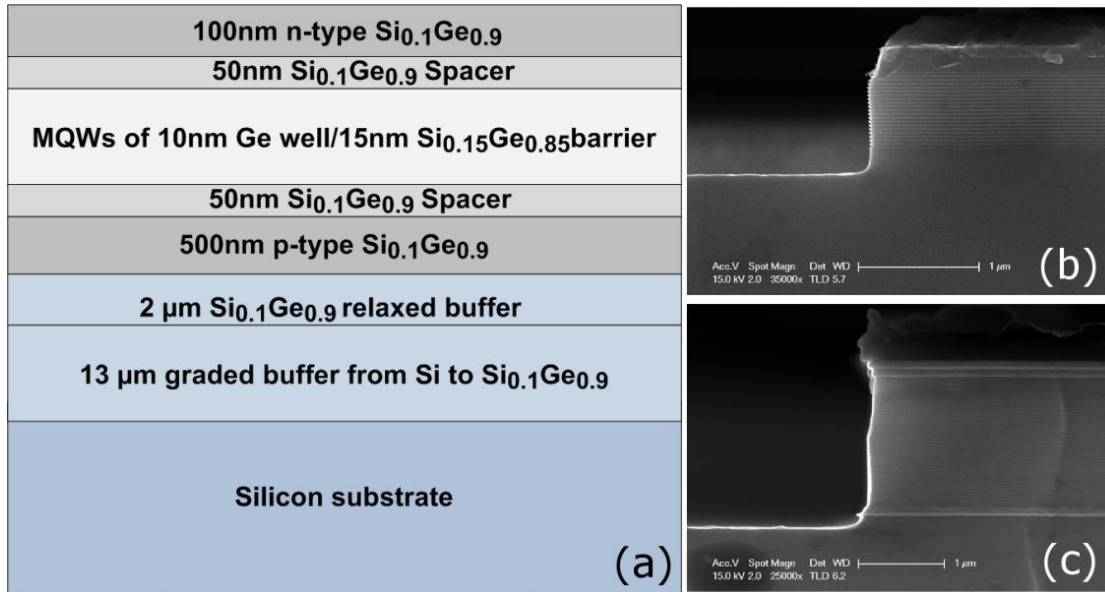


Figure 2.2: (a) Cross section of epitaxy steps for the Ge/SiGe MQWs used in this thesis, and SEM images of Ge/SiGe MQWs with (b) 20, and (c) 50 periods of Ge quantum wells.

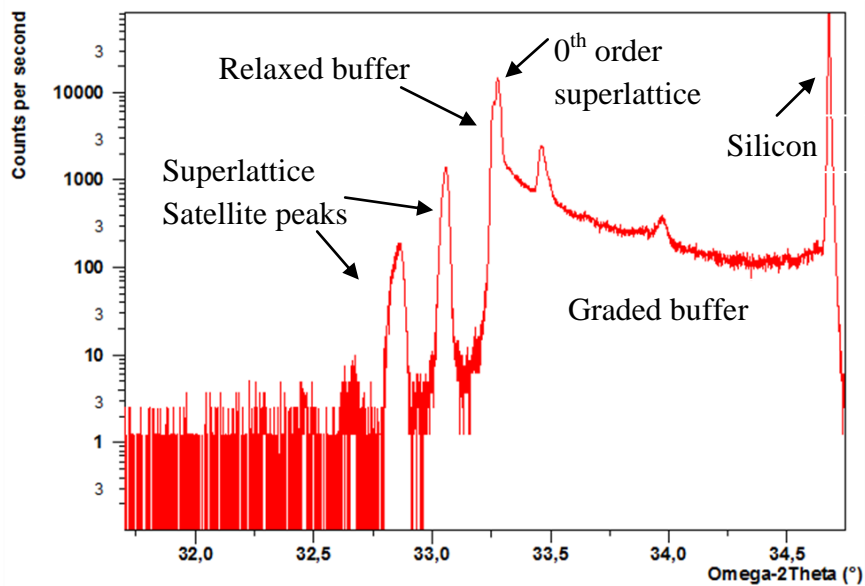


Figure 2.3: X-ray diffraction $\omega - 2\theta$ scan through the (004) reflection. The Si substrate (004) peak is clearly visible. The peak spacing gives a superlattice period of 26.2 nm, closed to the nominal values of 25 nm of 10 nm Ge well and 15 nm Si_{0.15}Ge_{0.85} barriers. The Ge content of the VS was found to be 89.99%, and the position of the zeroth order peak indicates an average composition of the MQW structure of 90.50%.

2.2 Fabrication of Ge quantum well optoelectronic devices

To study the possibility to use Ge QW structures for different optoelectronic functionalities, I developed and fabricated various kinds of optoelectronic devices. Different Ge quantum well devices had to be studied in order to observe both the intrinsic material properties from surfaced-illuminated structures and the device performances in a waveguide configuration for applications in photonic IC. Fig. 2.4 shows the schematic view of 4 different device configurations that I proposed, fabricated, and characterized during my PhD thesis. In section 2.2.1 fabrication steps of the DC surface illuminated p-i-n diode (Fig 2.3(a)) are reported; while, fabrication steps of the high speed devices and the planar waveguide (Fig 2.4(b), (c), and (d)) are reported in section 2.2.2.

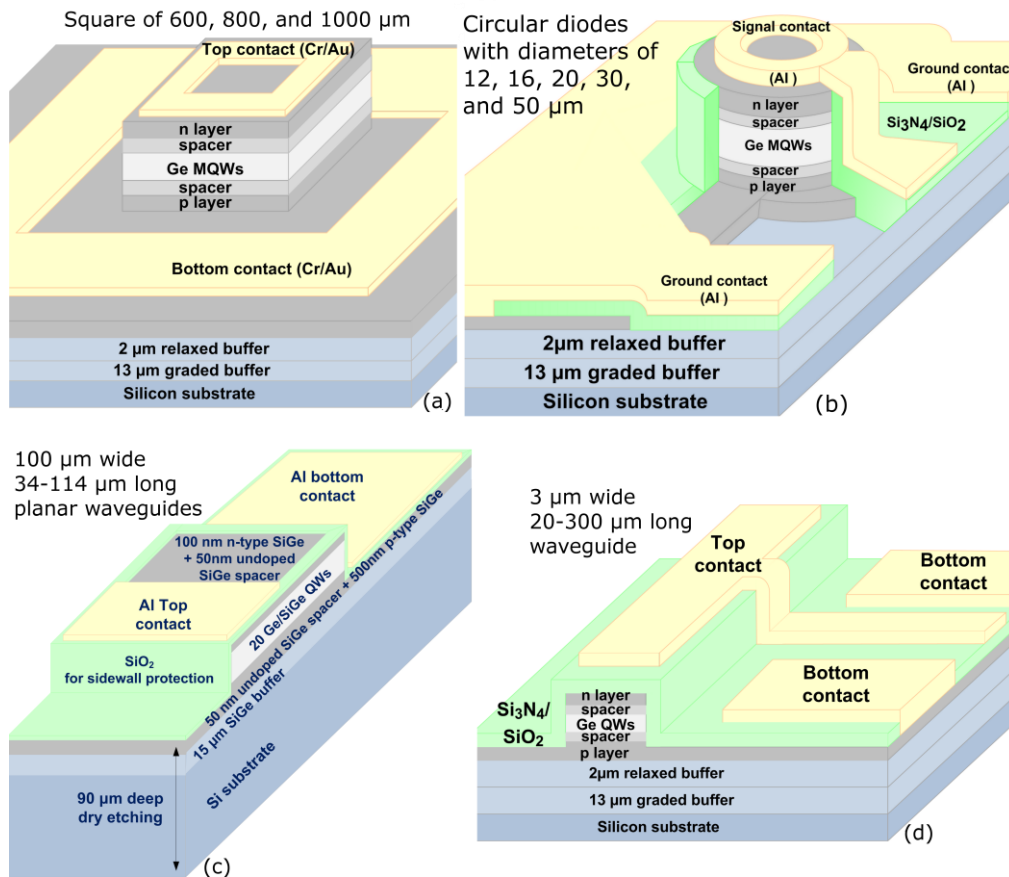


Figure 2.4: Schematic views of optoelectronic devices fabricated in this work:

- (a) DC surface illuminated p-i-n diode; (b) high frequency surface illuminated diode with coplanar electrode; (c) DC diode in planar waveguide structure; and (d) high frequency 3 μm wide waveguide diode with coplanar electrode.

2.2.1 DC surface illuminated p-i-n diode fabrication

At the beginning, simple vertical p-i-n diodes as shown in Fig 2.4 (a) were developed in order to verify the existence of the QCSE from Ge/SiGe MQWs grown by LEPECVD, which is the first step before investigating its rapidity and other photonic functionalities. The mesa is a square with side width of either 600, 800, or 1000 μm . The top contact was designed to facilitate the characterization with vertically coupled light. A microscope image of a fabricated vertical p-i-n diode is shown in Fig. 2.5.

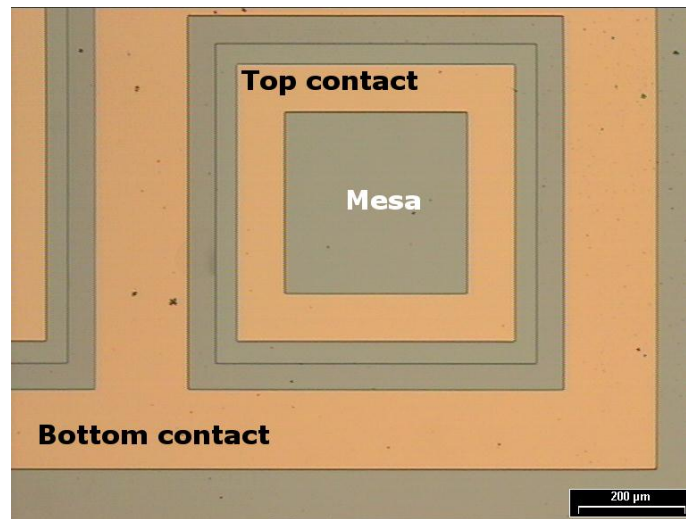


Figure 2.5: optical microscope image of a 600 μm square surface illuminated p-i-n diode.

The DC surface illuminated p-i-n diodes were realized by two lithography steps for mesa etching and metal evaporation. Simplified process flow including both lithography steps is given in Fig 2.6. The detailed procedure can be read from section 2.2.2, in which similar procedures were used in mesa etching and metallization. In brief, firstly the mesa was defined using UV lithography (MJB4) with i-line photoresist and a subsequent dry etching to pattern the structure onto the wafer. A dummy wafer was employed to ensure that the etching stopped within the p-typed layer to obtain a p-i-n diode. Then the lift off technique was employed for metallization, using an image reversal resist from MicroChemicals [128]. The photoresist patterning consisted of a lithography step with classical alignment procedure, then a reverse bake, a flooding exposure (a lithography without photomask), and photoresist development, which will be explained in detail in section 2.2.2. Subsequently, 20 nm of Chromium (Cr) and

200 nm of gold (Au) were deposited by E-beam evaporation technique (Plassys Modele MEB 550S) following by an acetone lift-off. Au is served as a conducting layer for the on-wafer probing and Cr is served as an adhesive material between Au and $\text{Si}_{0.1}\text{Ge}_{0.9}$ surface. For all devices used in this thesis, CMOS compatible metal like Al could be used as well. Indeed, every high speed devices described in the next section was realized by using Al for metallization.

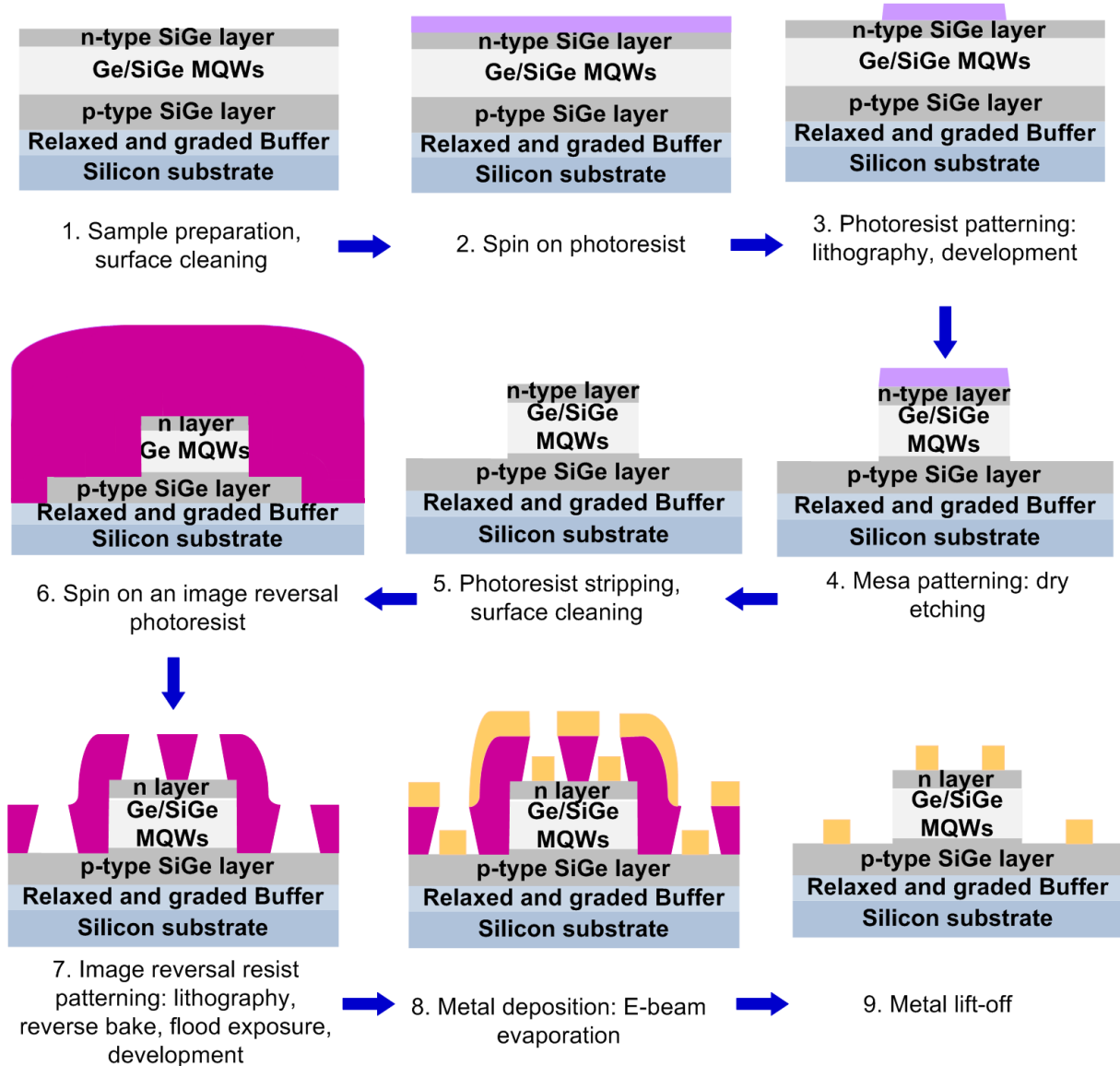


Figure 2.6: Process flow used to fabricate a DC surface illuminated p-i-n diode.

2.2.2 High speed surface-illuminated and waveguide optoelectronic device fabrication

This section will thoroughly cover the fabrication procedures utilized for the realization of three different optoelectronic devices: high speed waveguide p-i-n diode, high speed surface illuminated p-i-n diode, and DC planar waveguide p-i-n diode. All of the devices are fabricated on the same wafer. Therefore, the devices were designed to use the same fabrication procedure, consisting of 4 main lithography steps for mesa etching, mesa isolation etching, $\text{Si}_3\text{N}_4/\text{SiO}_2$ insulation layer patterning, and metallization and an optional fifth lithography step for deep etching of waveguide devices as shown in the Fig 2.7. Fig 2.8 shows SEM image of three different optoelectronic devices fabricated on the same wafer with the same fabrication procedures.

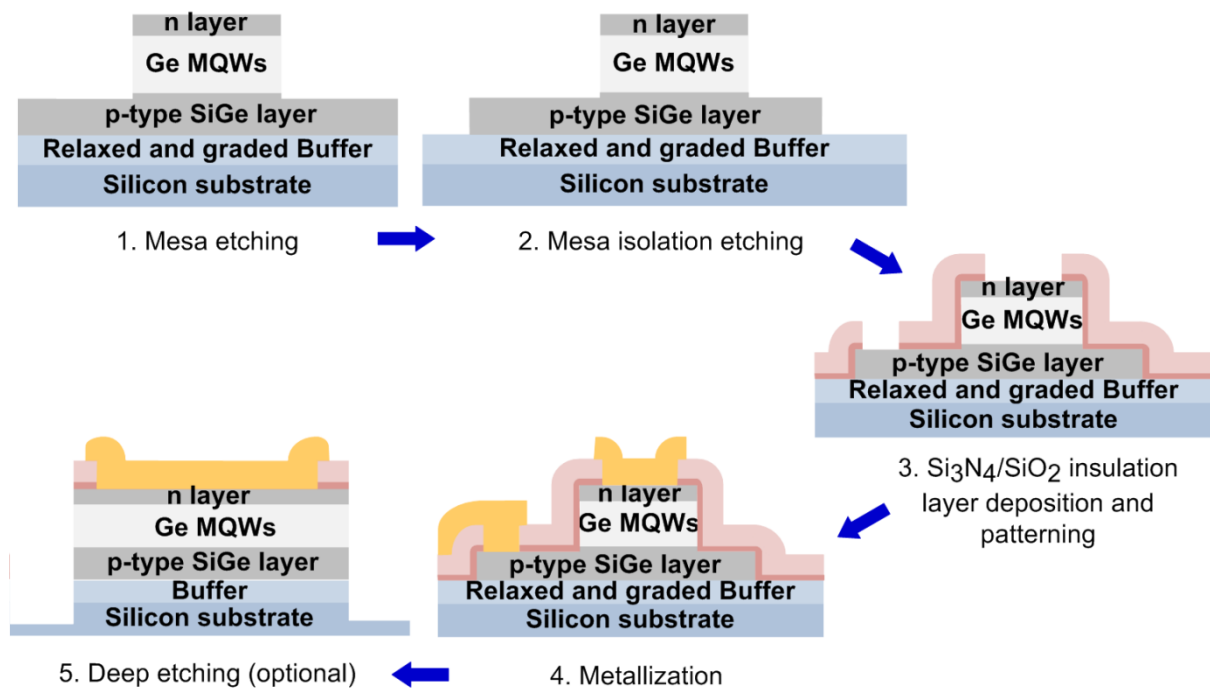


Figure 2.7: Simplified process flow used to fabricate high speed waveguide p-i-n diode, high speed surface illuminated p-i-n diode, and/or DC planar waveguide p-i-n diode.

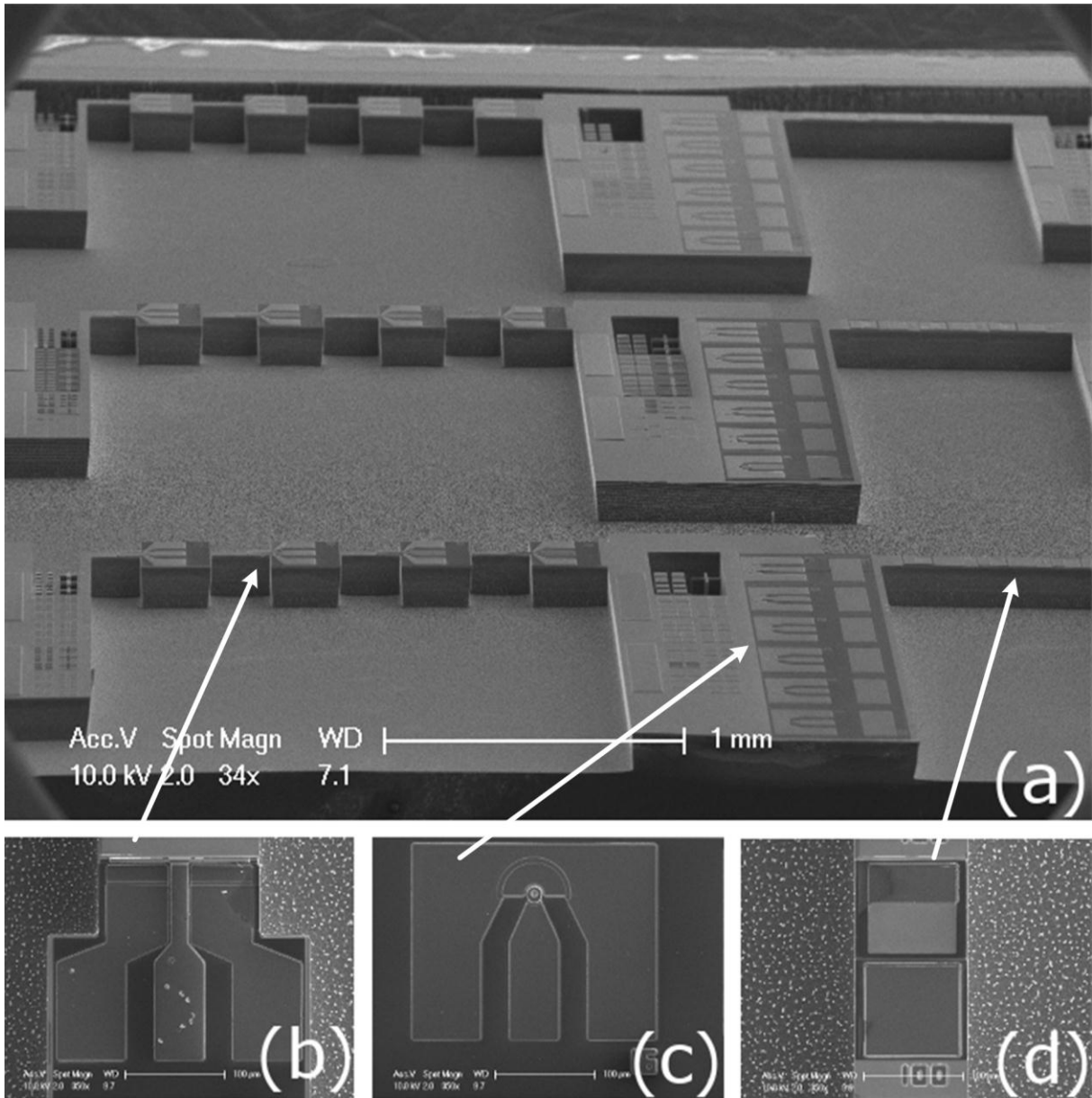


Figure 2.8: SEM images of (a) three different configurations of fabricated optoelectronic devices designed to use the same fabrication steps, and close-up images of high speed (b) waveguide, and (c) surface illuminated p-i-n diode with coplanar electrode, and (d) DC planar waveguide.

2.2.2.1 Mesa patterning

Fig 2.9 describes the processing procedure employed for the mesa patterning. To begin with, (1) a sample piece of around 2 cm square was cleaved from 100 mm Si wafer on which Ge/SiGe MQWs epitaxy was done at L-NESS laboratory, Como, Italy. Then, (2) a surface cleaning was conducted using acetone and isopropanol. It should be noted that the standard piranha cleaning consisting of sulfuric acid and hydrogen peroxide (H_2SO_4 and H_2O_2) widely used with Si technology cannot be employed here as they quickly etch Ge and Ge-rich SiGe. Next, (3) a proper baking was needed to remove the absorbed H_2O molecules on the sample surface. (4) A 500 nm thick positive photoresist was then spun on the sample surface in the order of 3000 – 4000 round per minutes (rpm). The choice of photoresist and spin speed are different in each fabrication step depending on the require feature size to be patterned, surface topology of the sample, the nature of the process to be subsequently performed etc. (5) A softbake step was required in order to decrease the remaining solvent in the coated photoresist. This will prevent the photoresist from contaminating and/or sticking to the mask. Moreover, the soft bake will also help prevent too much creation of N_2 during the exposure which will result in a possible foaming of the photoresist. (6) For the exposure step, an i-line photoresist was patterned by a UV lithography machine (MJB4 from SUSS MicroTec), which is specially designed for small substrate sample typically used in academic research. The exposure dose and gap were selected according to different types of photoresist and needed resolution of each fabrication steps. For the mesa patterning step, a prevacuum contact was typically used in order to obtain devices with as exact dimension as possible to the designed values. (7) The exposed area of the photoresist was then become soluble in a developer. A development time was needed to be optimized so that all of the exposed photoresist can be completely removed, but the unexposed area of photoresist remains on the sample. (8) The sample was checked under optical microscope to ensure that the photoresist was developed according to the intended structure and dimensions. (9) A dry etching was done with SF_6 plasma to define the mesa. This is a critical step; it is necessary to verify that the etching stops within the p-type region and preferably with as thick as possible remaining p layer to ensure a p-i-n diode with a low serial resistance. (10) A dummy sample, which was etched at the same time as the real sample, was inspected under scanning electron microscope (SEM) to ensure a good etching quality. (11) The photoresist was removed using acetone and isopropanol.

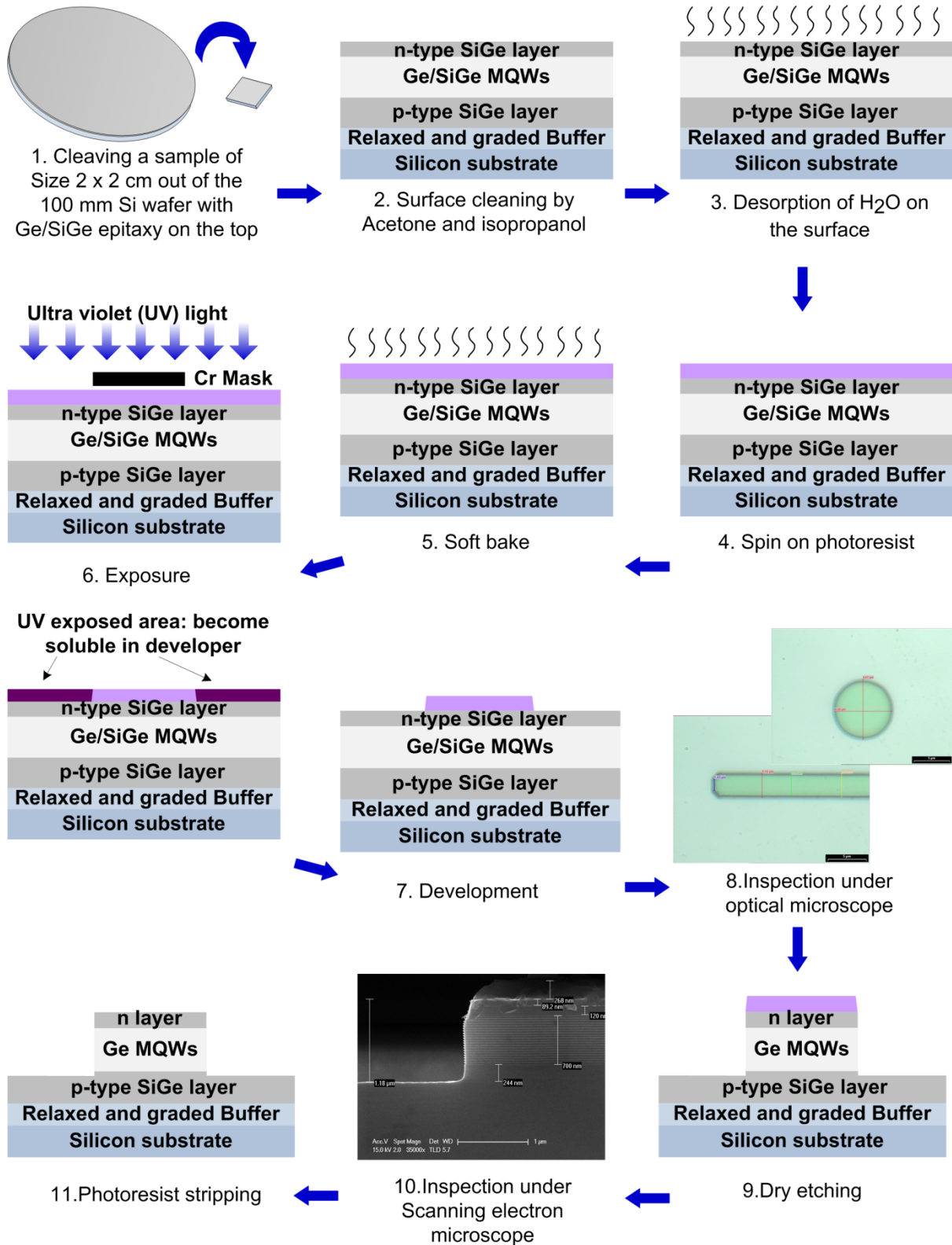


Fig 2.9: The processing procedure of the mesa patterning step.

2.2.2.2 Mesa isolation

The second major step is to isolate each mesa by dry etching down to the relaxed buffer layer. This is used to electrically separate each mesa and avoid a possible parasitic capacitance between the p layer and the coplanar electrode. If we avoid performing such etching, the parasitic capacitance would be included in the high frequency characterization of the diode, which would prevent us from obtaining the accurate information on the high speed performance of the materials. As shown in Fig. 2.10, (1) the sample with patterned mesas from the first step was prepared by a proper surface cleaning and baking. (2) A positive photoresist, thicker than that used in the first step in order to well cover the mesas, was spun on the sample surface. (3) A softbake step was done to decrease the remaining solvent in the coated photoresist. (4) An alignment between the glass photomask with a Cr layer of the aimed pattern and the mesa was performed using a standard mask aligner thanks to specific alignment marks and the photoresist was then exposed by UV light. After the development process (5) in which the exposed area of photoresist was removed, (6) the sample was inspected under the optical microscope to verify the obtainment of the aimed pattern. (7) Then, dry etching with SF₆ plasma was performed to remove the p-type layer between each mesa. (8) Finally, the photoresist was removed using acetone and isopropanol.

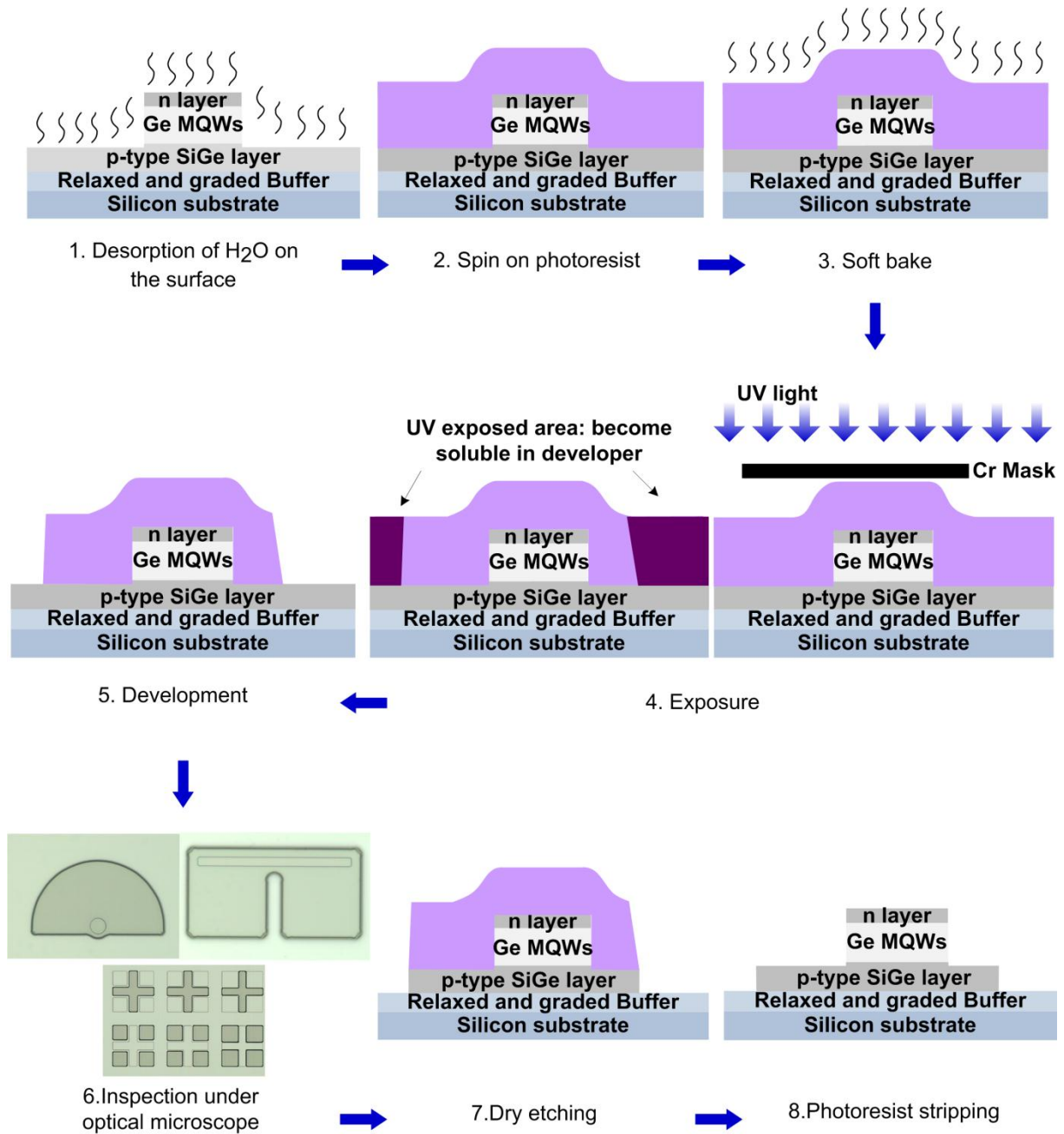


Fig 2.10: The processing procedure of the mesa isolation step.

2.2.2.3 Deposition and patterning of SiO₂/Si₃N₄ insulation stack

The third major step is described in Fig. 2.11. It aims to pattern the insulation stack consisting of 100 nm SiO₂ and 400 nm Si₃N₄ layers which were deposited by plasma enhanced chemical vapor deposition (PECVD) technique. The insulation stack is required to insulate the coplanar electrode from the mesa side wall and the substrate. In order to have a functional p-i-n diode, the electrode needs to connect only with the p-type and n-type contact region. Using Si₃N₄ as a top insulation layer allows a fast dry etching of Si₃N₄ by CF₄ gas with a rather thin photoresist (higher resolution); moreover, the dry etching stops effectively on the SiO₂ layer which has a much slower etching rate by CF₄. The use of SiO₂ layer as the last insulation layer allows it to be removed by buffered HF (BHF) wet etching, preventing any potential irradiation damage to the contact caused by dry etching. (1) The first fabrication step was to clean and bake the sample surface to ensure the cleanness of the structure. (2) Then, 100 nm of SiO₂ and 400 nm of Si₃N₄ were deposited at 300°C using PECVD machine (STS system) under a high frequency (HF) mode. (3) To pattern the insulation stack, a 1.3 μm thick positive photoresist was spun on the sample, and (4) the soft bake was done to decrease the remaining solvent. (5) A photomask with a Cr layer of the desired contact via pattern was aligned with the mesa using the mask aligner; this step is critical as the required alignment precision of 1 μm is in the same order of the aligner capability. The sample was exposed to the UV light in order to transfer the Cr pattern on the mask to the coated positive photoresist. (6) The development in a suitable developer was performed to remove the part of the photoresist that was exposed to the UV light. (7) The developed sample was then inspected under an optical microscope to ensure that both top and bottom contact vias were successfully developed on the photoresist. This is another critical step as the size of the top and bottom contact vias are considerably different. The developing rates are not the same between them; therefore, a compromised development time is necessary to be found. (8) In order to open the insulation stack for both top and bottom contacts, CF₄ plasma was used to etch Si₃N₄ layers with reactive ion etching (RIE) machine (Advanced Vacuum Vision). (9) A wet etching using BHF solution was employed so as to remove the remaining SiO₂ layer. A dry etching was avoided to retain a good crystalline quality of the p and n layers. (10) The sample was inspected under an optical microscope to ensure that SiO₂ and Si₃N₄ layers were successfully removed from the top and bottom contact vias. (11) The photoresist was stripped using acetone and isopropanol.

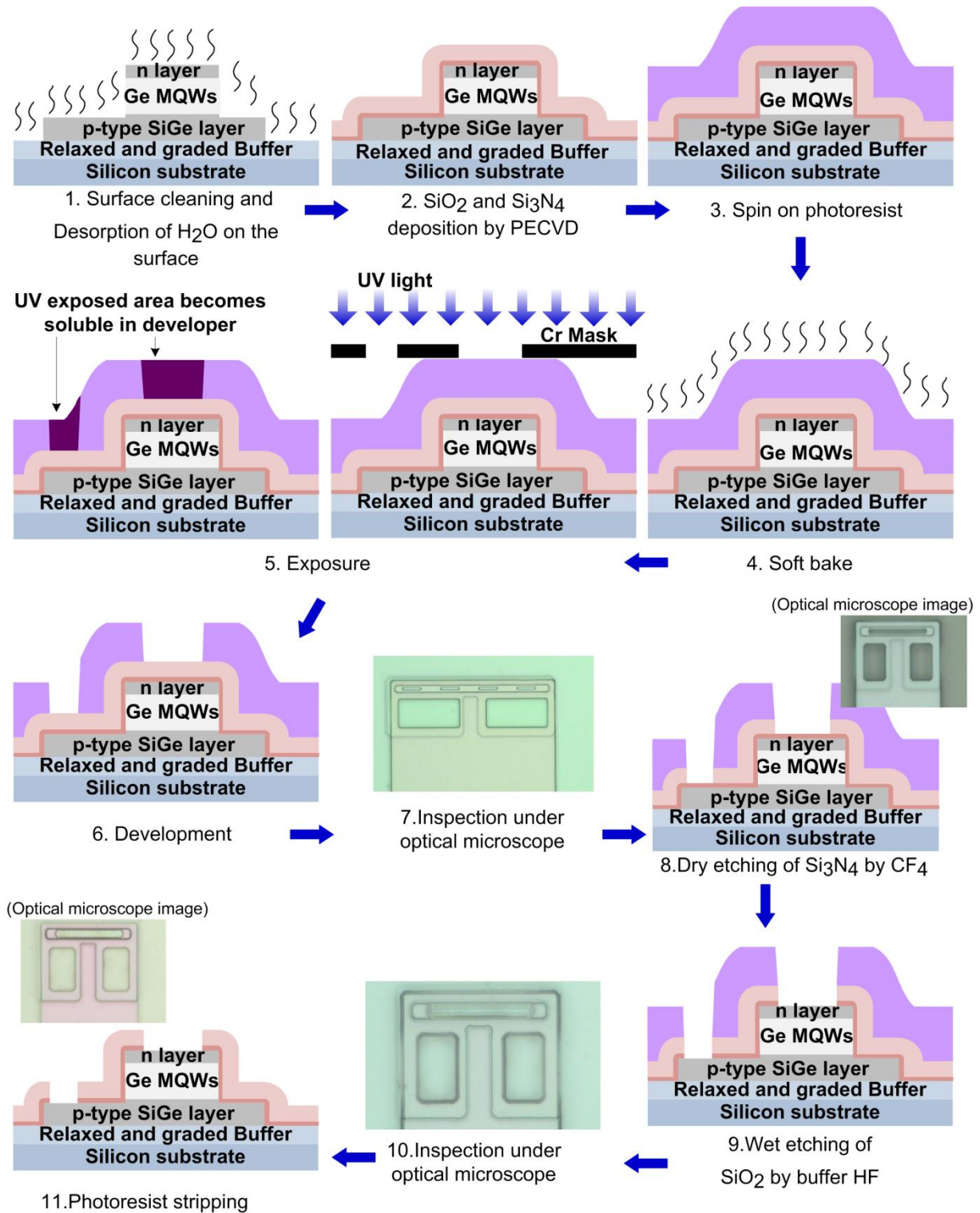


Fig 2.11: The processing procedure for the deposition and patterning of the $\text{SiO}_2/\text{Si}_3\text{N}_4$ insulation stack.

2.2.2.4 Metallization

The fourth major step is metallization as described in Fig. 2.12. To accommodate the metal lift-off process, a thick image reversal photoresist was selected in order to have a good undercut profile for efficient metal lift-off. (1) The process started with cleaning and baking the surface of the sample. (2) The image reversal photoresist was spun on the sample at a predetermined spin speed and duration and (3) a softbake was done to reduce the remaining solvent in the photoresist. (4) An alignment with the photomask with a Cr layer of the desired contact pattern was performed. After this step, the photoresist still acts as a typical positive photoresist of which the exposed area will be soluble in the developer. However, as an image reversal photoresist is used, the exposed area of the photoresist will finally remain on the sample and the unexposed area will be finally removed and the deposited metal will take the pattern of the photomask. To explain, (5) after the exposure, the sample was left at 40°C in order to outgas N₂ which was generated during the exposure and (6) a reversal bake was performed at a much higher temperature in order to crosslink the exposed area; hence, making it permanently insoluble in the developer. The unexposed area of the photoresist was still photoactive. (7) Next, a flooding exposure was done. This makes the formerly-unexposed area of the photoresist become soluble in the developer. (8) The sample was developed in a suitable developer, and the exposed area of the first exposure step remained on the sample. An undercut profile in the developed photoresist was preferable in order to facilitate the metal lift-off process. Therefore, an over development time of around 30% was used. (9) The developed sample was inspected under an optical microscope to ensure that both top and bottom contact metal patterns were successfully developed on the photoresist, and the photoresist had an undercut profile. (10) Just before the metallization step, the sample was cleaned by a diluted HF solution in order to remove GeO₂ potentially oxidized on the surface. (11) 1 μm of Al were deposited by E-beam evaporation technique (Plassys Modelle MEB 550S). A good deposition angle was needed in order to ensure that the metal was well deposited not only on the sample surface but also on the side wall of the diode, to connect the top contact metal to its probing area for on-wafer characterization. (12) A metal lift-off process was done with acetone and isopropanol.

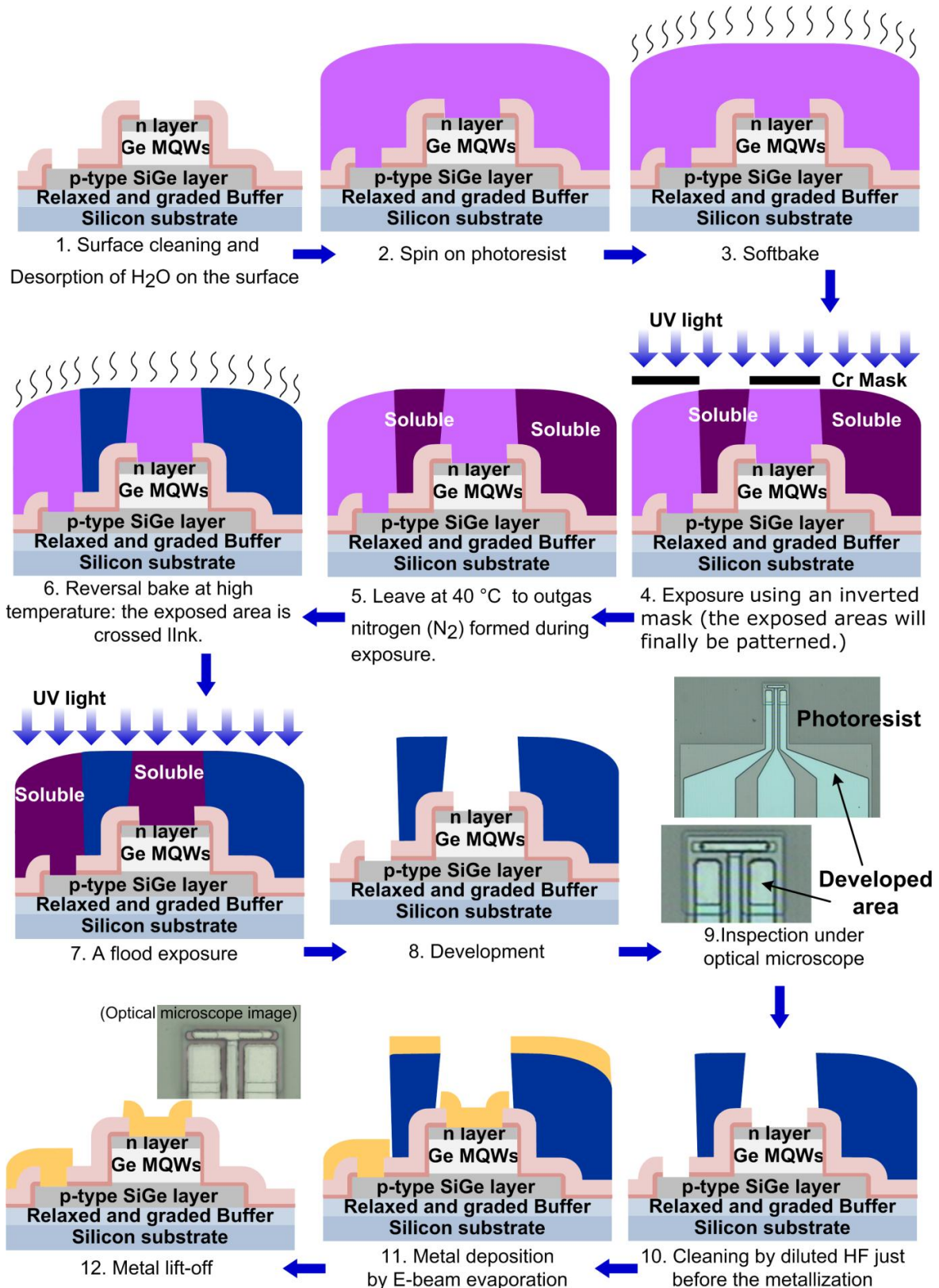


Fig 2.12: The processing procedure of the metallization step.

2.2.2.5 Deep etching (optional)

The fifth optional major step of deep etching is described in Fig. 2.13. This step is designed to facilitate the characterization of 30 – 300 μm long waveguide devices which are too short to be handled by a conventional approach of cleaving and polishing. Therefore, a deep etching of 90 – 100 μm is required in order to bring the lensed fiber to the input facet of the waveguide device. To perform the etching, 5-6 μm thick photoresist is preferred; it is thick enough to protect the sample through the whole deep etching process, and not thicker than the alignment tolerance of this fabrication step. Therefore, double layers of 2.8 μm thick positive photoresist are employed for this fabrication procedure. (1) To begin with, cleaning and baking the surface of the sample obtained from the previous step was done. (2) The first layer of photoresist was spun on the sample and (3) a softbake was done. (4) Then the second layer of the same photoresist was coated at the same spin speed and duration. (5) A second softbake step was also performed to reduce the solvent content in the photoresist. It is worth noting that the temperature and duration of both softbake steps need to be carefully optimized. It is necessary to have a sufficient softbake in order to reduce the solvent content in the photoresist and hence, prevent bubbling and foaming of the photoresist due to the N_2 generated during the exposure. However, too much softbake will decompose a fraction of the photo active compounds within the photoresist; hence, reducing the development rate. In these processes, as the first layer of photoresist has to undergo two softbake steps, it is important to have a compromised temperature and duration of the softbake process. (6) The first alignment and exposure step was performed using approximately half of the necessary exposure time to avoid bubbling of the photoresist due to too much N_2 generated in the double layers of thick photoresist. (7) The sample was developed with approximately half of the necessary development time. (8) The second alignment and exposure step was performed with the remaining of the required exposure time. It should be noted that as the alignment tolerance of this particular fabrication step of 5-6 μm is not critical; therefore, this method of two exposure and development steps does not importantly affect the outcome of the device configuration. (9) The sample was developed for the remaining development time. (10) The Bosch process [10], consisting of alternating cycles of isotropic etching by SF_6 and C_4F_8 polymer deposition, was employed for the deep etching procedure (STS Inductively Coupled Plasma (ICP) etcher). (11) The sample was diced using a wafer dicing machine (Disco 341 Wafer Dicing Saw). (12) Finally, the photoresist was stripped using acetone and isopropanol.

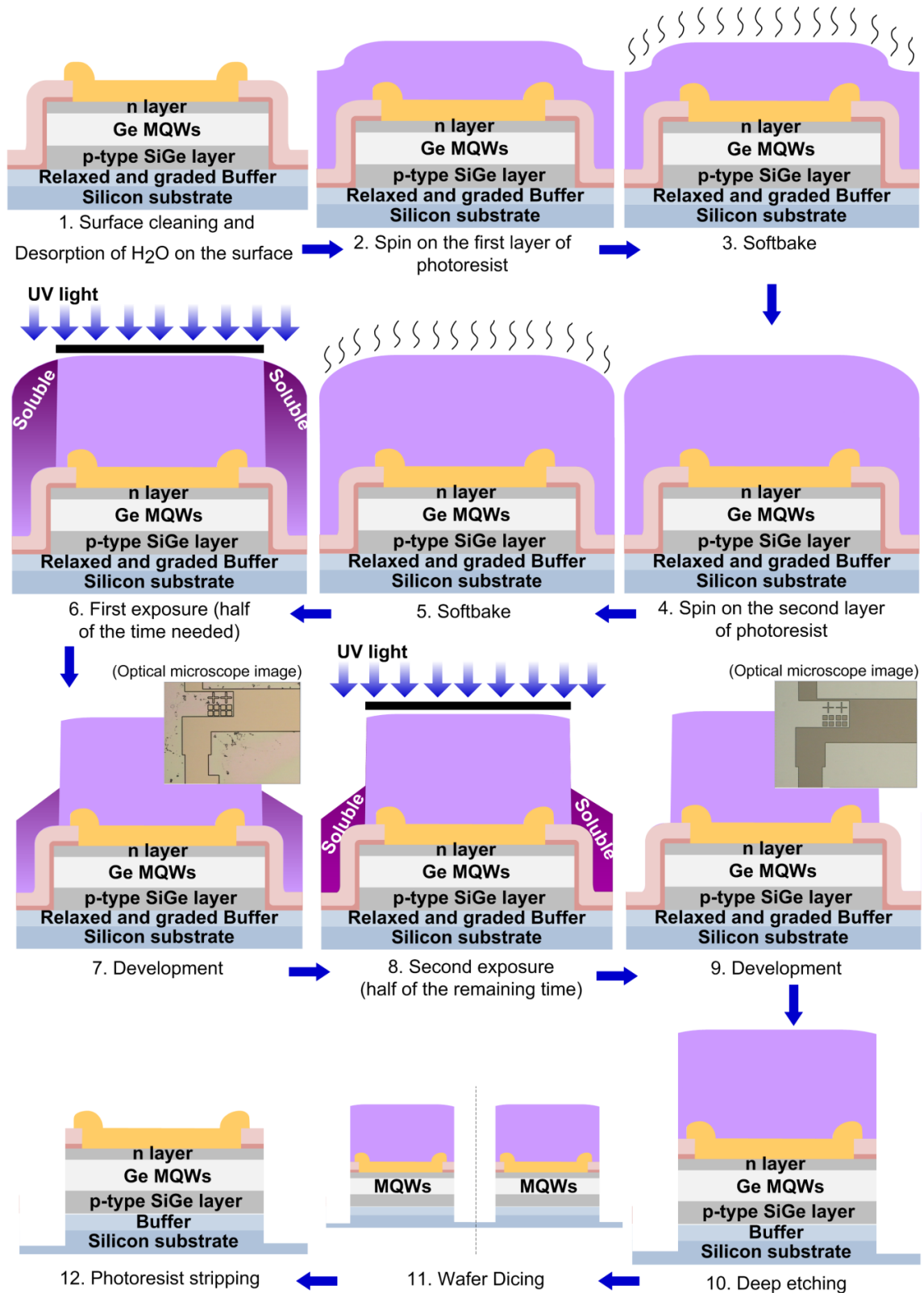


Fig 2.13: The processing procedure of the deep etching step.

2.3 Conclusion

This chapter summarizes the epitaxy and fabrication procedures employed in this thesis. The first section explains the LEPECVD technique and the epitaxy steps used to grow the Ge/SiGe MQW structures which is done by G. Isella and D. Chrastina from Laboratory for Epitaxial Nanostructures on Silicon and Spintronics (L-NESS). In the following sections, I thoroughly present the fabrication steps that I developed and performed for both DC surface illuminated p-i-n diode and the high speed surface illuminated and waveguide p-i-n devices. Significant amount of time and several tests were used to stabilize the presented fabrication process.

The next chapter will focus on the characterization setup and experimental results on the Ge/SiGe MQWs modulation characteristics of the fabricated devices. Modulation properties are measured and reported from the DC surface illuminated p-i-n diode, DC planar waveguide p-i-n diode, and high speed waveguide p-i-n diode.

Chapter 3. Light modulation by QCSE from Ge/SiGe MQWs

In this chapter, experimental investigations and developments of high performance Ge MQW EA modulators based on QCSE will be presented. Various characterization techniques and experimental demonstrations on the modulation properties of Ge/SiGe MQWs will be reported. To investigate the modulation characteristics of Ge/SiGe MQWs, I characterized three different device configurations including DC surface illuminated, DC planar waveguide, and RF 3 μm wide waveguide diodes, which I fabricated in the previous chapter.

At the beginning of this work QCSE was not demonstrated in the Ge/SiGe MQW structures grown by LEPECVD techniques from L-NESS laboratory, Politecnico di Milano. In fact at that time, only the research team from Stanford University managed to experimentally demonstrate QCSE from Ge/SiGe MQWs at room temperature. Therefore to begin our investigation, firstly we decided to fabricate *large square surface-illuminated diodes* to verify and characterize room temperature QCSE in our Ge/SiGe MQW samples. Three different experiments, including optical transmission, differential optical transmission, and photocurrent measurements, were employed to confirm significant QCSE from the structures.

Next, we proceeded to investigate modulation properties of Ge/SiGe MQWs in waveguide configurations which are more relevant to integrated optic applications. QCSE with light propagating parallel to the plane of the QWs was investigated from *100 μm width planar waveguide devices*. As shown in chapter 1, all of the previous works on Ge/SiGe MQWs were focused on surface illuminated devices or prism-shaped structures [129]. Nevertheless, The absorption and modulation characteristics of Ge MQWs when light propagates parallel to the QW planes as in waveguide configuration are different from those when light propagates perpendicular to the QW planes as in the surface illuminated devices. Indeed, the difference in the interaction lengths (typically around a micrometer in surface illuminated structure and around 10 to 100 μm in waveguide configuration) as well as the optical overlap factors (typically 100% in surface illuminated structure and smaller in waveguide configuration) indicates that the absorption and modulation characteristics obtained from the surface illumination characterization are not necessarily applicable in a

waveguide configuration. In addition, characterization of QCSE from Ge/SiGe MQWs in a waveguide configuration allows us to assess EA of Ge/SiGe MQWs with both TE and TM polarization incident light. This can be observed only from waveguide devices in which light with electric field vector parallel (transverse-electric mode, TE) and perpendicular (transverse-magnetic mode, TM) to the plane of QWs are accessible. On the opposite, for the surface illuminated configuration the electric field vector is always parallel to the plane of QWs.

Finally, a *3 μm wide and 90 μm long Ge/SiGe MQWs waveguide embedded in coplanar electrodes* was fabricated and characterized in order to measure its high speed modulation performance. The potential of using EA effect from the Ge/SiGe MQWs for a waveguide modulator in electronics-photonics IC was assessed by both DC and RF measurements. Tab. 3.1 summarizes device configurations, characterization methods, and principal optical modulation properties reported from each device.

Table 3.1. Summary of device configurations, characterization techniques, and measured optical modulation properties reported in this chapter.

Device configurations	Characterization techniques	Highlight modulation properties
Large surface illuminated p-i-n diode	Optical transmission, differential transmission, and photocurrent measurements at different bias voltages	Quantum-confined Stark effect
Planar waveguide p-i-n diode	Optical transmission measurements at different bias voltages	Polarization dependence quantum-confined Stark effect, and modulation performance
3 μm wide waveguide embedded in coplanar electrodes	Optical transmission at different bias voltages, and RF measurements	Optical modulation performance and 3-dB modulation bandwidth

3.1 QCSE measurements from surface illuminated Ge/SiGe MQWs p-i-n diode

In order to confirm the existence of room temperature QCSE from Ge/SiGe MQWs grown by LEPECVD technique, three different measurements were performed at room temperature on surfaced illuminated square p-i-n diode with 10, 20, and 50 periods of QWs. The schematic and optical microscope images are shown in Fig 2.3 (a) and 2.4 respectively. The fabrication process and the dimensions of the diode are given in the section 2.2.1.

Optical transmission measurements were used to directly observe the absorption spectra of the Ge/SiGe MQWs at different reverse bias voltages. Photocurrent measurements gave the information on the corresponding photo-generated carriers at each reverse bias voltage. Finally, Differential transmission measurements were used to confirm that there was no thermal effect contributing to the observed red shift of the absorption spectra at different reverse bias voltages, assuring that possible quasi-static shifts due to thermal effects were eliminated.

3.1.1 Optical transmission measurements

Optical transmission measurements allow direct observation of the absorption spectra at different bias voltages of the Ge/SiGe MQWs. The optical output spectra were collected by an optical power meter placed at the device output. The characterization setup of the optical transmission measurement for surfaced-illuminated Ge/SiGe MQWs diode is shown in Fig. 3.1. Light from a tunable laser was focused on the top surface of the diode using an objective lens and an afocal system which focused and collimated light of approximately 100 μm diameter spot size onto surface illuminated diodes of a 1 mm diameter square mesa size. A separate visible light source (not included in the figure) was also used to confirm that the input light was correctly focused on the sample top surface. A lens was placed after the diode in order to focus transmitted light into the photodetector. Moreover, to observe the absorption spectra at different reverse bias voltages, a DC reverse bias was applied to the diode by using two DC electrical probes. An optical microscope was employed to enable the alignment of the sample, the probing system, and the input light. The measurement data at different wavelengths at each reverse bias voltage were collected by a computer using LABVIEW software.

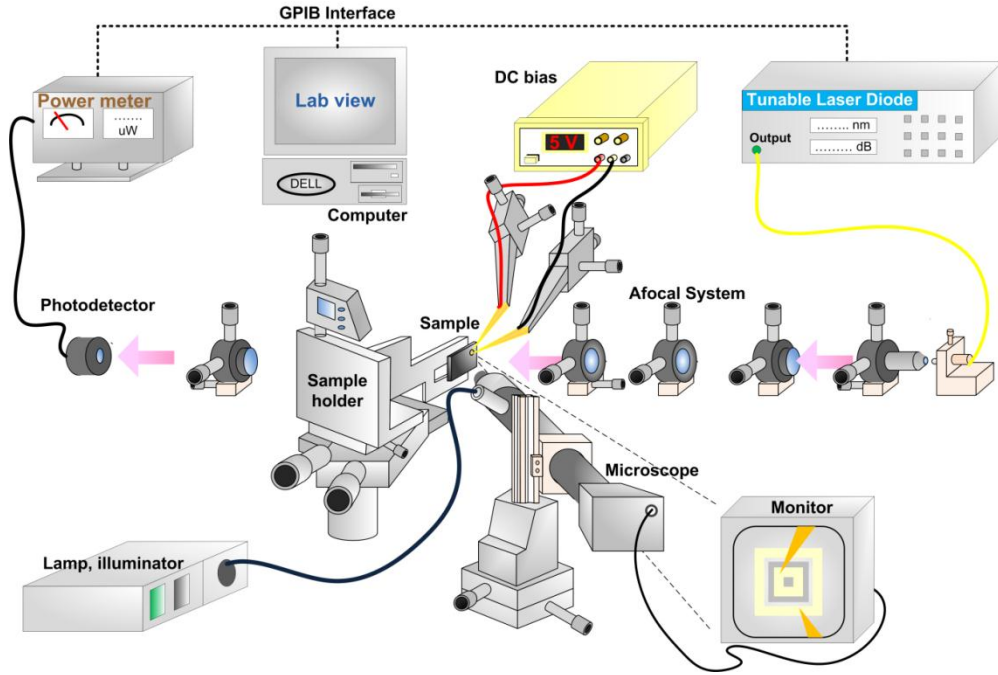
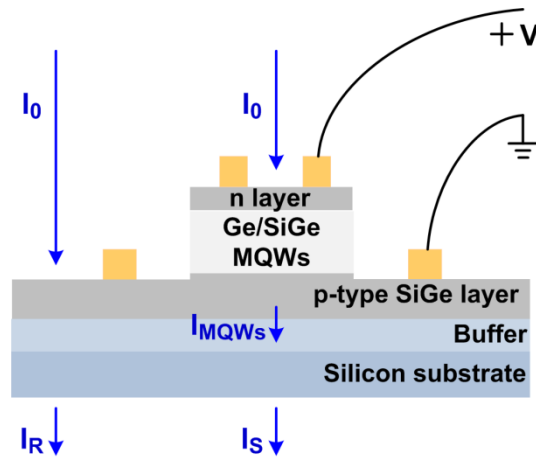


Figure 3.1: Schematic view of the optical transmission measurement employed for surface-illuminated Ge/SiGe MQW p-i-n diode.



I_0 : Incident optical power with correction of light reflection.

I_{MQWs} : Optical power out of MQWs region.

I_S : Output optical power at the position with MQWs.

I_R : Output optical power at the reference position.

Figure 3.2: Optical powers at the input and output of the sample from the optical transmission measurement of a surface illuminated diode.

Because of the short thickness of QWs compared with light wavelength, it was demonstrated that optical absorption normal to the plane of MQW structures cannot be expressed as an absorption coefficient in cm^{-1} but should be specified as a fraction of light absorbed per well $\gamma_{\text{well}}(\lambda)$ independent of well thickness [130]. As absorption coefficient is defined with the assumption that light intensity decreases exponentially with the absorbing distance, it is not physical in the case of QWs for normal incident light in which QW thickness is shorter than light wavelength. From the transmission measurements, the fraction of light absorbed per well can be found as follows:

$$-N\gamma_{\text{well}}(\lambda) = \frac{I_S(\lambda) - I_R(\lambda)}{I_R(\lambda)} \quad (3.1)$$

provided that $\gamma_{\text{well}}(\lambda) \ll 1$. $I_S(\lambda)$ is the measured power at the output of the MQW sample and $I_R(\lambda)$ is the measured power at the output of the reference, which is an area of the same wafer near the fabricated diode where the MQWs have been removed by dry etching, and N is the number of quantum wells. To explain, as shown in Fig 3.2, optical power at the sample output in a MQWs region I_{MQWs} can be expressed as

$$I_{MQWs} = I_0(1 - \gamma_{\text{well}})^N \quad (3.2)$$

where I_0 is the incident optical power on the top surface of the sample with correction of light reflection. Consequently, the experimentally measured optical power of light passing through the MQWs and the SiGe buffer and Si substrate can be expressed as

$$I_S = I_0(1 - \gamma_{\text{well}})^N(1 - A) \quad (3.3)$$

where A is the substrate absorption. In the same manner, the measured transmitted optical power of light passing through the reference area near the diode can be expressed as

$$I_R = I_0(1 - A) \quad (3.4)$$

Therefore,

$$\frac{I_R - I_S}{I_R} = 1 - (1 - \gamma_{\text{well}})^N \cong N \times \gamma_{\text{well}}, \text{ Provided that } \gamma_{\text{well}} \ll 1 \quad (3.5)$$

The absorption spectra at different reverse bias voltages obtained from the transmission measurements of a surfaced illuminated p-i-n diode of Ge/SiGe MQWs with 50 QW periods are reported in Fig. 3.3. The absorption edge is shifted from the 0.8 eV of bulk Ge due to both the confinement effect in the QWs and the strain between the Ge QWs and the virtual substrate. Without bias voltage a clear exciton peak at room temperature is observed around 0.88 eV, which can be attributed to the transition between the heavy hole of the first valence band and the first electronic state at Γ (HH1-c Γ 1). The half-width at half maximum (HWHM) of the exciton peak is about 5.6 meV, which is significantly less than the 8 meV reported in Ref. 89 despite the fact that 50 QWs are employed in this measurement instead of 10 in Ref. 96. This indicates the good quality of the Ge/SiGe MQWs grown by LEPECVD, which enabling a fast growth of $\text{Si}_x\text{Ge}_{1-x}$ graded buffer on which high quality Ge/SiGe MQWs can be deposited.

With increasing reverse bias voltages, two main characteristics of QCSE are observed: the Stark (red) shift of the absorption spectra and the reduction of the exciton related absorption peak. Fig 3.4 describes energy levels and wavefunctions for valence and conduction states in a Ge QW without and with electric field. With applied electric field, the potential profile of the QW system is tilted and the separation energy between the conduction and valence allowed energy level is decreased. The absorption then happens at lower energy (longer wavelength). Moreover, electron and hole wavefunctions are pull to the opposite site of the quantum well system by the electric field. This reduces the wavefunction overlaps between the electron and hole states and hence the absorption peak due to the Coulomb attraction between electron-hole pairs. Additionally, as shown in Fig 3.3, with an electric field of 1×10^4 V/cm (2V reverse bias), the device exhibits only a small shift in absorption spectra, which is in agreement with the QCSE observed in III–V materials [131], indicating that an electric field larger than 10^4 V/cm is required to observe QCSE.

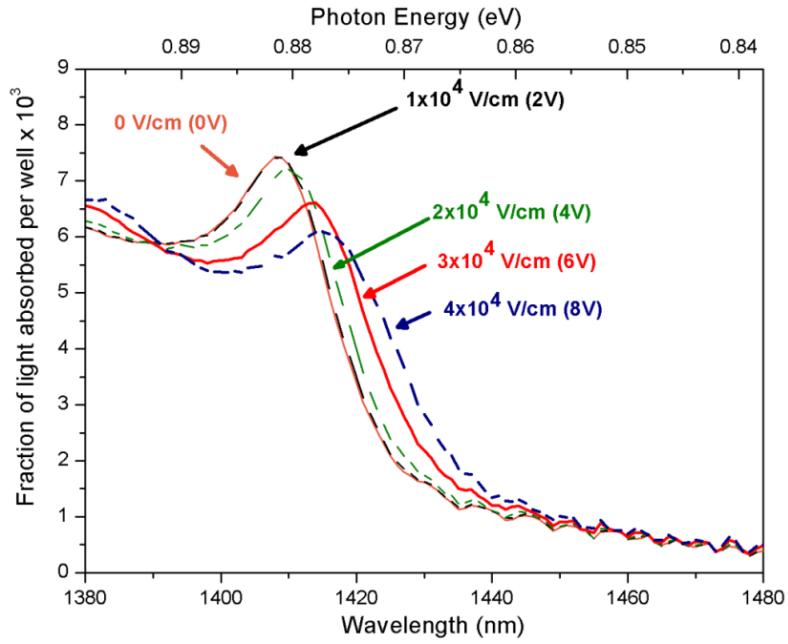


Figure 3.3: Fraction of light absorbed per well as a function of wavelength and photon energy for different electrical fields obtained from optical transmission measurement of a surfaced illuminated p-i-n diode of Ge/SiGe MQWs with 50 QW periods.

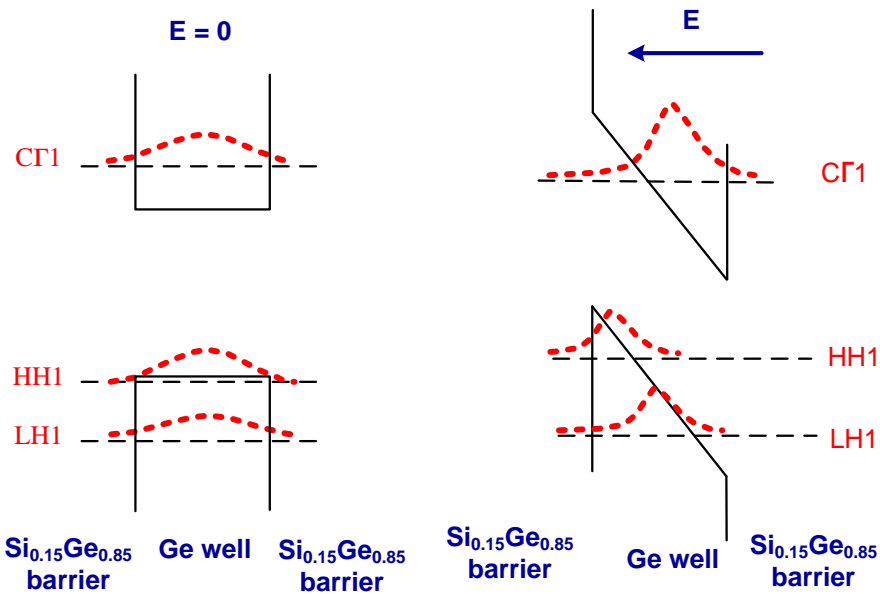


Figure 3.4: Energy levels and wave functions for valence and conduction states in a Ge/SiGe QWs (a) without and (b) with electric field applied perpendicularly to the QW plan. With electric field, the potential profile of the QW system is tilted and the electron and hole wave functions are pulled towards opposite sides of the QWs. These result in the Stark (red) shift of the absorption spectra and the reduction of the exciton related absorption peak.

From the transmission measurements of Ge/SiGe MQWs with 50 QW periods, QCSE is clearly demonstrated. Nevertheless, the required bias voltages of 6 – 8 V to obtain a significant shift of the absorption spectra are considerably higher than those of 0.5 – 3 V available in the present CMOS IC [132]. Therefore, Ge/SiGe MQWs with a number of QW periods reduced to 20 and 10 were also comparatively measured as shown in Fig 3.5. This was to demonstrate that a significant shift of the absorption spectra can also be obtained at lower reverse bias voltages by using devices with thinner active region, enabling higher electric field at the lower values of reverse bias voltages.

Fig 3.5 (a) and (b) show the measured absorption spectra in term of the fraction of light absorbed per well at different reverse bias voltages for the Ge/SiGe MQWs with QW periods of 20 and 10 respectively. Comparing to the case of 50 period Ge/SiGe MQWs, a stronger shift of the absorption spectra was obtained at the same values of reverse bias voltages. For example, with 50 period Ge/SiGe MQWs to obtain around 10 nm shift of the absorption band edge, a reverse bias voltage of 8 V was required. However, it take only 4 and 2 V for 20 and 10 period Ge/SiGe MQWs in order to approximately obtain the same shift of the absorption spectra. This confirms that Ge/SiGe MQWs has the potentials to operate at low reverse bias voltages, compatible with the available voltage in the modern CMOS integrated circuits. Moreover, thanks to a sharp absorption band edge obtained from the quantum confinement effect, it can be seen that a good modulation performance could be expected with a reverse bias voltage of 2 V (Fig 3.5 (b)). The quantitative modulation performance of the Ge/SiGe MQWs will be further investigated with waveguide structure devices in the following sections.

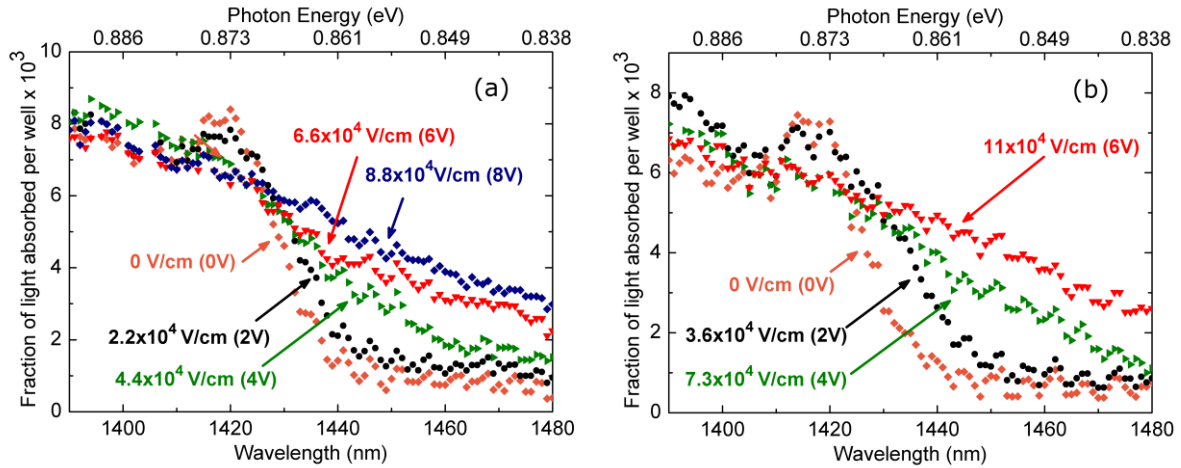


Figure 3.5: Fraction of light absorbed per well as a function of wavelength and photon energy for different electrical fields obtained from optical transmission measurements of a surfaced illuminated p-i-n diode of Ge/SiGe MQWs with (a) 20 QW periods for reverse bias voltages of 0, 2, 4, 6, and 8 V corresponding to electric fields of approximately 0, 2.2, 4.4, 6.6, and 8.8×10^4 V/cm and (b) 10 QW periods for reverse bias voltages of 0, 2, 4, and 6 V corresponding to electric fields of approximately 0, 3.6, 7.3, and 11×10^4 V/cm.

3.1.2 Photocurrent measurements

Photocurrent measurements have been performed to confirm the previous results from optical transmission measurements. This method consists of collecting photo-generated carriers, and hence is sensitive only to the absorption of the active region (in the intrinsic region of the PIN diode). Therefore unlike the transmission measurement, background losses due to the substrate and buffer layers are excluded from the experiments. The characterization setup of the photocurrent measurement for surfaced-illuminated Ge/SiGe MQWs diode is shown in Fig. 3.6. Light from a tunable laser was focused on to the top surface of the diode, to which a DC reverse bias was applied by using two electrical probes. A chopper was added to modulate the input light at 1 kHz, which was also used as the reference for the lock-in amplifier employed to extract the photocurrent signal from the dark current signal. A computer with LabVIEW was used to control the tunable laser and the lock-in amplifier for wavelength scanning and data acquisition.

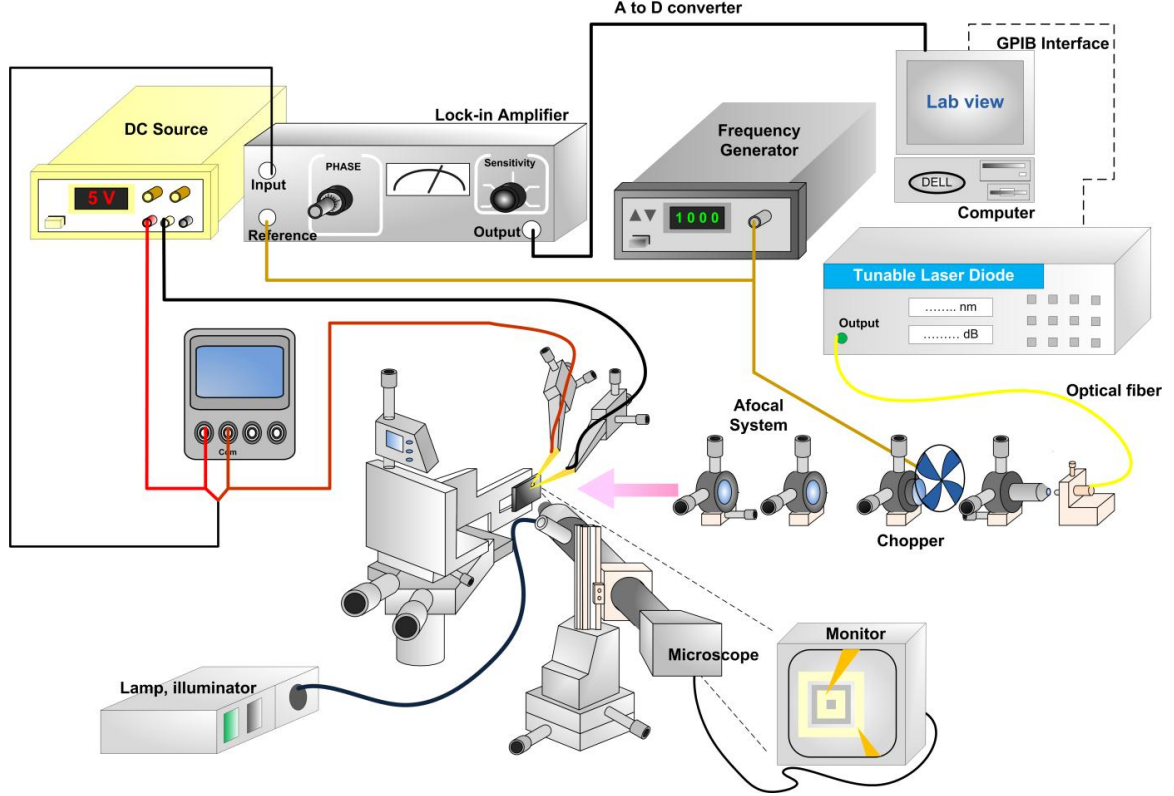


Figure 3.6: Schematic view of the photocurrent measurement employed for surface-illuminated Ge/SiGe MQWs p-i-n diode.

From the photocurrent measurement, the fraction of light absorbed per well $\gamma_{\text{well}}(\lambda)$ is deduced from the diode responsivity, assuming an ideal internal quantum efficiency of 100% and correcting for light reflection at the sample surface as follows:

$$I_{\text{ph}}(\lambda) = \frac{eI_0 N \gamma_{\text{well}}(\lambda) \lambda}{hc} \quad (3.6)$$

provided that $\gamma_{\text{well}}(\lambda) \ll 1$. $I_{\text{ph}}(\lambda)$ is the photocurrent values, e is the elementary charge, I_0 is the incident light power with correction of light reflection, ($R = 0.68$ according to refractive index of Ge and air), N is the number of quantum wells, h is planck's constant, and c is light velocity. Equation 3.6 can be explained by the following mathematical derivation. From Fig 3.2, optical power absorbed by the MQWs can be written as

$$\Delta I = I_0 - I_{\text{MQWs}} \quad (3.7)$$

$$= I_0 \left\{ 1 - (1 - \gamma_{\text{well}})^N \right\} \quad (3.8)$$

$$\cong I_0 N \gamma_{\text{well}}, \quad \text{provided that } \gamma_{\text{well}}(\lambda) \ll 1 \quad (3.9)$$

The number of photons absorbed by the MQWs can be written as $\Delta I / h\nu$. Therefore, by assuming that one electron is generated for every absorbed photon, the number of generated electron can be written as:

$$N_e = \frac{\Delta I}{h\nu} \quad (3.10)$$

Hence, the generated photocurrent can be written as:

$$I_{\text{ph}} = eN_e = e \frac{\Delta I}{h\nu} \quad (3.11)$$

$$I_{\text{ph}}(\lambda) = \frac{eI_0 N \gamma_{\text{well}}(\lambda)}{h\nu} = \frac{eI_0 N \gamma_{\text{well}}(\lambda) \lambda}{hc} \quad (3.12)$$

The absorption spectra deduced from the photocurrent measurements for reverse bias voltages larger than 4 V are well comparable with those obtained from the transmission measurements in terms of both fraction of light absorbed per well values and HH1-c Γ_1 exciton peak positions, as shown in Fig. 3.7, indicating reliable measurements and also reaffirming the existence of a significant QCSE at room temperature from the Ge/SiGe MQWs grown by LEPECVD. In addition, it is clear from the photocurrent measurements that the photogenerated carriers cannot be fully collected at bias lower than 2 V; this means that the intrinsic region is not fully depleted at these reverse bias voltages. This can be related to the absorption spectra obtained from transmission measurements from which only a very small shift in absorption spectra is observed with the application of a 2 V bias.

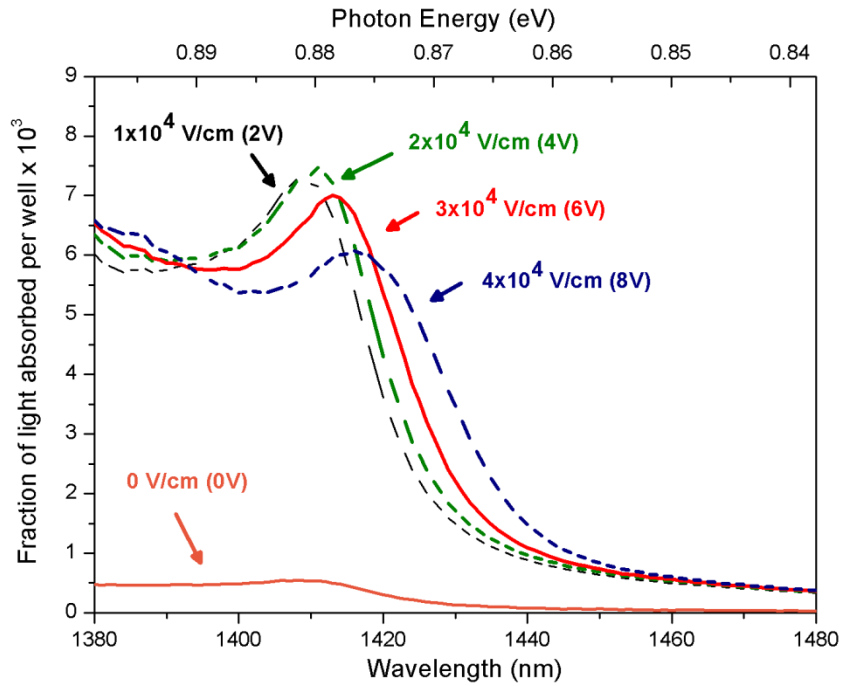


Figure 3.7: Fraction of light absorbed per well as a function of wavelength and photon energy for different electrical fields obtained from the photocurrent measurement of a surface illuminated p-i-n diode of Ge/SiGe MQWs with 50 QW periods.

3.1.3 Differential transmission measurements

In the optical transmission and photocurrent measurements, two characteristics of QCSE, the Stark (red) shift of the absorption spectra and the reduction of the exciton related absorption peak were clearly observed from the Ge/SiGe MQWs using constant DC reverse bias voltages of 0, 2, 4, 6, and 8 V. Finally, a differential transmission measurement was used to confirm that there was no thermal effect contributing to the previous measurements. To obtain the differential transmission spectra shown in Fig 3.8, 1 kHz sinusoidal reverse bias from 0 to 4 V, 0 to 6 V, or 0 to 8 V was applied to the diode and a lock-in amplifier was used to measure the amplitude of the modulated optical transmission as a function of light wavelength. Using this method, possible quasi-static shifts due to thermal effects were eliminated.

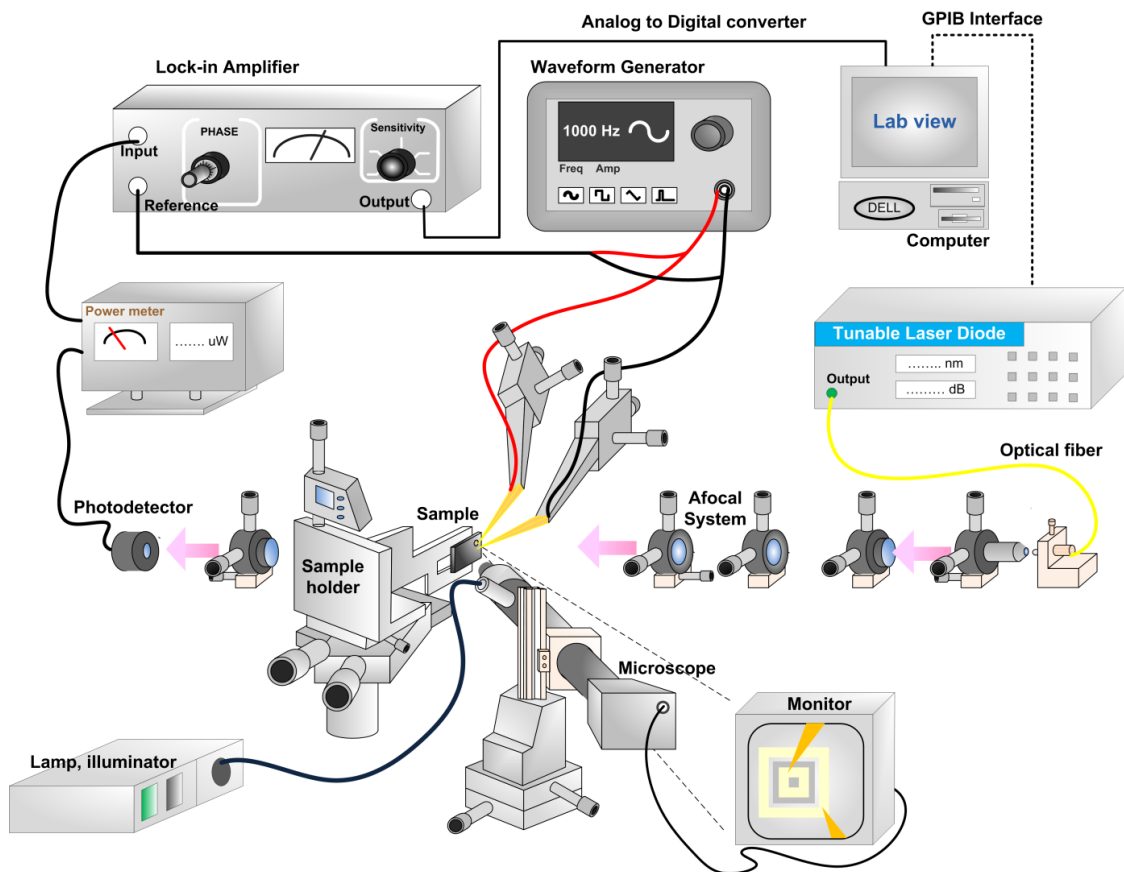


Figure 3.8: Schematic view of the differential transmission measurement employed for surface-illuminated Ge/SiGe MQWs p-i-n diode.

Referring to Fig. 3.3 of the absorption spectra from the optical transmission measurements, the maximum changes in the fraction of light absorbed per well between 0 and 4 V, 0 and 6 V, and 0 and 8 V are found to be 0.70×10^{-3} , 1.72×10^{-3} , and 2.24×10^{-3} at 1416, 1419, and 1422 nm, respectively. These wavelength values are well matched with the peak positions of the differential transmission spectra obtained by AC bias voltage measurements shown in Fig. 3.9, indicating that there was no thermal contribution to the observed red shifts of absorption spectra.

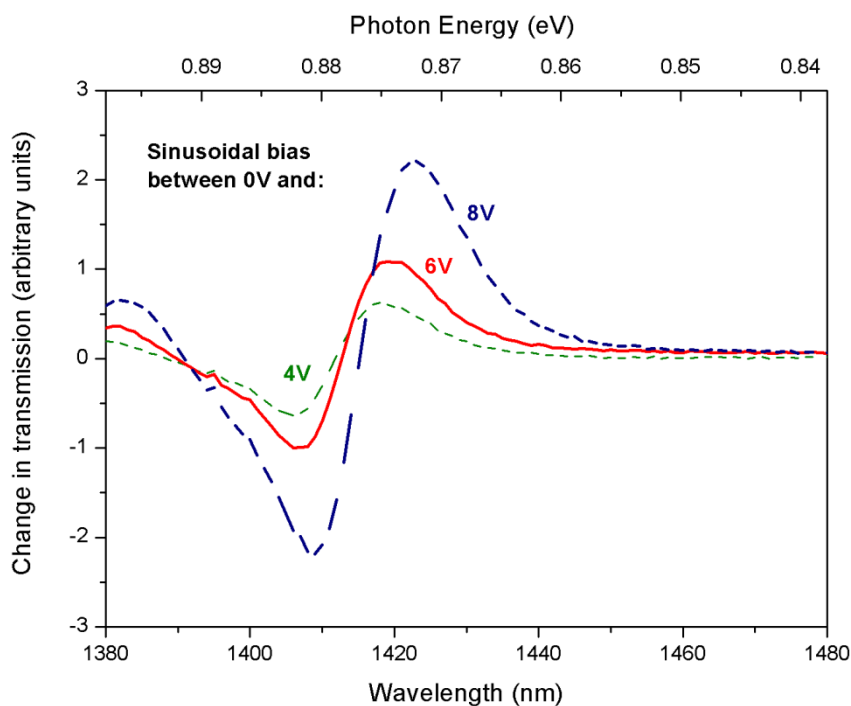


Figure 3.9: Differential transmission as a function of wavelength and photon energy using 1 kHz sinusoidal bias from 0 to 4 V, 0 to 6 V, and 0 to 8 V.

Therefore, QCSE from Ge/SiGe MQWs was experimentally observed using optical transmission, photocurrent, and differential transmission measurements at room temperature. These results confirm the existence and good performance of QCSE from Ge/SiGe MQWs grown by LEPECVD technique from L-NESS laboratory, Politecnico di Milano. The characteristics of the absorption spectra at different reverse bias voltages are consistent using two measurement techniques: optical transmission measurement and photocurrent measurement. A differential transmission measurement was used to confirm that there was no thermal effect contributing to the observed red shift of observed QCSE.

3.2 QCSE measurements from Ge/SiGe MQWs planar waveguides for TE and TM polarization light

In the previous section, QCSE was investigated from surface illuminated Ge/SiGe MQW p-i-n diodes using three different measurements, confirming the existence of significant QCSE in our materials. Nevertheless, for integrated circuit applications it is preferable to operate in a waveguide configuration. Therefore, in this section QCSE with light propagating parallel to the plane of the QWs is investigated from Ge/SiGe MQW planar waveguides embedded in p-i-n diodes. These allow us to assess both TE and TM polarization dependence characteristics of the QCSE and the modulation efficiency of Ge/SiGe MQWs in a waveguide structure.

To investigate the absorption spectra of Ge/SiGe MQWs in waveguide configurations at different reverse bias voltages, I fabricated 100- μm -wide planar waveguides with 10 and 20 QW period embedded in p-i-n diodes. The fabrication procedure consisted of mesa etching, Si_3N_4 and/or SiO_2 deposition and patterning, metallization, and 90 μm deep etching as thoroughly explained in the section 2.2.2.1, 2.2.2.3, 2.2.2.4, and 2.2.2.5 respectively. Fig 3.10(a) shows a schematic view of a fabricated Ge/SiGe MQW planar waveguide. A few tens of nanometers of SiO_2 served as a passivation layer on the left and right walls of the waveguide to reduce leakage current. 600 nm of Al was evaporated and lifted off for both p and n contacts. The top contact covered only part of the waveguide ridge to minimize absorption from the metal. As the waveguide lengths were 34 and 64 μm , a deep etching of 90 μm was performed to bring the input fiber and output objective to the input and output facets of the waveguides as partly shown in Fig 3.10(b). In this configuration, light is guided in the 3 (10 QWs) or 3.2 (20 QWs)- μm -thick planar waveguide comprising the MQW structure and the relaxed $\text{Si}_{0.1}\text{Ge}_{0.9}$ buffer, due to the refractive index variation in the graded buffer. Fig 3.11 shows the plot of the first three optical modes calculated by a complex effective index mode solver.

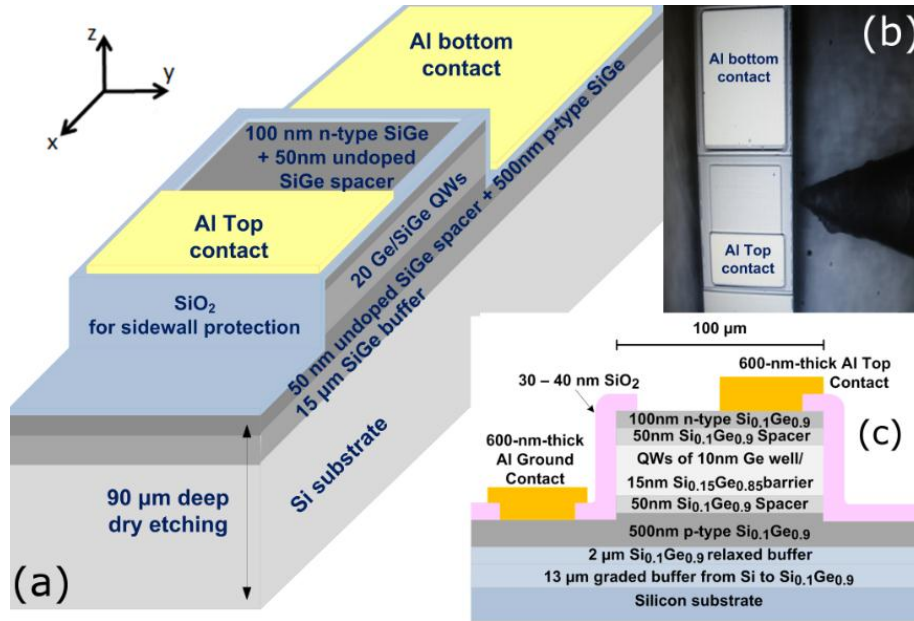


Figure 3.10: (a) Schematic view of the fabricated Ge/SiGe MQW planar waveguides. (b) Optical microscope view of the device with an input fiber injecting light into the waveguide. (c) Cross section of the planar waveguides.

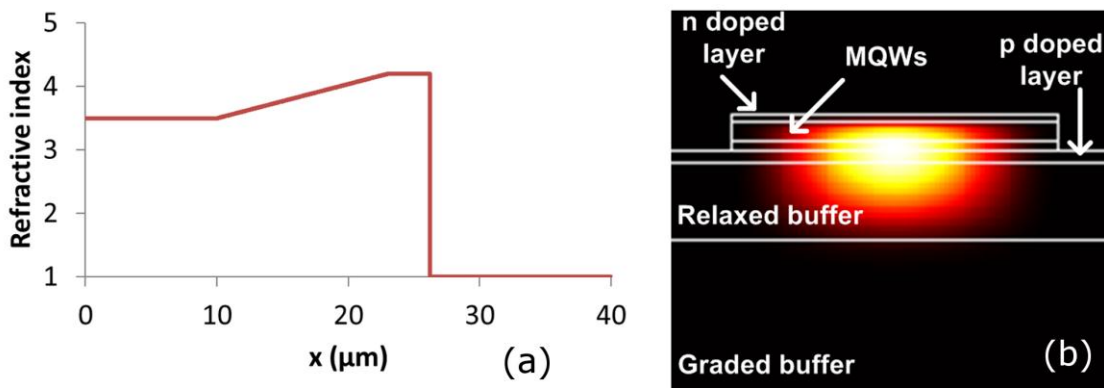


Figure 3.11: (a) Refractive index profiles in vertical direction of the planar waveguide used in the optical modes calculation. From 0 to 10 μm: Si substrate (3.5). From 10 to 23 μm: a linear increase of refractive index from Si (3.5) to Si_{0.1}Ge_{0.9} (4.2) (according to Ge refractive index of 4.3 [133]). From 23 to around 26 μm: a constant refractive index of 4.2 for 2 μm Si_{0.1}Ge_{0.9} relaxed buffer and Ge/SiGe p-i-n structures having the same Ge concentration of Si_{0.1}Ge_{0.9} relaxed buffer. (b) Optical intensity profile of the first mode obtained from calculation at the wavelength of 1.4 μm.

Experimental setup, shown in Fig 3.12, employed light from Tunic PRI Tunable Laser Diode. Laser light was then injected via an optical fiber into MT9820A All-Band Optical Component Tester, enabling the optical transmission measurements to be simultaneously performed over a wide wavelength range with the wavelength resolution of as low as 5 pm. From the output of MT9820A All-Band Optical Component Tester, light propagating in an optical fiber underwent polarization control by an In-Line Polarization Controllers (PLC-900). A linear optical polarizer was used afterward to ensure the polarization of the light. After the polarizer, a polarization-maintaining fiber was used in order to maintain the desired polarization state of light, which was then coupled into the fabricated waveguide by a taper-lensed fiber. The fabricated sample was placed on the Elliot Marlock Photonic Alignment Systems providing complete precision positioners for testing of the photonic components. At the output of fabricated waveguide, light was collected by an objective lens, placing in the position at which a parallel beam was obtained out of the objective. Subsequently, in order to measure the output intensity of the fabricated waveguide, the collected output light was injected into a single mode optical fiber by using another objective. Finally, light was transmitted via the optical fiber to the detector input at the MT9820A All-Band Optical Component Tester, which would determine the resulting transmission spectra by comparing the intensity of the input signal received from Tunic PRI Tunable Laser Diode to the intensity of the output signal received at the detector. A computer was connected to the Tunic PRI Tunable Laser Diode and the MT9820A All-Band Optical Component Tester via GPIB interface allowing the simultaneous acquisition of the transmission spectra.

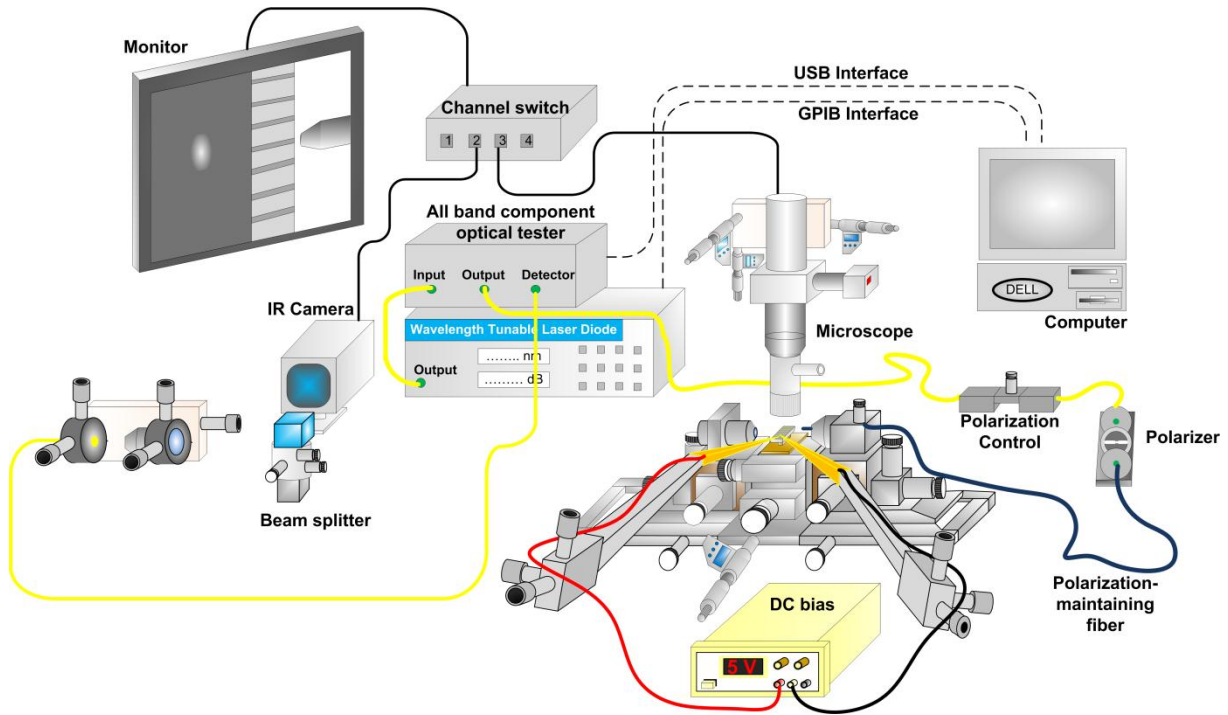


Figure 3.12: Schematic view of the transmission measurement employed for Ge/SiGe MQWs waveguides embedded in p-i-n diodes.

Transmission measurements were performed at room temperature with a spectral resolution of 0.13 nm. In all measurements, a tunable laser emitting light from 1340 to 1430 nm or 1390 to 1540 nm was used. The taper-lensed fiber was positioned to inject light where there was no top metal to avoid optical loss as shown in Fig. 3.10(b). The position of the input fiber was optimized by photocurrent measurements in order to maximize the overlap between the optical beam and the MQW region. The coupling losses were dissociated from the absorption in the MQWs using the fact that the coupling losses can be considered as constant while the absorption in the MQWs depends on wavelength. The measured transmission was then normalized so that zero absorption was obtained at 1540 nm, the longest wavelength of the measurements. Indeed, separate photocurrent measurements allowed us to evaluate that the absorption in this planar waveguide is lower than 1 dB at 1540 nm [134]. Therefore, although this method of coupling loss subtraction was somewhat imprecise, the precision of the deduced absorption level in the MQWs should be better than 1 dB.

In the following sections, the experimental results obtained from 100- μm -wide Ge/SiGe MQW planar waveguide using the above characterization setup and techniques will be reported. First, the polarization dependence of the HH1-c Γ 1 and LH1-c Γ 1 transition will be presented from the Ge/SiGe MQWs with 10 QW periods. Subsequently, modulation efficiency of the Ge/SiGe MQWs around its HH1-c Γ 1 transition, the spectral range giving an efficient EA effect with limited insertion loss, will be reported from the Ge/SiGe MQWs with 20 QW periods.

3.2.1 Polarization dependence of quantum-confined Stark effect in Ge/SiGe quantum well planar waveguides

The selection rules for interband transition in a QW system are shown in the Tab. 3.2, summarizing the values of transitions matrix elements at the Γ point for light propagating along and perpendicular to the QW plan obtained from quantum mechanical calculations [135]. The transition matrix element determines the transition strength between two energy levels [136]. From Tab. 3.2, for a plane wave propagating perpendicular to the QW plan (z direction in Fig 3.10), electric field vector can only oscillate in the x or y direction. Both heavy hole (HHn-c Γ n) and light hole (LHn-c Γ n) transitions are allowed, and the heavy hole related transition is stronger than the light hole related transition. The former has a higher transition matrix element value ($\pi/\sqrt{2}$) than that of the latter ($\pi/\sqrt{6}$). For a plane wave propagating along the QW plan (y direction in Fig 3.10), electric field vector can only oscillate in the x or z direction. For electric field in x direction, the selection rule is the same as the previous case of perpendicular propagating light, due to the fact that electric field vector is parallel to the QW plan in both cases. However, for electric field in z direction, only light hole related transition is allowed with higher values of the transition matrix elements ($2\pi/\sqrt{6}$). The schematics of the band diagram showing allowed and forbidden transitions in a QW system is also given in Fig 3.13. These predicted selection rules of QW systems were experimentally demonstrated in III-V QW systems [111] and partially observed in Ge QW systems using prism-shaped structures [129]. The first experiment in this section aims to fully prove these selection rules in the Ge QW systems using a waveguide configuration.

Table 3.2. Selection rules for interband transitions obtained from the absolute values of the transition matrix elements at the Γ point [135]. z is the direction perpendicular to the QW plan; x and y are the direction parallel to the QW plan as in Fig 3.10. E_x , E_y , and E_z are electric fields oscillate in the x , y , and z directions respectively.

Propagation direction	Direction of electric field component as in Fig 3.10.			Type of transitions
	E_x	E_y	E_z	
z direction	$\frac{\pi}{\sqrt{2}}$	$\frac{\pi}{\sqrt{2}}$	impossible	$HHn - c\Gamma n$
y direction	$\frac{\pi}{\sqrt{2}}$	impossible	forbidden	$HHn - c\Gamma n$
z direction	$\frac{\pi}{\sqrt{6}}$	$\frac{\pi}{\sqrt{6}}$	impossible	$LHn - c\Gamma n$
y direction	$\frac{\pi}{\sqrt{6}}$	impossible	$\frac{2\pi}{\sqrt{6}}$	$LHn - c\Gamma n$

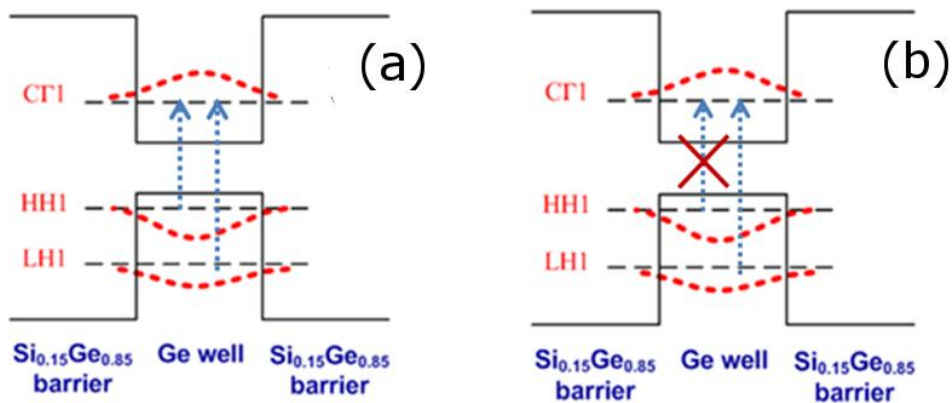


Figure 3.13: (a) Polarization dependence light absorption in QW systems for light propagating along the QW plan with electric field vector (a) parallel and (b) perpendicular to the QW plan.

Fig. 3.14 presents the measured absorption spectra at 0 V for incident light with TE (electric field in x direction) and TM (magnetic field in x direction and electric field mainly in z direction) polarizations. The spectra were measured from a 114- μm -long Ge/Si_{0.15}Ge_{0.85} MQW waveguide with 10 QWs. Light was injected and propagated parallel to the QW plane (y direction). The measurement was performed using 2 tunable lasers from 1340 to 1430 nm and 1390 to 1540 nm. The latter covers the HH1-c Γ 1 transition of the Ge/SiGe MQWs; while, the former covers its LH1-c Γ 1 transition. For TE polarization incident light, the absorption edge is shifted from the 0.8 eV of bulk Ge due to both the confinement effect in the QWs and the strain between the Ge QWs and the virtual substrate as also observed from the surface illuminated device in section 3.1.1. A clear exciton peak observed around 0.886 eV is attributed to the HH1-c Γ 1 transition, while the exciton peak associated with the LH1-c Γ 1 transition is observed at a higher energy of around 0.91 eV. With TM polarization incident light, only LH1- c Γ 1 transition is observed. The LH1- c Γ 1 transition is greatly enhanced consistent with its highest absolute values of transition matrix elements (see Tab. 3.2.)

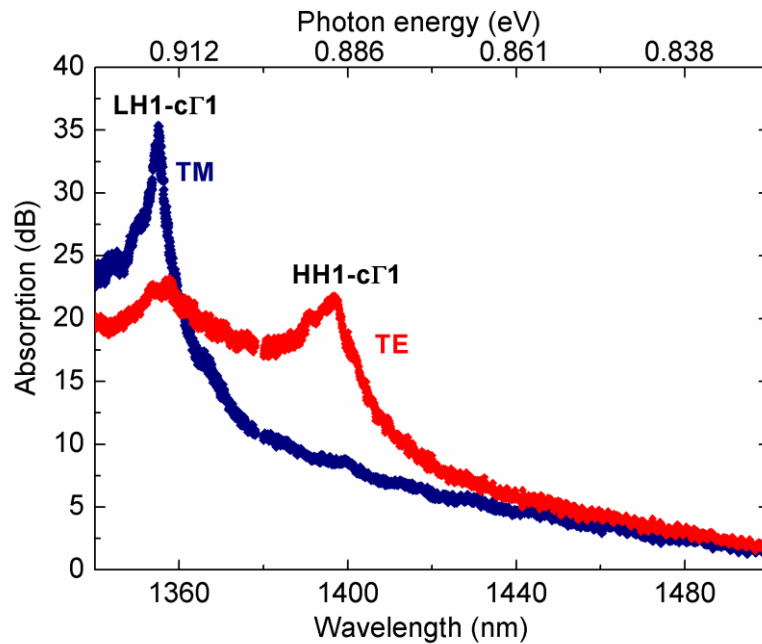


Figure 3.14: Room-temperature absorption spectra at 0 V bias of the 100- μm -wide 114- μm -long Ge/Si_{0.15}Ge_{0.85} MQW waveguide with 10 QW periods obtained with TE and TM polarization incident light.

Theoretically, the measured absorption peaks should be proportional to the square of the corresponding transition matrix elements in Tab. 3.2 [109]. Therefore, in theory for TE polarization incident light, HH1-c Γ 1 and LH1-c Γ 1 absorption peaks are expected to be proportional to $\pi^2/2$ and $\pi^2/6$ respectively. In the case of TM polarization incident light, HH1-c Γ 1 transition is expected to vanish and LH1-c Γ 1 transitions is expected to be proportional to $4\pi^2/6$. In other words, the absorption from the HH1-c Γ 1 transition will be 3 times stronger than that from the LH1-c Γ 1 transition for TE polarization incident light. In contrast for TM polarization incident light, only the LH1-c Γ 1 transition is allowed with the combined strength of the HH1-c Γ 1 and LH1-c Γ 1 transitions in the TE case. The First row of Tab. 3.3 summarizes the theoretical values of oscillator strength ratios among the HH1-c Γ 1 and LH1-c Γ 1 transitions at the Γ point for TE and TM polarization incident light.

To quantitatively compare the measured absorption spectra with the theory, a semi-empirical line shape model explained in Ref. 137 was employed to determine the relative oscillator strengths of the excitonic HH1-c Γ 1 and LH1-c Γ 1 transitions in both polarizations obtained from the measurements. In this fitting method, the absorption spectra are described as the sum of Gaussian excitons and continuum absorption using the following equation [137]:

$$\alpha(\hbar\omega) = \alpha_h \exp\left[-\frac{(\hbar\omega - \hbar\Omega_h)^2}{2(\hbar\Gamma_h)^2}\right] + \alpha_l \exp\left[-\frac{(\hbar\omega - \hbar\Omega_l)^2}{2(\hbar\Gamma_l)^2}\right] + \frac{\alpha_c}{1 + \exp\left(\frac{\hbar\Omega_c - \hbar\omega}{\hbar\Gamma_c}\right)} \times \frac{2}{1 + \exp\left\{-2\pi\left[\frac{\hbar\Omega_c - \hbar\omega}{R_y}\right]^{1/2}\right\}} \quad (3.13)$$

The first (resp. second) term of Eq. 3.13 is a Gaussian function representing the absorption, α , of heavy (resp. light) hole related transition at different frequency, ω . $\hbar\Omega_h$ ($\hbar\Omega_l$) and $\hbar\Gamma_h$ ($\hbar\Gamma_l$) are the energy and HWHM in eV of the heavy (light) hole absorption peak obtained from measurement results. For the third term, it describes a continuum absorption above the band edge. $\hbar\Omega_c$ is the energy of absorption edge. R_y is material Rydberg constant $R_y = e^2 \mu^* / 2\varepsilon^2 \hbar^2$ where μ^* is electron hole reduced mass and ε is material dielectric

constant. α_h , α_l , and α_c are constants obtained via a semi-empirical fitting with the measured absorption spectra.

To explain the fitting procedure, the measured absorption spectra in Fig. 3.14 in dB were translated into absorption coefficients, α , considering that absorbed light in dB equal to $10 \cdot \log(e^{\Gamma \alpha L})$ where Γ is the overlap factor between guided optical mode and the Ge/SiGe MQWs region of 10% and L is the device length of 114 μm . The absorption due to the 2 μm thick relax buffer and the indirect-gap absorption of Ge was removed from the measurement results assuming that it linearly increase with respect to the photon energy. The values of HWHM for each exciton width used in the calculation were determined from the low energy side of the measured absorption spectra, which are 5.7 meV and 3 meV for the excitonic transitions for TE and TM polarization incident light respectively. The fitting curves in comparison with the experimental results for both TE and TM polarizations are shown in Fig 3.15(a) and (b).

Tab. 3.3 summarizes the oscillator strength ratio of the excitonic HH1-c Γ 1 and LH1-c Γ 1 transitions obtained from the semi-empirical line shape model of the measured absorption spectra in comparison with the theoretical values and the previous experiments on GaAs QWs for both TE and TM polarizations. From Fig 3.15(a) and (b), the absorption peak ratio between HH1-c Γ 1 and LH1-c Γ 1 transitions for TE polarization incident light is ~ 0.526 . The absorption peak ratio of LH1-c Γ 1 transition for TM polarization incident light over HH1-c Γ 1 transition for TE polarization incident light is ~ 1.63 . Our values of Ge QWs are similar with the previous experiment on III-V QWs; hence, the experiment demonstrated that direct-gap transition of Ge QWs exhibit strong polarization dependence as strong as that of III-V based QWs. Any discrepancies from the theory are due to the valence-band mixing in the exciton wave function [111].

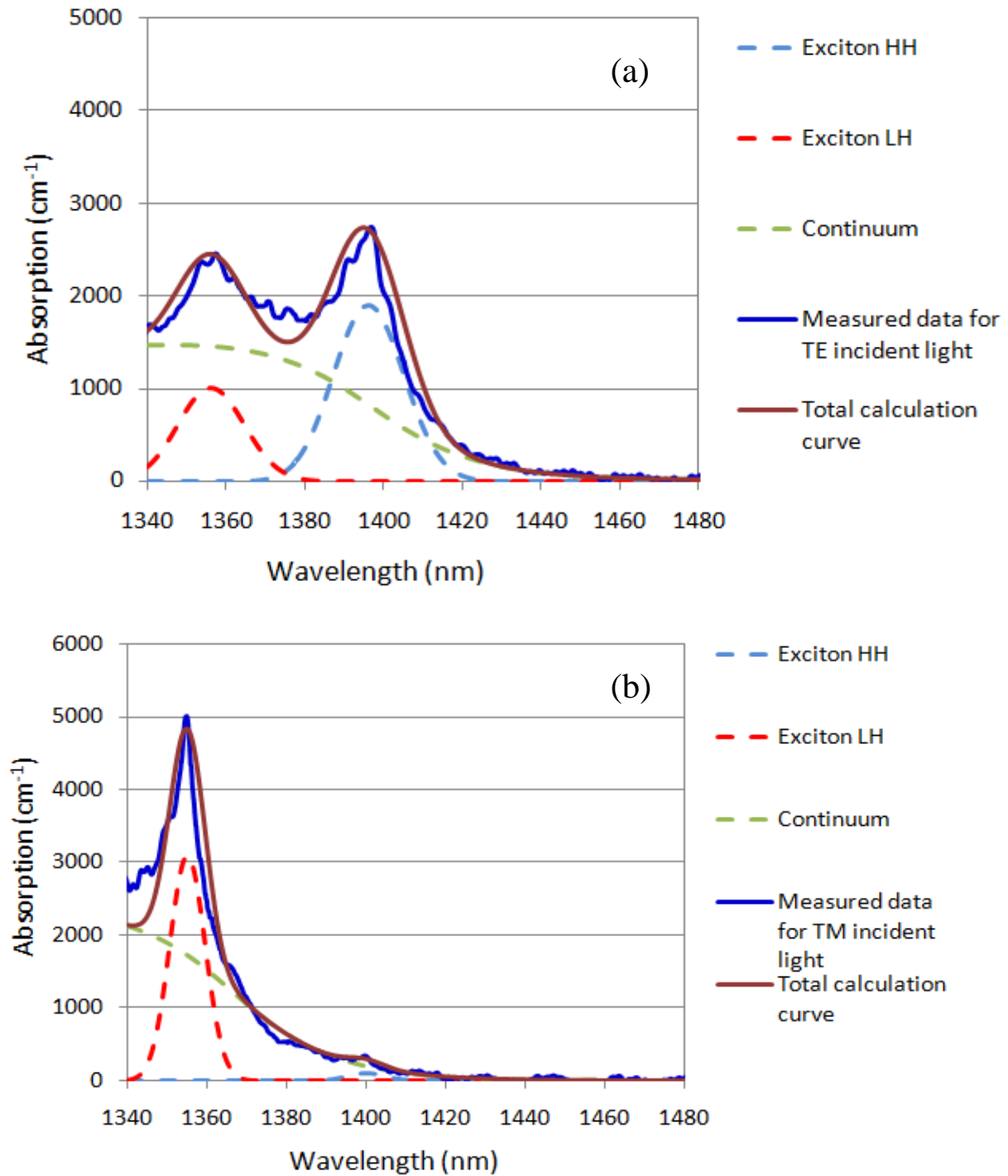


Figure 3.15: A semi-empirical line shape model to determine the relative oscillator strengths of the excitonic HH1-c Γ 1 and LH1-c Γ 1 transitions obtained from the measurements for (a) TE polarization and (b) TM polarization incident light. The absorption spectra are described as the sum of Gaussian excitons and continuum absorption spectra.

Table 3.3. Oscillator strength ratios of exciton peaks for TE and TM polarization incident light based on the theoretical values the Γ point.

	$\frac{HH_{TM}}{HH_{TE}}$	$\frac{LH_{TE}}{LH_{TM}}$	$\frac{LH_{TE}}{HH_{TE}}$	$\frac{LH_{TM}}{HH_{TE}}$
Theory	0	1/4	1/3	4/3
GaAs QWs [104]	0.05-0.1	0.44-0.56	0.56-0.79	1.1-1.5
Ge QWs [This work]	~ 0.053	~ 0.323	~ 0.526	~ 1.631

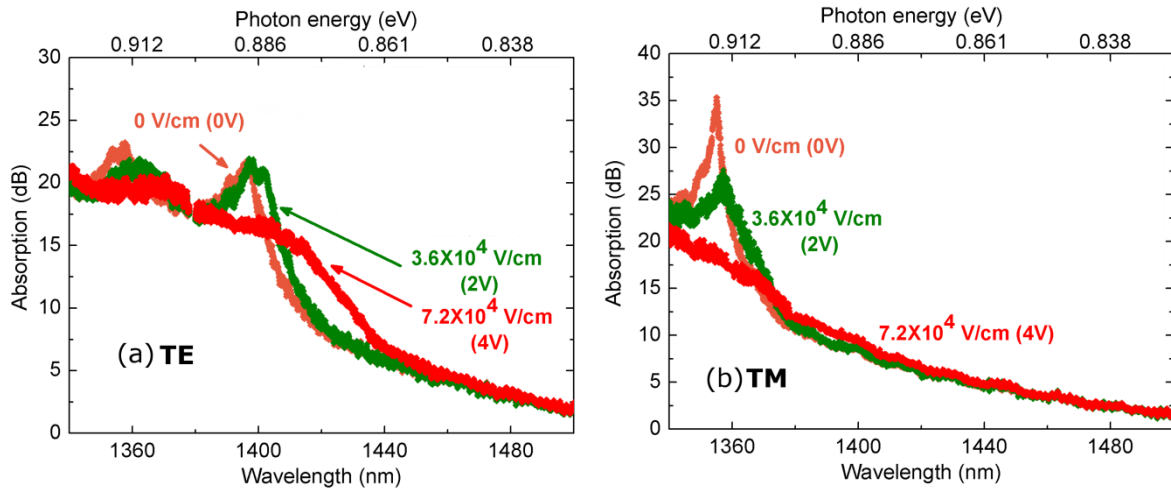


Figure 3.16: QCSE of the 100- μm -wide 114- μm -long 10-QW-period Ge/Si_{0.15}Ge_{0.85} MQW planar waveguide for (a) TE polarization and (b) TM polarization incident light.

Optical transmission measurements at different reverse bias voltages were also performed with this 100- μm -wide 114- μm -long 10-QW-period Ge/Si_{0.15}Ge_{0.85} MQW planar waveguide. Fig. 3.16(a) and (b) shows the absorption spectra for both TE and TM polarizations at different reverse bias voltages. With increasing reverse bias voltages, the Stark (red) shift of the absorption spectra and the reduction of the exciton related absorption peak were observed indicating the presence of QCSE for both LH and HH transitions. Significantly, it can be observed that the light modulation was significantly enhanced for TM polarization incident light at the LH1-c Γ 1 transition. At the same electric field, while light modulation of around 5 dB could be obtained for TE polarization using HH1-c Γ 1 transition, light modulation of about 15 dB was achieved for TM polarization using LH1-c Γ 1 transition.

This is consistent with the theoretical prediction that the second excitonic transition (LH1-c Γ 1) was expected to have stronger absorption modulation than HH1-c Γ 1 transition [138]. This large modulation is enabled due to the fact that with TM polarization incident light only LH1- c Γ 1 transition is allowed with enhanced oscillator strength; therefore, strong light modulation at the excitonic transition of LH1-c Γ 1 can be obtained as in Fig 3.16(b). With a proper design to maximize the interaction between the optical mode and the active region, this feature could be beneficial for the realization of an ultra-low energy electro-absorption modulator for chip scale optical interconnects, in which device's compactness and energy efficiency are highly desirable.

3.2.2 QCSE for optical modulation in planar waveguides

To be effectively used as a waveguide EA modulator, the Ge/SiGe MQW structures must demonstrate the ability to operate with high extinction ratio (ER) and low insertion loss (IL), despite the indirect gap absorption. Therefore, optical modulation characteristics were investigated in Ge/SiGe MQWs planar waveguides around their HH1-c Γ 1 transition (spectral range giving an efficient EA effect with limited insertion loss in TE polarization).

I fabricated and characterized 100- μ m wide Ge/SiGe MQW planar waveguides with 20 QW periods and 34 and 64 μ m length. 20 QWs were used in order to increase the overlap between the optical mode and the MQWs in the waveguide structure containing a 2 μ m thick relaxed buffer. 34 and 64 μ m long devices were used to reduce device's IL, although higher ER can be expected with longer Ge/SiGe MQW waveguides.

The absorption spectra of a 34 μ m long waveguide at different reverse bias voltages obtained are reported in Fig. 3.17 for TE polarization incident light. By increasing the reverse bias voltages, the red shift of the absorption spectra and the reduction of the exciton related absorption peak are clearly observed. The energy shift of the absorption edge according to the perpendicularly applied electric field is reported in the inset of Fig. 3.17. This shift is consistent with the theoretical calculation of the HH1-c Γ 1 transition in Ge/SiGe QWs from [138].

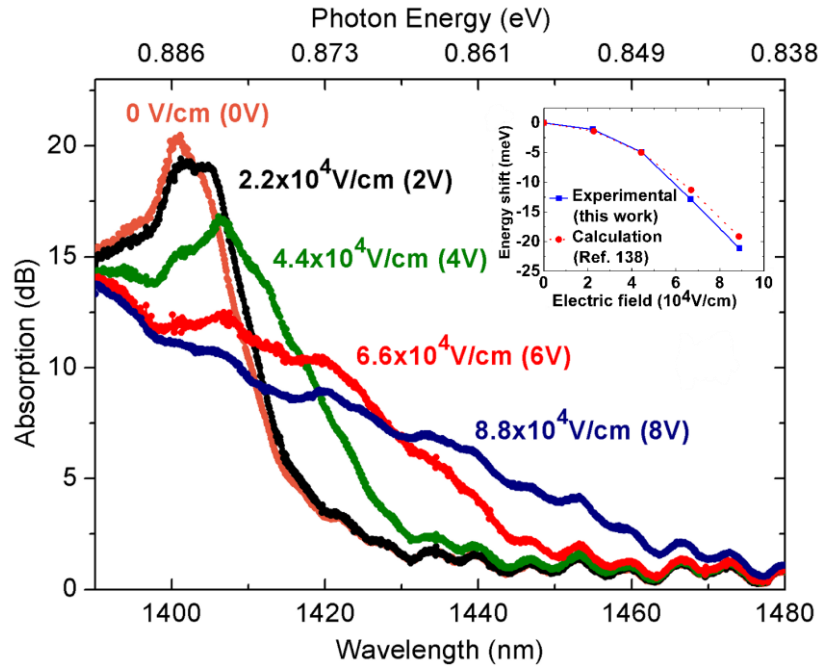


Figure 3.17: Light absorption of the 34 μm long Ge/SiGe MQW planar waveguide of 20 QWs obtained from optical transmission measurements for different electric fields as a function of wavelength and photon energy for TE polarization incident light. In the inset, the energy shift of the absorption edge as a function of electric field.

In Fig. 3.18, the extinction ratio between 0 and 6 V reverse bias and the IL at 0 V reverse bias are presented for TE polarization. As expected, the ER and IL of the 64 μm long device are higher than those of the 34 μm device. The 64 μm long waveguide has an ER larger than 5 dB for a wide spectral range (between 1413 and 1439 nm), and a maximal value of 10 dB between 1420 and 1427 nm. In addition ***5 dB ER is achieved simultaneously with IL lower than 4 dB for 11 nm wide spectral range (between 1428 and 1439 nm)***. For the 34 μm long device, an ER larger than 5 dB is obtained for wavelength from 1415 to 1431 nm. ***For the 14-nm-wide spectral range (between 1417 and 1431 nm), 5 dB ER is achieved simultaneously with an IL lower than 4 dB.***

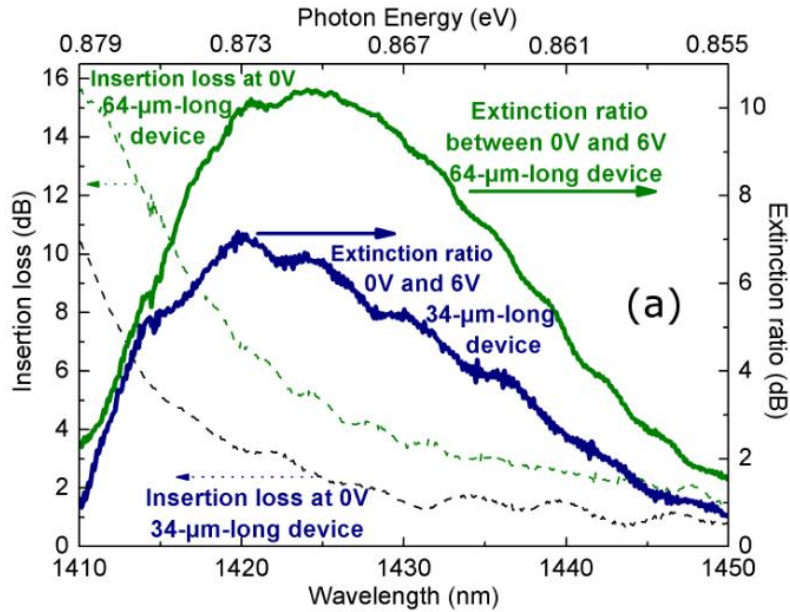


Figure 3.18: Modulation performances of the 34- and 64- μm -long Ge/SiGe MQW planar waveguides. Extinction ratio between 0 and 6 V reverse bias and the insertion loss at 0 V for TE polarization.

In conclusion, the first demonstration of room temperature QCSE in Ge/SiGe MQWs with light propagating parallel to the plane of the Ge/SiGe MQWs waveguide embedded in p-i-n diodes was presented. The device exhibits strong polarization dependence in good agreement with theory. In addition, a wide working regime with high extinction ratio and low insertion loss can be identified for TE polarization incident light.

3.3 High speed performance of Ge/SiGe MQW electro-absorption modulator

In the previous sections QCSE was demonstrated from surfaced illuminated and planar waveguide devices. This allowed us to observe DC performances of the Ge/SiGe MQWs. In this section, high frequency performance of the Ge/SiGe MQWs is investigated to evaluate their potentiality for future photonic IC. To achieve high speed devices, the equivalent capacitance of the reverse biased pin diode has to be reduced, which can be mainly achieved by a reduction of its surface. Therefore, I proceed to fabricate and characterize a **3 μm wide** Ge/SiGe waveguide. In addition, a coplanar electrode has been designed in order to apply the RF electrical signal along the **90 μm long** device.

The fabrication procedure of the waveguide is thoroughly presented in the chapter 2. The schematic and SEM views are presented in Fig 3.19(a) and (b) respectively. The detail cross section is shown in Fig 3.19(d), consisting of 20 period Ge QWs with the same well and barrier composition as that used in the previous section (see section 2.1 of chapter 2.) Mode calculations were performed using a film mode matching complex solver assuming a linear variation of refractive index in the graded buffer as shown in Fig 3.11(a). Light is guided within the Ge/SiGe MQWs and the 2 μm relaxed buffer thanks to the light confinement of the graded buffer. Assuming that 10 nm Ge/15 nm $\text{Si}_{0.15}\text{Ge}_{0.85}$ MQW region is equivalent to a $\text{Si}_{0.09}\text{Ge}_{0.91}$ homogeneous region, the overlap factor of the first TE mode with the MQW region was calculated to be 12%. The fundamental optical mode of the waveguide is shown in Fig. 3.19(c).

The measured absorption spectra of the waveguide at different reverse bias voltages are reported in Fig. 3.20(a). The wavelength separation of around 3 nm between each transmission peaks was consistent with the free spectral range of Fabry-Perot cavity induced by both input and output facets of the waveguide. The absorption edge was around 0.88 eV corresponding to the previous measurements. By increasing the reverse bias voltages, red shift of the absorption spectra was observed. Nevertheless, the absorption reduction at the excitonic transition wavelength when increasing the reverse bias voltages cannot be observed as in the case of surface-illuminated device in section 3.1 or shorter waveguide in section 3.2. This was explained to be due to the long absorption length of the waveguide configuration and will be discussed in detail in the next chapter of light detection properties from Ge/SiGe MQWs in section 4.1.2. From Fig. 3.20(b), an extinction ratio (ER) higher than 6 dB for a spectral range as wide as 20 nm (between 1425 and 1446 nm) was obtained, with a maximal ER value of around 10 dB achieved between 1433 and 1442 nm for a reverse bias of 5 V and between 1433 and 1437 nm for a reverse bias of 4 V; this is comparable to an EA modulator based on III-V semiconductors with similar device geometry and applied electric field [144]. From Fig 3.20(c) with a voltage swing of 2 V between 2 and 4 V and between 3 and 5 V, an ER higher than 6 dB was obtained for 14 nm from 1426 to 1439 nm and for 12 nm from 1433 to 1444 nm respectively. Moreover, from Fig 3.20(d) with a voltage swing of 1 V between 3 and 4 V, an ER higher than 6 dB was obtained from 1433 to 1437 nm. As seen in Fig 3.20(a), the absorption loss at 0 V of the Ge/SiGe waveguide used in this work was around 5.5 – 12 dB in the wavelength range between 1433 and 1444 nm. This absorption loss could be decreased by optimizing the light confinement in the MQW region. Indeed the overlap of the first optical

mode with the MQW region is only 12 %, and part of the optical loss also comes from the overlap between the optical mode and the 2 μm thick $\text{Si}_{0.1}\text{Ge}_{0.9}$ relaxed buffer and the doped region, as shown in Fig. 3.19(c). With an optimized optical overlap in the QW region, it was theoretically predicted that a waveguide device as short as 20 μm would be enough to obtain a sufficiently high ER (~ 5 dB) from Ge/SiGe MQWs with low optical loss (~ 3 dB) [139].

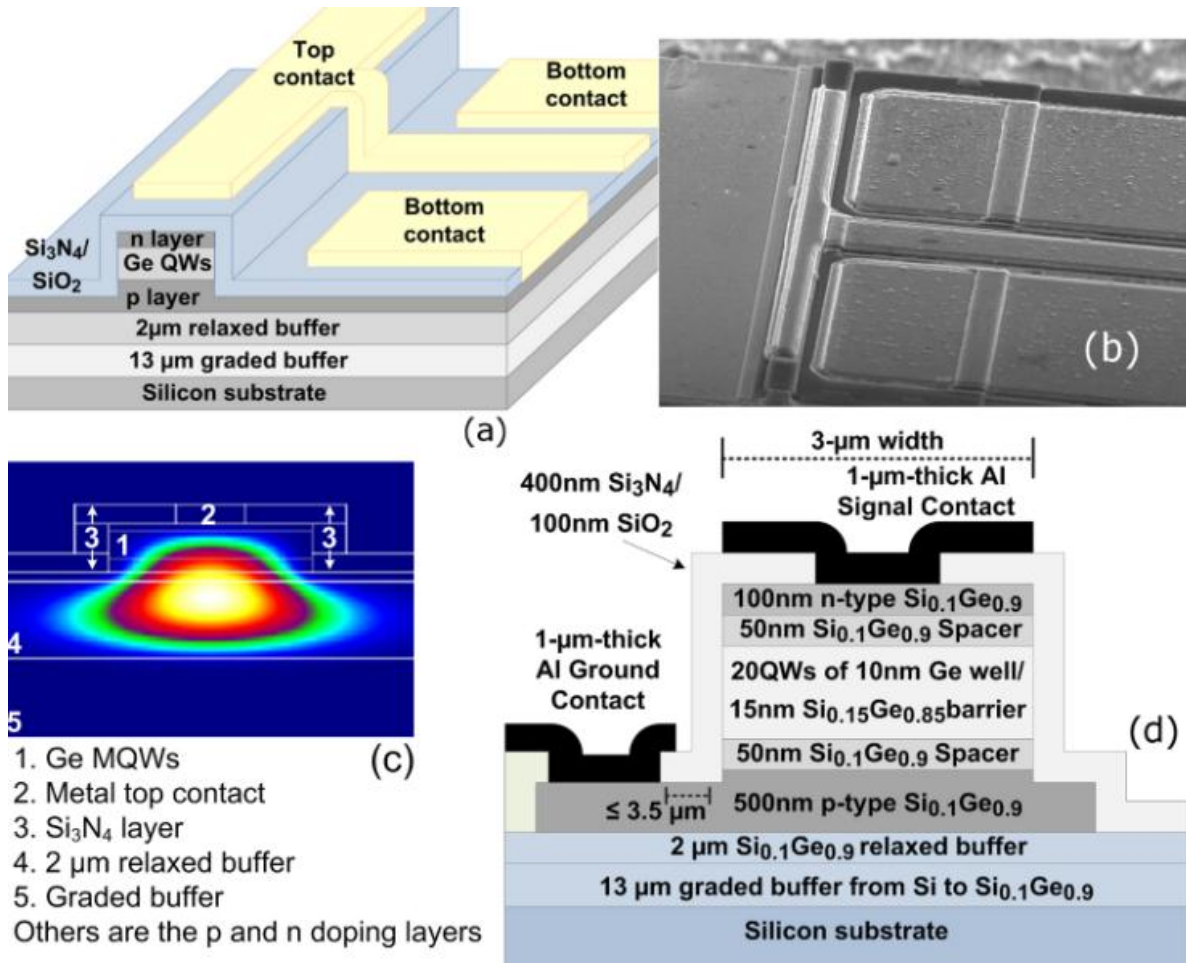


Figure 3.19: (a) Schematic view and (b) scanning electron microscope (SEM) images of the fabricated device; (c) The fundamental optical mode of the waveguide; (d) Detailed cross section of the fabricated diode.

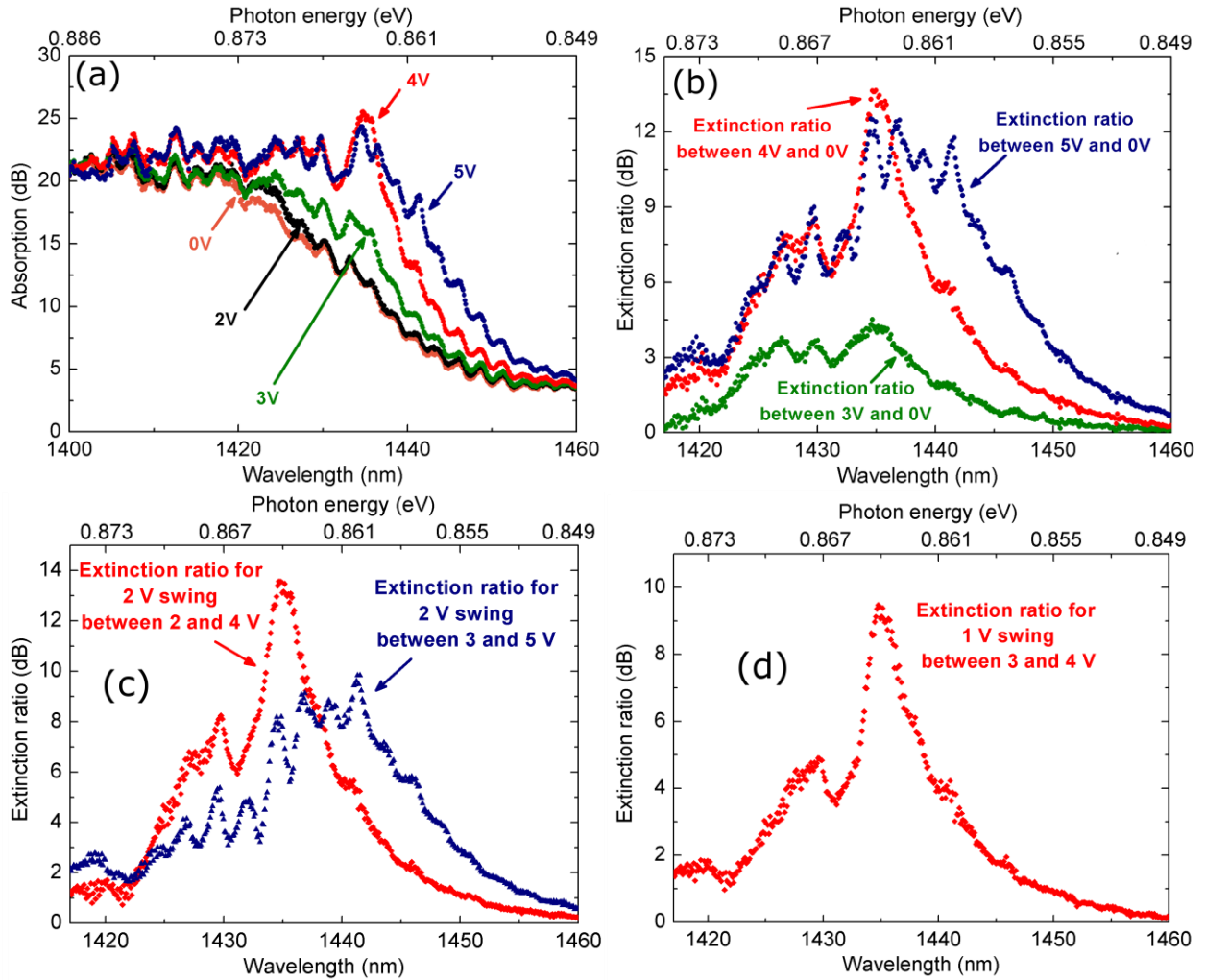
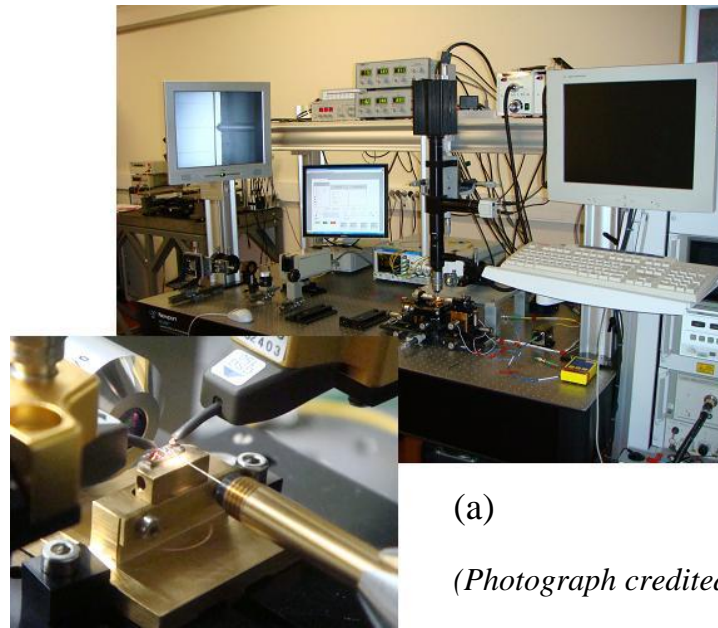


Figure 3.20: (a) Absorption spectra of 3 μm wide 90 μm long Ge/SiGe MQW waveguide as a function of wavelength and photon energy for reverse bias voltages of 0, 2, 3, 4, and 5 V. Extinction ratio of the waveguide (b) between 0 and 3, 4, 5 V (c) for a voltage swing of 2 V between 2 and 4 V and 3 and 5 V and (d) for a voltage swing of 1 V between 3 and 4 V.

The frequency response of the modulator was evaluated at 1448 nm, where the signal level is larger. As shown in Fig. 3.21(a) and (b), optical light was butt-coupled into the waveguide, and an ac signal generated by an opto-RF vector network analyzer (Agilent 86030A) coupled with a dc bias Tee was used to drive the modulator using coplanar electrodes. The modulated optical signal was coupled back to the opto-RF vector network analyzer by objective lenses. The normalized optical response at the dc reverse bias of -4.5 V as a function of frequency is given in Fig. 3.22. A 3 dB cut-off frequency of 23 GHz was experimentally obtained from the waveguide modulator.



(a)

(Photograph credited to G. Rasigades)

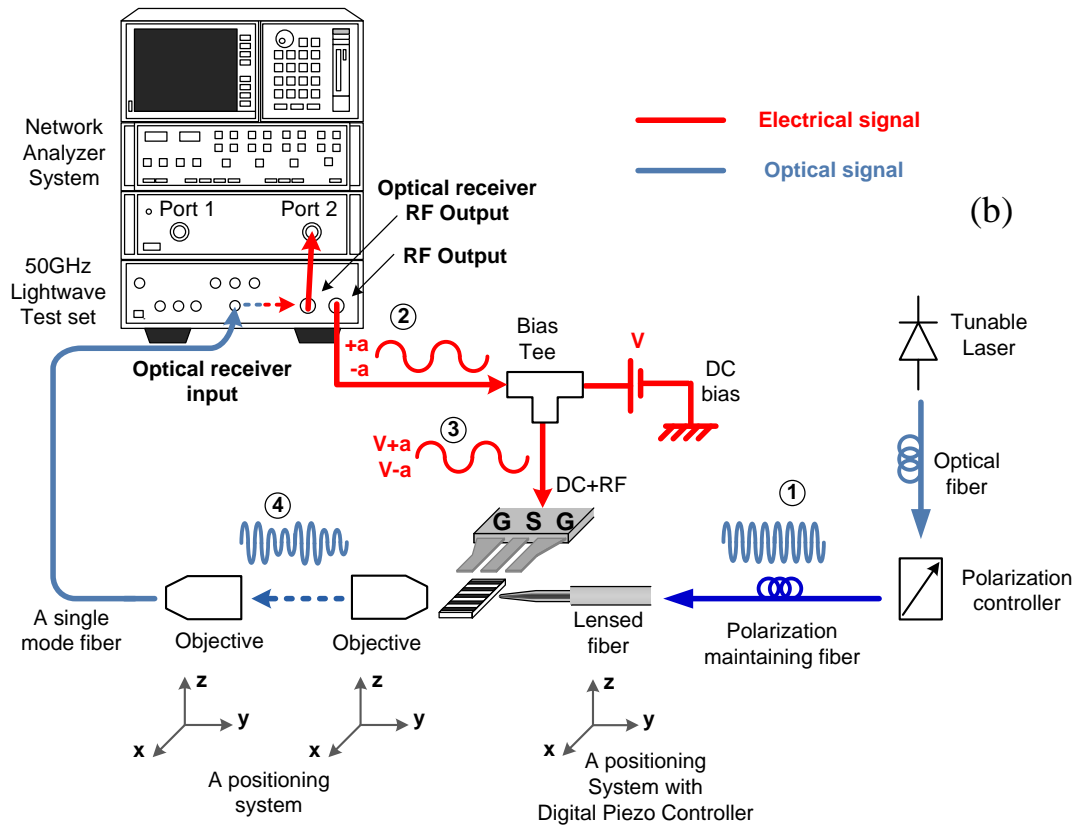


Figure 3.21: (a) Photograph and (b) Diagram of the system for measuring frequency response of the Ge/SiGe MQW modulator.

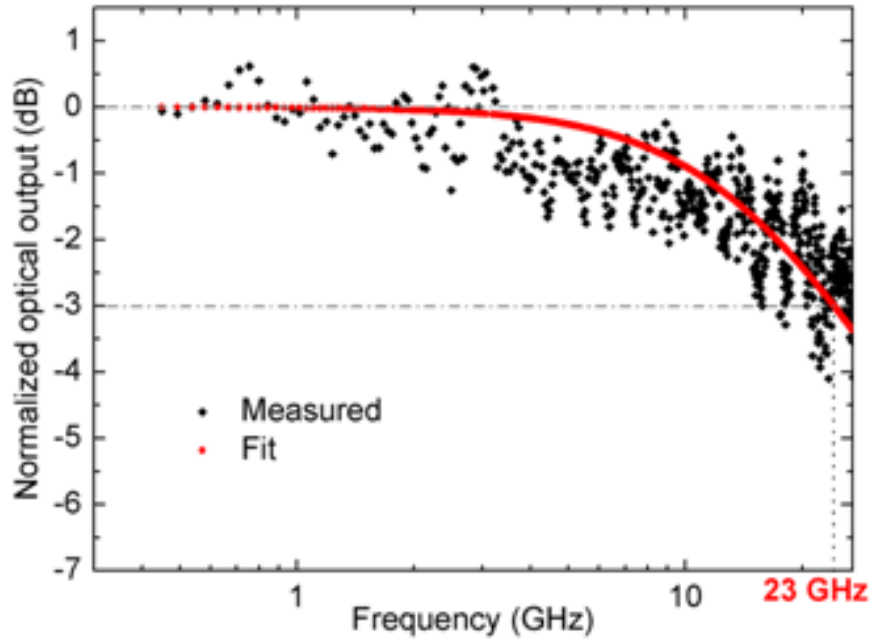


Figure 3.22: Normalized optical response at the dc reverse bias of -4.5 V as a function of the frequency.

Significantly, low energy consumption is one of the main requirements of optical interconnects to be competitive with copper wires for the chip scale applications. For example, it has been suggested that to effectively replace copper wire, optical output devices with an energy consumption of less than 100 fJ/bit will be required by 2020 [14]. For our modulator, the dynamic energy consumption was calculated using the formula of energy/bit = $1/4CV_{pp}^2$ [82] in which C is the junction capacitance and V_{pp} is the peak-to-peak bias voltage between the “off” and “on” states.

From S_{11} parameter measurements and by using Advanced Design System (ADS) simulation tool, the device capacitance was deduced to be 62 fF from the reverse bias voltage of 1 to 5 V, which also indicates that the intrinsic region was effectively depleted at the reverse bias of 1 V. This capacitance value is also consistent with the calculation using a parallel plate capacitor model of $C=\epsilon A/d$, where ϵ is the Ge dielectric constant of 16, A is the surface area of the diode of $3 \times 90 \mu\text{m}$, and d is the intrinsic region thickness of 615 nm. Therefore, the dynamic energy consumption per bit of this waveguide EA modulator is estimated to be 16 fJ/bit for a voltage swing of 1 V (between 3 and 4 V biases.) For higher voltage swing of 2 V (between 3 and 5 V biases), and 4 V (between 0 and 4 V biases), the dynamic energy consumption is estimated to be 62 and 248 fJ/bit. For much higher voltage

swing of 5 V (between 0 and 5 V biases), energy consumption of 388 fJ/bit is obtained. These values are very competitive compared to silicon MZI modulators [48, 50-51], and of the same order of magnitude as demonstrated bulk Ge modulators [73, 82-83]. Furthermore, the energy consumption of Ge/SiGe MQW modulators could be further reduced by simply using devices with smaller width and/or shorter length. In the last option, good modulation performances can still be obtained by increasing the overlap factor between the optical mode and the active region, for example by optimizing the thickness of the relaxed buffer and the doped layers. Additionally, it is worth mentioning that dark leakage and photogenerated current during the “on” and “off” states also contribute to the energy dissipation of the EA modulator. In our devices, as to be shown in the chapter 4, relatively low dark leakage current values of 200 mA/cm² at -1 V bias were measured with a flat increase in reverse current up to a bias of - 8 V; therefore, this power dissipation is not expected to contribute dominantly in our structures. Photogenerated currents depend on the input power level and operating conditions and were not included in the calculation.

3.4 Conclusion

This chapter reports on the experimental investigation and development of high performance Ge MQW EA modulator based on QCSE. The characterization setup and experimental results on the modulation properties and performance of the Ge/SiGe MQWs are thoroughly presented. The modulation properties of the Ge/SiGe MQWs were investigated from square surface-illuminated diodes, 100 μm wide planar waveguide diodes, and a 3 μm wide and 90 μm long Ge/SiGe MQWs waveguide embedded in coplanar electrodes. The significant room temperature QCSE from the Ge/SiGe MQWs growth by LEPECVD was verified. Electro-absorption performance was assessed from Ge/SiGe MQWs waveguide for both TE and TM polarizations. Finally, high speed modulation performance was also demonstrated up to 23 GHz. With only 12% overlap factor between the optical mode and the MQW active region, the Ge/SiGe MQWs exhibited a wide spectral range with an ER greater than 9 dB and with an estimated energy consumption of as low as 108 fJ per bit. By improving the overlap factor between the optical mode and the Ge/SiGe MQW region, smaller devices with even lower energy consumption and comparable ER can be expected. *These results are then very promising for the demonstration of high performances, compact and low power optical modulator based on Ge/SiGe MQW for silicon photonics.* In addition,

as it could be beneficial if the same photonic structures can be employed for different functionalities in terms of manufacture cost and process integration, the next chapter will investigate light detection and emission properties from the same Ge/SiGe MQW structures.

Chapter 4. Light detection and emission characteristics of Ge/SiGe MQWs

Considering the results I achieved using Ge/SiGe MQW structures for light modulation shown in chapter 3, I then investigated the same Ge/SiGe MQWs to realize high speed photodetector and light emitter based on the quantum confined direct gap transition of the Ge QWs. As for optical modulator, the tested photodetector and light emitter were fabricated using the fabrication process presented in chapter 2.

For light detection, this chapter experimentally reports on the DC and high speed detection characteristics of photodetectors in surface-illuminated and waveguide configurations at room temperature. In both cases, dark currents and optical responsivities are reported. From surface-illuminated vertical p-i-n diodes, intrinsic detection bandwidths are studied at various diode diameters and reverse bias voltages. For waveguide photodetectors, high speed operation up to 10 Gb/s is demonstrated simultaneously with high optical responsivity.

Then, light emission properties of the Ge/SiGe MQWs are investigated from edge emitting p-i-n diodes. For the first time, room temperature direct gap electroluminescence (EL) from Ge/Si_{0.15}Ge_{0.85} MQWs is experimentally demonstrated. The dependences of the EL intensity on the injection current and temperature are measured. The Varshni coefficient is used to calculate the temperature variation, based on the experimentally observed red shift of the EL spectra. Significantly, EL spectra of the Ge direct-gap transition exhibits better efficiency at higher temperature, due to carrier promotion from L to Γ valley because of the heating effect. Moreover, the direct-gap EL from Ge/SiGe MQWs is shown to be transverse-electric (TE) polarized, confirming that the EL originates from recombination with the HH state. These results confirm that the direct-gap transition of Ge/SiGe MQWs can electrically emit light at room temperature and hence could be considered as one of the candidates for monolithically integrated light sources on the Si platform.

4.1 High speed light detection from Ge/SiGe MQWs

The ability to use the same materials for both light modulation and detection is beneficial. Significantly, it decreases the fabrication complexity as the same process can be used for both optical functionalities. Moreover, it can be envisioned that Ge/SiGe MQW optoelectronic devices with varied optimum QW thickness values for light modulation and detection can be deposited at the same time, thanks to the local loading effect of different growth window sizes [140]. This section reports detection characteristics including dark currents, optical responsivities, and high speed performance of Ge/SiGe MQWs at room temperature in both surfaced-illuminated and waveguide configurations. The Ge/SiGe MQW thickness and composition are the same as those used in the development of high speed EA modulator in chapter 3.

4.1.1 Surface-illuminated Ge/SiGe MQW photodiodes

Practically, photodiodes with surface-illuminated configuration are useful for free-space or fiber-optic coupling applications. Moreover, due to its easy optical coupling conditions, it is widely employed to evaluate physical properties of new optoelectronic materials and functionalities [60, 74, 84]. This section reports on dark currents, optical responsivities, and optical bandwidths at room temperature of the surface-illuminated Ge/SiGe MQW photodiodes. The devices were fabricated using the procedures described in section 2.2.2 without the use of the deep etching step. The detail cross section, optical microscope view, and SEM image of the fabricated photodiode are given in Fig. 4.1(a), (b), and (c), respectively. The schematic view of the fabricated devices can also be seen in chapter 2 (Fig. 2.3(b)). Light was vertically injected on the top surface of the photodiode with different diameters of 12, 16, 20, 30, and 50 μm . As shown in Fig 4.1(b), the p-i-n diode was embedded in a coplanar electrode to facilitate high speed electro-optical characterization.

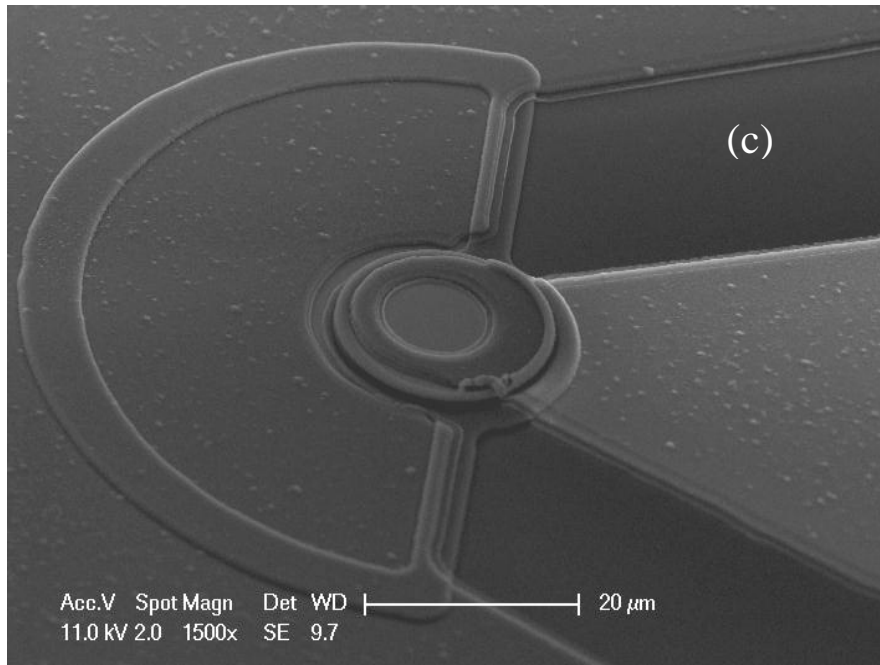
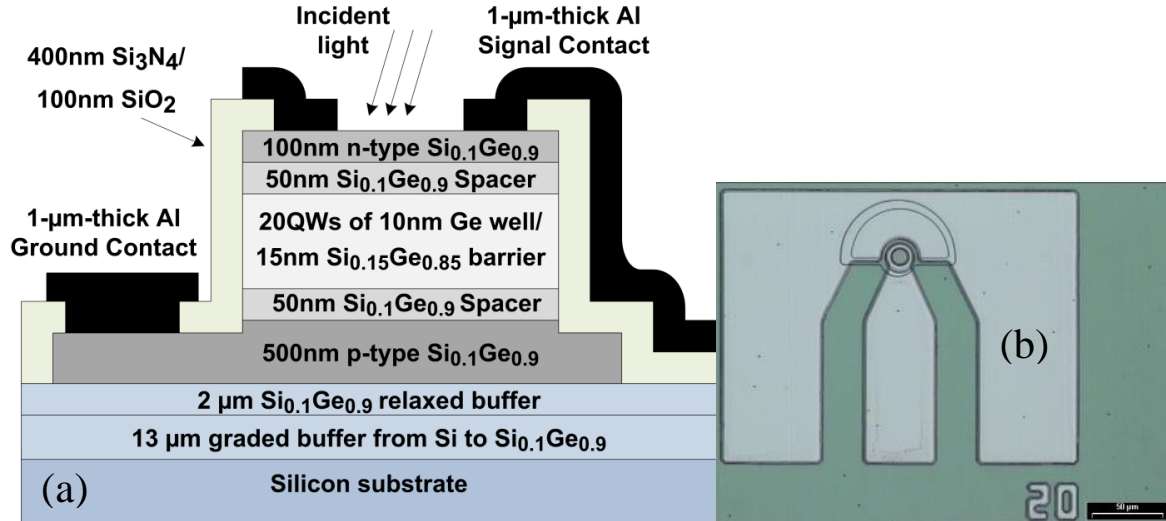


Figure 4.1: (a) Cross section of the Ge/SiGe MQW surface-illuminated p-i-n photodiode. The mesa diameters are 12, 16, 20, 30, and 50 μm . The doping concentration is $\sim 1 \times 10^{18} \text{ cm}^{-3}$ for both p- and n-type contacts. Light was vertically injected on to the diode top surface. (b) Optical microscope and (c) SEM views of a fabricated surface-illuminated p-i-n photodiode.

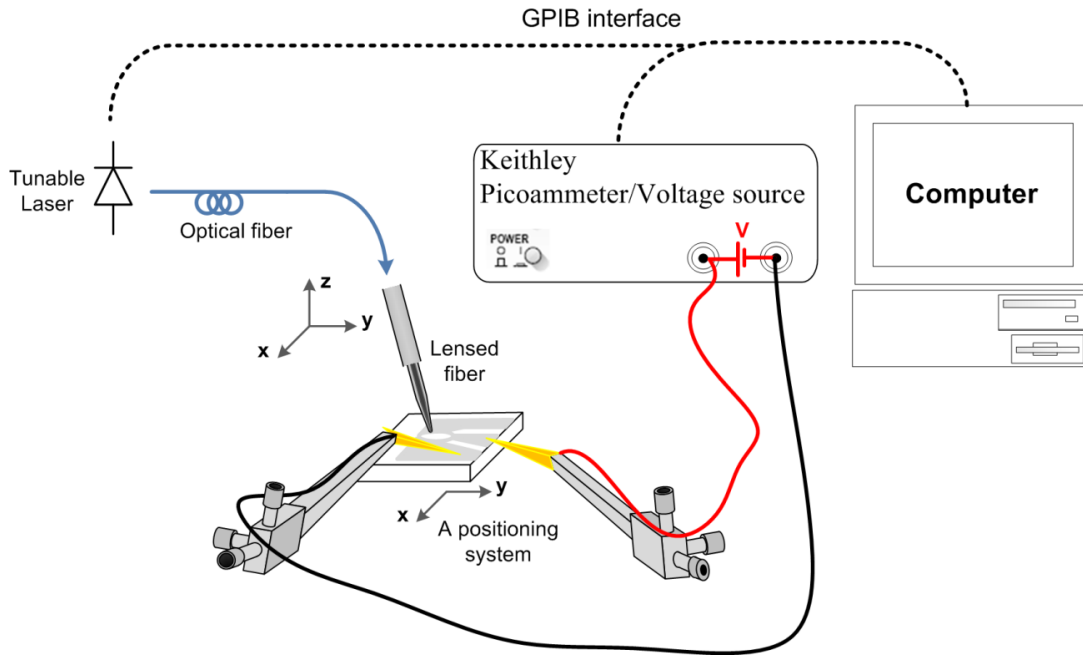


Figure 4.2: Diagram of the system for measuring current-voltage characteristics from the fabricated Ge/SiGe MQW surface-illuminated photodiodes.

First of all, the current-voltage (I-V) characteristics with and without illumination were measured using the experimental setup as described in Fig. 4.2. Light from a tunable laser diode from 1390 to 1480 nm was injected via a taper-lensed fiber onto the top surface of the photodiode. At the same time, reverse bias voltage was applied to the photodiode by a voltage source, which also recorded the values of corresponding photo-generated current at each bias voltage and input light wavelength. A computer was connected to the tunable laser diode and the voltage source via GPIB interface allowing the simultaneous acquisition of the I-V characteristics.

The measured I-V characteristics without illumination (dark currents) from the fabricated Ge/SiGe MQW photodiodes with different diameters at different reverse bias voltages are reported in Fig. 4.3. Under -1 V bias, the dark currents were measured to be 231, 423, 696, 1500, and 4200 nA for the photodiodes with diameters of 12 μm , 16 μm , 20 μm , 30 μm , and 50 μm respectively. This was equivalent to a current density of around 214 mA/cm^2 . The value of dark current density was found to be well consistent among photodiodes with different diameters. This indicated that the $\text{Si}_3\text{N}_4/\text{SiO}_2$ passivation layer effectively prevented the sidewall leakage currents. Comparing to bulk Ge, conventionally used for silicon

photonics IC, the values of dark current from the Ge/SiGe MQW photodiodes in this thesis were comparable to those of around 150 mA/cm^2 obtained from high performance surface-illuminated Ge-on-Si photodiodes with similar mesa dimensions [141]. The relatively low dark currents from the Ge/SiGe MQW photodiodes indicated the good crystalline quality of the Ge/SiGe MQWs.

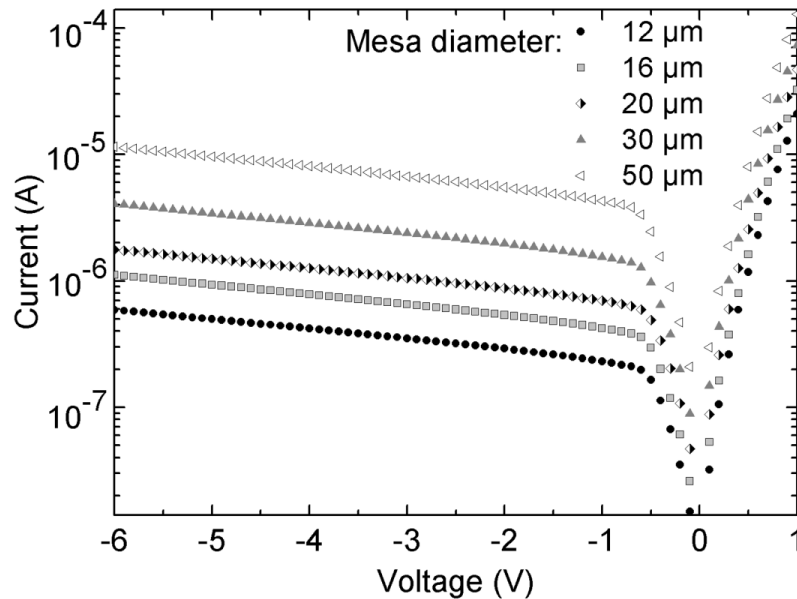


Figure 4.3: Dark currents (without illumination) as a function of reverse bias voltage for the Ge/SiGe MQW photodiodes with various mesa diameters.

The optical responsivities of $50 \mu\text{m}$ diameter surface-illuminated diode as a function of reverse bias voltage and light wavelength is reported in Fig. 4.4. The responsivity values were obtained by dividing the difference in currents under illumination for two values of optical power by the difference of the input optical power using I-V characteristics under different illuminations as shown in Fig. 4.5. The peak value of optical responsivities was found at around 1405 nm (0.88 eV) at -1 V bias. This corresponds well to the excitonic transition between HH1 and $\text{c}\Gamma_1$ in the Ge/Si_{0.15}Ge_{0.85} MQWs at room temperature as previously shown in chapter 3. Moreover, at increasing reverse bias voltages, the optical responsivity values also exhibited two main characteristics of QCSE, the Stark (red) shift in the absorption spectra and the reduction in the exciton-related absorption peak. From Fig. 4.4, it is clear that light modulation and detection can be obtained at the same wavelength region from 1395 to 1440 nm .

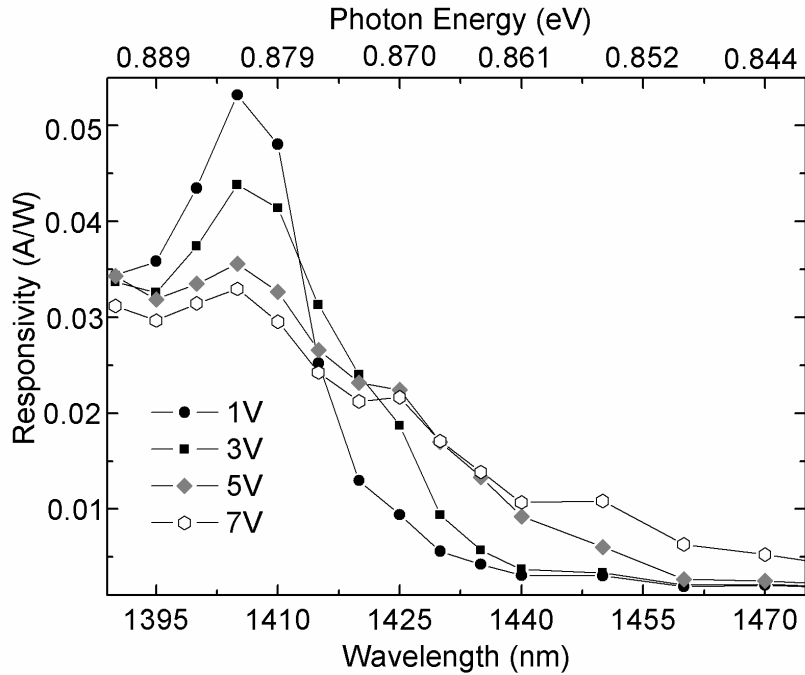


Figure 4.4: The optical responsivities as a function of reverse bias voltage and light wavelength.

Additionally for comparison with bulk Ge, the obtained responsivities of around 0.03-0.05 A/W are comparable to that of around 0.035 A/W reported from a number of high performance surface-illuminated bulk Ge photodiodes with similar total Ge thickness [60, 142]. It should be noted that the optical responsivity of a surface-illuminated photodiode can be further improved by optimizing the number of Ge QWs. In other words, the thickness of the absorbing layer has to be well-chosen: a sufficiently thick absorbing layer is required to obtain high optical responsivities, while a short spacing between the top and bottom contacts is preferred in order to achieve good high speed detection performance. This bandwidth/responsivity trade-off can be overcome by using a waveguide configuration and it will be shown in the next section.

Significantly, from I-V characteristics of 50 μm diameter photodiode with illumination at a wavelength of 1405 nm (Fig. 4.5), a peak in light absorption due to the quantum confinement effect can be clearly observed at -1 V, which is compatible with the optical responsivity reported in Fig 4.4. Therefore, from the Ge/SiGe MQW photodiodes, the highest photo-generated currents can be obtained with the bias voltage of only -1 V thanks to the excitonic enhancement between the HH1 and $c\Gamma_1$ transition in the Ge/SiGe MQWs. This feature could be beneficial in the short scale optical interconnect applications in which low energy consumption is highly desirable.

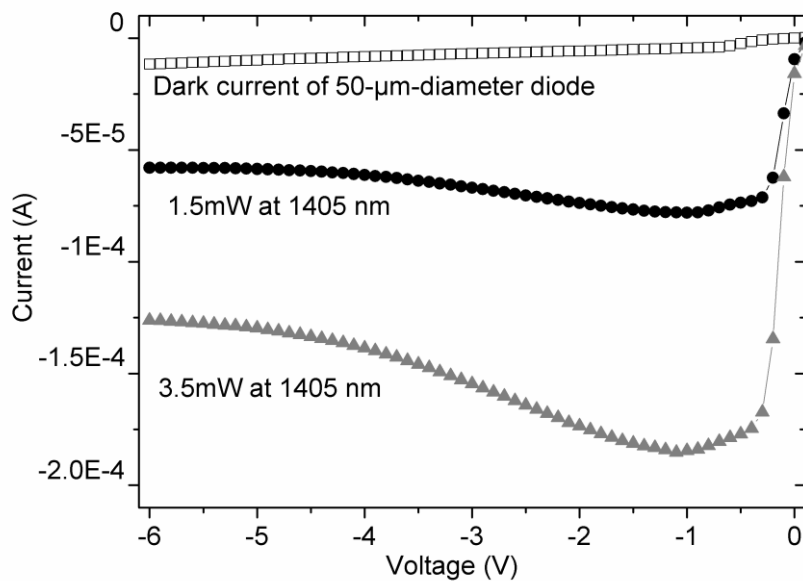


Figure 4.5: I-V characteristics with and without illumination at 1405 nm for a 50 μm diameter photodiode.

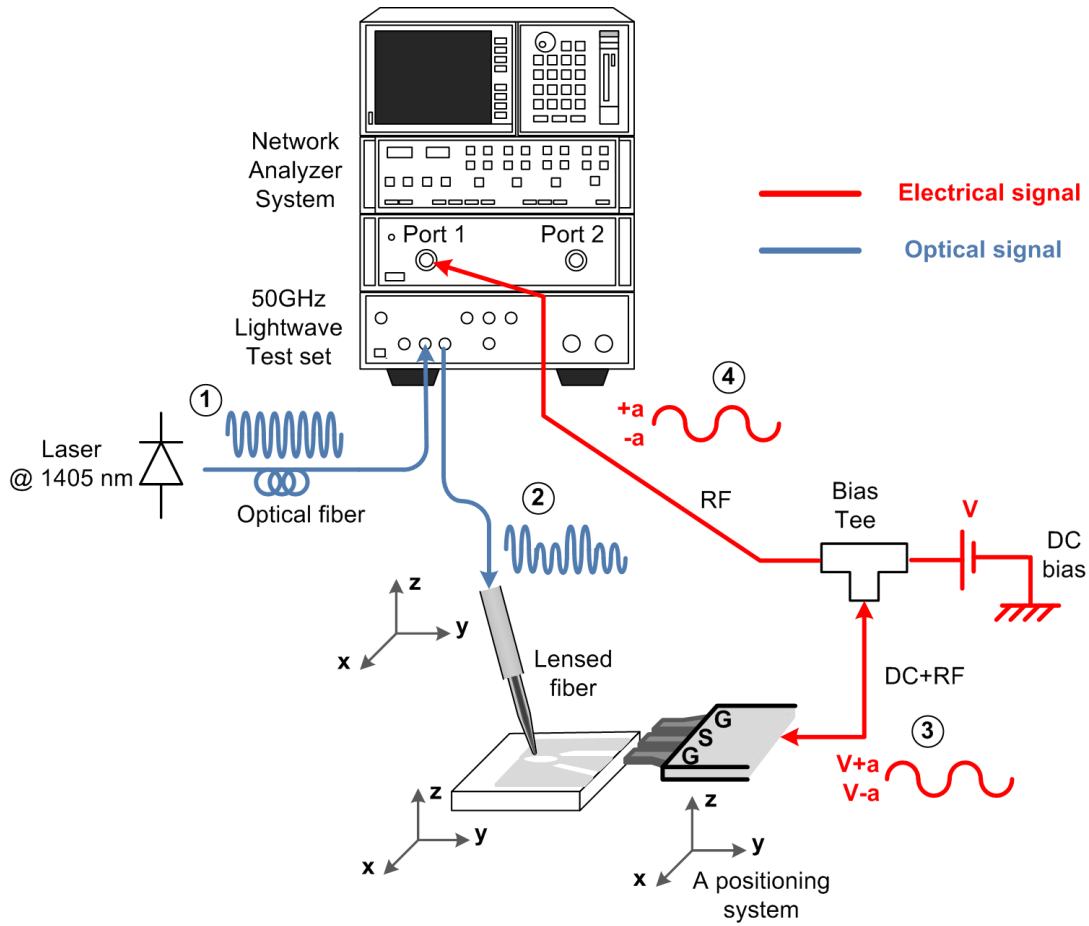


Figure 4.6: Diagram of the system for measuring small-signal frequency response of the Ge/SiGe MQW surface-illuminated photodiodes.

The small-signal frequency response of the Ge/SiGe MQW surface-illuminated photodiodes at a wavelength of 1405 nm was measured using an Agilent 86030A lightwave component analyzer (LCA) with measurement capability up to 50 GHz. The diagram of the experimental setup is shown in Fig. 4.6. (1) Optical light from a laser emitting at 1405 nm was butt-coupled via optical fiber into the optical input of the lightwave test set. The optical signal was then modulated via a lithium niobate modulator driven by the LCA at different frequencies from 50 MHz upto 50 GHz. (2) The modulated optical signal was illuminated on the top surface of the photodiodes via a taper-lensed fiber. (3) Different values of reverse bias voltages were applied on the photodiodes through a RF probe coupled with a bias tee in order to collect the photo-generated carriers as a function of frequency for all bias voltage. (4) The corresponding photocurrents were detected at the RF input of the vector network analyzer system. The electrical RF power from 50 MHz up to 50 GHz was then recorded.

The frequency response of the Ge/SiGe MQW photodiodes with diameters of 12 μm , 16 μm , 20 μm , 30 μm , and 50 μm were measured at a wavelength of 1405 nm with reverse bias voltages from 0 to -7 V. The normalized optical responses at -4 V bias of the Ge/SiGe photodiodes with different mesa diameters are shown in Fig. 4.7(a). The relative responsivity (RR) was defined by $RR(f)=10\cdot\log_{10}[R(f)/R_{LF}]$ where $R(f)$ is the Ge/SiGe photodiode responsivity at the frequency f and R_{LF} is its low frequency responsivity. The optical bandwidths were measured to be 4.2, 11.7, 16, 21.2, and 26 GHz for the photodiodes with mesa diameter of 50 μm , 30 μm , 20 μm , 16 μm , and 12 μm , respectively. Fig. 4.7(b) shows normalized optical responses of the 12 μm photodiode at different bias voltages; the optical bandwidth was shown to be 30 GHz under a reverse bias of -7 V. In Fig. 4.7(c), the measured optical bandwidths are summarized as a function of reverse bias voltages and mesa diameters. Clear dependences of the -3 dB bandwidth on the mesa size and bias voltage were observed. The optical bandwidth of 10 GHz can be achieved with only -1 V bias for 12 and 16 μm Ge/SiGe MQWs photodiodes.

S_{11} parameter measurements and analysis via ADS simulation tool indicated that the bandwidth of the device was limited by resistance–capacitance (RC) and transit time constants. Assessed device capacitances varied between 0.36 pF for the largest diode to 0.02 pF for the smallest diode. RC limitation was then dominant for largest diodes, whereas for small surface diodes, the bandwidth limitation came more from intrinsic mechanisms related to the carrier dynamics in the Ge/SiGe MQWs, in which the carriers need to escape out of the QWs in order to reach p- and n-doped regions [110]. Assuming no carrier confinement due to the presence of QW structures, carrier drift in bulk $\text{Si}_{0.1}\text{Ge}_{0.9}$ diodes with an intrinsic thickness D_i of 750 nm (as in our Ge/SiGe MQW diode) would result in a transit time limited bandwidth, $f_{\text{transit}}=0.44v_{\text{sat}}/D_i$ [143], of about 35 GHz assuming a saturation velocity, v_{sat} , of 6×10^6 $\text{cm}\cdot\text{s}^{-1}$. As mentioned above, the additional time required for carriers to escape out of the QWs increases the carrier transit time and hence decreases the achievable bandwidth, which is consistent with the measured results. Additionally, by comparing with a similar structure without QWs, the measured high speed response of bulk Ge photodetectors with comparable intrinsic region thickness was reported to reach 38 GHz [143]. This is well consistent with the maximum detection bandwidth of 30 GHz obtained from our Ge QW detector.

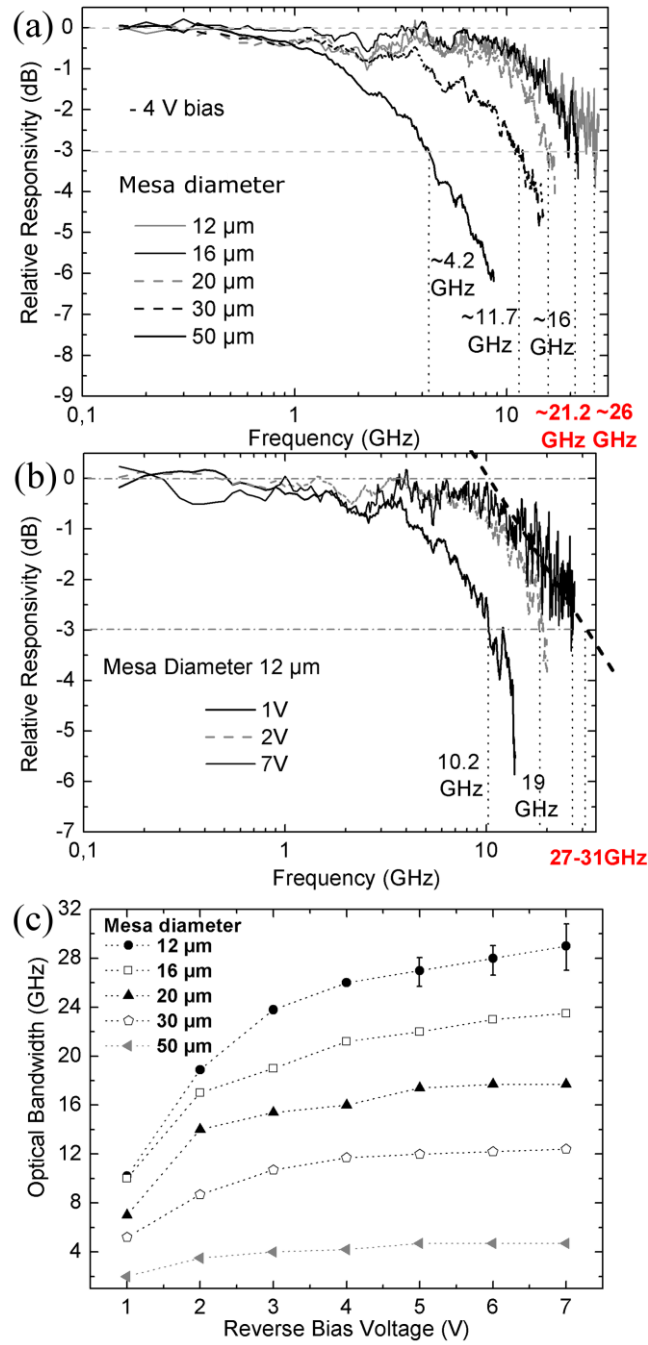


Figure 4.7: (a) Normalized optical response of the Ge/SiGe MQWs photodiode at - 4 V bias with different mesa diameter. The optical bandwidths were measured to be 4.2, 11.7, 16, 21.2, and 26 GHz for photodiodes with mesa diameter of 50 μm, 30 μm, 20 μm, 16 μm, and 12 μm, respectively. (b) Normalized optical responses of the 12 μm photodiode at different bias voltages. The measured optical bandwidth was larger than 30GHz at a reverse bias of - 7 V. (c) The measured optical bandwidth as a function of reverse bias and mesa diameter.

To summarize section 4.1.1, detection properties of surface-illuminated Ge/SiGe MQW photodiodes were demonstrated at room temperature. Main characteristics including dark currents, optical responsivities, and high speed detection bandwidths were measured. The photodiodes were shown to have a dark current as low as 200 mA/cm^2 , and the enhancement in optical detection due to the quantum confinement of the excitonic $\text{HH1-c}\Gamma_1$ transition was clearly observed. It was also shown that Ge/SiGe MQW photodiode with high speed performance very close to the fundamental carrier transit time limitation can be obtained with an attainable detection bandwidth compatible with 40 Gb/s data transmission. The next section investigates detection characteristics of Ge/SiGe MQW waveguide photodetector, with a view to achieving Ge/SiGe MQW photodetectors that demonstrates high optical responsivities simultaneously with a good high speed performance.

4.1.2 Ge/SiGe MQW waveguide photodetector

Waveguide photodetectors are advantageous for many reasons. First, they enable easy integrated with other photonic or optoelectronic components on photonic IC. Moreover, waveguide structures naturally increase the absorption length and dissociate it from the carrier collection paths [7]. As a result, it allows a photodetector with higher optical responsivities than that with surface-illuminated structures while maintaining a good high speed performance. This section reports the dark currents, optical responsivities, and high speed performance of waveguide Ge/SiGe MQW photodiodes at room temperature. The device employs exactly the same configuration as that used for the waveguide EA modulator in section 3.3. Also, the waveguide photodetectors were fabricated by using the same procedure as waveguide modulator described in section 2.2.2 including the deep etching step. The detail cross section of the fabricated waveguide photodiode is also given here in Fig. 4.8. The schematic and SEM views of the fabricated devices can be seen in chapter 2 (Fig. 2.3(d) and Fig. 2.7(b)). The waveguide is $3 \text{ }\mu\text{m}$ wide and 20 or $80 \text{ }\mu\text{m}$ long. Light was injected into the input facet of the waveguide photodetector as shown in the inset of Fig 4.8. A coplanar electrode was employed to enable high speed characterizations of the waveguide photodetector.

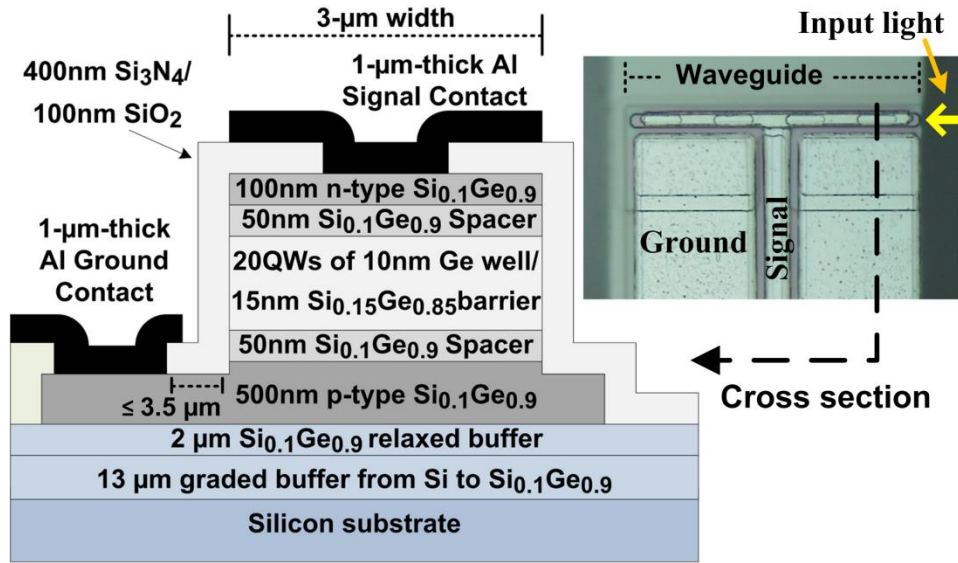


Figure 4.8: Schematic view showing cross section of Ge/SiGe MQW waveguide photodetector. In the inset, optical microscope view of a waveguide photodetector.

Length of the waveguide photodetector is either 20 or 80 μm .

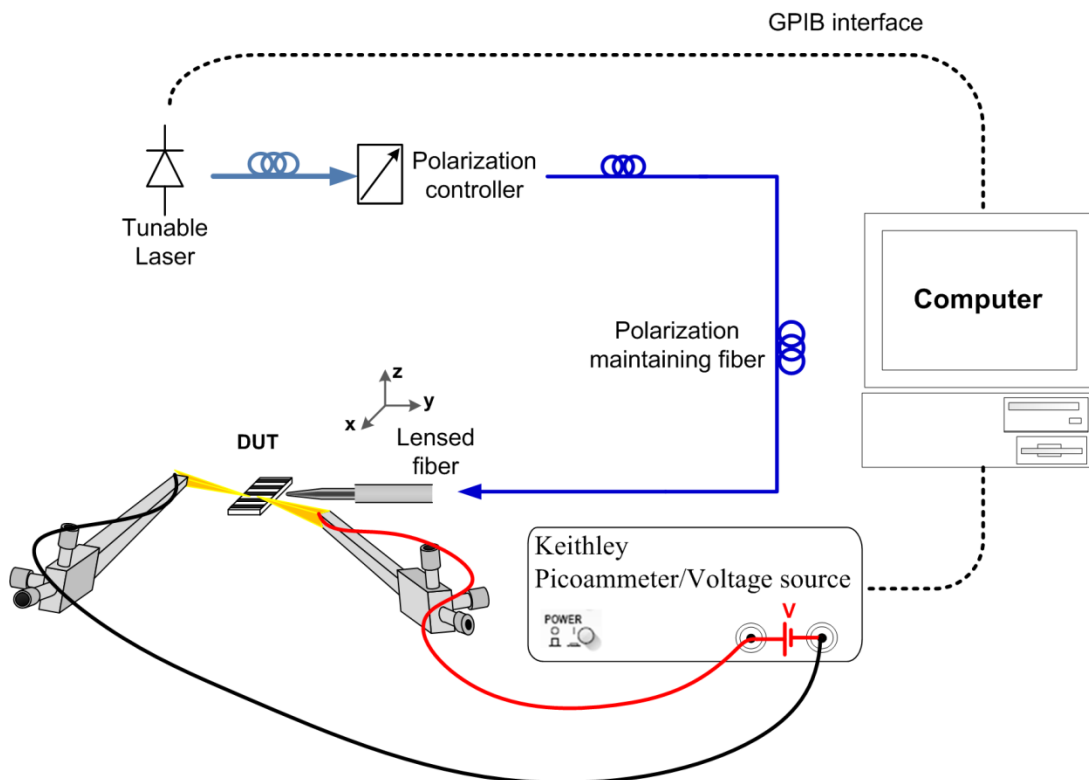


Figure 4.9: Diagram of the system for measuring I-V characteristics from the waveguide Ge/SiGe MQW photodetector.

The current-voltage I-V characteristics of waveguide photodetectors with and without illumination were measured using the experimental setup described in Fig 4.9. Firstly, light from a tunable laser diode emitting from 1390 to 1480 nm was undergone a polarizer controller in order to have light with TE polarization owing to the polarization sensitivity of the Ge/SiGe MQW waveguide discussed in section 3.2. TE polarized light was then maintained using a polarization-maintaining fiber and injected into the waveguide detector via a taper-lensed fiber. The position of the input fiber was optimized to obtain the highest photogenerated current from the device, ensuring a maximized overlap between the optical mode from the input fiber and the MQW region. As in the characterization of surface-illuminated diodes, reverse bias voltages were applied to the waveguide photodetector by a voltage source, which also recorded the values of corresponding photo-generated current at each bias voltage and input light wavelength. A computer was connected to the tunable laser diode and the voltage source via GPIB interface allowing the simultaneous acquisition of the I-V characteristics.

The measured dark current characteristics from 3 μm wide waveguide Ge/SiGe MQW photodetectors are shown in Fig 4.10. Under - 1 V bias, 113 and 474 nA were measured for the waveguide lengths of 20 and 80 μm respectively. These values correspond to current densities of 189 and 198 mA/cm^2 , consistent with the surface illuminated devices in the previous section. Furthermore, these current density values are comparable or much lower than that of high performance p-i-n Ge-on-Si waveguide detectors [57-59, 143].

Fig. 4.11 shows I-V characteristics without illumination (Dark) and with illumination for two input powers of 0.11 and 0.22 mW at a wavelength of 1405 nm and different reverse bias voltages. Reverse bias voltages up to - 8 V can be applied on the diode without reaching a breakdown zone. With illumination, we can notice that a bias voltage of only - 1 V was required to efficiently collect the photogenerated carriers.

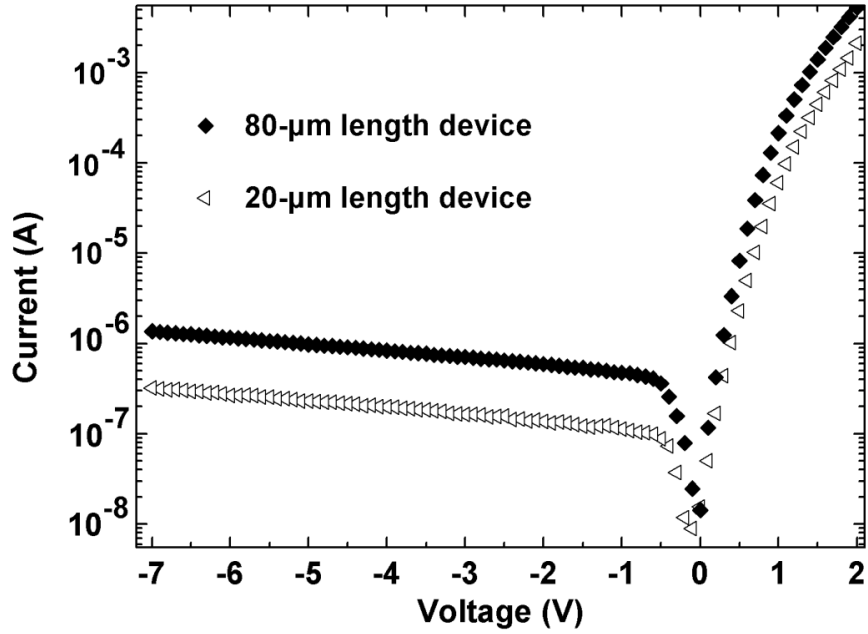


Figure 4.10: Dark currents (without illumination) as a function of reverse bias voltage from waveguide Ge/SiGe MQW photodetectors.

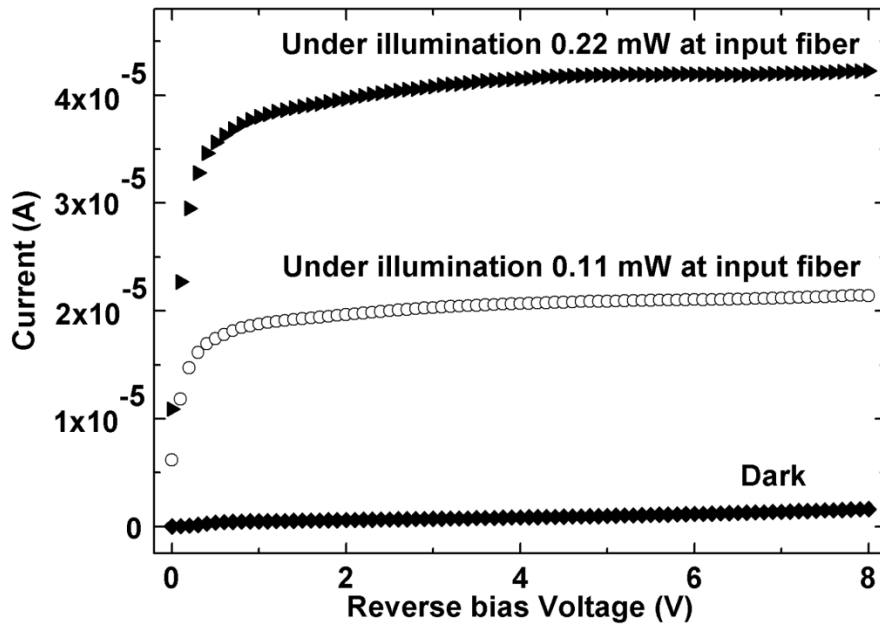


Figure 4.11: I-V characteristics under different reverse bias voltages of the 80 μm long waveguide photodetector with and without illumination at a wavelength of 1405 nm for two values of input optical power.

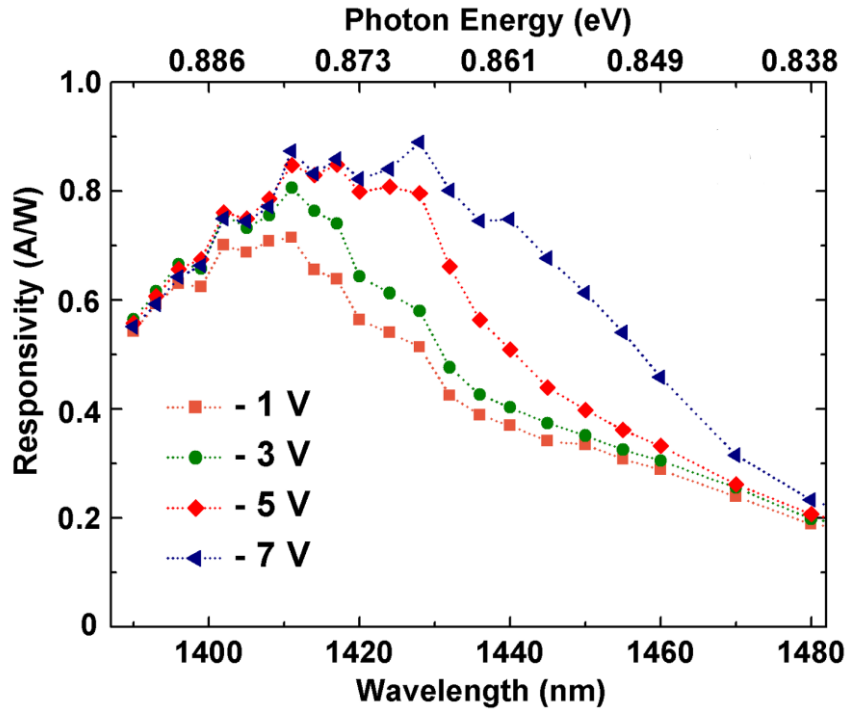


Figure 4.12: Optical responsivity spectra at different reverse bias voltages.

In Fig. 4.12, the optical responsivity as a function of the reverse bias voltage and wavelength is reported. The responsivity was retrieved by dividing the photocurrent by the input optical power. The input optical power was corrected by the coupling loss between the input fiber and the Ge/SiGe MQW waveguide, which included the mode mismatch and the reflection loss and were estimated to be 6 dB (25% coupling efficiency) from a similar Ge/SiGe MQW waveguide [115]. The responsivity reached 0.8 A/W under - 3 V at a wavelength of 1411 nm (around 0.88 eV), which corresponded to the excitonic $HH1-c\Gamma1$ transition. This value of 0.8 A/W is close to the theoretical limit of 1.13 A/W for Ge photodetectors at 1.4 μm with 100% quantum efficiency. The Stark (red) shift of the reponsivity spectra was clearly observed in Fig 4.12, but with large increase in the reponsivities with increased reverse bias at longer wavelength. The increased responsivities under higher reverse bias were observed in a number of previously-published works on III-V MQW waveguides [144-146] with no clear explanation provided yet.

To understand these phenomena and to compare the measured responsivity values with the theoretical ones, we developed a theoretical model to calculate theoretically the photodiode responsivity. Firstly, mode calculations were performed using a film mode matching complex solver (Fimmwave software). Although the presence of Al metal on top of

the waveguide could be responsible for absorption loss, optical loss of the first TE mode due to this metallic region (refractive index of Al = 1.23 + j13.2) was calculated to be only 1.4 cm^{-1} , thanks to a low overlap of the optical mode with the metallic region of $10^{-3} \%$. This loss can then be assumed negligible in comparison to the absorption in the MQW region. Assuming the scattering and radiation losses in the waveguide are negligible in comparison with the absorption loss, the responsivity (assuming 100% quantum efficiency) can be expressed as:

$$R(A/W) = I/(P \cdot \phi) = q\lambda/hc \cdot (1 - \exp(-\Gamma\alpha(\lambda, V)L)) \quad (4.1)$$

Where I is photocurrent, P is incident optical power, ϕ is coupling efficiency, α is Ge/Si_{0.15}Ge_{0.85} MQWs absorption coefficient, Γ is overlap factor in the QW region, L is device length, q is elementary charge, λ is wavelength, h is the Planck constant, and c is speed of light. The overlap factor of the first TE mode with the MQW region was calculated to be 12% as previously discussed in the section 3.3. The values of Ge/Si_{0.15}Ge_{0.85} MQWs absorption coefficient used in the calculation are as reported in Ref. 96.

The calculated responsivities shown in Fig. 4.13 indicated that the spectra shapes are strongly modified when the absorption length increases. At short length (500 nm), the calculated responsivities spectra are close to the surface illuminated measurements while at longer absorption length (50-100 μm), the values of the calculated responsivities as a function of the reverse bias voltage become rather constant at the wavelength of 1390–1405 nm, and increase according to the increasing reverse bias voltages at longer wavelength. This is well consistent with the experimental results from our 80 μm -long waveguide. Therefore, we demonstrate that the increase in the responsivities with increased reverse bias at longer wavelength in Fig. 4.12 is due to the long absorption length of the waveguide configuration. Indeed, as the generated current, I, is proportional to $1 - \exp(-\Gamma\alpha L)$, the photocurrent spectra is representative of the material absorption spectra ($I \propto \alpha$) only if the absorption length (L) is short enough. Moreover, from calculation in Fig 4.13(b) and (c), maximum responsivity of around 1 A/W was obtained at 1405 nm for 80 μm long waveguide. The lower experimental responsivity of 0.8 A/W obtained from the measurement is potentially due to the assumption on scattering and radiation losses and on the exact value of the absorption coefficient and coupling loss. Additionally, calculation with a much higher overlap factor showed that there would be no significant increase in the responsivity, indicating that 80 μm is long enough to absorb almost all light.

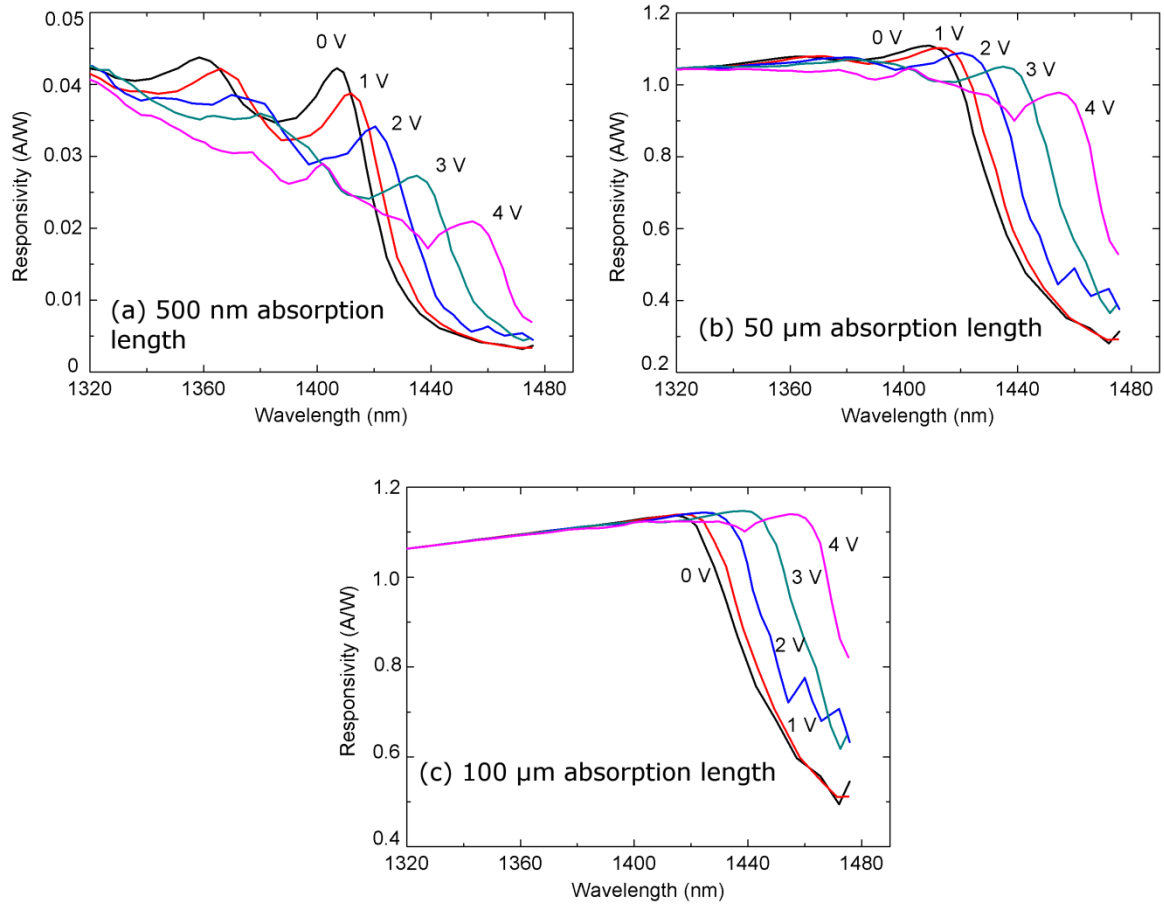


Figure 4.13: Calculated responsivity of Ge/SiGe MQWs as a function of absorption length of (a) 0.5 μ m, (b) 50 μ m, and (c) 100 μ m using Eq. 4.1, and Ge/SiGe MQW absorption coefficients from Ref. 96.

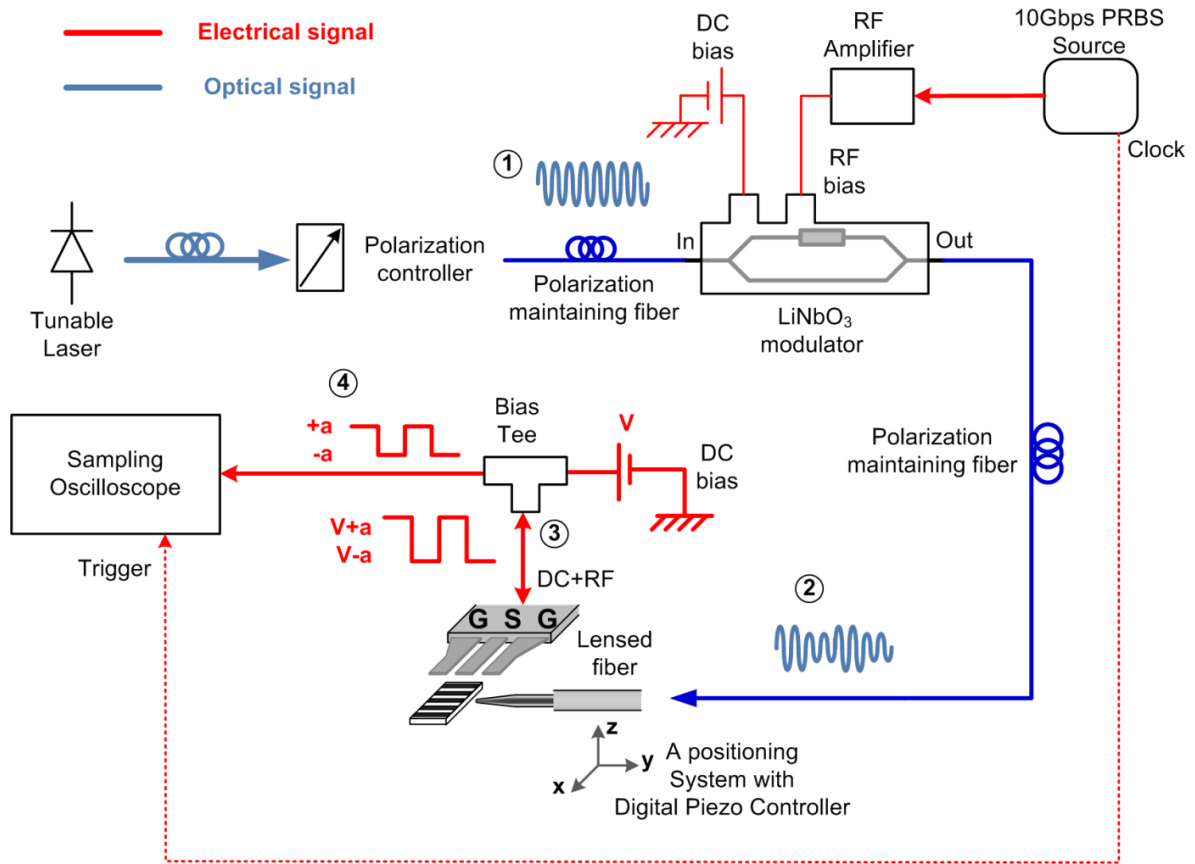


Figure 4.14: Diagram of the system for measuring eye diagram of the Ge/SiGe MQW waveguide photodetector at 10 Gb/s.

High speed performance of the photodetectors was demonstrated by measuring 10 Gbit/s eye diagrams at the light wavelengths of 1405 and 1420 nm. The diagram of the experimental setup is shown in Fig 4.14. (1) Optical light from the tunable laser was injected into a commercial 10 Gb/s LiNbO₃ modulator which was driven by a constant dc bias coupled via a bias tee with 10 Gbit/s Pseudo-Random Bit Sequence (PRBS) electrical signal with a pattern length of $2^{10}-1$ generated by a Centellax G2P1A pattern generator. (2) The modulated optical signal at 10 Gb/s, obtained from the output of the LiNbO₃ modulator, was guided to the device via a polarization maintaining fiber, and coupled into the input facet of the waveguide photodetector via a taper-lensed fiber. (3) A constant reverse bias voltage was applied on the photodiodes through a RF probe coupled with a bias tee in order to efficiently collect the photo-generated carriers. (4) The electrical output of the Ge/SiGe photodetector was recorded by a 86100C Agilent oscilloscope with 86106B optical module. The generated photocurrents were collected by a 40 GHz RF probe and recorded by the electrical input of the oscilloscope with 50- Ω input impedance.

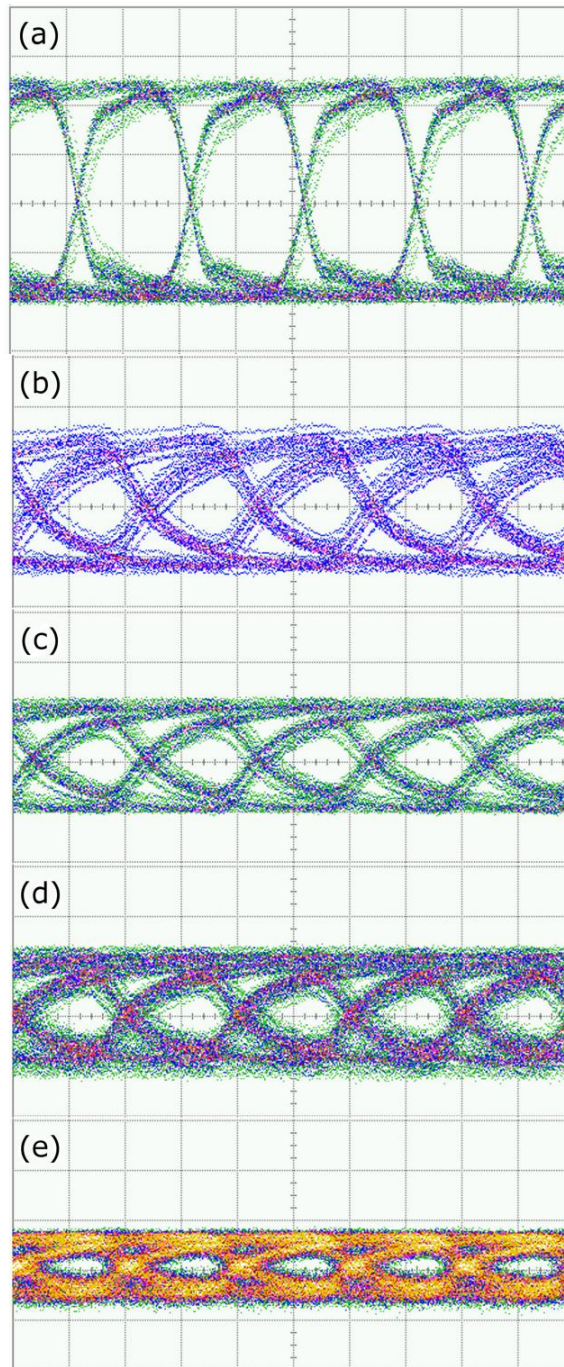


Fig 4.15: (a) 10 Gb/s optical output at 1405 nm of a commercial LiNbO₃ modulator, detected by the optical input of the oscilloscope. (b-e) 10 Gb/s electrical outputs of the Ge/SiGe MQW waveguide photodetectors for 80 μm long photodetector at wavelengths of (b) 1405 and (c) 1420 respectively, and for 20μm long photodetector at wavelengths of (d) 1405 and (e) 1420 nm respectively. In all cases a reverse bias of -3V was used. The vertical axis of (a) is 45μW/div and of (b-e) is 1 mV/div; the horizontal axis is 50 ps/div.

Fig 4.15(a) presents 10 Gb/s optical signal of the commercial LiNbO₃ modulator at 1405 nm, detected by the optical input of the oscilloscope. This signal was used to inject into the waveguide photodetector. The electrical response of the photodetector with different lengths and wavelengths is shown in Fig 4.15(b-e). Open eye diagrams presented in Fig. 4.15(b) and (c) demonstrate 10 Gb/s operation of the 80 μm waveguide photodetector under -3 V bias at the wavelength of 1405 and 1420 nm respectively. Also, from Fig. 4.15(d) and (e) 10 Gb/s operation can be obtained with the 20 μm waveguide photodetector at both wavelengths with the same bias voltage. Obviously, the generated electrical signal from the 80 μm waveguide was stronger than that from the 20 μm waveguide, and the generated electrical signal at 1405 nm was higher than that at 1420 nm, which was consistent with the photocurrent response reported in Fig. 4.12. Furthermore, it can be noticed that the on-off level difference of the modulator optical output of around 180 μW (\sim 213 and 33 μW for ON and OFF levels) at 1405 nm in Fig. 4.15(a) results in an on-off level difference of the voltage at the output of the 80 μm photodetector of around 2 mV at -3 V as in Fig. 4.15(b). This corresponds to a photocurrent difference of 40 μA , which is consistent with the optical responsivity of 0.8 A/W at 1405 nm at -3 V. Additionally, it should be noted that the level of the recorded electrical signal from the photodetector is not very strong (μW), which is simply due to the absence of optical amplifiers in our experimental setup.

To conclude section 4.1.2, light detection characteristics of Ge/SiGe MQWs in waveguide configuration were experimentally studied. The waveguide photodetector employs the same configuration as the waveguide EA modulator in section 3.3. The waveguide photodetector exhibited the same level of dark current density as that obtained with the surface-illuminated one. Contrary to the case of surface-illuminated structures, it was shown that using waveguide structures allows us to have a photodetector with high optical responsivities and good high speed performance at the same time. Optical responsivity as high as 0.8 A/W was demonstrated simultaneously with 10 Gb/s transmission data rate.

In the next section, light generation behaviors of the same Ge/SiGe MQWs will be reported using electrical injection.

4.2 Room temperature direct-gap electroluminescence from Ge/SiGe MQWs

As briefly discussed in chapter 1, bulk Ge has recently emerged [75-77] as an interesting candidate for future electrically-pumped light source around the telecommunication wavelength range ($\geq 1.55 \mu\text{m}$) monolithically integrated on silicon. This is, in fact, one of the ultimate goals in semiconductor research [5, 147]. Despite being an indirect gap material, optical gain around telecommunication wavelength has been demonstrated from Ge direct-gap transition [148, 149]. The “quasi” direct-gap nature of Ge due to the small (approximately 140 meV) energy difference between its direct and indirect conduction band minima at room temperature makes it possible to exploit Ge direct-gap transition rather efficiently as referred in chapter 1. Moreover, the direct optical transition in Ge is a very fast process with a radiative recombination rate five orders of magnitude higher than the one of the indirect transition [150]. Therefore, as the direct-gap emission in Ge should be as efficient as that of direct-gap III-V materials, research efforts have been put to achieve population inversion at center of the Brillouin zone (Γ point) of Ge. Tensile strain to further reduce the energy difference between conduction band minima at Γ and L points and n-doping to fill the indirect L valleys forcing the injected electrons to occupy the higher energy states in direct gap Γ and indirect gap L valleys have been used recently [75-77, 148, 149].

QW structures are one of the most employed structures to enhance light emitting performance of conventional photonic devices based on III-V materials [89-92]. This is due to favorable density of states in the QWs which allows lower current density to obtain population inversion. Selection rules in QW structures also allow material engineering to achieve gain either from TE or TM polarization light [151]. Therefore, it is interesting to study light emitting properties of Ge/SiGe MQWs.

This section reports on the first experimental demonstration of room temperature direct gap electroluminescence (EL) from a Ge/Si_{0.15}Ge_{0.85} MQWs. 3 μm wide and 80 or 300 μm long edge emitting p-i-n diodes were used. Light emission of the excitonic HH1- Γ c1 transition was studied at different current injections and temperatures in order to understand the related physical mechanisms. Polarization properties of the emitted light were also studied to confirm that the EL originates from recombination with a HH state.

The tested devices of 3 μm wide and 80 or 300 μm long waveguides have the same configurations, fabrication steps, and epitaxial growth as those of waveguide EA modulator and photodetector shown in the section 3.3 and 4.1.2, respectively. The optical microscope image, the cross section, and typical I-V characteristics of the devices can be seen in the Fig 4.8 and 4.10.

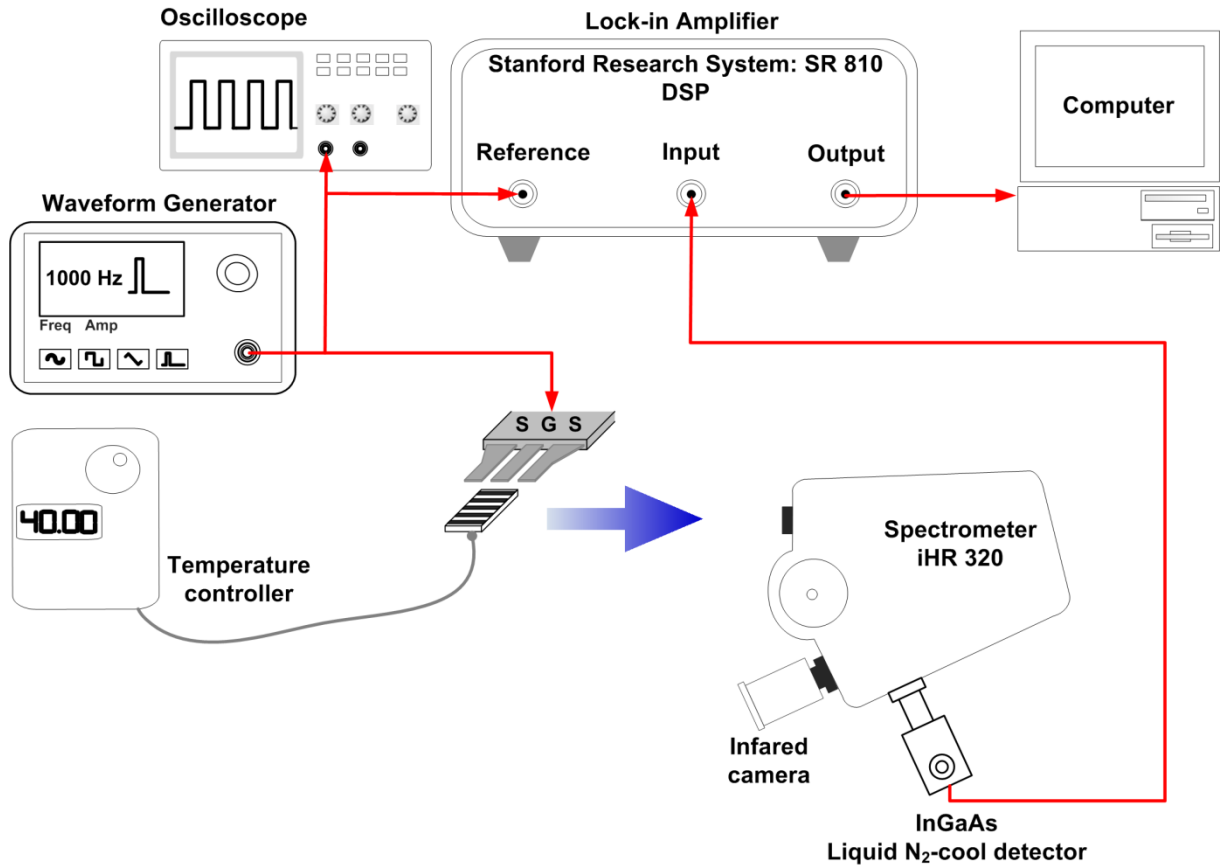


Fig 4.16: Diagram of the measurement system of room temperature electroluminescence of Ge/SiGe MQWs.

Room temperature EL spectra of the Ge/SiGe MQWs were investigated using the measurement systems shown in Fig 4.16. The EL spectra were recorded with a 2 nm measurement step using a spectrometer (Jobin Yvoni HR320) coupled with a liquid nitrogen-cooled InGaAs detector. Emission intensity as a function of injection current and emission wavelength within the 1260-1530 nm range was collected from the edge of the waveguide structure by an objective. The electrical injection of the devices was provided by pulse forward bias between 0 and 1.8-2.2 V with 30% duty cycle and 1 kHz repetition rate, and this

signal was used as the reference for lock-in detection. The temperature at the sample stage could be controlled by a thermoelectric temperature controller.

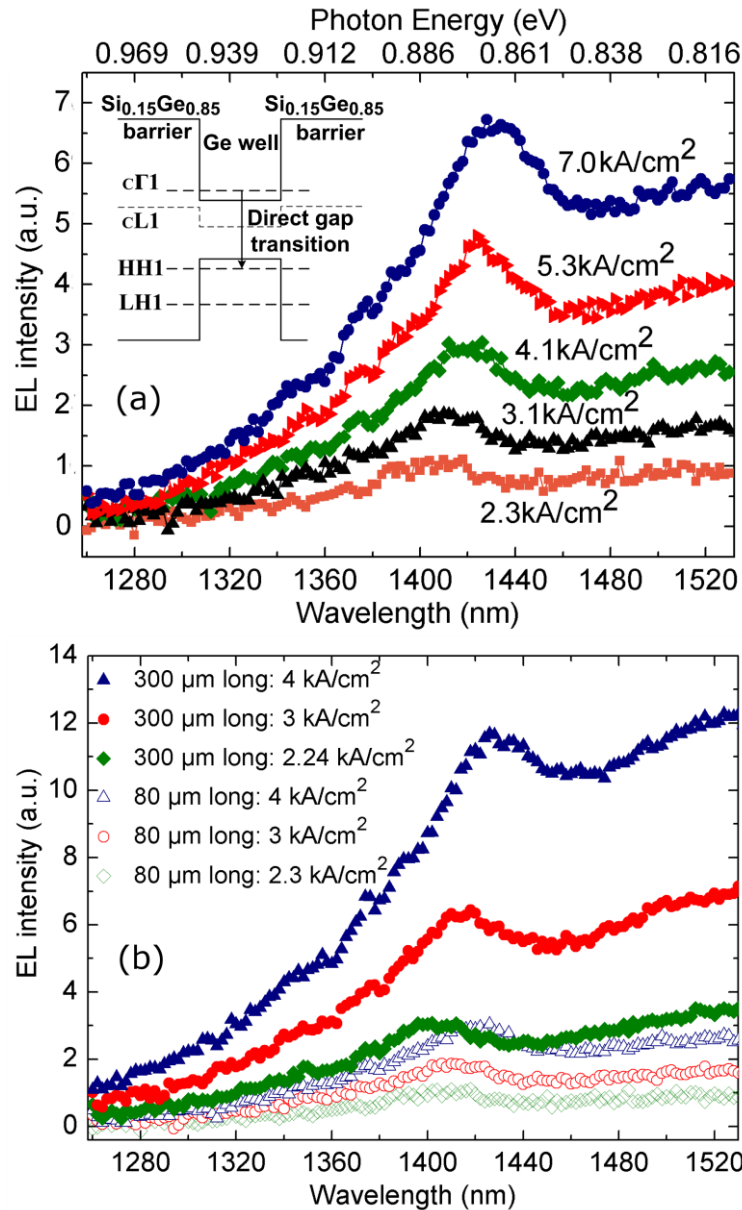


Fig 4.17: (a) Room temperature EL spectra of the 80 μm long Ge/SiGe MQW diode as a function of injection currents. In the inset, the band diagram of the Ge/SiGe MQWs (energies not to scale): $c\Gamma_1$ and cL_1 are the energies of the lowest confined QW states in the conduction band at Γ and L valleys, respectively, and HH_1 and LH_1 are the lowest confined QW states in the valence bands, associated with the heavy and light holes, respectively. A clear peak in the EL was seen at around 1420 nm corresponding to the excitonic HH_1 - $c\Gamma_1$ transition.

(b) Comparison between EL spectra from 80 and 300 μm long Ge/SiGe MQW diodes at three values of injection current.

Fig. 4.17(a) shows the measured room temperature EL spectra from the Ge/SiGe MQW diode, without any temperature stabilization. The measured EL peaks cover and are consistent with the spectral region of the HH1-c Γ 1 PL peak at room temperature from the absorption spectra of the same Ge/SiGe MQW structures reported in this thesis. A clear excitonic HH1-c Γ 1 transition was observed in the EL spectra. An increase in the EL intensity with increasing injection currents was obtained, indicating that the measured optical signal was due to the injected electrons. At low injection current, there was a broad peak in the EL at around 0.88 eV, shifted from the 0.80 eV of bulk Ge due to both the confinement effect in the QWs and the strain between the Ge QWs and the virtual buffer as observed in all previous modulation and detection investigations. Fig. 4.17(b) shows EL spectra from 80 and 300 μ m long edge emitting diode at given values of injection currents. An increase in EL intensity by factor of approximately 3.5 was consistently observed at every current density, corresponding well to the increase in diode length. As well, this indicated that the detected EL spectra originated from the Ge/SiGe MQW devices.

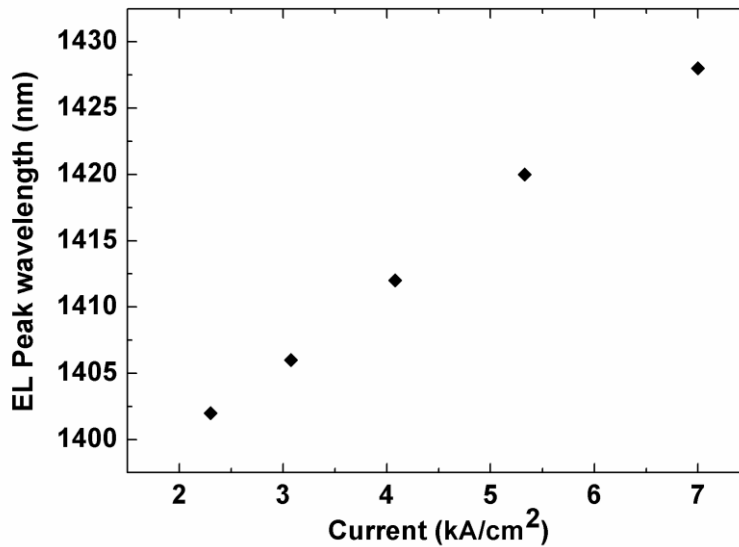


Fig. 4.18: EL peak wavelength (excitonic HH1-c Γ 1 transition) as a function of current density.

As shown in Fig 4.18, the HH1-c Γ 1 transition shifted to lower energy (longer wavelength) with higher injection currents due to heating of the sample, resulting in a bandgap reduction. As the injected current increased from 2.3 to 3.1, 4.1, 5.3, and 7.0

mA/cm^2 , the HH1-c Γ 1 transition show red shift from 1402 to 1406, 1412, 1420, and 1428 nm, respectively. From the shift of the EL peak with the current and by using Varshni coefficient for the direct gap of Ge [152] and assuming that confinement and strain effects of QW structure do not depend on temperature, a temperature increase of approximately 36°C for the higher injection current was estimated. To explain, the Varshni coefficient relate the dependence of semiconductor band gaps on temperature by

$$E_g(T) = E_0 - \alpha T^2 / (T + \beta) \quad (4.2)$$

Where α and β are fitting parameters, which are characteristics of a given material. For Ge, α is 5.82×10^{-4} and β is 296 [152]. T is temperature in Kelvin (K), and $E_g(T)$ is the gap energy at different temperatures. From the Varshni coefficients (α and β), comparing to the lowest injected current of $2.3 \text{ mA}/\text{cm}^2$ it could be estimated that the device temperature increased for 6 K, 14 K, 25 K and 36 K at the current injections of $3.1 \text{ mA}/\text{cm}^2$, $4.1 \text{ mA}/\text{cm}^2$, $5.3 \text{ mA}/\text{cm}^2$, and $7.0 \text{ mA}/\text{cm}^2$, respectively.

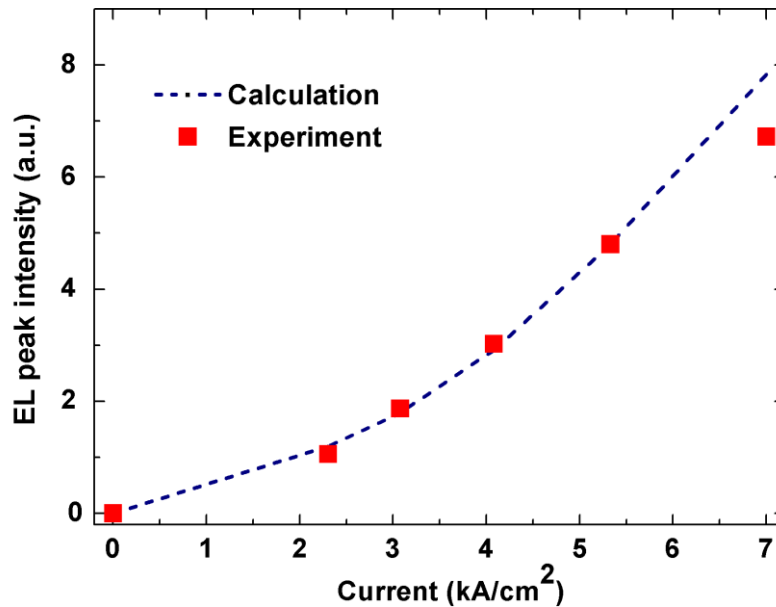


Fig. 4.19: EL peak intensity (excitonic HH1-c Γ 1 transition) as a function of current density.

To investigate EL mechanisms, the peak EL intensity of HH1-c Γ 1 transition at different injection currents from Fig 4.17 is reported in Fig 4.19. A superlinear behavior of EL was seen as a function of injected current, as in tensile strained n-doped Ge [78] where it was

attributed to the thermal promotion of carriers from L to Γ . The same reasoning can be used to explain the behaviors of our Ge/SiGe MQWs. Indeed, the measured values showed a good comparison with the curve obtained by the equation:

$$EL_{\text{direct-gap}} \propto A \cdot J \cdot \exp(-\Delta E_{\Gamma L}/kT) \quad (4.3)$$

where J is the current density, T is the temperature for each value of the current density, estimated from the Varshni coefficient method, $\Delta E_{\Gamma L}$ is the energy difference between Γ and L, k is the Boltzmann constant, and A is a proportionality constant. Taking into account strain and confinement effects, the energy difference between Γ and L was found to be $\Delta E_{\Gamma L}$ 180 meV [119] in our sample. $\Delta E_{\Gamma L}$ in Ge QWs is higher than that in bulk Ge of 140 meV because the compressive strain raises the bottom of the conduction band at Γ valley faster than at that at L valley. Equation 4.3 shows that EL is proportional to both the injection currents and the carrier statistics between Γ and L valleys, which depends on the temperature. The agreement between measurements and modeling indicated that the superlinear behavior of EL as a function of injected current can indeed be attributed to the thermal promotion of carrier from L to Γ .

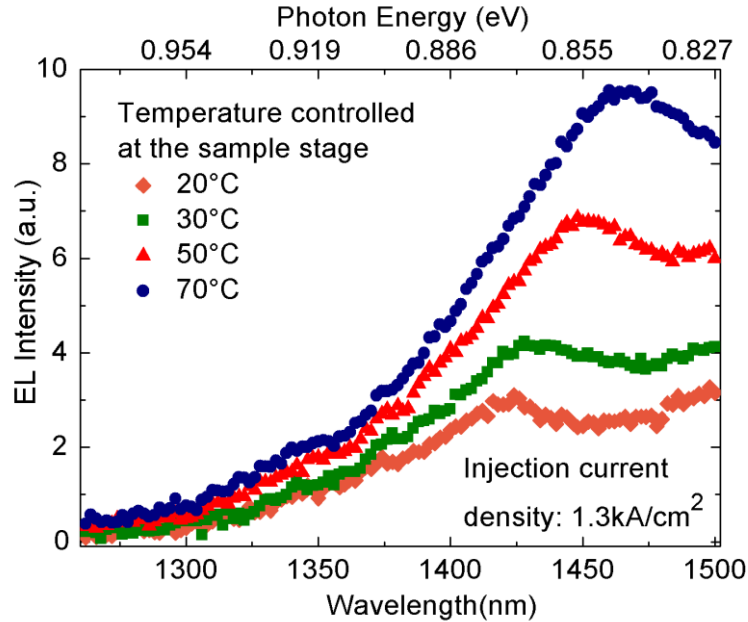


Fig. 4.20: EL spectra at different temperatures and constant current density of 1.3 kA/cm² from a 300 μm long waveguide.

Additionally, this thermal promotion of electrons from L to Γ was confirmed by a measurement on the dependence of the EL spectra on temperature at a fixed current density. This was achieved through externally controlling the temperature of a 300 μm long waveguide device. As shown in the Fig. 4.20, EL spectra at direct gap exhibited better efficiency at higher temperature. A factor of two is obtained between 20 °C and 50°C, which was consistent with the above equation and the value of $\Delta E_{\Gamma L}$. These results were also in good agreement with PL measurement of a similar Ge/SiGe MQWs in Ref. 119 which also observed the promotion of carriers from L to Γ due to the heating effect. Red shift of EL spectra in Fig. 4.20 was observed as expected due to the band gap shrinkage with higher temperature.

Moreover, as it has been shown that only TE polarized light (electric field parallel to the QWs plane) can be absorbed by the HH1-c Γ 1 transition in Ge/SiGe QW structures, thanks to dipole selection rules in QW structures, the polarization of the EL from the Ge/SiGe MQWs was also investigated here. The polarization of the EL was measured by the use of an optical polarizer, which can be adjusted to transmit either TE or TM polarized light, placed between the output facet of the waveguide and the detector, which was checked to have similar sensitivity for both polarizations. As shown in Fig. 4.21, no EL signal was observed in TM polarization at every injection current. Furthermore, the EL spectra in TE polarization were consistent with the EL spectra obtained with no optical polarizer at every injection current; any difference in the EL intensity level was due to the polarizer losses. These results indicated that the EL spectra were fully TE polarized, confirming that the EL originated from recombination with a HH state.

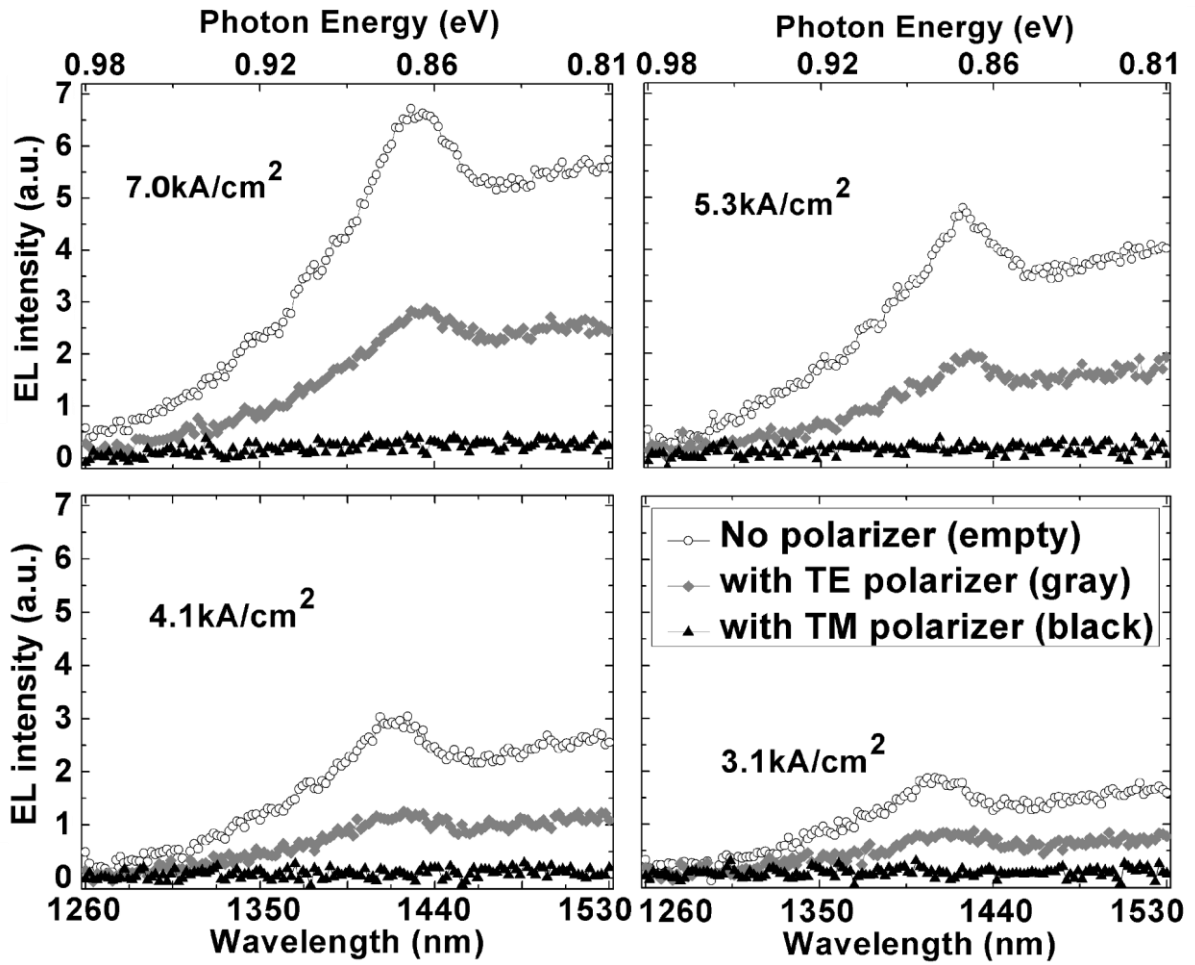


Fig. 4.21: EL spectra from 80 μm long diode for different injection currents obtained with and without an optical polarizer between the output facet of the waveguide and the detector. EL spectra in TE polarization were consistent with the EL spectra obtained with no optical polarizer. No EL was observed in TM polarization.

4.3 Conclusion

In conclusion, light detection and emission characteristics of the Ge/SiGe MQWs were studied. Good high speed performance was obtained for both surface-illuminated and waveguide photodetectors and an enhancement in optical responsivities using waveguide devices was successfully shown. Capability of the Ge/SiGe heterostructures to work at a bandwidth compatible with 40 Gb/s data transmission was firstly demonstrated. For light emission, the EL characteristics of the Ge/SiGe MQW waveguides were studied for the first time. At room temperature, EL signal was successfully measured confirming that the direct-gap excitonic HH1-c Γ 1 transition can electrically emit light at room temperature. The EL is more efficient at higher temperature due to the thermal promotion of electrons from L to Γ valleys. Due to the selection rules of the QW structure, the EL from the Ge/SiGe MQWs was shown to have a pure TE polarization behavior. These results show that Ge/SiGe MQWs could be a candidate for to realize a monolithically integrated light source on the Si platform. Chapter 5 will summarize the PhD thesis and suggests possible future research direction to be done in this topic.

Chapter 5. Conclusions and perspectives

5.1 General conclusions

This thesis is devoted to study electro-optic properties at room temperature of Ge/SiGe MQWs for silicon-compatible photonic integrated circuit applications.

The first aim of the thesis was to investigate material modulation properties and then develop a high speed and low energy silicon-compatible electro-absorption modulator based on quantum-confined Stark effect from Ge/SiGe MQWs system. Later, light detection and emission properties at room temperature of the Ge/SiGe MQWs were also investigated with a view to potentially employing them as a ubiquitous photonic building block for future electronic-photonic integration. To achieve these objectives, I performed extensive hands-on cleanroom fabrication of several optoelectronic devices and experimental investigations regarding the DC and RF electro-optical characteristics of the fabricated devices which I designed. Moreover, simple theoretical models were employed to describe various experimentally-obtained optoelectronic properties of the Ge/SiGe MQWs.

Through collaboration, the Ge/SiGe MQW epitaxial samples were obtained from Dr. Giovanni Isella, Dr. Daniel Chrastina, and Jacopo Frigerio at L-NESS laboratory, Politecnico di Milano, Italy. The device fabrication was developed and performed at the in-house 1000 m² cleanroom at IEF, Université Paris-Sud and summarized in chapter 2. For DC p-i-n diodes, the developed fabrication processes are described in the section 2.2.1. DC surface illuminated p-i-n diodes were fabricated using first optical lithography followed by dry etching gas and second optical lithography followed by metallization of Cr and Au. For high speed optoelectronic device fabrication, the fabrication process consisted of five optical lithography steps: mesa etching, mesa isolation, SiO₂/Si₃N₄ insulation layer deposition and patterning, metallization, and 90 μm deep etching as described in the section 2.2.2.

For device characterization, chapter 3 reports characterization setup and experimental results on the electro-absorption properties and performance of the Ge/SiGe MQWs based on quantum-confined Stark effect. Firstly, various DC electro-optic characterizations were performed to verify the existence of the QCSE from Ge/SiGe MQWs grown by LEPECVD, which was the first step before investigating its rapidity and other photonic functionalities. As

shown in section 3.1, QCSE from Ge/SiGe MQWs was experimentally observed using optical transmission, photocurrent, and differential transmission measurements at room temperature.

One of the primary aims was to investigate light modulation properties of the Ge/SiGe MQWs in waveguide configurations as usually preferred in integrated optics. As shown in section 3.2, the first demonstration of room temperature QCSE in Ge/SiGe MQWs with light propagating parallel to the plane of the Ge/SiGe MQWs waveguide was experimentally achieved using 100 μm wide planar waveguides. The strong polarization dependence of QCSE from Ge/SiGe MQWs was successfully shown for the first time. The waveguide configuration allowed the electro-absorption performance to be assessed with both TE and TM polarizations.

Subsequently, I proceeded to experimentally investigate modulation properties and high speed performance of a 3 μm wide and 90 μm long Ge/SiGe MQWs waveguide embedded in coplanar electrodes. High speed modulation performance from Ge/SiGe MQWs was firstly demonstrated upto 23 GHz. The Ge/SiGe MQWs exhibited a wide spectral range with ER greater than 9 dB with the use of only 90 μm long device with an estimated energy consumption of as low as 108 fJ per bit. Interestingly, this rather impressive modulation performance was obtained with only 12% overlap factor between the optical mode and the MQW active region, opening an opportunity to have further significant improvement in its performance with optimized structures.

Moreover, as the ability to use the same materials for both light modulation and detection can be desirable, light detection performance using the same Ge/SiGe MQWs was investigated in Section 4.1 of chapter 4. I studied detection characteristics of Ge/SiGe MQWs in both surface-illuminated and waveguide configurations. Surface-illuminated diodes were firstly employed to evaluate physical properties due to its easy optical coupling conditions. Later, Ge/SiGe MQW waveguide photodetectors were developed to assess its performance for integrated optic applications. From both kinds of photodetectors, main characteristics including dark currents, optical responsivities, and high speed performance were investigated. For the surface-illuminated detector, the enhancement in optical detection due to the quantum confinement of the excitonic $\text{HH1-c}\Gamma\text{1}$ transition was clearly observed. The photodiodes were shown to have a relatively low dark current of around 200 mA/cm^2 . It was also shown that Ge/SiGe MQW photodiode with high speed performance very close to the fundamental carrier transit time limitation can be obtained. An optical bandwidth compatible with 40 Gb/s

data transmission was demonstrated for the first time from Ge/SiGe MQWs. For the waveguide photodetectors, similar dark current values were obtained. An enhancement in optical responsivity values were achieved because waveguide structures naturally increase the absorption length and dissociate it from the carrier collection paths to maintain good high speed performance. 10 Gb/s detection was demonstrated from the waveguide photodetectors at high values of optical responsivity.

Finally, in section 4.2, I studied light emitting properties of the Ge/SiGe MQWs. The first experimental demonstration of room temperature direct gap electroluminescence (EL) from Ge/SiGe MQWs was reported. The EL characteristics of the Ge/SiGe MQW waveguide were successfully measured. Light emission enhancement due to quantum confinement at Ge direct-gap excitonic HH1-c Γ 1 transition was demonstrated through electrical injections at room temperature. The measured EL signal had a superlinear dependence on the level of current injections due to the thermal promotion from L to Γ valleys. As a result, it was demonstrated that the EL was more efficient at higher temperature. Polarization properties of the emitted light were also studied to confirm that the EL originated from recombination with a HH state.

5.2 Perspectives and future works

Regarding future works, although it can be envisioned from the experimental results that Ge/SiGe MQWs could be useful for light modulation, detection, and emission applications on silicon platforms, there are a number of necessary further investigation and improvement to be performed in order to well understand optical characteristics, demonstrate and improve device performance for various possible applications of the Ge/SiGe MQWs for Si photonics-electronics integrated circuits.

5.2.1 Optimized Ge/SiGe MQW waveguide for high performances electro-absorption modulator and photodetector

It was shown in chapter 3 (Fig 3.19) that only 12 % of the optical mode was overlap with the MQW region in the waveguide structure under investigation. By improving the overlap factor between the optical mode and the Ge/SiGe MQW region, smaller devices with

even lower energy consumption and comparable ER could be expected. This could be obtained by optimizing the thickness of the relaxed buffer, spacer, and p and n doping regions. Moreover the number of quantum wells should be further reduced in order to obtain large change in absorption coefficients with lower bias voltage.

It is also worth mentioning that due to the contradictory requirements between low insertion loss of an optical modulator and high optical responsivity of a photodetector, it can be observed from chapter 4 (Fig 4.12) that the optimal operating wavelength of the waveguide modulator (1430 – 1450 nm) and waveguide photodetector (< 1430 nm) is slightly different at the same level of bias voltage. Among several options, selective growth of Ge/SiGe MQWs into different growth window sizes can be used to simultaneously deposit Ge/SiGe MQWs that optimally modulate, detect, and generate light at the same wavelength region thanks to the local loading effect of different growth window sizes [140].

5.2.2 Operating wavelength

Generally, bandgap properties of semiconductor materials can be tuned by the use of external strain through the dielectric layers or the choice of buffer layer. Therefore, considering that strain-compensated Ge/Si_{0.15}Ge_{0.85} MQWs has optimum working wavelength at room temperature around 1.4-1.45 μm , it is interesting to investigate the use of Ge/SiGe MQWs at near-by popular telecommunication wavelength of 1.31 μm and 1.55 μm .

In the later part of this PhD works, I have proposed a strain-balanced design of *10 nm thick Ge well and 15 nm thick Si_{0.35}Ge_{0.65} barriers* on relaxed Si_{0.21}Ge_{0.79} virtual substrate to obtain strong QCSE around 1.31 μm . Diode fabrication and measurement were performed by Mohamed-Said Rouifed, a PhD student, with whom I have been working during the third year of my PhD works and which I trained on clean-room fabrication and characterization set-up.

In details, the MQWs were grown on Si (001) substrate using Si_{1-y}Ge_y graded buffer from Si to Si_{0.21}Ge_{0.79}. Then 2 μm of Si_{0.21}Ge_{0.79} relaxed virtual substrate was grown. The active regions consisted of a 500nm boron-doped Si_{0.21}Ge_{0.79} layer, a 50 nm Si_{0.21}Ge_{0.79} spacer, 20 periods of 10 nm Ge well and 15nm Si_{0.35}Ge_{0.65} barrier, a 50nm Si_{0.21}Ge_{0.79} cap layer, and 100 nm phosphorus-doped Si_{0.21}Ge_{0.79} n-type layer. The typical QCSE at 1.3 μm achieved through photocurrent measurements is shown in Fig 5.1. The blue shift of the absorption spectra to 1.3 μm is due to the fact that Ge QWs is under higher compressive strain

by using $\text{Si}_{0.21}\text{Ge}_{0.79}$ relaxed buffer. The $\text{Ge}/\text{Si}_{0.35}\text{Ge}_{0.65}$ MQWs was designed to have the same Ge concentration as that in the relaxed buffer; hence, a high quality strain-balanced MQWs can be grown.

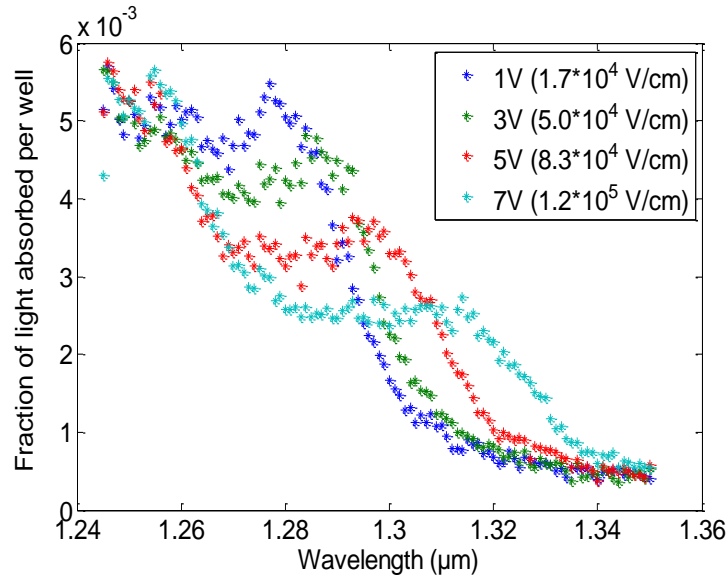


Figure 5.1: Light absorption at different bias voltages from surfaced-illuminated diode based on the proposed strain-balanced $\text{Ge}/\text{Si}_{0.35}\text{Ge}_{0.65}$ MQWs. (Figure credited to M.S. Rouifed)

5.2.3 Light emission efficiency

Efficient electrically-pump laser monolithically integrated on Si has been one of the ultimate goals in semiconductor research for many years. This thesis confirmed that excitonic direct-gap transition of high quality Ge QWs can electrically emit light at room temperature and light emission enhancement due to the quantum confinement was observed through electrical injections. In the next step, it is important to improve its quantum efficiency in order to possibly realize an efficient light source. The effect of additional strain and/or n-doping to occupy the L valleys should be studied to conclude on the possibilities of using Ge/SiGe MQW as a reliable and efficient light source material on Si platform.

5.2.4 Direct growth of Ge/SiGe MQWs on Si and waveguide integration with SOI platform

It is particularly challenging to integrate Ge/SiGe MQWs grown on a thick graded buffer in the presently well-established silicon-on-insulator (SOI) platforms for silicon-compatible photonic IC. Direct growth of high quality Ge/SiGe MQWs on Si with thin buffer would be more desirable for efficient integration with SOI waveguide. Also, growing the Ge/SiGe MQWs into a selective area on patterned silicon substrate has been recently shown to be one of the possible approaches to realize the objective [153].

J. Frigerio, a PhD student at L-NESS laboratory, has been working on the development of direct growth of high quality Ge/SiGe MQWs on unpatterned Si substrate. A high quality Ge/SiGe MQWs with estimated dislocation density of 10^7 cm^{-2} and less than 1 nm surface roughness have been obtained on Si with only 380 nm thick of buffer layer using cyclic annealing technique. P-i-n diodes fabricated by M. S. Rouifed and myself from various Ge/SiGe MQW wafers based on the developed thin buffer have shown good IV characteristics. Absorption spectra obtained from photocurrent measurement show a clear excitonic transition and QCSE at different reverse bias. These results pave the way toward the development of waveguide-integrated Ge/SiGe MQWs on silicon-on-insulator platform, which is commonly used in silicon photonic industry.

5.2.5 Ge/SiGe MQWs on SiGe waveguide

Besides silicon-on-insulator waveguide, Ge-rich SiGe waveguide could be a potential candidate to alleviate 4% lattice mismatch between Si and Ge, which poses a serious challenge of developing efficient photonic integrated circuits based on Ge optoelectronic devices on Si. As the lattice mismatch will be significantly decreased between the Ge-rich SiGe waveguide and the active device, higher quality of Ge-based optoelectronic devices could be expected with thinner and less sophisticated buffer layers. As shown in Fig 5.2, optical absorption at room temperature of Ge-rich SiGe can be chosen to be sufficiently low around the photon energy of 0.8 eV corresponding to popular telecommunications wavelength of 1550 nm. For instance, $\text{Si}_{0.15}\text{Ge}_{0.85}$ material would have less than 1 cm^{-1} absorption loss at wavelengths larger than 1400 nm, which is the working wavelength of Ge/Si_{0.1}Ge_{0.9}

MQWs. This $\text{Si}_{0.15}\text{Ge}_{0.85}$ can then be used as a relatively low loss (~ 5 dB/cm) optical waveguide, with a low lattice mismatch to Ge/ $\text{Si}_{0.15}\text{Ge}_{0.85}$ MQWs.

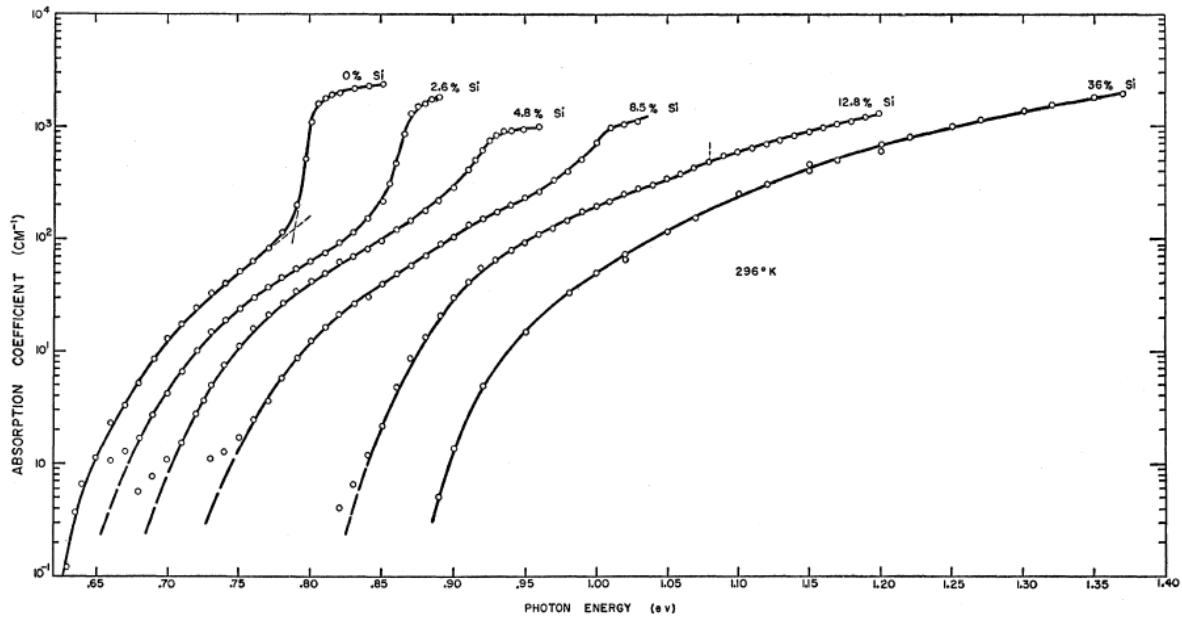


Figure 5.2: Intrinsic optical absorption spectra of Ge-rich SiGe alloys at 296°K. [154]

In this context, I have been working on design, fabrication, and on-going characterization of a proof of concept low-energy optical link based on Ge/ $\text{Si}_{0.1}\text{Ge}_{0.85}$ MQWs on Ge-rich SiGe waveguide with lower Ge concentration. The evanescent optical coupling between the $\text{Si}_{0.2}\text{Ge}_{0.8}$ waveguide and the $\text{Si}_{0.1}\text{Ge}_{0.9}$ MQWs is enabled by the use of an optical taper at the MQW section to decrease light reflection as shown in Fig 5.3. An optical microscope view of a successfully-fabricated optical link consisting of a waveguide-integrated Ge/ $\text{Si}_{0.1}\text{Ge}_{0.85}$ MQWs optical modulator connected with a waveguide-integrated Ge/ $\text{Si}_{0.1}\text{Ge}_{0.85}$ MQWs photodetector through $\text{Si}_{0.2}\text{Ge}_{0.8}$ waveguide is shown in Fig. 5.4(a). Fig. 5.4(b) and (c) show microscope view of the waveguide-integrated optical modulator and photodetector at higher magnification. The on-going characterization indicates that rather efficient light coupling is successfully obtained and good I-V characteristics can be obtained from various waveguide-integrated devices. Moreover, a successful data transferring via the optical link can be obtained as well with a low bias voltage of 0 – 1 V at both 100 μm long modulator and detector. According to the on-going characterization, first comprehensive optical link characteristics could be expected in the following months.

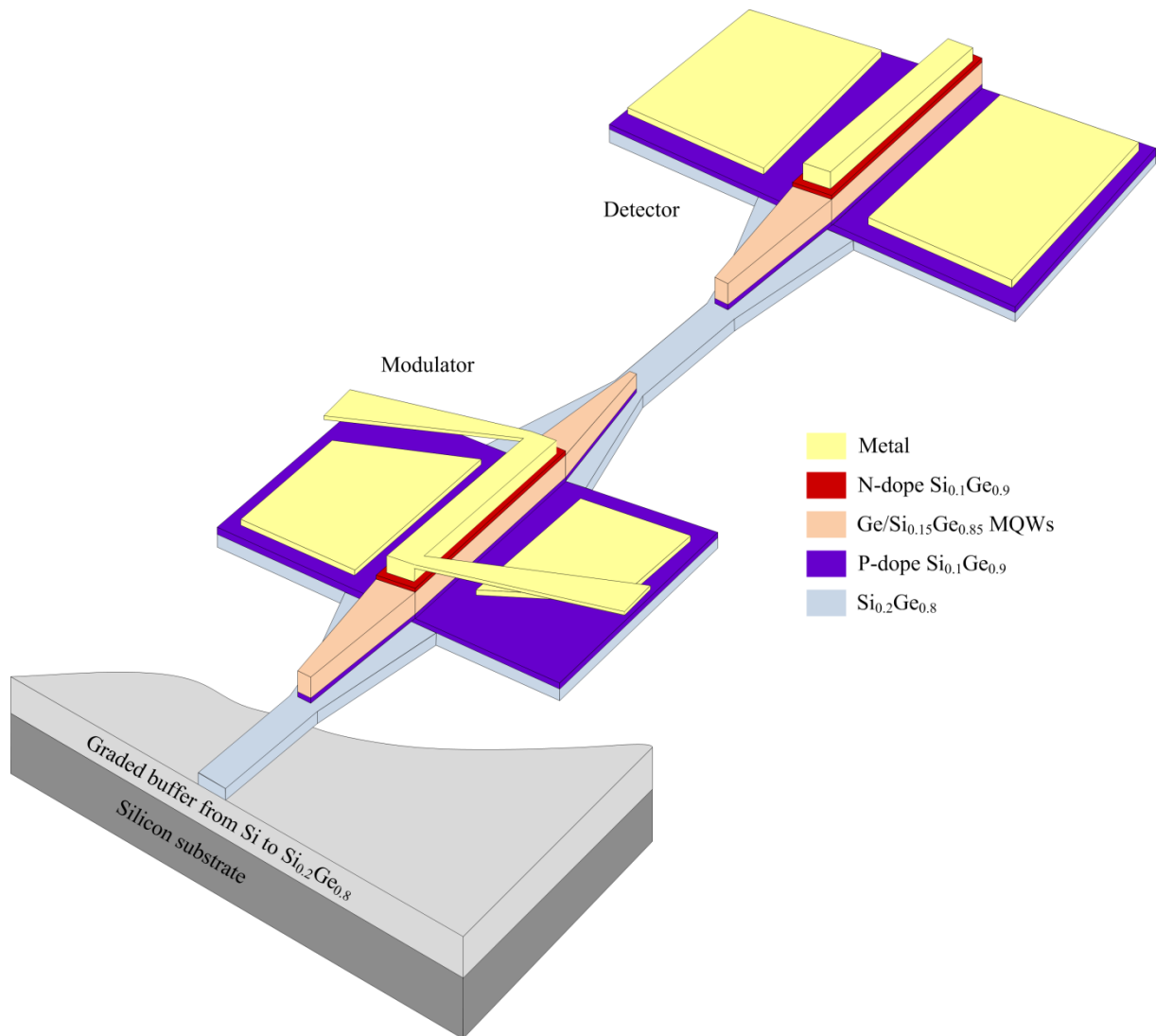


Figure 5.3: A schematic view of the fabricated optical link consisting a $\text{Si}_{0.2}\text{Ge}_{0.8}$ waveguide-integrated $\text{Ge}/\text{Si}_{0.15}\text{Ge}_{0.85}$ MQWs modulator and detector. The evanescent optical coupling between the waveguide and the MQWs is enabled by the use of an optical taper to decrease light reflection.

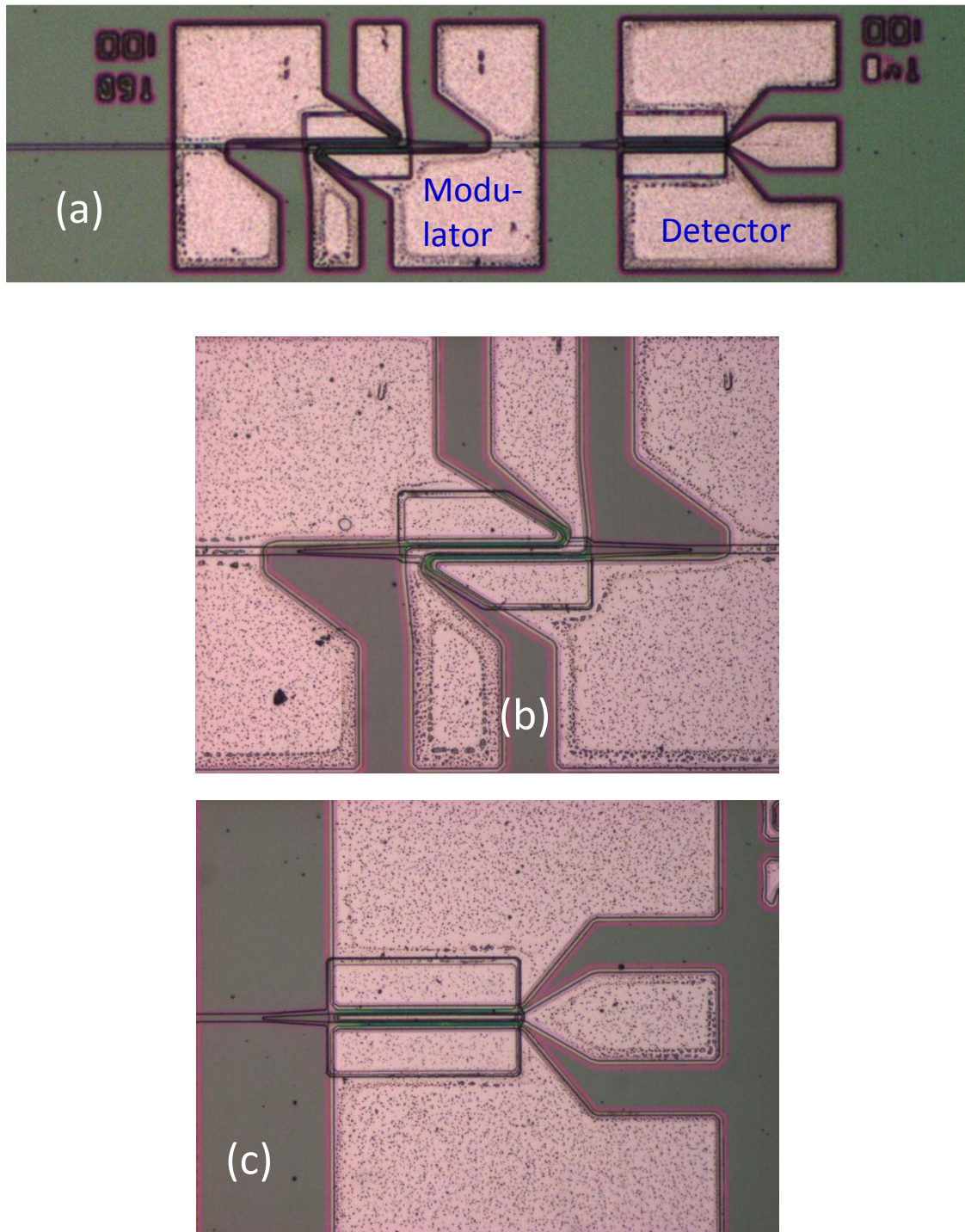


Figure 5.4: An optical microscope view of (a) a fabricated optical link consisting of a $\text{Ge}/\text{Si}_{0.1}\text{Ge}_{0.85}$ MQWs optical modulator connected with a $\text{Ge}/\text{Si}_{0.1}\text{Ge}_{0.85}$ MQWs photodetector through $\text{Si}_{0.2}\text{Ge}_{0.8}$ waveguide, and individual $\text{Si}_{0.2}\text{Ge}_{0.8}$ waveguide-integrated (b) optical modulator and (c) photodetector.

Publications

News & Awards

- 1 “*High-speed germanium quantum well modulator*”
P. Chaisakul, D. Marris-Morini, M.-S. Rouifed, G. Isella, D. Chrastina, J. Frigerio, X. Le Roux, S. Edmond, J.-R. Coudevylle, and L. Vivien
SPIE Newsroom, 8 June 2012, DOI: 10.1117/2.1201205.004197.
- 2 “*Modulateur à électro-absorption rapide à puits quantiques Ge/SiGe*”
Faculty of Science newsletter, Univ. Paris-Sud, April/May 2012.
- 3 Best Student Paper Award of the “Silicon Photonics and Photonic Integrated Circuits conference” at SPIE Photonics Europe, Bruxelles Belgium, 16-19 April 2012.
<http://spie.org/x86827.xml#Tuesday>

International Journals

- 1 “*Strong quantum-confined Stark effect from light and heavy hole related transitions in Ge quantum wells*”
P. Chaisakul, D. Marris-Morini M. S. Rouifed, J. Frigerio, G. Isella, D. Chrastina, J.-R. Coudevylle, X. Le Roux, S. Edmond, D. Bouville, and L. Vivien (*submitted*).
- 2 “*23 GHz Ge/SiGe multiple quantum well electro-absorption modulator*”
P. Chaisakul, D. Marris-Morini, M.-S. Rouifed, G. Isella, D. Chrastina, J. Frigerio, X. Le Roux, S. Edmond, J.-R. Coudevylle, and L. Vivien,
Optics Express 20, 3219-3224 (2012).
- 3 “Quantum-confined Stark effect at 1.3 μm in Ge/Si_{0.35}Ge_{0.65} quantum-well structure”
M. S. Rouifed, **P. Chaisakul**, D. Marris-Morini, J. Frigerio, G. Isella, D. Chrastina, S. Edmond, X. Le Roux, J.-R. Coudevylle, and L. Vivien,
Optics Letters 37, 3960-3962 (2012).
- 4 “*Room temperature direct gap electroluminescence from Ge/Si_{0.15}Ge_{0.85} multiple quantum well waveguide*”
P. Chaisakul, D. Marris-Morini, G. Isella, D. Chrastina, N. Izard, X. Le Roux, S. Edmond, J.-R. Coudevylle, and L. Vivien,
Applied Physics Letters 99, 141106 (2011).
- 5 “*Ge/SiGe multiple quantum well photodiode with 30 GHz bandwidth*”
P. Chaisakul, D. Marris-Morini, G. Isella, D. Chrastina, X. Le Roux, S. Edmond, E. Cassan, J.-R. Coudevylle, and L. Vivien,
Applied Physics Letters 98, 131112 (2011).

- 6 “*Polarization dependence of quantum-confined Stark effect in Ge/SiGe quantum well planar waveguides*”
P. Chaisakul, D. Marris-Morini, G. Isella, D. Chrastina, X. Le Roux, S. Edmond, J.-R. Coudevylle, E. Cassan, and L. Vivien,
Optics Letters 36, 1794-1796 (2011).
- 7 “*Quantum-confined Stark effect measurements in Ge/SiGe quantum-well structures*”
P. Chaisakul, D. Marris-Morini, G. Isella, D. Chrastina, X. Le Roux, E. Gatti, S. Edmond, J. Osmond, E. Cassan, and L. Vivien,
Optics Letters 35, 2913-2915 (2010).
- 8 “*10-Gb/s Ge/SiGe Multiple Quantum-Well Waveguide Photodetector*”
P. Chaisakul, D. Marris-Morini, G. Isella, D. Chrastina, M.-S. Rouified, X. Le Roux, S. Edmond, E. Cassan, J.-R. Coudevylle, and L. Vivien,
IEEE Photonic Technology Letters 23, 1430-1432 (2011).

Conference with proceedings

- 1 “*High Speed Electro-Absorption Modulator based on Quantum-Confined Stark Effect from Ge/SiGe Multiple Quantum Wells*”
P. Chaisakul, M.-S. Rouified, D. Marris-Morini, G. Isella, D. Chrastina, J. Frigerio, X. Le Roux, S. Edmond, J.-R. Coudevylle, and L. Vivien, IEEE 9th International Conference on Group IV Photonics (GFP), San Diego USA, 29 –31 August 2012. (*Finalist, best student paper*)
- 2 “*Room temperature direct-gap electroluminescence in Ge/SiGe quantum well waveguides*”
P. Chaisakul, D. Marris-Morini, G. Isella, D. Chrastina, J. Frigerio, M.-S. Rouified, N. Izard, X. Le Roux, S. Edmond, J.-R. Coudevylle, and L. Vivien, SPIE Photonics Europe Bruxelles Belgium, 16-19 April 2012. (*Best student paper award*)
- 3 “*High Extinction Ratio, Low Energy Consumption Ge Quantum Well Electro-Absorption Modulator with 23 GHz Bandwidth*”
G. Isella, **P. Chaisakul**, D. Marris-Morini, M.-S. Rouified, D. Chrastina, J. Frigerio, X. Le Roux, S. Edmond, J.-R. Coudevylle and L. Vivien, Electrochemical Society Transactions, Honolulu, Hawaii 2-7 October 2012.
- 4 “*Ge/SiGe Multiple Quantum Well Optoelectronic Devices for silicon photonics*”
P. Chaisakul, D. Marris-Morini, M.-S. Rouified, G. Isella, D. Chrastina, J. Frigerio, X. Le Roux, S. Edmond, J.-R. Coudevylle, and L. Vivien, 6th International SiGe Technology and Device Meeting (ISTDM), Berkeley, California USA, 4-6 June 2012.

- 5 *Invited* “Low power consumption Ge/SiGe quantum well optical modulator”
D. Marris-Morini, **P. Chaisakul**, M.-S. Rouifed, G. Isella, D. Chrastina, J. Frigerio, X. Le Roux, S. Edmond, J.-R. Coudevylle, and L. Vivien, Asia Communications and Photonics Conference (ACP), 20121107 – 20121110, Guangzhou (Canton), China
- 6 *Invited* “Si/Ge quantum well photonics and waveguide-integrated detectors”
L. Vivien, D. Marris-Morini, **P. Chaisakul**, M.-S. Rouifed, J. Frigerio, G. Isella, D. Chrastina, L. Virot, J.-M. Hartmann, E. Cassan, C. Baudot, F. Boeuf, J.-M. Fédéli
EOS Annual Meeting 2012, Aberdeen UK, 25 - 28 September 2012.
- 7 “*Ge quantum well electro-absorption modulator with 23 GHz bandwidth*”
P. Chaisakul, D. Marris-Morini, M.-S. Rouifed, G. Isella, D. Chrastina, J. Frigerio, X. Le Roux, S. Edmond, J.-R. Coudevylle, and L. Vivien, IEEE Optical interconnects conference (OI conference), Santa Fe, New Mexico USA, 20-23 May 2012.
- 8 “*Electroabsorption based on quantum-confined Stark effect from Ge/SiGe multiple quantum wells*”
P. Chaisakul, D. Marris-Morini, G. Isella, D. Chrastina, M.-S. Rouifed, J. Frigerio, E. Gatti, X. Le Roux, S. Edmond, J.-R. Coudevylle, and L. Vivien, SPIE Photonics Europe Bruxelles Belgium, 16-19 April 2012.
- 9 “*Quantum-confined Stark effect at 1.3 μm in Ge/SiGe quantum-well structures*”
M.-S. Rouifed, **P. Chaisakul**, D. Marris-Morini, J. Frigerio, G. Isella, D. Chrastina, X. Le Roux, S. Edmond, J.-R. Coudevylle, and L. Vivien, 16th European Conference on integrated optics, Barcelona, Spain, 18-20 April 2012.
- 10 “*High performance Ge/SiGe quantum well electro-absorption modulator*”
P. Chaisakul, D. Marris-Morini, M.-S. Rouifed, G. Isella, D. Chrastina, J. Frigerio, X. Le Roux, S. Edmond, J.-R. Coudevylle, and L. Vivien, 16th European Conference on integrated optics, Barcelona, Spain, 18-20 April 2012.
- 11 *Invited* “*Si/Ge quantum well photonics and waveguide-integrated detectors*”
L. Vivien, D. Marris-Morini, G. Rasigade, M. Ziebell, **P. Chaisakul**, M.-S. Rouifed, E. Cassan, N. Abadia, J.-M. Hartmann, J.-M. Fédéli, European Optical Society, Aberdeen UK, 25-28 September 2012.
- 12 *Invited* “*High speed optoelectronic devices in silicon*”
L. Vivien, D. Marris-Morini, G. Rasigade, X. Le Roux, **P. Chaisakul**, M. Ziebell, E. Cassan, J.-M. Fédéli, International Conference on Solid State Devices and Materials (SSDM 2011), Nagoya, Japan, 28-30 September 2011.
- 13 “*Quantum-confined Stark effect in Ge/SiGe quantum well waveguides*”
P. Chaisakul, D. Marris-Morini, G. Isella, D. Chrastina, X. Le Roux, S. Edmond, J.-R. Coudevylle, E. Cassan, and L. Vivien, European Material Research Society Spring meeting (E-MRS), Nice France, 9-13 May 2011.

- 14 “*30 GHz Ge/SiGe Multiple Quantum Well Photodiode*”
P. Chaisakul, D. Marris-Morini, G. Isella, D. Chrastina, X. Le Roux, S. Edmond, E. Cassan, J.-R. Coudeville, and L. Vivien, IEEE 8th International Conference on Group IV Photonics (GFP), London UK, 14 -16 September 2011.
- 15 “*Ge/SiGe quantum wells structures for optical modulation*”
P. Chaisakul, D. Marris-Morini, G. Isella, D. Chrastina, X. Le Roux, E. Gatti, S. Edmond, J. Osmond, E. Cassan, and L. Vivien, IEEE 7th International Conference on Group IV Photonics (GFP), Beijing China, 1-3 september 2010.
- 16 *Invited* “*Silicon photonics : high speed optical modulator and detector*”
D. Marris-Morini, L. Vivien, G. Rasigade, X. Le Roux, **P. Chaisakul**, M. Ziebell, E. Cassan, J.M. Fédéli, European Material Research Society Spring meeting (E-MRS), Nice France, 9-13 May 2011.
- 17 *Invited* “*Silicon photonics: recent results on high speed optoelectronic devices*”
L. Vivien, D. Marris-Morini, G. Rasigade, M. Ziebell, **P. Chaisakul**, M.-S. Rouified, E. Cassan, J.-M. Fédéli, Micro- and nano-photonic materials and devices, Trento, Italy, 16-18 January 2012.
- 18 *Invited* “*Optical modulation and detection in silicon platform*”
L. Vivien, D. Marris-Morini, G. Rasigade, X. Le Roux, **P. Chaisakul**, M. Ziebell, E. Cassan, J.-M. Fédéli, Asia Communications and Photonics Conference, *Shanghai China*, 8-12 december 2010.
- 19 *Invited* “*Recent advances in silicon-based photonic devices*”
D. Marris-Morini, L. Vivien, G. Rasigade, **P. Chaisakul**, X. Le Roux, E. Cassan, J.-M. Fédéli, D. Chrastina, G. Isella, Spring meeting of German Physical Society Regensburg Germany, 21-26 march 2010.
- 20 *Invited* “*Silicon-based optical modulators*”
G. Rasigade, **P. Chaisakul**, D. Marris-Morini, L. Vivien, X. Le Roux, S. Edmond, E. Cassan, J.-M. Fédéli, D. Chrastina, G. Isella, *IEICE Si Photonics Symposium*, Tokyo Japan, 2010.

Conference without proceedings

- 1 *Invited* “*Modulateur optique haute fréquence intégré sur substrat SOI*”
L. Vivien, D. Marris-Morini, G. Rasigade, X. Le Roux, **P. Chaisakul**, M. Ziebell, E. Cassan, J.-M. Fédéli, Journées Nationales d'Optique Guidée (JNOG), Besançon, France 22-26 octobre 2010.
- 2 *Invited* “*Silicon photonics: The recent developments of high speed optoelectronic devices*”
L. Vivien, D. Marris-Morini, G. Rasigade, M. Ziebell, **P. Chaisakul**, E. Cassan
Photonic Devices and Applications Study Group, 20110927 – 20110927, Tokyo, Japan

- 3 “*Quantum-confined Stark effect in Ge/SiGe multiple quantum well planar waveguides*”
P. Chaisakul, D. Marris-Morini, G. Isella, D. Chrastina, X. Le Roux, S. Edmond, E. Cassan, J.-R. Coudevylle, and L. Vivien, Journées Nationales du Réseau Doctoral en MicroElectronique JNRDM 11, Paris, 23-25 May 2011.
- 4 “*Optical properties of Ge/SiGe quantum wells structure for optical modulation*”
P. Chaisakul, D. Marris-Morini, L. Vivien, G. Isella, D. Chrastina, X. Le Roux, E. Gatti, S. Edmond, E. Cassan, Journées Nationales du Réseau Doctoral en MicroElectronique JNRDM 10, Montpellier, 7 – 9 june 2010.

Seminars & Courses

- 1 “*Ge multiple quantum wells for light modulation, detection, and emission*”
P. Chaisakul, Université Paris-Sud, Institut d'Electronique Fondamentale / CNRS, 15 February 2012.
- 2 D. Marris-Morini, **P. Chaisakul**, L. Vivien, “Ge and GeSi based optical modulators Delphine”, CEA Leti, France, 26 May 2011.
- 3 D. Marris-Morini, G. Rasigade, M. Ziebell, **P. Chaisakul**, L.Vivien, “Si and Ge/SiGe optical modulaotrs,” Silicon Photonics Summer School 2011 University of St Andrews, UK 3-8 July 2011.

Bibliography

1. S. Lardenois, D. Pascal, L. Vivien, E. Cassan, S. Laval, R. Orobtchouk, M. Heitzmann, N. Bouzaida, and L. Mollard, "Low-loss submicrometer silicon-on-insulator rib waveguides and corner mirrors," *Opt. Lett.* 28, 1150-1152 (2003).
2. A.G. Rickman, G.T. Reed, and F. Namavar, "Silicon-on-insulator optical rib waveguide loss and mode characteristics," *Journal of Lightwave Technology* 12 (10), 1771-1776 (1994).
3. P. Dumon, W. Bogaerts, V. Wiaux, J. Wouters, S. Beckx, J. Van Campenhout, D. Taillaert, B. Luyssaert, P. Bienstman, D. Van Thourhout, R. Baets, "Low-loss SOI photonic wires and ring resonators fabricated with deep UV lithography," *IEEE Photonics Technology Letters*, 16(5), 1328-1330 (2004).
4. A. Liu, R. Jones, L. Liao, D. Samara-Rubio, D. Rubin, O. Cohen, R. Nicolaescu & M. Paniccia, "A high-speed silicon optical modulator based on a metal-oxide-semiconductor capacitor," *Nature* 427, 615–618 (2004).
5. D. Liang and J. E. Bowers, "Recent progress in lasers on silicon," *Nature Photonics* 4, 511-517 (2010).
6. G. T. Reed, G. Z. Mashanovich, F. Y. Gardes, and D. J. Thomson, "Silicon optical modulators," *Nature photonics* 4, 518–526 (2010).
7. J. Michel, J. F. Liu, and L. C. Kimerling, "High-Performance Ge-on-Si Photodetectors," *Nature Photonics* 4, 527-534 (2010).
8. <http://www.luxtera.com> (6 November 2011).
9. <http://www.kotura.com> (6 November 2011).
10. G.T. Reed, and A. P. Knights, "Silicon Photonics: An Introduction", Wiley (2004).
11. T. Baehr-Jones, T. Pinguet, P. L. Guo-Qiang, S. Danziger, D. Prather & M. Hochberg, "Myths and rumours of silicon photonics," *Nature Photonics* 6, 206 – 208 (2012).
12. D. A. B. Miller, "Energy consumption in optical modulators for interconnects," *Optics Express* 20, A293-A308 (2012).
13. M.E. Groenert, A.J. Pitera, R.J. Ram and E.A. Fitzgerald, "Improved room-temperature continuous wave GaAs/AlGaAs and InGaAs/GaAs/AlGaAs lasers fabricated on Si substrates via relaxed graded $\text{Ge}_x\text{Si}_{1-x}$ buffer layers," *J. Vac. Sci. Tech. B* 21(3), 1064-1069 (2003).

14. D. A. B. Miller, "Device requirements for optical interconnects to silicon chips," Proceedings of the IEEE 97, 1166–1185(2009).
15. R. Kirchain, & L. Kimerling, "A roadmap for nanophotonics," Nature Photonics 1, 303 - 305 (2007).
16. G. E. Moore, "Cramming more components onto integrated circuits," Electronics 38, 114-117 (1965).
17. Semiconductor Industry Association, 2007 International Technology Roadmap for Semiconductors, Interconnect (2007).
18. D. A. B. Miller and H. M. Ozaktas, "Limit to the Bit-Rate Capacity of Electrical Interconnects from the Aspect Ratio of the System Architecture," Special Issue on Parallel Computing with Optical Interconnects, J. Parallel and Distributed Computing 41, 4252 (1997).
19. D. A. B. Miller, "Optical Interconnects to Silicon," IEEE Journal of Selected Topics in Quantum Electronics 6, 1312-1317 (2000).
20. http://newsroom.intel.com/community/intel_newsroom/blog/2011/05/04/intel-reinvents-transistors-using-new-3-d-structure. (Retrieved on 5 November 2011)
21. L. Wood, "Shining a light on the chip-interconnect bottleneck," Computerworld, 9 February, 2011
22. T. Trader, "Without Silicon Photonics, Moore's Law Won't Matter," HPCwire, 9 February, 2011.
23. <http://techresearch.intel.com/ResearchAreaDetails.aspx?Id=26> (Intel Silicon photonics research, retrieved on 6 November 2011)
24. D. A. Muller, "A sound barrier for silicon?," Nature Materials 4, 645 - 647 (2005)
25. "Intel® Multi-Core Technology," http://www.intel.com/p/en_US/embedded/hwsw/technology/multi-core (retrieved on 21 January 2012).
26. J. Miller, J. Psota, G. Kurian, N. Beckmann, J. Eastep, J. Liu, M. Beals, J. Michel, L. Kimerling, A. Agarwal, "ATAC: A Many core Processor with On-Chip Optical Network," Computer Science and Artificial Intelligence Laboratory Technical Report, May 5, 2009.
27. D. A. B. Miller, "Physical Reasons for Optical Interconnection," Special Issue on Smart Pixels, Int. J. Optoelectronics 11 (3), 155-168 (1997).

28. D. A. B. Miller, "Rationale and Challenges for Optical Interconnects to Electronic Chips," Proceedings of the IEEE 88 (6), 728-749 (2000).
29. K. G. Koffman and A. M. Odzko, "Growth of the Internet," AT&T Labs. Research (2001).
30. L. Pavesi, "Introduction to silicon photonics," Silicon photonics course by Helios FP7 European project (2010).
31. <http://techresearch.intel.com/ResearchAreaDetails.aspx?Id=26>, (Intel Silicon photonics research, retrieved on 6 November 2011).
32. G.T. Reed, "Silicon Photonics: The State of the Art," Wiley (2008).
33. <http://www.intel.de/pressroom>, "Photonics – The key technology for tomorrow's computers and entertainment electronics," (2010).
34. M. Paniccia, "Integrating silicon photonics," Nature Photonics 4, 498-499 (2010).
35. http://www.intel.com/pressroom/archive/releases/2010/20100727comp_sm.htm?iid=pr1marqmain_si-photonics, "The 50 Gbps photonic link: a research milestone from Intel labs" (Retrieved on 6 November 2011).
36. Y.A. Vlasov, S. Assefa, W. M. J. Green, M. Yang, C. L. Schow, A. Rylyakov, "CMOS integrated nanophotonics: enabling technology for exascale computer Systems," SEMICON, SEMI Technology Symposium (STS), Tokyo (2010).
37. B. J. Offrein, "Silicon Photonics Packaging Requirements," Silicon Photonics Workshop," Munich Trade Fair Center, Munich (2011).
38. A.W. Fang, H. Park, O. Cohen, R. Jones, M.J. Paniccia and J.E. Bowers, "Electrically pumped hybrid AlGaInAs silicon evanescent laser," Optics Express 14(20), 9203-9210 (2006).
39. G. Morthier, R. Kumar, F. Raineri, R. Raj, J. Hofrichter, N. Chrysos, B.J. Offrein, R. Zhang, J. van der Tol, O. Raz, H. Dorren, "Overview of the EU FP7-project HISTORIC," Proceedings of SPIE - Silicon Photonics and Photonic Integrated Circuits II (invited), 7719 (2010).
40. J. Van Campenhout, P. Rojo Romeo, P. Regreny, C. Seassal, D. Van Thourhout, S. Verstuyft, L. Di Cioccio, J.-M. Fedeli, C. Lagahe, R. Baets, "Electrically pumped InP-based micro disk lasers integrated with a nanophotonic silicon-on-insulator waveguide circuit," Optics Express 15(11), 6744-6749 (2007).

41. F. Mandorlo, P.R. Romeo, J.M. Fedeli, H.M.D. Sohrab, R. Orobtcouk, "Mode Density Reduction and Coupling in Microdisk LASERs Processed on a 200-mm CMOS Pilot Line," *IEEE Photonics Technology Letters* 23, 1183-1185 (2011).
42. M. Lamponi, S. Keyvaninia, C. Jany, F. Poingt, F. Lelarge, G. de Valicourt, G. Roelkens, D. Van Thourhout, S. Messaoudene, J.-M. Fédéli, and G.H. Duan, "Low-threshold heterogeneously integrated InP/SOI lasers with a double adiabatic taper coupler," *IEEE photonics technology letters* 24, 76-78 (2011).
43. T. Chu, N. Fujioka, and M. Ishizaka, "Compact, lower-power-consumption wavelength tunable laser fabricated with silicon photonic-wire waveguide micro-ring resonators," *Opt. Express* 17, 14063-14068 (2009).
44. Q.Xu, B. Schmidt, S. Pradhan, and M. Lipson, "Micrometre-scale silicon electroopticModulator," *Nature* 435, 325–327 (2005).
45. W. M. J. Green, M. J. Rooks, L. Sekaric, and Y. A. Vlasov, "Ultra-compact, low RF power, 10 Gb/s silicon Mach-Zehnder modulator," *Optics Express* 15(25), 17106–17113 (2007).
46. L. Liao, A. Liu, D. Rubin, J. Basak, Y. Chetrit, H. Nguyen, R. Cohen, N. Izhaky, and M. Paniccia, "40 Gbit/s silicon optical modulator for high speed applications," *Electronics Letter* 43(22), 1196–1197 (2007).
47. D. Marris-Morini, L. Vivien, J. M. Fédéli, E. Cassan, P. Lyan, and S. Laval, "Low loss and high speed silicon optical modulator based on a lateral carrier depletion structure," *Optics Express* 16(1), 334–339 (2008).
48. M. Ziebell, D. Marris-Morini, G. Rasigade, J.-M. Fédéli, P. Crozat, E. Cassan, D. Bouville, and L. Vivien, "40 Gbit/s low-loss silicon optical modulator based on a pipin diode," *Opt. Express* 20, 10591-10596 (2012).
49. A. Brimont, D. J. Thomson, P. Sanchis, J. Herrera, F.Y. Gardes, J. M. Fedeli, G. T. Reed, and J. Martí, "High speed silicon electro-optical modulators enhanced via slow light propagation," *Optics Express* 19, 20876-20885 (2011).
50. F. Y. Gardes, D. J. Thomson, N. G. Emerson, and G. T. Reed, "40 Gb/s silicon photonics modulator for TE and TM polarisations," *Optics Express* 19, 11804-11814(2011).
51. D. J. Thomson, F. Y. Gardes, Y. Hu, G. Mashanovich, M. Fournier, P. Grosse, J-M. Fedeli, and G. T. Reed, "High contrast 40 Gbit/s optical modulation in silicon," *Optics Express* 19, 11507-11516 (2011).

52. N.-N. Feng, S. Liao, D. Feng, P. Dong, D. Zheng, H. Liang, R. Shafiqi, G. Li, J. E. Cunningham, A. V. Krishnamoorthy, and M. Asghari, "High speed carrier-depletion modulators with 1.4V-cm $V_{\pi L}$ integrated on 0.25 μ m silicon-on-insulator waveguides," *Optics Express* 18, 7994-7999 (2010).
53. T.-Y. Liow, K.-W. Ang, Q. Fang, J.-F. Song, Y.-Z. Xiong, M.-B. Yu, G.-Q. Lo, and D.-L. Kwong, "Silicon modulators and germanium photodetectors on SOI: monolithic integration, compatibility and performance optimization," *IEEE Journal of Selected Topics in Quantum Electronics* 16(1), 307–315 (2010).
54. M. R. Watts, W. A. Zortman, D. C. Trotter, R. W. Young, and A. L. Lentine, "Low-voltage, compact, depletion-mode, silicon Mach Zehnder modulator," *IEEE Journal of Selected Topics in Quantum Electronics* 16(1), 159–164 (2010).
55. H. Yu, W. Bogaerts, K. Komorowska, R. Baets, D. Korn, L. Alloatti, D. Hillerkuss, C. Koos, W. Freude, J. Leuthold, J. Van Campenhout, P. Verheyen, J. Wouters, M. Moelants, P. Absil, "Doping Geometries for 40G Carrier-Depletion-Based Silicon Optical Modulators," *OFC/NFOEC 2012, United States*, (2012).
56. L. Alloatti, D. Korn, R. Palmer, D. Hillerkuss, J. Li, A. Barklund, R. Dinu, J. Wieland, R. Fournier, J.-M. Fedeli, H. Yu, W. Bogaerts, P. Dumon, R. Baets, C. Koos, W. Freude, J. Leuthold, "42.7 Gbit/s electro-optic modulator in silicon technology," *Optics Express* 19(12), 11841-11851 (2011).
57. T. Yin, R. Cohen, M. M. Morse, G. Sarid, Y. Chetrit, D. Rubin, and M. J. Paniccia, "31 GHz Ge n-i-p waveguide photodetectors on Silicon-on-Insulator substrate," *Optics Express* 15(21), 13965–13971 (2007).
58. L. Vivien, J. Osmond, J. M. Fédéli, D. Marris-Morini, P. Crozat, J. F. Damlencourt, E. Cassan, Y. Lecunff, and S. Laval, "42 GHz p.i.n Germanium photodetector integrated in a silicon-on-insulator waveguide," *Optics Express* 17(8), 6252–6257 (2009).
59. D. Ahn, C. Y. Hong, J. Liu, W. Giziewicz, M. Beals, L. C. Kimerling, J. Michel, J. Chen, and F. X. Kärtner, "High performance, waveguide integrated Ge photodetectors," *Optics Express* 15(7), 3916–3921 (2007).
60. M. Jutzi, M. Berroth, G. Wöhl, M. Oehme, and E. Kasper, "Ge-on-Si Vertical Incidence Photodiodes with 39-GHz Bandwidth," *IEEE Photonics Technology Letters* 17, 1510-1512 (2005).

61. S. Liao, N.-N. Feng, D. Feng, P. Dong, R. Shafiiha, C.-C. Kung, H. Liang, W. Qian, Y. Liu, J. Fong, J. E. Cunningham, Y. Luo, and M. Asghari, "36 GHz submicron silicon waveguide germanium photodetector," *Optics Express* 19, 10967-10972 (2011).
62. S. Assefa, F. Xia, S. W. Bedell, Y. Zhang, T. Topuria, P. M. Rice, and Y. A. Vlasov, "CMOS-integrated high-speed MSM germanium waveguide photodetector," *Optics Express* 18, 4986-4999 (2010).
63. J. Wang, W. Y. Loh, K. T. Chua, H. Zang, Y. Z. Xiong, S. M. F. Tan, M. B. Yu, S. J. Lee, G. Q. Lo, and D. L. Kwong, "Low-voltage high-speed (18GHz/1V) evanescent-coupled thin-film-Ge lateral PIN photodetectors integrated on Si waveguide," *IEEE Photonics Technology Letters* 20(17), 1485–1487 (2008).
64. L. Chen, and M. Lipson, "Ultra-low capacitance and high speed germanium photodetectors on silicon," *Optics Express* 17(10), 7901–7906 (2009).
65. L. Vivien, A. Polzer, D. Marris-Morini, J. Osmond, J. M. Hartmann, P. Crozat, E. Cassan, C. Kopp, H. Zimmermann, and J. M. Fédéli, "Zero-bias 40Gbit/s germanium waveguide photodetector on silicon," *Opt. Express* 20, 1096-1101 (2012).
66. Y.-H. Kuo, "Germanium-Silicon electroabsorption modulators," PhD dissertation, Stanford University, June 2006.
67. D. A. B. Miller, 'Optical interconnects to electronic chips', *Applied Optics* 49(25), F59–70 (2010).
68. K. Wada, "A new approach of electronics and photonics convergence on Si CMOS platform: How to reduce device diversity of photonics for integration," *Advances in Optical Technologies* 2008, 807457-1 - 807457-7 (2008).
69. M.E. Groenert, C.W. Leitz, A.J. Pitera, V. Yang, H. Lee, R.J. Ram and E.A. Fitzgerald, "Monolithic integration of room-temperature cw GaAs/AlGaAs lasers on Si substrates via relaxed graded GeSi buffer layers," *Journal of Applied Physics* 93(1), 362-367 (2003).
70. H. Liu, T. Wang, Q. Jiang, R. Hogg, F. Tutu, F. Pozzi, A. Seeds, "Long-wavelength InAs/GaAs quantum-dot laser diode monolithically grown on Ge substrate," *Nature Photonics* 5, 416-419 (2011).
71. R. Chen, T.-T. D. Tran, K. W. Ng, W. S. Ko, L. C. Chuang, F. G. Sedgwick, and C. C.-Hasnain, "Nanolasers grown on silicon," *Nature Photonics* 5, 170-175(2011).

72. Y. Ishikawa, K. Wada, J. F. Liu, D. D. Cannon, H. C. Luan, J. Michel and L. C. Kimerling, "Strain-induced enhancement of near-infrared absorption in Ge epitaxial layers grown on Si substrate," *Journal of Applied Physics* 98,013501(2005).
73. J. Liu, M. Beals, A. Pomerene, S. Bernardis, R. Sun, J. Cheng, L. C. Kimerling and J. Michel, "Waveguide-integrated, ultralow-energy GeSi electro-absorption modulators," *Nature Photonics* 2,433 - 437 (2008).
74. S. Jongthammanurak, J. F. Liu, K. Wada, D. D. Cannon, D. T. Danielson, D. Pan, L. C. Kimerling and J. Michel, "Large electro-optic effect in tensile strained Ge-on-Si films," *Applied Physics Letters* 89, 161115 (2006).
75. J. Liu, X. Sun, D. Pan, X. Wang, L. C. Kimerling, T. L. Koch, and J. Michel, "Tensile-strained, n-type Ge as a gain medium for monolithic laser integration on Si," *Optics Express* 15, 11272–11277, (2007).
76. J. Liu, X. Sun, R. C.-Aguilera, L. C. Kimerling, and J. Michel, "Ge-on-Si laser operating at room temperature," *Optics Letter* 35, 679-681 (2010).
77. R. E. Camacho-Aguilera, Y. Cai, N. Patel, J. T. Bessette, M. Romagnoli, L. C. Kimerling, and J. Michel, "An electrically pumped germanium laser," *Opt. Express* 20, 11316-11320 (2012).
78. S.-L. Cheng, J. Lu, G. Shambat, H.-Y. Yu, K. Saraswat, J. Vuckovic, and Y. Nishi, "Room temperature 1.6 μm electroluminescence from Ge light emitting diode on Si substrate," *Opt. Express* 17, 10019 (2009).
79. T.-H. Cheng, C.-Y. Ko, C.-Y. Chen, K.-L. Peng, G.-L. Luo, C. W. Liu, and H.-H. Tseng, "Competitiveness between direct and indirect radiative transitions of Ge," *Applied Physics Letters* 96, 091105 (2010).
80. S.-L. Cheng, G. Shambat, J. Lu, H.-Y. Yu, K. Saraswat, T. I. Kamins, J. Vuckovic, and Y. Nishi, "Cavity-enhanced direct band electroluminescence near 1550 nm from germanium microdisk resonator diode on silicon," *Applied Physics Letters* 98, 211101 (2011).
81. M. de Kersauson, R. Jakomin, M. El Kurdi, G. Beaudoin, N. Zerounian, F. Aniel, S. Sauvage, I. Sagnes, and P. Boucaud, "Direct and indirect band gap room temperature electroluminescence of Ge diodes," *Journal of Applied Physics* 108, 023105 (2010).

82. N.-N. Feng, D. Feng, S. Liao, X. Wang, P. Dong, H. Liang, C.-C. Kung, W. Qian, J. Fong, R. Shafiiha, Y. Luo, J. Cunningham, A. V. Krishnamoorthy, and M. Asghari, "30GHz Ge electro-absorption modulator integrated with 3 μ m silicon-on-insulator waveguide," *Optics Express* 19, 7062-7067 (2011).
83. A. E.-J. Lim, T.-Y. Liow, F. Qing, N. Duan, L. Ding, M. Yu, G.-Q. Lo, and D.-L. Kwong, "Novel evanescent-coupled germanium electro-absorption modulator featuring monolithic integration with germanium p-i-n photodetector," *Optics Express* 19, 5040-5046 (2011).
84. Y. Luo, J. Simons, J. Costa, I. Shubin, W. Chen, B. Frans, M. Robinson, R. Shafiiha, S. Liao, N.-N. Feng, X. Zheng, G. Li, J. Yao, H. Thacker, M. Asghari, K. Goossen, K. Raj, A. V. Krishnamoorthy and J. E. Cunningham, "Experimental studies of the Franz-Keldysh effect in CVD grown GeSi_{0.1} on SOI," *Proc. SPIE* 7944, 79440P (2011).
85. R. K. Schaevitz, "Electroabsorption mechanisms in Germanium quantum well material," PhD dissertation, Stanford University, August 2011.
86. D. A. B. Miller, D. S. Chemla, T. C. Damen, A. C. Gossard, W. Wiegmann, T. H. Wood, and C. A. Burrus, "Band-edge electroabsorption in quantum well structures: the quantum-confined Stark effect," *Phys. Rev. Lett.* 53, 2173-2176 (1984).
87. D. Marris-Morini, L. Vivien, G. Rasigades, "Optical modulators in Silicon photonic circuits," Silicon photonics course by Helios FP7 European project (2010).
88. J. S. Weiner, D. A. B. Miller, D. S. Chemla, T. C. Damen, C. A. Burrus, T. H. Wood, A. C. Gossard, and W. Wiegmann, "Strong polarization sensitive electroabsorption in GaAs AlGaAs QW waveguide," *Appl. Phys. Lett.* 47, 1148 (1985).
89. K. Iga, F. Koyama, and S. Konoshita, "Surface emitting semiconductor lasers," *IEEE J. Quantum Electron.* 24, 1845-1855 (1988).
90. J. L. Jewell, A. Scherer, S. L. McCall, Y. H. Lee, S. Walker, J. P. Harbison, and L. T. Florez, "Low-threshold electrically pumped vertical-cavity surface-emitting microlasers," *Electron. Lett.* 25, 1123-1124 (1989).
91. P. Steinmann, B. Borchert, B. Stegmüller, "Improved behavior of monolithically integrated laser/modulator by modified identical active layer structure", *IEEE, Photonics Technology Letters* 9, 1561-1563 (1997).

92. W. Kobayashi, M. Arai, T. Yamanaka, N. Fujiwara, T. Fujisawa, T. Tadokoro, K. Tsuzuki, Y. Kondo, and F. Kano, "Design and Fabrication of 10-/40-Gb/s, Uncooled Electroabsorption Modulator Integrated DFB Laser With Butt-Joint Structure," *J. Lightwave Technol.* 28, 164-171 (2010).
93. Hideki Fukano, Takayuki Yamanaka, and Munehisa Tamura, "Design and Fabrication of Low-Driving-Voltage Electroabsorption Modulators Operating at 40 Gb/s," *J. Lightwave Technol.* 25, 1961-1969 (2007).
94. J. E. Bowers and Y. G. Wey, High-speed photodetectors. In M. Bass, editor, *Handbook of Optics: Fundamentals, Techniques and Design*, McGraw-Hill Inc., 2nd edition (1995).
95. A. Larsson, P.A. Andrekson, S.T. Eng, and A. Yariv, "Tunable superlattice pin photodetectors: Characteristics, theory, and applications," *IEEE J. Quantum Electron.* QE-24, 787, 1988.
96. Y.-H. Kuo, Y. K. Lee, Y. Ge, S. Ren, J. E. Roth, T. I. Kamins, D. A.B. Miller, and J. S. Harris, "Strong quantum-confined Stark effect in a germanium quantum-well structures on silicon," *Nature* 437, 1334–1336 (2005).
97. Y.-H. Kuo, Y. K. Lee, Y. Ge, S. Ren, J. E. Roth, T. I. Kamins, D. A. B. Miller, and J. S. Harris Jr., "Quantum-confined stark effect in Ge/SiGe quantum wells on Si for optical modulators," *IEEE J. Sel. Top. Quantum Electron.* 12, 1503-1513 (2006).
98. D. A.B. Miller, "Rationale and devices for optical interconnects to chips," CIOMP-OSA international summer session: Lasers and their applications, Changchun, China (2011).
99. R. People, "Physics and applications of $\text{Ge}_x\text{Si}_{1-x}/\text{Si}$ strained-layer heterostructure," *IEEE J. Quantum. Electron.* 22 (9), 1696-1709 (1986).
100. F. Schaffler, "High-mobility Si and Ge structures," *Semicond. Sci. Technol.* 12 (12), 1515–1549 (1997).
101. J. D. Cressler, "SiGe HBT technology: a new contender for Si-Based RF and microwave circuit applications," *IEEE Trans. Microw. Theory Tech.* 46 (5), 572–589 (1998).
102. E. O. Kane, "Band Structure of Indium Antimonide," *J. Phys. Chem. Solids* (1), 249–261 (1957).
103. M. Cardona and F. H. Pollak, "Energy-band structure of germanium and silicon: the k,p method," *Phys. Rev.* 142 (2), 530–543 (1996).
104. G. G. MacFarlane, T. P. McLean, J. E. Quarrington, and V. Roberts, "Fine structure in the absorption-edge spectrum of Ge," *Phys. Rev.* 108 (6), 1377–1383, (1957).

105. W. C. Dash and R. Newman, "Intrinsic Optical Absorption in Single-Crystal Germanium and Silicon at 77 K and 300 K," *Phys. Rev.* 99 (4), 1151-1155 (1955).
106. S. Galdin, P. Dollfus, V. Aubry-Fortuna, P. Hesto, and H. J. Osten, "Band offset predictions for strained group IV alloys: $\text{Si}_{1-x-y}\text{Ge}_x\text{C}_y$ on Si(001) and $\text{Si}_{1-x}\text{Ge}_x$ on $\text{Si}_{1-z}\text{Ge}_z(001)$," *Semicond. Sci. Technol.* 15 (6), 565–572 (2000).
107. G. E. Stillman, V. M. Robbins, N. Tabatabaie, "III-V compound semiconductor devices: optical detectors," *IEEE Trans. Electron. Devices*, vol.31, no. 11, pp. 1643-1655, Nov. 1984.
108. J. Weber and M. I. Alonso, "Near-band-gap photoluminescence of Si-Ge alloys" *Physical Review B* 40, 5683-5693(1989).
109. M. Bonfanti, "Ge Multiple Quantum Wells Electronic States and Optical Properties," PhD dissertation, Università Degli studi di Milano-Bicocca, 2008.
110. S. A. Claussen, E. Tasyurek, J. E. Roth, and D. A. B. Miller, "Measurement and modeling of ultrafast carrier dynamics and transport in germanium/silicon-germanium quantum wells," *Optics Express* 18, 25596-25607(2010).
111. J. S. Weiner, D. S. Chemla, D. A. B. Miller, H. A. Haus, A. C. Gossard, W. Wiegmann, and C. A. Burrus, "Highly anisotropic optical properties of single quantum well waveguides," *Applied Physics Letters* 47 , 664–667 (1985).
112. J. E. Roth, O. Fidaner, R. K. Schaevitz, Y.-H. Kuo, T. I. Kamins, J. S. Harris, and D. A. B. Miller, "Optical modulator on silicon employing germanium quantum wells," *Opt. Express* 15, 5851-5859 (2007).
113. J. E. Roth, O. Fidaner, E. E. Englund, R. K. Schaevitz, Y.-H. Kuo, N.C. Helman, T. I. Kamins, J. S. Harris, and D. A. B. Miller, "C-band side-entry Ge quantum well electroabsorption modulator on SOI operating at 1 volt swing," *Electron. Lett.* 44, 49–50 (2008).
114. S. Tsujino, H. Sigg, G. Mussler, D. Chrastina, and H. von Känel "Photocurrent and transmission spectroscopy of direct-gap interband transitions in Ge/SiGe quantum wells," *Appl. Phys. Lett.* 89, 262119 (2006).
115. O. Fidaner, A. K. Okay, J. E. Roth, R. K. Schaevitz, Y.-H. Kuo, K.C. Saraswat, J.S. Harris, and D. A. B. Miller, "Ge-SiGe quantum-well waveguide photodetectors on silicon for the near-infrared," *IEEE Photon. Tech. Lett.* 19, 1631–1633(2007).

116. L. Lever, Y. Hu, M. Myronov, X. Liu, N. Owens, F. Y. Gardes, I. P. Marko, S. J. Sweeney, Z. Ikonić, D. R. Leadley, G. T. Reed, and R. W. Kelsall, "Modulation of the absorption coefficient at 1.3 μm in Ge/SiGe multiple quantum well heterostructures on silicon," *Opt. Lett.* 36, 4158-4160 (2011).
117. R. K. Schaevitz, D. S. Ly-Gagnon, J. E. Roth, E. H. Edwards, and D. A. B. Miller, "Indirect absorption in germanium quantum wells," *AIP Advances* 1, 032164 (2011).
118. S. Ren, Y. Rong, S. A. Claussen, R. K. Schaevitz, T. I. Kamins, J. S. Harris, and D. A. B. Miller, "Ge/SiGe quantum well waveguide modulator monolithically integrated with SOI waveguides," *IEEE Photon. Technol. Lett.* 24, 461 – 463 (2012).
119. E. Gatti, E. Grilli, M. Guzzi, D. Chrastina, G. Isella, and H. von Känel, "Room temperature photoluminescence of Ge multiple quantum wells with Ge-rich barriers," *Appl. Phys. Lett.* 98, 031106 (2011).
120. E. Gatti, E. Grilli, M. Guzzi, D. Chrastina, G. Isella, A. Chernikov, V. Bornwasser, N. Köster, R. Woscholski, and S. Chatterjee, "Photoluminescence and ultrafast inter-subband relaxation in Ge/SiGe multiple quantum wells," *Phys. Rev. B* 84, 245319 (2011).
121. G. Isella, D. Chrastina, B. Rössner, T. Hackbarth, H.-J. Herzog, U. König, H. von Känel, "Low-energy plasma-enhanced chemical vapor deposition for strained Si and Ge heterostructures and devices," *Solid-State Electronics* 48, 1317–1323 (2004).
122. T. Hackbarth, H. J. Herzog, M. Zeuner, G. Höck, E. A. Fitzgerald, M. Bulsara, C. Rosenblatt, H. von Känel, "Alternatives to thick MBE-grown relaxed SiGe buffers," *Thin Solid Films* 369 148-151 (2000).
123. S. B. Samavedam, and E. A. Fitzgerald, "Novel dislocation structure and surface morphology effects in relaxed Ge/Si-Ge(graded)/Si structures," *J. Appl. Phys.* 81, 3108 (1997).
124. H. von Känel, M. Kummer, G. Isella, E. Müller, and T. Hackbarth., "Very high hole mobilities in modulation-doped Ge quantum wells grown by low-energy plasma enhanced chemical vapor deposition," *Appl. Phys. Lett.* 80, 2922 (2002).
125. M. Rondanini, C. Cavallotti, D. Ricci, D. Chrastina, G. Isella, T. Moiseev, and H. von Känel, "An experimental and theoretical investigation of a magnetically confined dc plasma discharge," *J. Appl. Phys.* 104, 013304 (2008).

126. M. Rondaninia, S. Ceredab, F. Montalentib, L. Migliob, C. Cavallottia, “A multiscale model of the plasma assisted deposition of crystalline silicon,” *Surf. Coat. Technol.* 201 (22-23), pp. 8863-8867 (2007).
127. <http://lness.como.polimi.it/lepecvd.php>
128. <http://www.microchemicals.com/>
129. M. Virgilio, M. Bonfanti, D.Chrastina, A. Neels, G. Isella, E. Grilli, M. Guzzi, G. Grosso, H. Sigg, H. von Känel, “Polarization-dependent absorption in Ge/SiGe multiple quantum wells: Theory and experiment,” *Phys. Rev. B* 79, 075323, (2009).
130. P. Blood, “On the dimensionality of optical absorption, gain, and recombination in quantum-confined structures,” *IEEE Journal of Quantum Electronics* 36, 354–362 (2000).
131. D. A. B. Miller, D. S. Chemla, T. C. Damen, A. C. Gossard, W. Wiegmann, T. H. Wood and C. A. Burrus, “Electric Field Dependence of Optical Absorption near the Bandgap of Quantum Well Structures,” *Phys. Rev. B* 32, 1043-1060 (1985).
132. W. Bogaerts, “Silicon Photonics meets CMOS,” UKSP/HELIOS Silicon Photonics Summer School, University of St Andrews, 4 – 8 July 2011.
133. H. R. Philipp, and E. A. Taft, “Optical Constants of Germanium in the Region 1 to 10 ev,” *Phys. Rev.* 113, 1002–1005 (1959).
134. M. K. Chin, “A simple method using photocurrent and power transmission for measuring the absorption coefficient in electroabsorption modulators,” *IEEE Photon. Technol. Lett.* 4, 866 (1992).
135. G. Bastard, *Wave Mechanics Applied to Semiconductor Heterostructures*, New York, NY: Halstead Press (Les Editions de Physique), 1988.
136. J. Piprek, *Semiconductor Optoelectronic Devices: Introduction to Physics and Simulation*, Waltham Massachusetts, Academic Press, 1 edition, 2003.
137. D. Chemla, D. Miller, P. Smith, A. Gossard, W. Wiegmann, “Room temperature excitonic nonlinear absorption and refraction in GaAs/AlGaAs multiple quantum well structures,” *IEEE Journal of Quantum Electronics* 20, 265 – 275 (1984).
138. M. Virgilio and G. Grosso, “Quantum-confined Stark effect in Ge/SiGe quantum wells: A tight-binding description,” *Phys. Rev. B* 77, 165315 (2008).

139. R. K. Schaevitz, E. H. Edwards, J. E. Roth, E. T. Fei, Y. Rong, P. Wahl, T. I. Kamins, J. S. Harris, and D. A. B. Miller, "Simple electroabsorption calculator for designing 1310nm and 1550nm modulators using germanium quantum wells," *IEEE J. Quantum Electron.* 48, 187 – 197 (2012).
140. T. I. Kamins, "Pattern sensitivity of selective Si_{1-x}Ge_x chemical vapor deposition: pressure dependence," *J. Appl. Phys.* 74, 5799-5802 (1993).
141. J. Osmond, L. Vivien, J. M. Fédéli, D. Marris-Morini, P. Crozat, J. F. Damlencourt, E. Cassan, and Y. Lecunff, "40 Gb/s surface-illuminated Ge-on-Si photodetectors," *Appl. Phys. Lett.* 95, 151116 (2009).
142. T. H. Loh, H. S. Nguyen, R. Murthy, M. B. Yu, W. Y. Loh, G. Q. Lo, N. Balasubramanian, D. L. Kwong, J. Wang, and S. J. Lee, "Selective epitaxial germanium on silicon-on-insulator high speed photodetectors using low-temperature ultrathin Si_{0.8}Ge_{0.2} buffer," *Appl. Phys. Lett.* 91, 073503 (2007).
143. D. Feng, S. Liao, P. Dong, N.-N. Feng, H. Liang, D. Zheng, C.-C. Kung, J. Fong, R. Shafiiha, J. E. Cunningham, A. V. Krishnamoorthy, and M. Asghari, "High-speed Ge photodetector monolithically integrated with large cross-section silicon-on-insulator waveguide," *Appl. Phys. Lett.* 95, 261105 (2009).
144. Y.-H. Kuo, H.-W. Chen, and J. E. Bowers, "High speed hybrid silicon evanescent electroabsorption modulator," *Opt. Express* 16, pp. 9936–9941 (2008).
145. K. Wakita, Y. Kawamura, Y. Yoshikuni, H. Asahi, and S. Uehara, "Anisotropic electroabsorption and optical modulation in InGaAs/InAlAs multiple quantum well structures," *IEEE J. Quantum Electron.* QE-22, pp. 1831–1836 (1986).
146. D. H. Yeo, K. H. Yoon, H. R. Kim, and S. J. Kim, "Integration of waveguide-type wavelength demultiplexing photodetectors by the selective intermixing of an InGaAs–InGaAsP quantum-well structure," *IEEE J. Quantum Electron.* 37, pp. 824–829 (2001).
147. L. Pavesi, L. Dal Negro, C. Mazzoleni, G. Franzò, and F. Priolo, "Optical gain in silicon nanocrystals," *Nature* 408, 440 (2000).
148. J. Liu, X. Sun, L. C. Kimerling, and J. Michel, "Direct-gap optical gain of Ge on Si at room temperature," *Opt. Lett.* 34, 1738-1740 (2009).
149. M. de Kersauson, M. El Kurdi, S. David, X. Checoury, G. Fishman, S. Sauvage, R. Jakomin, G. Beaudoin, I. Sagnes, and P. Boucaud, "Optical gain in single tensile-strained germanium photonic wire," *Opt. Express* 19, 17925-17934 (2011).

150. J. R. Haynes and N. G. Nilsson, in Proc. VIIth Int. Conf. Phys. Semicond., Paris, France (Dunod, Paris, 1964), p. 21.
151. G. Jones, A. D. Smith, E. P. O'Reilly, M. Silver, A. T. R. Briggs, M. J. Fice, A. R. Adams, P. D. Greene, K. Scarrott, A. Vranic, "The influence of tensile strain on differential gain and Auger recombination in 1.5- μ m multiple-quantum-well lasers," IEEE Journal of Quantum Electronics 34,822 - 833 (1998).
152. Y. P. Varshni, Physica (Amsterdam) 34, 149 (1967).
153. S. Ren, Y. Rong, T. I. Kamins, J. S. Harris, and D. A. B. Miller, "Selective epitaxial growth of Ge/Si_{0.15}Ge_{0.85} quantum wells on Si substrate using reduced pressure chemical vapor deposition," Appl. Phys. Lett. **98**, 151108 (2011).
154. R. Braunstein, A. R. Moore, and F. Herman, "Intrinsic Optical Absorption in Germanium-Silicon Alloys," Phys. Rev. 109, 695–710 (1958).

Résumés: Cette thèse est consacrée à l'étude des propriétés optiques et optoélectroniques autour de la bande interdite directe des structures à puits quantiques Ge/SiGe pour la modulation, la photodétection et l'émission de lumière sur la plateforme silicium. Les principaux composants réalisés sont : un modulateur optique en guide d'onde, rapide et à faible puissance électrique, basé sur l'Effet Stark Confiné Quantiquement, les premières photodiodes Ge/SiGe dont le comportement fréquentiel est compatible avec les transmissions de données à 40 Gbit/s, et la première diode à électroluminescence à puits quantiques Ge/SiGe, basée sur la transition directe de ces structures et fonctionnant à température ambiante. Les caractérisations statiques et fréquentielles ont été réalisées sur l'ensemble des composants, qui ont tous été fabriqués avec la même structure épitaxiée et les mêmes procédés de fabrication. Des modèles théoriques simples ont ensuite été utilisés pour décrire et analyser les comportements observés. Finalement les études menées permettent de conclure que les structures à puits quantiques Ge/SiGe sont un candidat de choix pour la réalisation d'une nouvelle plateforme photonique à haut débit, totalement compatible avec les technologies silicium.

Resume : This PhD thesis is devoted to study electro-optic properties of Germanium/Silicon-Germanium (Ge/SiGe) multiple quantum wells (MQWs) for light modulation, detection, and emission on Si platform. It reports the first development of high speed, low energy Ge/SiGe electro-absorption modulator in a waveguide configuration based on the quantum-confined Stark effect (QCSE), demonstrates the first Ge/SiGe photodiode with high speed performance compatible with 40 Gb/s data transmission, and realizes the first Ge/SiGe light emitting diode based on Ge direct gap transition at room temperature. Extensive DC and RF measurements were performed on each tested prototype, which was realized using the same epitaxial growth and fabrication process. Simple theoretical models were employed to describe experimental properties of the Ge/SiGe MQWs. The studies show that Ge/SiGe MQWs could potentially be employed as a new photonics platform for the development of a high speed optical link fully compatible with silicon technology.